

SoLID (Solenoidal Large Intensity Device)
Updated Preliminary Conceptual Design Report

The SoLID Collaboration

November 2019

Contents

1	Executive Summary of the Responses to Recommendations from the 2015 Jefferson Lab Director's Review Committee	1
1.1	Overview	1
1.2	Physics Program	2
1.2.1	SIDIS Production of Charged Pions	2
1.2.2	PVDIS	3
1.2.3	J/ψ Production	3
1.3	Possible Expansions in the Physics Reach of SoLID	4
1.3.1	Generalized Parton Distributions (GPD)	4
1.3.2	SIDIS Production of Charged Kaons	6
1.4	Experimental Design, Simulation and Feasibility	6
1.4.1	Solenoidal Magnet	6
1.4.2	Acceptance, Efficiency and Systematics	7
1.4.3	Rates and Data Acquisition	8
1.5	Summary	9
2	Introduction and Overview of SoLID Experimental Programs	10
2.1	SoLID Project Introduction/Overview	10
2.1.1	Base Equipment Description	10
2.1.2	Dependencies to Base Equipment	10
2.1.3	Experiment-specific Dependencies	11
2.1.4	Enhancement to the Baseline Configuration	12
2.1.5	Research Program	12
2.2	SIDIS Program	13
2.2.1	Introduction	13
2.2.2	Transverse Structure and Semi-Inclusive Deep Inelastic Scattering	14
2.2.3	The Phenomenology TSSAs and TMDs	16
2.2.4	Overview of SIDIS program	17
2.2.5	Beam Time and Projections	18
2.2.6	Comparisons with SBS and CLAS12 SIDIS programs	20
2.2.7	SIDIS with Baseline and Enhanced Baseline Configurations	23
2.3	PVDIS Program	30
2.3.1	Motivation for PVDIS	30
2.3.2	Review of the Theory	30
2.3.3	Charge Symmetry Violation	32
2.3.4	Higher Twist	34
2.3.5	Data Sample and analysis	35
2.3.6	Beam Time and Projections	37
2.4	J/ψ Program	39
2.4.1	Introduction	39
2.4.2	Color Van der Waals forces	39
2.4.3	Emergence of hadron mass	40
2.4.4	LHCb charmed pentaquark	40
2.4.5	Overview of the J/ψ Program	41
2.4.6	Beam Time and Projections	42
2.5	Possible Expansion in Physics Reach	46

2.5.1	GPD Program	46
2.5.2	SIDIS Production of Charged Kaons	47
3	Technical Requirements and Experimental Setup	49
3.1	Summary of Requirements	49
3.2	SIDIS- ³ He Experiments	54
3.3	SIDIS-proton Experiment	57
3.4	PVDIS Experiment	59
3.5	J/ψ Experiment	61
4	Magnet	65
4.1	Requirements	65
4.2	SoLID magnet	65
4.3	Planned Modifications	66
4.4	Current Status	68
4.5	Planned Magnet Testing	69
5	Targets	71
5.1	Polarized ³ He Target	71
5.2	Transversely Polarized Proton Target	71
5.3	Cryogenic Target for PVDIS	74
6	Baffles	77
7	GEM Tracker	83
7.1	Design	83
7.2	GEM tracker Design Activities	93
7.2.1	GEM chamber construction facilities at UVA	93
7.2.2	GEM chamber programs in China	94
8	Light Gas Cherenkov	96
8.1	Design	96
8.1.1	Tank and Cherenkov Gas	96
8.1.2	Mirrors	96
8.1.3	PMTs	97
8.1.4	Magnetic Shielding and Winston Cones	97
8.2	Tank Support	99
8.3	Simulations	99
8.3.1	Collection Efficiencies	100
8.3.2	Background Rates	100
8.3.3	Pion Rejection	101
9	Heavy Gas Cherenkov	103
9.1	Design	103
9.1.1	Overview	103
9.1.2	Optical System	103
9.1.3	Tank and Window	104
9.2	Simulation	104
9.2.1	Photoelectron Yield	104

9.2.2	Pion Detection Efficiency and Kaon Rejection Factor	106
9.3	Performance of the PMTs in Magnetic Field	108
9.4	Gas and Gas System	108
10	Electromagnetic Calorimeter	111
10.1	Overview	111
10.2	Shower Detector Design Considerations	114
10.2.1	Total Length of the Calorimeter	114
10.2.2	Sampling Ratio	114
10.2.3	Lateral Size	115
10.3	Preshower Detector	116
10.4	Layout and Support	118
10.5	Light Readout	118
10.6	Radiation Effects	120
10.7	Performance	120
10.7.1	Intrinsic electron-pion separation	120
10.7.2	PID performance under realistic background simulation	123
10.7.3	Trigger capability	125
10.7.4	Shower Position Measurement	129
10.7.5	Supplemental Information: PID Selection Cuts	129
10.8	Scintillator Pad Detector (SPD) for SIDIS Experiments	131
10.9	EC Collaboration and Prototyping Status and Construction Outlook	133
11	MRPC	135
11.1	Overview	135
11.2	Structure of the MRPC Prototype	135
11.3	Gas system	135
11.4	Cosmic Ray Test	135
11.5	Beam Test at Hall A	137
11.5.1	Test Setup	137
11.5.2	HV Scan Result	138
11.5.3	Rate Scan Result	138
11.6	Radiation hardness and aging	138
11.7	Conclusions	139
11.8	R&D Plan for Better Time Resolution	139
12	Simulation and Reconstruction	147
12.1	End-to-End Software Framework	147
12.2	Simulation	149
12.2.1	Simulation Software	149
12.2.2	Simulation Status	150
12.2.3	Physics Event Generators	151
12.2.4	GEM Digitization	152
12.3	Reconstruction	152
12.3.1	Tracking	152
12.3.2	Additional Reconstruction Algorithms	156

13 Data Acquisition	157
13.1 Introduction and Requirements	157
13.1.1 SIDIS Trigger and Rate Estimate	158
13.1.2 J/ψ Trigger and Rate Estimate	158
13.1.3 PVDIS Trigger and Rate Estimate	158
13.1.4 Detector Rate and Occupancy	159
13.2 DAQ Hardware and Trigger	160
13.2.1 GEM readout	160
13.2.2 SIDIS Configuration	162
13.2.3 PVDIS Configuration	163
13.3 Event size from FADC	165
13.4 Data rates, event size, and tape storage	165
13.5 Hall DAQ installation	169
13.5.1 Experiment switch over	169
13.6 Managing data rates	170
13.7 Summary and Pre R&D plans	170
14 Radiation damage estimates and Activation	171
14.1 Radiation damage to GEM electronics	171
14.2 Power deposited	172
14.2.1 Power in 1st baffle (due to Möllers), (Cooling, activation)	173
14.2.2 Power in exit hole in magnet (elastics) (Cooling, activation)	173
14.2.3 Power in the entrance surface of the magnet (Cooling, activation) (external target configurations)	174
14.2.4 Heat load in magnet cryostat	175
14.3 Estimates for radiation damage in the Hall	176
14.3.1 Radiation damage to electronics in Hall	176
14.3.2 Radiation from beam pipe	177
14.3.3 Radiation with external targets	178
15 Slow Controls	185
15.1 General Requirements	185
15.2 Frontend GUIs	185
15.3 High/Low Voltage Controls	186
15.4 DAQ Crate Control	186
15.5 Gas Systems Requirements	186
15.6 Detector Systems	186
16 Electron Beam Polarimetry	187
16.1 The Hall A Compton Polarimeter	187
16.1.1 Laser System	188
16.1.2 Electron Detector	189
16.1.3 Photon Detector	190
16.1.4 Systematic Uncertainties in the Compton Polarimeter	191
16.2 Møller Polarimetry	197
16.3 The Hall A Møller Polarimeter	198

17 Integration and Expected Performance	202
17.1 Overview	202
17.2 SIDIS Program	202
17.3 PVDIS Program	206
17.3.1 Acceptances, efficiencies, and systematic uncertainties for PVDIS	206
17.3.2 Kinematics, Resolution and Calibration for PVDIS	208
17.4 J/ψ Program	213
18 Supports and Infrastructure	216
18.1 Magnet Support	216
18.2 Endcap Support Structure and Motion Mechanism	216
18.3 Support Structure for Equipment Located Inside Cryostat Bore	216
18.4 Power Requirements	216
19 Installation	218
19.1 Experimental Layout	218
19.2 Magnet Moving and Placement	218
19.3 Helium Dewar Support and Upper Access Platform	222
19.4 Endcap Forward Angle Detector Package Installation Structure	222
19.5 Large Angle Detector and Baffle Installation Mechanism	222
19.6 Light Gas Cherenkov Installation Structure	223
19.7 Installation Plan	223
Bibliography	224
Appendices	238
Appendix A Summary of Subsystems	238
A.1 Magnet	238
A.2 GEM	238
A.3 Light Gas Cherenkov	239
A.4 Heavy Gas Cherenkov	239
A.5 Electromagnetic Calorimeter and Scintillator-Pad Detector	239
A.6 MRPC	240
A.7 DAQ	240
Appendix B Software Development Effort Estimate	242
B.1 Total Effort Estimate	242
B.2 Comparison with GlueX	242
B.3 Effort Required for Project Goals	244

1 Executive Summary of the Responses to Recommendations from the 2015 Jefferson Lab Director’s Review Committee

1.1 Overview

To exploit the full potential of the Jefferson Lab (JLab) 12 GeV energy upgrade, a large acceptance high luminosity device, SoLID (Solenoidal Large Intensity Detector), was proposed for a rich and vibrant science program. Five SoLID experiments, one PVDIS (Parity-Violating Deep Inelastic Scattering), three SIDIS (Semi-Inclusive Deep Inelastic Scattering), and one J/ψ production, were approved with high ratings in 2010–2012 by the JLab Program Advisory Committee. After years of work by the collaboration, a robust, low risk and flexible design concept, capable of accomplishing this broad and varied physics program, was determined. A preliminary conceptual design report (pCDR) for SoLID was submitted to the JLab Director in 2014.

A JLab Director’s Review for SoLID was held in February 2015. The review committee concluded that SoLID was in a good state to move forward, but also identified a number of areas where additional work would be needed. Thirty-six recommendations were made in total (see Appendix ??), with some aiming at longer term efforts required by any project of similar magnitude, and others more specifically relevant for the nearer term. After discussions with the Physics Division and JLab management, the collaboration aspired to first address recommendations that are necessary to proceed with a Science Review as required for the DOE Critical Decision CD-0, while concurrently continuing to address the longer term recommendations to the extent possible with available resources. The collaboration completed this effort which culminated in a revised version of this pCDR document. The revised document was submitted, along with a change summary, to the review committee, who accepted it in October 2017, stating that the collaboration did “...an excellent job in addressing those recommendations in their updated Pre-CDR.” and “...the Committee believes that the SoLID Experiment is ready for its DOE Critical Decision Zero (CD0) Review.” To follow up regarding possibilities for the latter, a meeting was held in July 2018 at the DOE to discuss the SoLID plans and progress. All parties present at that meeting agreed that a cost update would be beneficial, thus this pCDR document was updated once more accordingly. A Director’s review focusing on the SoLID cost was conducted at Jefferson Lab in September, 2019. This pCDR has been revised once more following the excellent input from the review committee.

This chapter summarizes the preparatory work performed to reach the milestone of the DOE Science Review. It includes specific recommendations related to the three core measurements (SIDIS, PVDIS and J/ψ production), as well as ones related to the general performance of the instrumentation to reach the scientific goals. For PVDIS, the viability of the calibration procedure to determine Q^2 was studied including realistic misalignments of the detectors. The design of the baffles was re-examined including the choice of materials. For SIDIS, careful studies were performed to show the impact of SoLID compared to world data and other programs, including comparisons to projected data expected from the JLab CLAS12 and SBS programs. Examples of physics reach, such as measurements of the transversity distribution and tensor charge, were simulated and are presented in this document. For the J/ψ production, bin migration effects and trigger rates were simulated. Additional science topics that can be facilitated by SoLID, such as Generalized Parton Distributions and kaon identification in SIDIS, recommended in the review, were also considered and presented here.

Realistic simulations, as well as tracking and data acquisition development, have shown that the performance of the instrumentation will allow realization of SoLID scientific goals with the proposed design. The acceptances, efficiencies and systematic uncertainties were simulated in detail for each of the three core measurements. Meticulous magnet field modeling confirmed that the

forces are tolerable and, in particular, that the fringe field at the polarized target location in the ^3He SIDIS experiments can be controlled to the desired level. Effects of possible radiation damage were carefully evaluated. Significant progress has also been made in the development of a full simulation and a software framework for analysis.

Beyond the items listed above which were deemed critical to the near term path to a Science Review, work is continuing on the many recommended fronts. The coils, coil collars, and cryostat of the CLEO-II magnet arrived at JLab in 2016, and work on magnet instrumentation and controls has begun. In August 2019, the CLEO-II magnet iron pieces also arrived at JLab. Other activities include the development of GEM foil production in China and assessment of the associated risk factor, communication with expert groups in calorimeter design and R&D, and stability testing of the conductivity of MRPC glass. An initial study of the slow control system has been performed. A pre-R&D plan including a cost estimation was developed with inputs from the JLab management and has been submitted to DOE. Meanwhile, detector pre-R&D activities for some sub-systems are continuing and are supported by international collaborations (China and Canada), such as the calorimeter, the heavy gas Cherenkov counter, and the MRPC.

Our answers to all thirty-six recommendations from the Director’s Review Panel are summarized in the next few subsections, or merged into the original pCDR as updates. These recommendations with a brief answer to each one of them are included in Appendix ??.

At this stage, the collaboration considers the progress on SoLID to be adequately substantial to enable the next phase to begin, in particular a DOE Science Review. We therefore submit this recently revised pCDR, and look forward to subsequent guidance from the laboratory.

1.2 Physics Program

1.2.1 SIDIS Production of Charged Pions

The SoLID SIDIS program includes three approved experiments using transversely and longitudinally polarized ^3He targets and a transversely polarized proton (NH_3) target, respectively. With the combination of the high luminosity and the large acceptance with a full azimuthal coverage, the SoLID SIDIS experiments will allow for measurements in 4-dimensional bins with high statistics and well controlled systematics.

Compared to the CLAS12 and SBS SIDIS programs, SoLID has a better figure of merit (FOM) and thus higher statistics in the region $x = (0.05, 0.55)$, as shown in Figure 1. To demonstrate the physics impact of the SoLID SIDIS program, we performed the extraction of transversity based on [1, 2] with simulated data of CLAS12, SBS and SoLID, and compared the results in Figure 2. SoLID will improve the transversity uncertainty for u (d) quark by a factor of 3 (7) over CLAS12, and by a factor of 5 (10) compared to SBS. The tensor charge determination will have similar improvements which together with upcoming nucleon electric dipole moment (EDM) measurements will provide constraints on quark EDMs and consequently new physics beyond the Standard Model. The projected high precision results from SoLID will provide powerful tests of Lattice QCD calculations and more quantitative information about TMDs, and quark orbital angular momentum (OAM) contributions to the nucleon spin. The projected SoLID results shown in Fig. 1 and Fig. 2 are for the enhanced baseline configuration. In the baseline configuration where the international contributions are not accounted for, although the pion PID will be limited to momenta above 2.5 GeV/c, the impact of the SIDIS program remains very significant as shown in Section 2.2.7 (Figure 20 and Figure 21). The international contributions with the addition of MRPC detectors will enhance the pion PID to its full kinematic capability, namely for momenta above 1.0 GeV/c. The enhanced baseline configuration will enable the full impact offered by the 12-GeV upgrade as shown in Figure 20 and

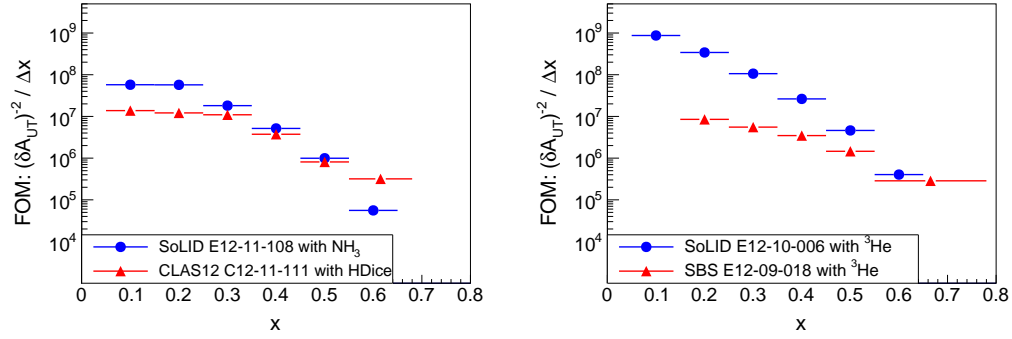


Figure 1: Comparisons of the FOM, defined as the sum of the inverse square of the statistical uncertainties of the single spin asymmetry (roughly proportional to statistics). The SoLID SIDIS experiment with the polarized NH_3 target is compared with the CLAS12 experiment in the left panel. The SoLID SIDIS experiments with polarized ^3He targets are compared with the SBS experiment in the right panel. In both comparisons, kinematic cuts of $W > 2.3 \text{ GeV}$ and $0.3 < z < 0.7$ are applied.

Figure 21 in Section 2.2.7.

1.2.2 PVDIS

The unique advanced feature of a large acceptance detector capable of operating in an extremely high luminosity environment that SoLID provides makes it possible to achieve the required high precision necessary to probe physics beyond the Standard Model (SM) of Particle Physics using parity violation deep inelastic scattering (PVDIS). Measurements of PVDIS on a deuterium target will determine the effective electron-quark neutral-weak coupling constants $2C_{2u} - C_{2d}$ that is inaccessible with other means. In a sufficiently sensitive measurement, the 6-GeV PVDIS collaboration published its result $2C_{2u} - C_{2d} = -0.145 \pm 0.068$ in Nature [3], showing for the first time that the C_{2q} are non-zero as predicted by the SM. PVDIS measurements in the valence quark region of large Bjorken x can also access a number of topics in hadronic physics, including searching for charge symmetry violation in the parton distribution functions and providing for a clean extraction of higher-twist effects caused by quark-quark correlations. PVDIS measurements on a hydrogen target at large Bjorken x will determine the d/u ratio in the proton without nuclear effects.

One way to quantify the reach of various experiments is to quote mass limits suitable for composite models [4], where the couplings are on the order of $4\pi/\Lambda^2$ with Λ being the compositeness mass scale. Such limits for the 6-GeV PVDIS Nature publication and the SoLID PVDIS experiment [5] are shown in Figure 3.

1.2.3 J/ψ Production

Hadrons, the emergent phenomena of QCD, are in the realm of the strong interaction region, where much of the dynamics of their constituents remains to be understood. While significant progress has been achieved in exploring QCD in its asymptotically free region, the theory in the strong coupling region is hardly tractable without numerical techniques. For example, an impressive success was achieved with the recent lattice QCD determination of the low-lying levels of the baryon spectrum [6] but there is a long road ahead to fully grasp the implications of QCD in this region, for

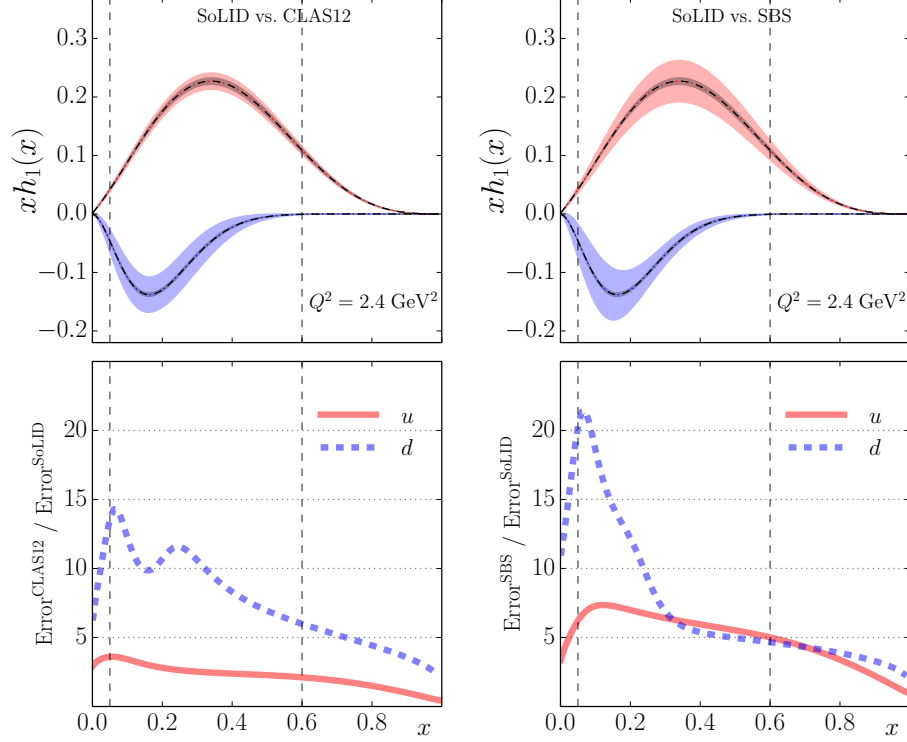


Figure 2: Comparisons of the impact on transversity extractions for up (red) and the down (blue) quarks, as the extension of published works [1, 2]. The left column shows the comparison between SoLID and CLAS12, and the right column shows the comparison between SoLID and SBS. In the upper panels, the light shaded bands show the uncertainties of the transversity function $h_1(x)$ expected from SBS or CLAS12, while the dark shaded bands show those expected from SoLID. The ratio of CLAS12 or SBS projected results to those of SoLID are displayed in the lower panels. All results are plotted at a typical JLab12 scale $Q^2 = 2.4 \text{ GeV}^2$.

example, to understand the origin of the nucleon mass.

The tandem of an impressive luminosity combined with the large acceptance detection offered by SoLID opens new opportunities for measurements of rare processes with unprecedented precision. In particular, measurement of the elastic production of J/ψ on the proton near threshold could provide unique and much needed information on the pure gluonic component of the QCD interaction, as well as to verify the nature of the charm “pentaquark” states recently observed at LHCb [7]. A measurement close to threshold (Figure 4), dominated by the real part of the scattering amplitude, where the cross section also drops rapidly can provide important independent information on the trace anomaly, which is responsible for most of the proton mass.

1.3 Possible Expansions in the Physics Reach of SoLID

1.3.1 Generalized Parton Distributions (GPD)

Once again the unique features of SoLID’s large acceptance and high luminosity make it an attractive device for the experimental study of GPDs. A number of groups have been working on developing a SoLID-GPD program. There are several GPD experiments in different stages of development. A proposal of Time-like Compton Scattering (TCS) from an unpolarized liquid hydrogen target has

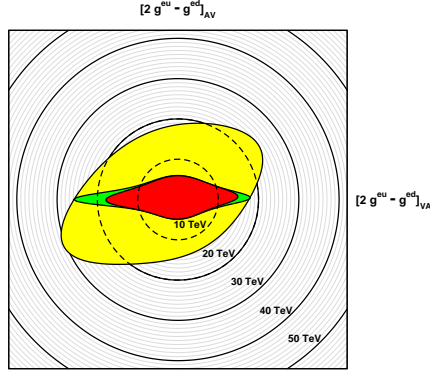


Figure 3: Projected mass limits for composite models from PVDIS. Red region is excluded by published data, and the green region is limit to be set by the Mainz P2 experiment. The projected reach with SoLID is in yellow.

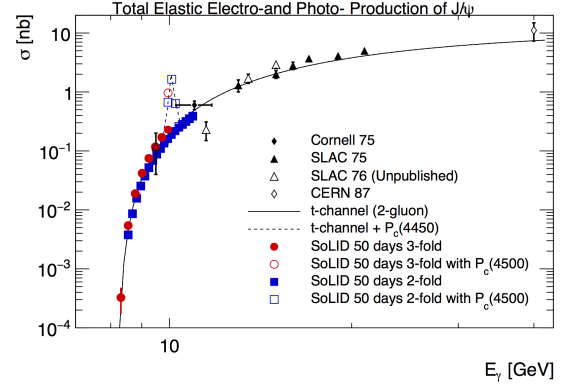


Figure 4: Projected uncertainties of total elastic J/ψ electro- and photo-production cross sections based on a 2-gluon exchange model including a projection of the LHCb pentaquark production assuming a coupling of 5%.

been approved as a run-group experiment to test the universality of GPDs, aiming to explore the underlying principles of factorization, and quantify the importance of higher twist effects. Double Deeply Virtual Compton Scattering (DDVCS) in the di-lepton channel on an unpolarized liquid hydrogen target was reviewed by the JLab PAC as a Letter-Of-Intent and the collaboration was encouraged to develop it as a two-stage program with the initial focus being a first significant DDVCS measurement (over a limited kinematic region) using the baseline SoLID setup. The Deep Exclusive Meson Production (DEMP) with the transversely polarized ^3He target has also been approved as a run-group experiment. A proposal for measurements of DVCS on a polarized ^3He is under development. These measurements, together with the planned CLAS12 and Hall A/C GPD experiments, will make significant contributions in disentangling different GPDs in the JLab 12-GeV kinematic region.

1.3.2 SIDIS Production of Charged Kaons

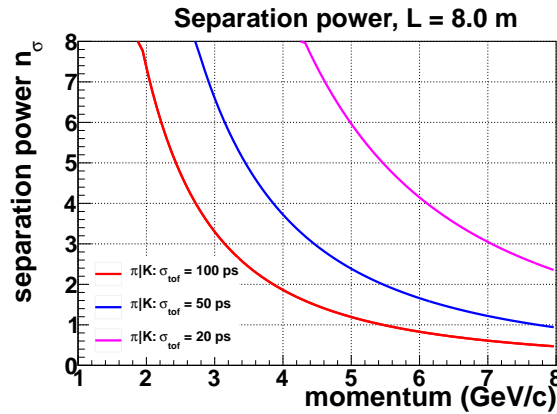


Figure 5: Kaon identification by TOF.

We have studied kaon identification with SoLID to potentially extend its physics program to the strange quark sector. Kaon identification is achievable via a detector enhancement of the SoLID baseline configuration that is being pursued by our international collaborators. While technically the implementation of a full RICH detector for kaon detection is a possible solution, a high resolution TOF is more practical given the cost of the former. SoLID needs kaon identification over a momentum range of 1 GeV/c to 7 GeV/c. Given the ~ 8 meter flight distance, a TOF resolution of 20 ps is required to obtain a 3 sigma separation between pions and kaons as shown in Figure 5. A promising avenue is to improve the timing of the planned SoLID TOF-MRPC detector in the enhanced baseline configuration. An R&D effort on the next generation MRPC technology for SoLID, sPHENIX and EIC is being actively pursued by a Chinese collaboration (Tsinghua University and USTC), aiming for a 20 ps resolution in a high-rate environment. Bench tests of thin-gap MRPC prototype detectors have demonstrated the potential to reach a resolution of sub-20 ps [8, 9], while 80 ps is the current standard. The Chinese collaboration has developed a prototype and readout electronics system already and has achieved a resolution of 17 ps from bench tests. The next steps are to carry out beam tests and finalize the detector and electronics design in a year.

1.4 Experimental Design, Simulation and Feasibility

While SoLID is a large and complex device, composed of many elements working in concert, no single element is high risk. A novel addition (high resolution MRPC) to the baseline SoLID detector configuration is being considered and developed by our international collaborators as noted, but we stress that the SoLID baseline design approach relies on existing, proven detector and magnet technology to achieve the goal of the core science program.

1.4.1 Solenoidal Magnet

The CLEO II magnet was removed from the CESR beamline by Cornell University and JLab personnel during the 2016 summer down. All ancillary power, cryogenic and control services were disconnected from the magnet in preparation for iron removal. The iron was removed layer by layer and stored at Cornell's laydown yard. With the cryostat exposed, the axial transport brackets were installed and the cryostat moved to the transport frame. The service turret and neck were removed to reduce the height of the cryostat for safe highway transit. The entire unit was wrapped in marine grade shrink wrap to provide a weather barrier for the trip to JLab. Three-axis accelerometers were mounted to the cryostat to monitor loads during the road trip. All loads remained under allowable thresholds specified in the Oxford CLEO II Operating Manual. Upon arrival at JLab in November 2016, the magnet was rolled into the Test Lab for climate controlled storage, as shown in Figure 6. In summer 2019, all the iron pieces were shipped to JLab and arrived in August 2019.



Figure 6: CLEO II magnet at JLab.

1.4.2 Acceptance, Efficiency and Systematics

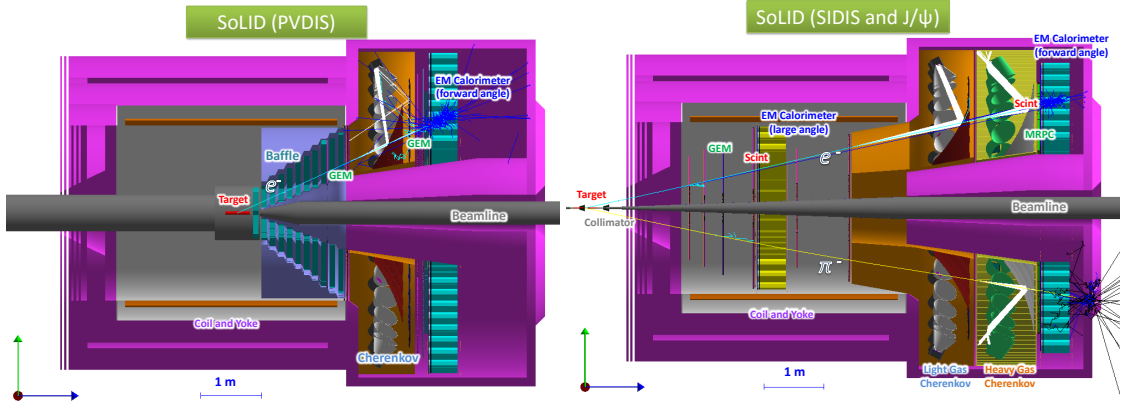


Figure 7: Left: SoLID PVDIS setup. Right: SoLID SIDIS and J/ψ setup.

The SoLID setups for the PVDIS and the SIDIS and J/ψ configurations are shown in Figure 7. Substantial progress has been made in developing a SoLID simulation package with realistic sub-system responses that includes all elements of the apparatus: EM showers in the electromagnetic calorimeter, optical processes in the two Cherenkov detectors, and energy deposition in the GEMs and MRPC and their digitizations. A new event generator was used for the estimation of hadron background rates. The simulation package allowed for detailed studies of the performance and feasibility of all core measurements, namely the PVDIS, SIDIS and J/ψ measurements.

Table 1: Average electron detection efficiencies of SoLID sub-detectors and the total SoLID efficiency.

Detector	EC	Cherenkov	Scintillator pad and MRPC	GEM tracking	Total
average efficiency	95%	95%	98%	90%	80%

A Kalman Filter based track finding and fitting algorithm is being developed and tested with

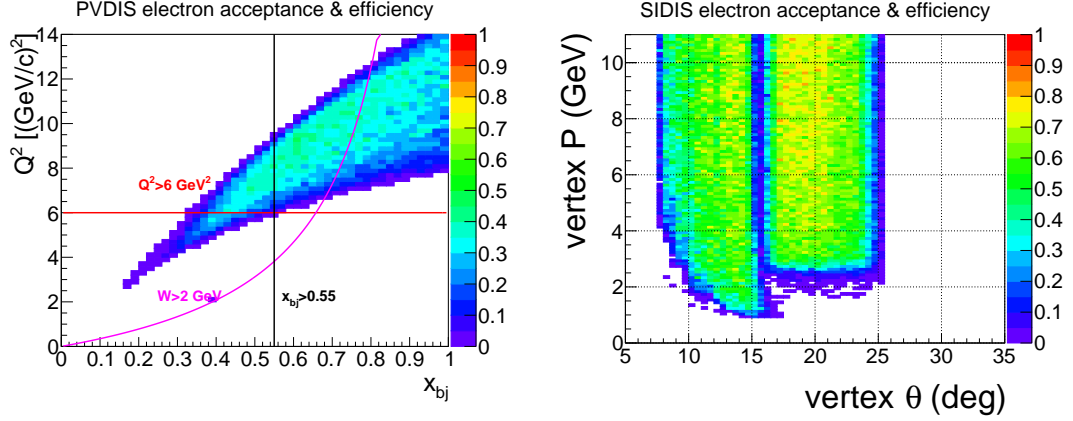


Figure 8: Left panel: electron acceptance and efficiency (except tracking) of SoLID PVDIS with the 40 cm LD2 target and the baffle. Curves show bounds of the kinematic range with $Q^2 > 6 \text{ GeV}^2$, $W > 2 \text{ GeV}$, and $x_{bj} > 0.55$. Right panel: electron acceptance and efficiency (except tracking) of SoLID SIDIS with the 40 cm ^3He target and two target window collimators. The result for J/ψ has a similar shape, but higher values because it has a 15 cm long target and no collimator.

digitized GEM simulation data. Tracking resolution from the simulated tracking fitting results including all material effects was studied. With background taken into account, the tracking efficiency was obtained with the simulation. We have good electron detection efficiency from all sub-detectors. They vary slightly across the phase space and the average efficiency values are shown in Table 1. The PVDIS setup with its 40 cm long LD₂ target has an acceptance of ~ 0.35 due to the baffle and the SIDIS setup with its 40 cm long ^3He target has an acceptance of ~ 0.7 due to the two target window collimators. Figure 8 shows the combined effect of acceptance and efficiency (except tracking) for the two configurations. Systematic uncertainties for PVDIS and SIDIS are summarized in Table 2. The total systematic uncertainty in the measurement of the absolute cross section for J/ψ is about 11%, dominated by the acceptance, while the bin-migration effect was found to be small. These results meet the requirements of the proposed science and were used as inputs to the physics projections.

Table 2: The systematic uncertainties on the asymmetry measurements of PVDIS and SIDIS.

PVDIS Systematic (rel.)		SIDIS Systematic (abs.)		SIDIS Systematic (rel.)	
Polarimetry	0.4%	Raw asymmetry	0.0014	Target polarization	3%
Q^2 determination	0.2%	Detector resolution	< 0.0001	Nuclear effects	(4 – 5)%
Radiative corrections	0.2%			Random coincidence	0.2%
Reconstruction errors	0.2%			Radiative corrections	(2 – 3)%
				Diffraction meson contam.	3%
Total	0.6%	Total	0.0014	Total	(6 – 7)%

1.4.3 Rates and Data Acquisition

The trigger rates were simulated with the full background, see Table 3. The SIDIS configuration, with an expected trigger rate of 100 kHz and total data rate of over 3 GB/s, represents the greatest

challenge for SoLID data acquisition. The recent performance of GlueX and HPS DAQs with extrapolations by the JLab data acquisition and fast electronics groups give confidence that trigger rates of 100 kHz and above are achievable. Data for each of the 30 sectors of SoLID will pass through two readout controllers (ROCs), a PC based ROC for GEM data, and a VME ROC for all other detectors. The portion of the total data rate for non-GEM detectors, about 400 MB/s, is less than 15 MB/s per VME crate, so will not limit the trigger rate at 100 kHz. The GEM readout will use the VMM3 which has a minimum rate capability of 100 kHz at full occupancy. The overall data rate required by SIDIS, which exceeds the rate currently achieved by GlueX, can be recorded by multiplexing data from the readout controllers to multiple event-building computers. Designing a DAQ system with 30 ROCs that can handle data rates of several GB/s will require some R&D, including firmware and software improvements, but is feasible using technology currently in use at JLab.

Table 3: Rates, approved beam time and total data volume estimated for PVDIS, SIDIS and J/ψ experiments. For PVDIS, each of the 30 sectors will have a separate DAQ.

Experiment	PVDIS	SIDIS ^3He	J/ψ
Trigger rate (expected) (kHz)	15×30 sectors	100	30
Data rate (GB/s)	0.12×30 sectors	3.2	2.5
Approved beam time (days)	169	125	60
Total data (PB)	105	70	25

1.5 Summary

The strong and unique physics program of SoLID, consisting of PVDIS, SIDIS and J/ψ production, was presented in the context of the worldwide effort. The science related recommendations from the 2015 Director's Review have been addressed. The device, while complex, is low risk with a high potential to deliver the proposed strong and rich physics program. The scientific reach, unique strength and feasibility of the SoLID program demonstrate that we are ready to proceed to the next step: the anticipated Science Review by DOE.

2 Introduction and Overview of SoLID Experimental Programs

2.1 SoLID Project Introduction/Overview

2.1.1 Base Equipment Description

The SoLID (Solenoidal Large Intensity Device) project will develop a large acceptance spectrometer and a detector system capable of handling very high rates. It is designed to satisfy the requirements of five approved experiments with high-scientific ratings, four A and one A-, as well as to become the base equipment for a continued program of physics in the 12 GeV era at Jefferson Lab that requires both high luminosity and large acceptance. The base equipment composing the SoLID project includes two configurations: the “SIDIS” (Semi-Inclusive Deep Inelastic Scattering) configuration and the “PVDIS” (Parity-Violating Deep Inelastic Scattering) configuration. Although the geometrical layouts for the detectors are not the same in the two configurations, most of the detector items are common as follows:

1. A solenoidal magnet with a power-supply and cryogenic system, identified as the CLEO-II magnet. With some modifications as described in the magnet section, this magnet meets the experimental requirements. The coils, coil collars, and cryostat of the CLEO-II magnet have arrived at JLab in 2016, and the iron pieces arrived at JLab in August 2019.
2. An electromagnetic calorimeter for electron identification. (In the SIDIS configuration, it is separated into two sectors, a forward sector and a large-angle sector).
3. A light gas Cherenkov detector for electron identification.
4. A heavy gas Cherenkov detector for pion (hadron) identification. This is for the SIDIS configuration only.
5. A Gas Electron Multiplication (GEM) detector based charged particle tracking system, to be built by the University of Virginia (UVa) GEM group.
6. Forward-angle and a large-angle scintillator-pad detectors (SPD) for photon rejection, and for time-of-flight (TOF) also in large angle SPD. These are for the SIDIS configuration only.
7. A set of baffles to reduce the low energy background. This is for the PVDIS configuration only.
8. A data acquisition system (DAQ). Part of the DAQ electronics, mainly FADCs, will be from the JLab Physics Division Shared Electronics Pool (see next section on Dependencies to Base Equipment).
9. Supporting structures for the magnet and the detectors.
10. Requisite Hall A infrastructure to accommodate the functioning of the above - cooling, cabling, and the like.

2.1.2 Dependencies to Base Equipment

The following items are requisite outside contributions to the SoLID base equipment:

1. DAQ electronics: JLab intends to have an electronics pool to share basic DAQ electronics among the four experimental halls. Some of these electronics, mainly 188 FADCs will be borrowed by SoLID. It was assumed that the mass storage silo will be able to handle 3 GB/s by the time the first SoLID experiment runs.
2. Magnet: JLab formally requested the CLEO-II magnet and received a positive response from Cornell University. JLab, in coordination with Cornell, had the magnet coils, coil collars and cryostat transported to JLab in the fall of 2016. The CLEO-II magnet iron pieces arrived at JLab in August 2019.
3. Beamline: The Hall A beam line with standard instrumentation is assumed to be in operational condition and is not included in the SoLID base equipment.
4. It is assumed that the experiment in Hall A directly before SoLID will be de-installed in advance of, or not interfere with, the SoLID installation. It is not yet known what experiment this will be, as it is dependent on future laboratory scheduling and resources that can not be foreseen at this time. Moreover, de-installation is a standard Hall operations procedure.

2.1.3 Experiment-specific Dependencies

The five approved experiments in the SoLID program will require not only the SoLID base equipment, but also components outside the base equipment of the SoLID project. A list of such additional components is given below, of which there are three types. Items 1-3 are either standard and existing at JLab or will be available for experiments planned before the SoLID experiments. Item 4 is a special case of scope contingency depending on the ordering of experiments. Items 5 and 6 may require additional resources and funding, the exact scope of which will depend on the ongoing evolution of the JLab Science program.

1. For SIDIS with a polarized ^3He target: The existing polarized ^3He target with performance already achieved from the 6 GeV transversity (E06-010) experiment is required. However, modifications to the stand, supports, and services may be required to accommodate integration into SoLID.
2. For J/Ψ : The standard cryogenic LH2 target system is assumed. This is standard Hall A equipment; however, the SoLID SIDIS configuration will require rearrangement of the detector system for the target and there may be significant modifications required for both to accommodate integration into SoLID.
3. For PVDIS: A Compton polarimeter and a superconducting Moller polarimeter (both also required by the MOLLER project) are assumed to be available.
4. For PVDIS: modifications to a custom, high-power cryotarget beyond what is required for SBS GEP and MOLLER experiments. The scope will be folded into JLab's planning. ESR2 is assumed to be available as required by the MOLLER project.
5. For SIDIS with transversely polarized proton: a transversely polarized proton target needs to be developed. The development of such a dynamic nuclear polarized target is required for other approved experiments in the JLab science program. An initial study has been performed by Oxford which concluded that such a target is feasible.

2.1.4 Enhancement to the Baseline Configuration

Following are the possible enhancements from international contributions:

1. An MRPC (Multi-Gap Resistive Plate Chamber) detector serving as a time-of-flight (TOF) detector to extend the baseline science reach of SoLID by enhancing the pion (hadron) identification in the base setup and providing kaon identification in addition: Two Chinese groups (Tsinghua University and USTC) have obtained national Natural Science Foundation of China (NSFC) funding to perform R&D for a high resolution MRPC and plan to apply for full funding to construct the required MRPC detector and its readout system for the SoLID project.
2. Contributions to the GEM detectors for tracking: A collaboration of five Chinese institutions (USTC, CIAE, Tsinghua, Lanzhou, and IMP) is performing R&D on GEM detector technology and associated readout systems; this collaboration plans to apply for funding from the Chinese funding agencies to make contributions towards GEM detector and GEM readout upgrades of the SoLID project.

While the SoLID baseline configuration will be able to satisfy the requirements of the core group of SoLID physics program (SIDIS-pion, PVDIS and J/ψ experiments), enhancements from international contributions will allow for additional physics topics such as SIDIS-kaon to be studied, improve performance (increase pion identification range) and reduce scheduling risk.

2.1.5 Research Program

The five currently-approved, highly rated experiments approved for the SoLID project are as follows:

1. SIDIS-transverse ^3He : Semi-inclusive deep-inelastic-scattering of electron beam on a transversely polarized ^3He target. It is focusing on charged pion production to study transverse spin (transversity) and other transverse momentum dependent parton distributions (TMDs). It will provide a 4-d (x, z, P_T, Q^2) mapping of the Collins, Sivers and pretzelosity asymmetries of the neutron in the valence quark region with high precision. Combined with the SIDIS measurement on the proton and the world e^+e^- data, the Collins asymmetries will allow for an extraction of one of the fundamental properties of the nucleon, the tensor charge of the u and d quarks to better than 10%, providing a benchmark test of lattice QCD. Together with the next generation of nucleon EDM experiments, the SoLID results on the u and the d quark tensor charge will help constrain quark EDM, and probe new physics. The Sivers and Pretzelosity asymmetries will allow for an extraction of the Sivers function and pretzelosity function, providing crucial information on the quark orbital motion.
2. SIDIS-longitudinal ^3He : Semi-inclusive deep-inelastic-scattering of electron beam on a longitudinally polarized ^3He target. It is focusing on charged pion production to study TMDs. Combined with transversely polarized ^3He target experiment, it will provide a precision 4-d (x, z, P_T, Q^2) mapping of the two worm-gear asymmetries of the neutron in the valence quark region, allowing for an extraction of the two so-called worm-gear TMDs (g_{1T} , longitudinal-transversity and h_{1L}^\perp , trans-helicity) with high precision, providing crucial information on the quark orbital motion and the spin-orbital correlations.
3. SIDIS-transverse proton: Same as in 1) but on the proton in order to provide the important flavor separated information on the u and the d quark using the same detection system.

4. PVDIS on the deuteron and the proton: PVDIS on the deuteron will provide a precision test of the Standard Model. It provides the best measurement of the C_2 coupling and also provides a precision measurement of $\sin^2 \theta_W$ at an intermediate value of Q^2 . The broad kinematical range enables the separation of the testing of the Standard Model and the study of fundamental hadron properties, including a precision measurement of possible charge symmetry violation at the partonic level and a unique measurement of the higher-twist effect (twist-4 term). The proton measurement provides a clean measurement of the d-quark over u-quark ratio in the high- x region without nuclear effects.
5. J/ψ production near threshold: This fully exclusive measurement of the electroproduction of J/Ψ mesons from protons near threshold will be sensitive to the non-perturbative gluonic interaction between the J/ψ and nucleon, and might reveal an enhancement of the cross section just above the production threshold. This in turn could be a manifestation of the important role of the conformal anomaly. A further consequence is whether or not J/ψ -nuclear bound states would exist in nature. This experiment could open a new window to study QCD in the non-perturbative region using charmonium in a multi-phase program.

All proposals are available at

https://www.jlab.org/exp_prog/generated/12GeV/halla.html

2.2 SIDIS Program

2.2.1 Introduction

Deep inelastic lepton-nucleon scattering (DIS) experiments have played a fundamental role in describing the partonic momentum structure of hadrons. The unpolarized parton distribution functions (PDF) have been extracted with excellent precision over a large range of x and Q^2 from DIS, Drell-Yan and other processes after several decades of experimental and theoretical efforts. The comparison of the structure functions in the large Q^2 range with QCD evolution equations has provided one of the best tests of QCD.

When the target and/or beam are polarized the essential properties of spin-angular momentum structure of hadrons is probed. Three decades of intensive experimental and theoretical investigation have resulted in a great deal of knowledge on the partonic origin of the nucleon spin structure. Motivated by the “spin crisis” from the European Muon Collaboration experiment in the 1980s [11], the longitudinal polarized parton distribution functions have been determined with significantly improved precision over a large region of x and Q^2 from polarized deep-inelastic (DIS) experiments carried out at CERN, SLAC, DESY in the last 20-30 years, and more recently at JLab and at RHIC from polarized proton-proton scattering (see [12, 13] for reviews and compilation of references). In particular, considerable knowledge has been gained from inclusive DIS experiments on the longitudinal structure – the x -dependence and the helicity distributions – in terms of the unpolarized (denoted $q^a(x)$ or $f_1^a(x)$) and helicity (denoted $\Delta q^a(x)$ or $g_1^a(x)$) parton distribution functions for the various flavors (indicated by a).

In more recent experimental and theoretical studies, it has become evident that precise knowledge of the transverse structure of partons is essential to unfold the full momentum and spin structure of the nucleon. This concerns in particular the investigations of the chiral-odd transversely polarized quark distribution function or transversity [14] (denoted as $\delta q(x)$, $h_1(x)$ or also $\Delta_T q(x)$) which is probed in transverse spin polarization experiments. Like the axial charge $\Delta q^a = \int_0^1 dx (g_1^a(x) + g_1^{\bar{a}}(x))$, the tensor charge $\delta q^a = \int_0^1 dx (h_1^a(x) - h_1^{\bar{a}}(x))$ is a basic property of the

nucleon. The essential role of the transversity distribution function emerges from a systematic extension of the QCD parton model to include transverse momentum and spin degrees of freedom. In this context, semi-inclusive deep-inelastic lepton nucleon scattering (SIDIS) has emerged as an essential tool to probe both the longitudinal and transverse momentum and spin structure of the nucleon. The azimuthal dependence in the scattering of leptons off transversely polarized nucleons is explored through the analysis of transverse single spin asymmetries (TSSAs). Recent work [15–17] predicts that these observables are factorized convolutions of leading-twist transverse momentum dependent parton distributions (TMDs) and fragmentation functions (FFs) at low transverse momentum. These functions provide *essential non-perturbative* information on the partonic sub-structure of the nucleon; they offer a rich understanding of the motion of partons inside the nucleon, of the quark orbital properties, and of spin-orbit correlations. They also provide essential information on multi-parton correlations at leading-twist, allowing us to explore and uncover the dynamics of the quark-gluon structure of the nucleon.

At leading twist if we integrate over the transverse momenta of quarks, the three quark distribution functions remain: the unpolarized parton distribution f_1 , the longitudinal polarized parton distribution g_1 , and the quark transversity distribution h_1 . Besides f_1 , g_1 and h_1 , there are five more transverse momentum dependent distribution functions [15, 16]. Fig. 9 tabulates all these eight TMDs according to the polarizations of the quark (f, g, h) and nucleon (U, L, T). Since these TMDs provide the description of the parton distributions beyond the collinear approximation, they depend not only on the longitudinal momentum fraction x , but also on the transverse momentum, k_T . An intuitive interpretation of the k_T dependent transversity distribution, h_1 , is that it gives the probability of finding a transversely polarized parton inside a transversely polarized nucleon with certain longitudinal momentum fraction x and transverse momentum k_T . The JLab 12 GeV upgrade provides a unique opportunity to extend our understanding of nucleon spin and momentum structure by carrying out multi-dimensional precision studies of longitudinal and transverse spin and momentum degrees of freedom from SIDIS experiments with high luminosity in combination with large acceptance detectors and a full azimuthal angular acceptance. Such a program will provide the much needed kinematic reach to unfold the momentum and flavor structure of the nucleon. In the next section, we summarize the essential role that transverse polarization studies play in unfolding this structure in SIDIS.

2.2.2 Transverse Structure and Semi-Inclusive Deep Inelastic Scattering

The transverse spin and momentum structure of the nucleon was first discussed in 1970s [18, 19] followed by renewed interest in late 1980s [14, 20]. The transversity function is a chirally odd quark distribution function, and the least known among the three leading twist parton distribution functions. It describes the net quark transverse polarization in a transversely polarized nucleon [20]. In the non-relativistic limit, the transversity distribution function $h_1(x, Q^2)$ is the same as the longitudinal quark polarization distribution function, $g_1(x, Q^2)$. Therefore, the transversity distribution function probes the relativistic nature of the quarks inside the nucleon.

There are several interesting properties of the quark transversity distribution. First it does not mix with gluons; that is, it evolves as a non-singlet distribution [21] and doesn't mix with gluons under evolution and thus has valence-like behavior [22]. Secondly in the context of the parton model it satisfies the Soffer bound [23], which is an inequality among the three leading twist distributions, $|h_1^q| \leq \frac{1}{2}(f_1^q + g_1^q)$, based on unitarity and parity conservation. QCD evolution of transversity was studied in Ref. [24], where it was shown that Soffer's inequality holds up to next to leading order (NLO) QCD corrections. In the past [25] and more recently [26], studies have been performed that consider the violation of this bound. Therefore, it is interesting to experimentally test the Soffer's

inequality as a function of Q^2 . Lastly, the lowest moment of h_1^q is the tensor charge, which has been calculated from lattice QCD [27] and various models [28–33]. Due to the valence-like nature of the transversity distribution, measuring transversity in the high- x region (JLab kinematics) is crucial to determine tensor charge of quarks. The experimental determination of the transversity function is challenging - it is not accessible in polarized inclusive DIS measurements when neglecting quark masses - h_1 decouples at leading twist in an expansion of inverse powers of the hard scale in inclusive deep-inelastic scattering due to the helicity conserving property of the QCD interactions. However, paired with another hadron in the initial state *e.g.* double polarized Drell-Yan processes (two transversity distributions) [19], or in the final state, *e.g.* semi-inclusive deep-inelastic [34] scattering (transversity and Collins fragmentation function), leading twist h_1 can be accessed without suppression by a hard scale.

The most feasible way to access the transversity distribution function is via an azimuthal single spin asymmetry, in semi-inclusive deep-inelastic lepto-production of mesons on a transversely polarized nucleon target, $e N^\uparrow \rightarrow e \pi X$. In this case the chiral-odd partner is the Collins fragmentation function, H_1^\perp [34], which has been extracted from charged pion pair production from e^+e^- annihilation [35]. Assuming factorization, schematically this transverse single spin asymmetry (TSSA) contains h_1 and H_1^\perp , $A_{UT} \sim h_1 \otimes H_1^\perp$ ($U \equiv$ unpolarized lepton beam, $T \equiv$ transversely polarized target) [16].

The first evidence of non-trivial transverse spin effects in SIDIS has been observed in the transverse single spin asymmetries measured by the HERMES [36–38], and the COMPASS [39, 40] experiments from a transversely polarized proton or deuteron target, where an unpolarized lepton beam is scattered off $l p^\uparrow \rightarrow l' h X$. Besides the non-zero Collins asymmetry, which contains h_1 and H_1^\perp discussed previously, another non-zero asymmetry (Sivers asymmetry), was also observed. The Sivers asymmetry is associated with a naive T-odd transverse momentum dependent (TMD) parton distribution function [41]. More recently, results on Collins and Sivers asymmetries on neutron were reported for the first time using a polarized ^3He target at JLab [42]. In contrast to inclusive deep-inelastic lepton-nucleon scattering where transverse momentum is integrated out, these processes are sensitive to the transverse-momentum scale, P_T , which is on the order of the intrinsic quark momentum, k_T ; that is $P_T \sim k_T$. This is evident by considering the generic structure of the TSSA for a transversely polarized nucleon target which is characterized by interference between helicity flip and helicity non-flip amplitudes $A_{UT} \sim \text{Im}(f^{*+} f^-)$. In the collinear limit of QCD, partonic processes conserve helicity and Born amplitudes are real [43]. For this structure to be non-zero at leading twist we must go beyond the collinear limit where such a reaction mechanism requires a recoil scale sensitive to the intrinsic quark transverse momentum. This is roughly set by the confinement scale $k_T \sim \Lambda_{\text{QCD}}$ [44]. Because strongly interacting processes conserve parity transverse spin asymmetries are described by T-odd correlations between transverse spin \mathbf{S}_T , longitudinal momentum \mathbf{P} and intrinsic quark momentum \mathbf{k}_T [34, 41], which are depicted by the generic vector product $i\mathbf{S}_T \cdot (\mathbf{P} \times \mathbf{k}_\perp)$. These correlations imply a leading twist reaction mechanism which is associated with a naive T-odd transverse momentum dependent (TMD) parton distribution [41] and fragmentation [34] function (PDF & FF).

A crucial theoretical breakthrough [45–47] was that the reaction mechanism is due to non-trivial phases arising from the color gauge invariant property of QCD. This leads to the picture that TSSAs arise from initial and final state interactions [48–50] (ISI/FSI) of the active quark with the soft distribution or fragmentation remnant in SIDIS, which manifests itself as a gauge link that links the bilocal quark configuration. This gauge link gives rise to the final state gluonic interactions between the active quark and target remnant. Thus, T-odd TMDs are of crucial importance because they possess transverse spin polarization structure as well as the necessary phases to account for TSSAs at leading twist. Further work on factorization theorems for SIDIS indicate that there are two

leading twist T-odd TMDs; the Sivers function, denoted as f_{1T}^\perp describing the probability density of finding unpolarized partons inside a transversely polarized proton, is one of these functions. All these aforementioned ingredients (TMD, FF, gauge link) enter the factorized [17] hadronic tensor for semi-inclusive deep-inelastic scattering.

Exploring the transverse spin structure of the TMD PDFs reveals evidence of a rich spin-orbit structure of the nucleon. When the transverse spin and momentum correlations are associated with the nucleon, where the quark remains *unpolarized*, the Sivers function [41] describes the helicity flip of the nucleon target in a helicity basis. Since the quark is unpolarized in the Sivers function, the orbital angular momentum of the quarks must come into play to conserve overall angular momentum in the process [51, 52]. Indeed a partonic description of the Sivers and Boer-Mulders functions requires wave function components with nonzero orbital angular momentum and thus provides information about the correlation between the quark orbital angular momentum (OAM) and the nucleon/quark spin, respectively [48, 53].

Unlike the Sivers function, which provides a clean probe of the QCD FSI, the functions g_{1T} and h_{1L}^\perp are (naive) T-even, and thus do not require FSI to be nonzero. Nevertheless, they also require interference between wave function components that differ by one unit of OAM and thus require OAM to be nonzero. Recently, a first ever determination of g_{1T} was reported [54] using a polarized ^3He target at JLab, in which a positive azimuthal asymmetry for π^- production on ^3He and the neutron was observed, while the π^+ asymmetries are consistent with zero. Finally, the pretzelosity h_{1T}^\perp requires interference between wave function components that differ by two units of OAM (e.g. p-p or s-d interference). Combining the wealth of information from all these functions could be invaluable for disentangling the spin orbit correlations in the nucleon wave function, thus providing important information about the quark orbital angular momentum.

Complementary to Generalized Parton distributions (or Impact Parameter Dependent distributions), which describe the probability of finding a parton with certain longitudinal momentum fraction and at certain transverse position b (1-D momentum space and 2-D coordinate space), TMDs give a description of the nucleon structure in 3-D momentum space. Furthermore, by including the transverse momentum of the quark, the TMDs reveal important information about the nucleon/parton spin-orbital angular momentum correlations.

2.2.3 The Phenomenology TSSAs and TMDs

All eight leading twist TMDs can be accessed in SIDIS. The transversity, Sivers, and pretzelosity TMDs can be accessed through a transversely polarized target. There are three mechanisms which can lead to the single (transversely polarized target) spin azimuthal asymmetries, which are the Collins asymmetry, the Sivers asymmetry, and the pretzelosity asymmetry. As mentioned previously, the quark transversity function in combination with the chiral-odd Collins fragmentation function [34] gives rise to an azimuthal (Collins) asymmetry in $\sin(\phi_h + \phi_S)$, where azimuthal angles of both the hadron (pion) (ϕ_h) and the target spin (ϕ_S) are with respect to the virtual photon axis and relative to the lepton scattering plane. The Sivers asymmetry [41, 55, 56] refers to the azimuthal asymmetry in $\sin(\phi_h - \phi_S)$ due to the correlation between the transverse target polarization of the nucleon and the transverse momentum of the quarks, which involves the orbital angular momentum of the unpolarized quarks [48, 51]. The pretzelosity asymmetry is similar to Collins asymmetry except it is due to quarks polarized perpendicularly to the nucleon spin direction in the transverse plane in a transversely polarized nucleon. It has an azimuthal angular dependence of $\sin(3\phi_h - \phi_S)$. One can disentangle these angular distributions by taking the azimuthal moments of the asymmetries as has been done by the HERMES Collaboration [38], the COMPASS Collaboration [40], and most recently by the JLab E06-010 collaboration [42]. With a longitudinally polarized lepton beam,

and a transversely polarized target, the double spin asymmetry from SIDIS has an azimuthal angular dependence of $\cos(\phi_h - \phi_S)$ that allows for the determination of the g_{1T} TMD as was done in [54]. With a longitudinally polarized target, the single target spin asymmetry with an azimuthal angular dependence of $\sin(2\phi_h)$ is sensitive to h_{1L}^\perp , while the double spin asymmetry allows for the determination of the helicity TMD, g_1 .

In recent years a great deal of understanding of transverse spin effects, final state interactions, and the spin orbit structure of partonic-hadronic interactions has been gained from model calculations of the TMDs and fragmentation functions. In particular the final state interactions in TSSAs through the Sivers function has been studied in spectator models and the light-cone wave function approach [48–50, 57–61] as well as the bag model [62] and the NJL jet model [66]. The Collins function has been calculated in [63–65] while studies of the universality of T-odd fragmentation functions have been carried out in [67–69]. The Boer-Mulders function has been calculated in [50, 59, 61, 70, 71] and the spin orbit effects of the pretzelosity function have been studied in both light-cone constituent quarks models [72–75], while model predictions of azimuthal and transverse spin asymmetries have been predicted in [59, 76, 77].

The first model dependent extractions of the transversity distribution have been carried out [78] by combining SIDIS [37, 38, 79, 80] data with e^+e^- data [35] on the Collins function. Within the uncertainties, the Soffer bound is respected. In addition, the extraction of the Sivers function [81–85] has been performed by combining SIDIS data from the HERMES [38] on the proton and COMPASS data [40] on the deuteron. Complementing the data from the HERMES [37, 38], COMPASS [80], and BELLE [35] experiments, the recent results from the JLab Hall A experiment E06-010 [42] on the neutron (with polarized ^3He) will facilitate a flavor decomposition of the transversity distribution function, h_1 [20, 86] and the Sivers distribution function f_{1T}^\perp [41] in the overlapping kinematic regime. However a model-independent determination of these leading twist functions requires data in a wider kinematic range with high precision in *four dimensions* of (Q^2, x, z, P_T) .

2.2.4 Overview of SIDIS program

The 12-GeV energy upgrade at CEBAF together with the newly proposed SoLID opens a great new window to perform precision studies of the transverse spin and transverse-momentum-dependent structure in the valence quark region for both the proton and the neutron. The experimental program on TMDs is one of the main thrusts of the 12-GeV physics program at JLab.

Currently, there are three A rated SoLID experiments (E12-10-006 [87], E12-11-007 [88], and E12-11-108 [89]) on TMD physics with two involving a transversely (longitudinally) polarized ^3He (neutron) target, and one employing a transversely polarized NH_3 (proton) target. To extract TMDs with precisions from single and double spin asymmetry measurements, the detection system should have the capability to handle large luminosities, a full azimuthal angular coverage, good kinematic coverage in terms of Q^2, x, z, P_T for SIDIS, and good particle identification for electrons and charged pions. Further, the influence due to the residual magnetic field of the spectrometer magnet needs to be negligible for polarized targets. SoLID is such a device that has been proposed and designed for these newly approved SIDIS experiments.

These new SIDIS experiments employ a superconducting solenoid magnet, a detector system consisting of forward-angle detectors and large-angle detectors, and a high-pressure polarized ^3He target or a polarized NH_3 target positioned upstream of the magnet. The polarized ^3He target is based on the technique of spin-exchange optical pumping of hybrid Rb-K alkali atoms. Such a target was used successfully in the completed SSA experiment in JLab Hall A [42, 54] with a 6-GeV electron beam at JLab and an in-beam polarization of 55-60% was achieved. For the polarized

proton experiment E12-11-108, an upgraded version of the JLab/UVa/SLAC polarized NH_3 target will be used. The main upgrade will involve using a new magnet to replace the aging Helmholtz-coil magnet and to have fast spin-flip capability with the Adiabatic Fast Passage (AFP) technique. Preliminary design study has been carried out for such a magnet with a vertical opening angle of $\pm 25^\circ$ to satisfy the requirement of the experiment. The target is based on the principle of dynamic nuclear polarization (DNP) by using microwave pumping to reach high proton polarizations [90, 91]. The CLEO-II magnet with new end caps and modification of the yolks has been identified as the magnet of the choice for SoLID based on both the requirements of the experiments and the availability of the magnet. Six layers of GEM detectors will be placed inside the coils as tracking detectors. A combination of an electromagnetic calorimeter, gas Cherenkov counters, and a layer of Multi-gap Resistive Plate Chamber (MRPC) (in the enhanced baseline configuration) will be used for particle identification in the forward-angle region. As only electrons will be identified in the large-angle region, a shashlyk-type [92, 93] electromagnetic calorimeter will be sufficient to provide the pion rejection. The SoLID SIDIS configuration will also have a forward-angle and a large-angle scintillator-pad detectors (SPD) for photon rejection, and for time-of-flight (TOF) in large angle SPD. More details about SoLID experimental setup, kinematic coverage, particle identification, and other important considerations for SIDIS can be found in Section 3.2 and 3.3.

2.2.5 Beam Time and Projections



E12-10-006 Experiment E12-10-006 was approved 90 days of total beam time with $15\ \mu\text{A}$, 11/8.8 GeV electron beams on a 40-cm long, 10 amgs transversely polarized ^3He target. 69 days is for beam on the polarized ^3He target, and 10 days for a dedicated study of the $x - z$ factorization with Hydrogen and Deuterium gas using a reference target cell. Additional 3.0 days is requested with a longitudinal target polarization to study the systematics of potential A_{UL} contamination, where U stands for an unpolarized beam and L for a longitudinally polarized target. A total overhead time of 8 days is requested. This overhead time will be shared among activities such as unpolarized target runs, target spin flip and target polarization measurements, as has been done in the past during other Hall A polarized ^3He target experiments. Although beam polarization is not required for the proposed SSA measurements, polarized beam with polarization of 85% or higher will be used for for parasitic measurements of A_{LT} , which can be used to access, g_{1T} as demonstrated in [54].

Projected data from E12-10-006 are binned into 4-dimensional (x, P_h, z, Q^2) bins. For a typical z and Q^2 bin ($0.40 < z < 0.45$, $2\ \text{GeV}^2 < Q^2 < 3\ \text{GeV}^2$), data projections for Sivers asymmetry measurements, left panel for π^+ and right panel for π^- , are shown in Fig. 10 as examples. Also shown are results from the 6-GeV experiment E06-010 [42], and predictions of Sivers asymmetries from Anselmino *et al.* [94] with model uncertainties. For complete projections which consist of 1400 data points, we refer to the proposal [87].

E12-11-007 Experiment E12-11-007 was approved 35 days of total beam time with $15\ \mu\text{A}$, 11/8.8 GeV electron beams on a 40-cm long, 10 amgs longitudinally polarized ^3He target to match about 50% statistics of experiment E12-10-006. When combined with experiment E12-10-006, this experiment will not require any beam time for calibration data, including reference cell runs and detector calibrations.

A maximum likelihood method [95] was used to extract angular modulations with combined, projected data sets from both E12-11-007 and E12-10-006. Projected data are binned into 4-dimensional (x, P_h, z, Q^2) bins. For a typical z and Q^2 bin ($0.40 < z < 0.45$, $2\ \text{GeV}^2 < Q^2 < 3\ \text{GeV}^2$, one of the total 48 $z - Q^2$ bins), data projections are shown in Fig. 11 as examples. For complete projections, we refer to the proposal [88].

Leading Twist TMDs

 : Nucleon Spin
  : Quark Spin

		Quark polarization		
		Un-Polarized (U)	Longitudinally Polarized (L)	Transversely Polarized (T)
Nucleon Polarization	U	$f_1 = \text{Nucleon Spin} \cdot \text{Quark Spin}$		$h_1^\perp = \text{Boer-Mulder}$
	L		$g_1 = \text{Helicity}$	$h_{1L}^\perp = \text{Helicity} \cdot \text{Transversity}$
	T	$f_{1T}^\perp = \text{Sivers}$	$g_{1T}^\perp = \text{Sivers} \cdot \text{Helicity}$	$h_{1T}^\perp = \text{Transversity}$

Figure 9: Leading twist TMDs classified according to the polarizations of the quark (f, g, h) and nucleon (U, L, T).

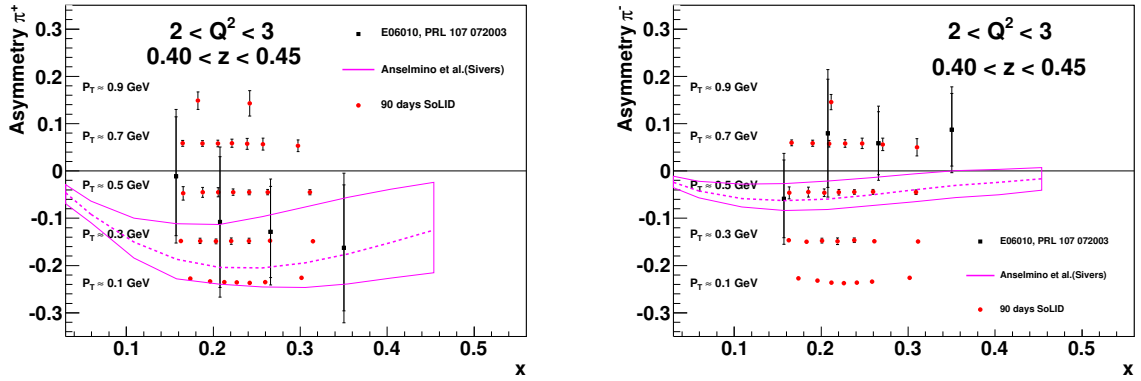


Figure 10: The left panel shows the projected Sivers asymmetry measurement for π^+ for a typical z and Q^2 bin ($0.40 < z < 0.45$, $2 \text{ GeV}^2 < Q^2 < 3 \text{ GeV}^2$) as a function of x with different ranges of the hadron transverse momentum labeled. The right panel shows the projection for the corresponding π^- Sivers asymmetry measurement. Also shown are the results from the 6-GeV experiment E06-010 [42].

E12-11-108 Experiment E12-11-108 was approved 94 days of total beam time with 100 nA, 11/8.8 GeV electron beams on a 3-cm long, polarized NH₃ target. The 8.8 GeV beam energy will provide precision data on the radiative corrections along with the increased Q^2 coverage. 90 days are for beam on a transversely polarized NH₃ target including 7.5 days for dilution measurements, optics, and detector calibrations. Also 4 days are requested with a longitudinal target polarization to study the systematics of potential A_{UL} contamination. Although beam polarization is not required for the proposed SSA measurements, a longitudinally polarized beam will be used for a parasitic measurement of the A_{LT} , which can be used to access g_{1T} . In addition, there will be an overhead time of 26 days for regular target annealing which does not need an electron beam.

Projected data from E12-11-108 are binned into 4-dimensional (x, P_h, z, Q^2) bins. For a typical z and Q^2 bin ($0.40 < z < 0.45$, $2 \text{ GeV}^2 < Q^2 < 3 \text{ GeV}^2$), data projections for Collins asymmetry measurements, left panel for π^+ and right panel for π^- , are shown in Fig. 12 as examples. Also shown are predictions of Collins asymmetries from Anselmino *et al.* [94] with model uncertainties. For complete projections of E12-11-108, we refer to the proposal [89].

The combination of these three experiments will allow for accessing important information about TMDs from proton and neutron, and the flavor separation of the TMDs (transversity, Sivers, pretzelosity, and g_{1T}) for u and d quark. A good example based on a study in Ref. [2] to demonstrate the impact of this program is shown in Fig. 13 in which the projected transversity distributions for u and d quarks are shown at a typical $Q^2 = 2.4 \text{ GeV}^2$ based on the up-to-date knowledge of evolution of the transverse momentum dependent distribution and fragmentation functions. The expected improvement in the knowledge of the transversity distribution is enormous: from the wide error bands based on the current knowledge to the narrow bands from the SoLID program, and the access to the valence quark region, which has been essentially unexplored as of now. In fact the proposed SoLID SIDIS program will allow for studies of the k_T dependence, and the Q^2 evolution of the TMDs also. Furthermore, the SoLID SIDIS program will provide precise information on the tensor charge of the nucleon, an important property of the nucleon like spin or magnetic moment, and is determined by the valence quarks inside the nucleon. A quantitative study [2] demonstrates that the SoLID SIDIS program will improve the accuracy of the tensor charge determination by one order of magnitude, and allows for benchmark tests of lattice QCD predictions. The high impact of these data on the extraction of the tensor charge of the u and d quark is shown in Fig. 14.

2.2.6 Comparisons with SBS and CLAS12 SIDIS programs

In Table 4, we compare the experimental conditions of the SIDIS experiments with SoLID, SBS and CLAS12. The values of solid angle coverage in the table are simplified descriptions. A more realistic acceptance from GEMC is used for the estimation of the physics impact. Compared with SBS, the statistics of SIDIS events with SoLID are much better due to the large acceptance. This will allow us to have 4-dimensional bins with SoLID, while SBS will only have 3-dimensional bins.

A comparison of the Figure of Merit (FOM), which is calculated by the sum of the inverse square of the statistical uncertainties of the SSA, is shown in Figure 15 and Figure 16. In these comparisons, we applied the same kinematic cuts of $W > 2.3 \text{ GeV}$ and $0.3 < z < 0.7$. Compared with CLAS12, SoLID has higher statistics in smaller x region and has comparable (or slightly lower) statistics in larger x region. Compared with SBS, SoLID has higher statistics up to about $x \sim 0.55$, while SBS has more coverage in large x region.

The physics impact of SoLID is the precise measurement of the TMD's in the valence region. One highlight is the Collins SSA, which is related to the transversity distribution, which in turn is dominated by the valence quark distribution. To compare the improvement on the determination of transversity, we model the transversity distributions with the recent global fit of [1], which includes

	SoLID	SBS	SoLID	CLAS12
Experiment	E12-10-006 Approved (A)	E12-09-018 Approved (A-)	E12-11-108 Approved (A)	C12-11-111 Conditional
Targets	^3He (“n”)	^3He (“n”)	NH_3 (“p”)	HDice (“p”)
Polarization (P)	65% (60% in beam)	65% (<60% in beam)	70%	60%
Dilution (f)	0.15~0.3	0.15~0.3	0.13	0.33 \times 80%
Luminosity ($L \text{ cm}^{-2}\text{s}^{-1}$)	1.0×10^{36}	2.7×10^{36}	1.0×10^{35}	1.4×10^{33}
Solid angle ($\Omega_e \times \Omega_h \text{ sr}^2$)	0.482×0.139	0.044×0.063	0.482×0.139	1.14×1.16

Table 4: Comparison of the experimental conditions of SoLID, SBS, and CLAS12.

the TMD evolution effect. We estimate the errors with the standard Hessian method [297]. The Hessian is the second derivatives of the χ^2 with respect to the parameters at the least χ^2 point. It reflects not only the uncertainties of the parameters but also the correlations of the parameters. The Hessian of the world data is obtained from the covariant matrix of the global fit [1]. The Hessians of SoLID, CLAS12, and SBS are calculated with the simulated data. To ensure that the SIDIS events are in the current fragmentation region, which can be described by TMD factorization, we adopt the recent theoretical study on the criteria of the current fragmentation kinematics [10] and only use the bins in the current fragmentation region to study the physics impact. The impacts on the transversity extractions are compared in Figure 17 and Figure 18. In the comparison, only statistical uncertainties are used to compare with CLAS12 and SBS. The improvement from SoLID data including systematic errors is also shown in Figure 18. To remove the model dependence as much as possible, we take the ratio between the prior uncertainties and the post uncertainties to show the improvements from the SoLID, CLAS12, and SBS SIDIS experiments. SoLID can improve the transversity uncertainty for u (d) quark by a factor of 3 (7) over CLAS12, and by a factor of 5 (10) compared to SBS.

The tensor charge, which is the integral of transversity distributions, is a fundamental quantity in QCD. It describes the coupling between a nucleon and a tensor current. Note that in QCD, this correlation is different from the correlation between the longitudinal quark spin with the longitudinal spin of the nucleon which is measured by the structure function g_1 . The impacts of the determination of the tensor charge from SoLID, CLAS12, and SBS are compared in Table 5. The improvements are shown in two ways, the typical measured x region by the experiments and the full x region.

One of the advantages of SoLID SIDIS experiments is that the high statistics allows us to have four-dimensional bins. This will help study TMDs, which are three dimensional distributions. To show the impact of SoLID on TMD measurements, we take the Sivers function as an example. In the analysis, we do a global fit with both unpolarized multiplicity data and Sivers asymmetry data. The fitting result is used as the input model for future SoLID, CLAS12, and SBS pseudo-data. The uncertainties from the world data and from inclusion of SoLID, CLAS12, and SBS are estimated in the same framework. Similar to the case of transversity extraction, we only select the bins that pass the kinematic cuts of the current fragmentation criteria. In Figure 19, we show the improvement from SoLID on the extraction of the Sivers function, and compare it with CLAS12 and SBS.

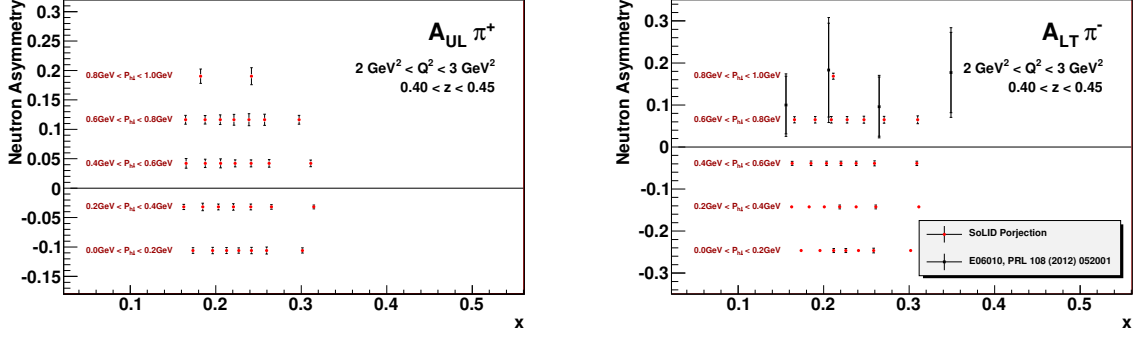


Figure 11: The left panel shows the projection for a typical z and Q^2 bin ($0.40 < z < 0.45$, $2 \text{ GeV}^2 < Q^2 < 3 \text{ GeV}^2$, one of the total 48 $z - Q^2$ bins) for the π^+ single target spin asymmetry $A_{UL}^{\sin(2\Phi_h)}$ measurement as a function of x with different ranges of the hadron transverse momentum labeled. The right panel shows the projection for the corresponding $z - Q^2$ bin for the π^- double spin asymmetry $A_{LT}^{\cos(\Phi_h - \Phi_S)}$ measurement. Also shown are the results from the 6-GeV experiment E06-010 [54].

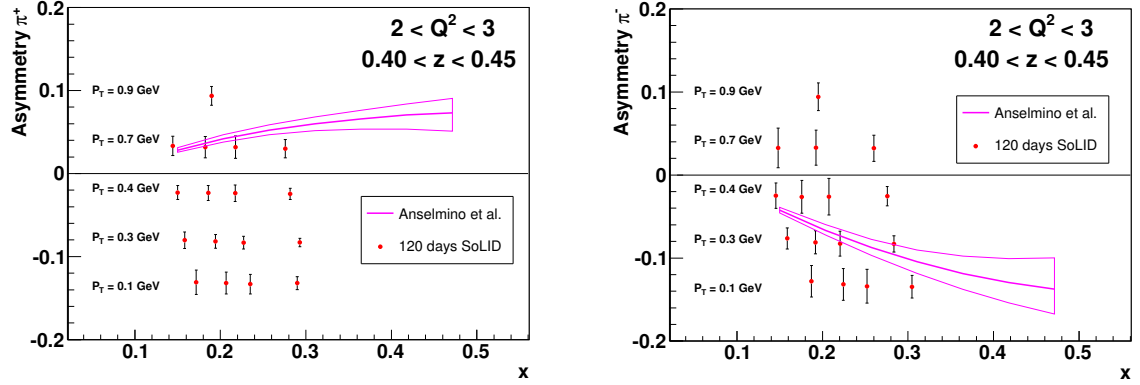


Figure 12: The left panel shows the projection for a typical z and Q^2 bin ($0.40 < z < 0.45$, $2 \text{ GeV}^2 < Q^2 < 3 \text{ GeV}^2$) for the π^+ Collins asymmetry measurement as a function of x with different ranges of the hadron transverse momentum labeled. The right panel shows the projection for the corresponding $z - Q^2$ bin for the π^- measurement. Also shown are predictions of Collins asymmetries from Anselmino *et al.* [94] with model uncertainties.

	World vs. SBS+CLAS12	World vs. SoLID	SBS+CLAS12 vs. SoLID	World vs. SoLID including systematics
$\delta u^{\text{measured}}$	6.1	16	2.8	6.7
$\delta d^{\text{measured}}$	1.9	17	9.3	11
δu^{full}	5.4	16	3.0	5.9
δd^{full}	1.8	17	10	10

Table 5: Comparison of improvements to tensor charge extractions. “World” represents all world available data by 2015. In the first three comparisons, only statistical errors are used, while in the last comparison both statistical and systematic errors are included. The values in the table give the ratio between the prior error and the post error. The measured region is the integral over x from 0.05 to 0.6, and the full region is the integral over x from 0 to 1.

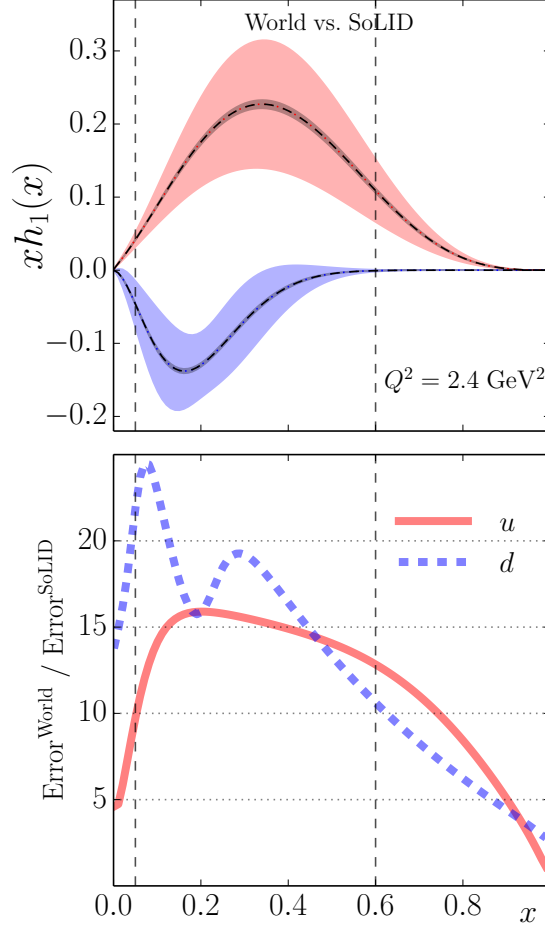


Figure 13: The impact on u and d quark transversity distributions by the SIDIS program using SoLID. The wide error bands show the current knowledge from the global analysis of the world data, and the narrow error bands show the SoLID projections. The lower panel shows the improvements, which are the ratios between the current errors and the projected errors.

2.2.7 SIDIS with Baseline and Enhanced Baseline Configurations

The results shown in the previous sections are for the enhanced baseline configuration. For the baseline configuration (without the MRPC), the SIDIS program is already projected to have a major impact on improving the precision of various TMDs and related physics. As an example, we present the improvement of the transversity and tensor charge uncertainties in Figure 20, and Sivers uncertainties in Figure 21. On average, a factor of 3 for u quark and 10 for d quark over the current world data can be achieved. However, we still miss low momentum pion data at the forward angle, and the corresponding low transverse momentum coverage is not ideal. The planned change from the baseline to enhanced baseline configuration by adding a plane of MRPC detectors at the forward angle will fill this gap. The ability to achieve a timing resolution of better than 100 ps in the high rate environment of SoLID will enable us to identify pions below 2.5 GeV by using time-of-flight. This enhanced kinematic coverage of the SIDIS program will improve the data at the low transverse momentum region and a moderate z region. We also show in Figure 20 and Figure 21 that the SoLID uncertainties on the transversity, tensor charge, and Sivers extractions from the enhanced

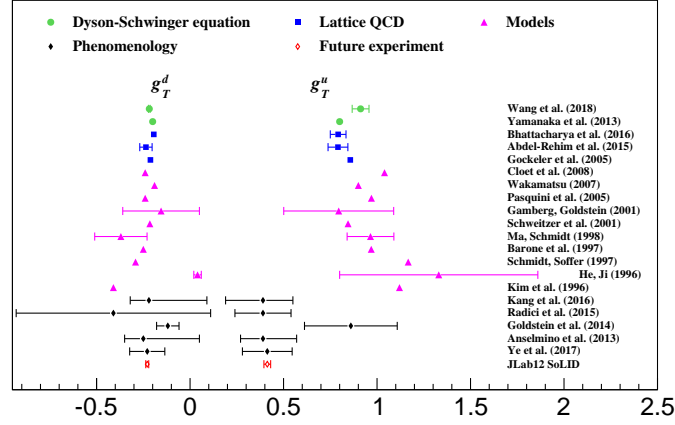


Figure 14: The impact of the projected SoLID measurement of the tensor charge together with current knowledge from models, Dyson-Schwinger equations, global analyses, and lattice QCD simulations.

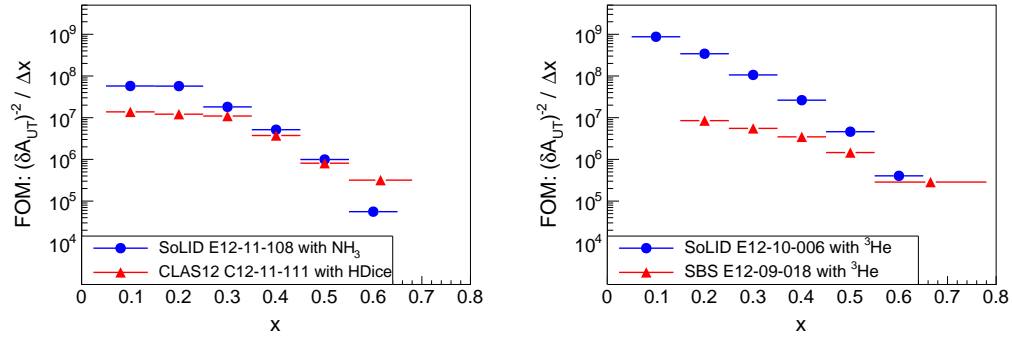


Figure 15: Comparison of the FOM at different x regions. SoLID SIDIS experiment with the proton target is compared with CLAS12 in the left panel. SoLID SIDIS experiments with the neutron target are compared to the SBS experiment in the right panel. In both comparisons, the same kinematic cuts of $W > 2.3$ GeV and $0.3 < z < 0.7$ are applied.

baseline configuration measurement will be further reduced on average by a factor of 1.5 for both u and d quark compared with those from the baseline configuration.

For kaon production in SIDIS process, kaon identification from 1 GeV/c to 7 GeV/c is needed. An high-resolution MRPC (20-30ps) will satisfy the requirement. The enhanced baseline configuration (with an high-resolution MRPC) will expand the physics reach to have kaon SIDIS program.

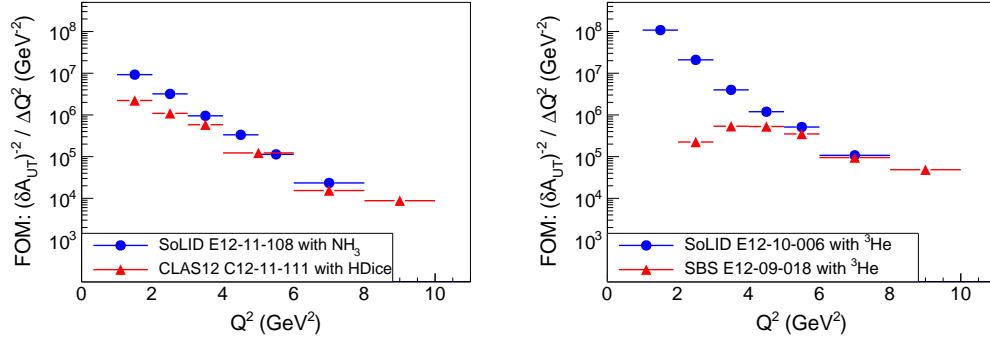


Figure 16: Comparison of the FOM at different Q^2 regions. SoLID SIDIS experiment with the proton target is compared with CLAS12 in the left panel. SoLID SIDIS experiments with the neutron target are compared to the SBS experiment in the right panel. In both comparisons, the same kinematic cuts of $W > 2.3$ GeV and $0.3 < z < 0.7$ are applied.

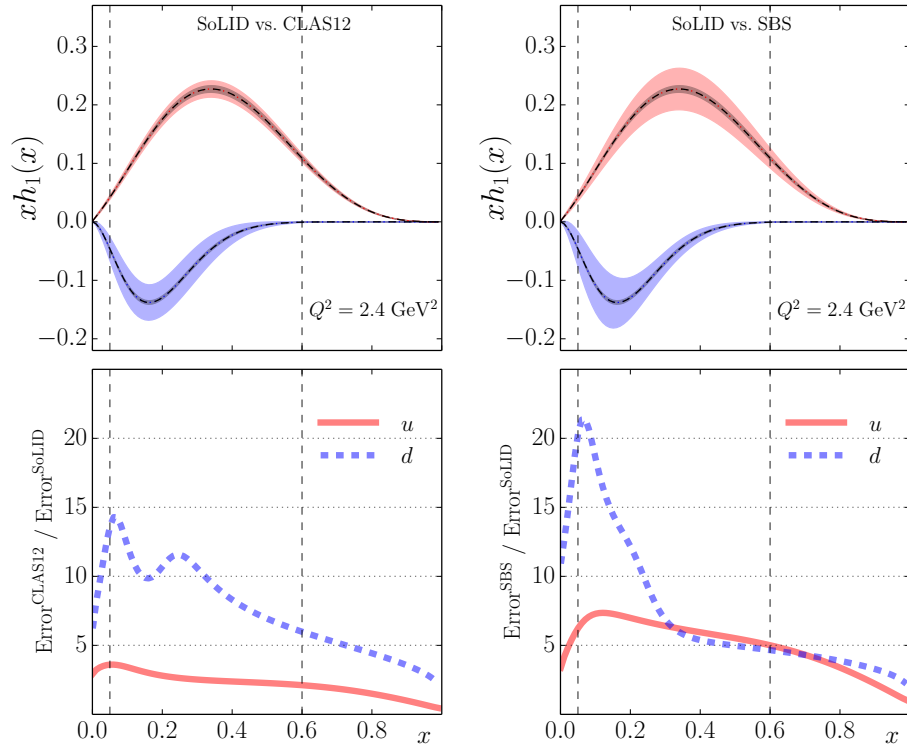


Figure 17: Comparisons of the impact on transversity extractions for up (red) and the down (blue) quarks, as the extension of published works [1, 2]. The left column shows the comparison between SoLID and CLAS12, and the right column shows the comparison between SoLID and SBS. In the upper panels, the light shaded bands show the uncertainties of the transversity function $h_1(x)$ expected from SBS or CLAS12, and the dark shaded bands show the uncertainties expected from SoLID. The ratio of CLAS12 or SBS expected results to those from SoLID are shown in the lower panels. All results are plotted at a typical JLab12 scale $Q^2 = 2.4$ GeV².

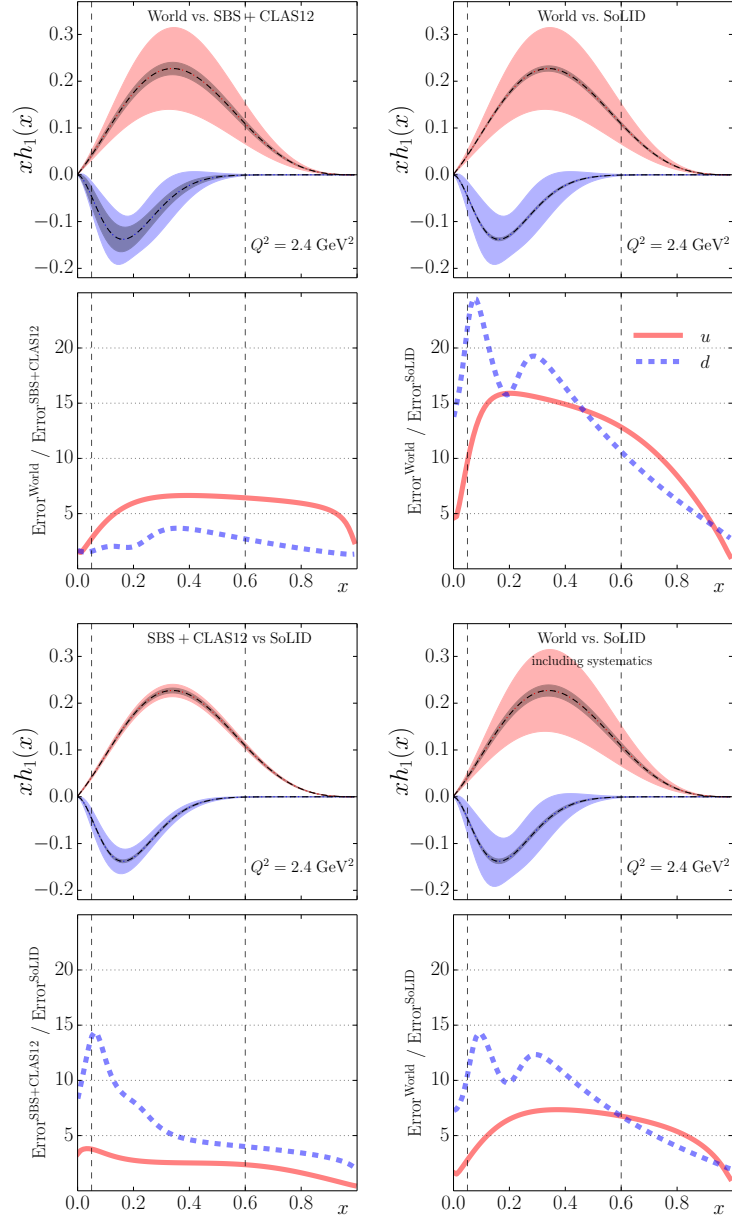


Figure 18: Comparison of the impact on the transversity extractions. The “World” represents all world available data by 2015. The upper left panel shows the improvement from future JLab12 data, i.e. SBS and CLAS12, before SoLID on the base of world available data by 2015. The upper right panel shows the improvements from SoLID data. The lower left panel shows the further improvement from SoLID data after the expected SBS and CLAS12 data. The lower right panel shows the improvements from SoLID data including the systematic uncertainties. The current uncertainties are from the global fit [1], and the future uncertainties are obtained by including the pseudo-data from these experiments with only statistical errors for the first three, and with both statistical and systematic errors for the last one. The curves in the lower panels show the improvement, which is the ratio between the prior uncertainties and the post uncertainties. The x -range between the two vertical dashed lines is directly measured by SoLID.

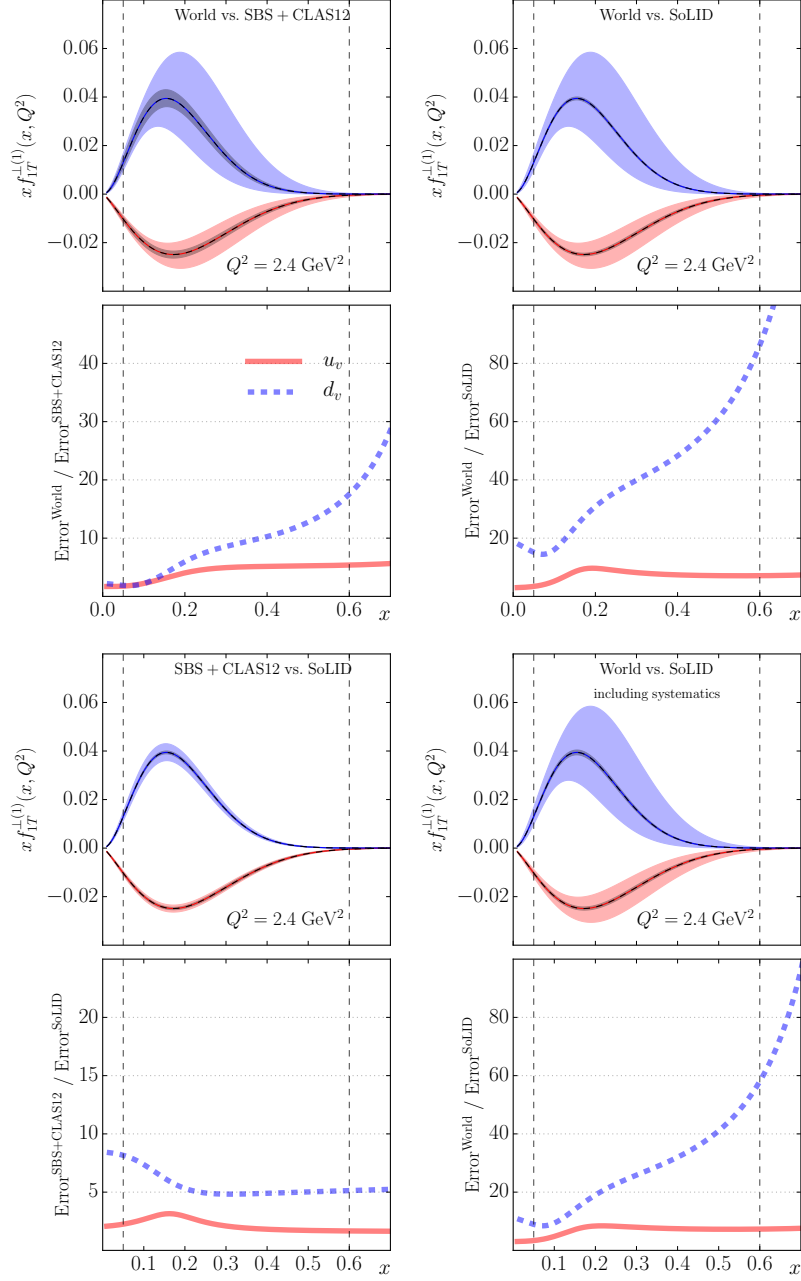


Figure 19: Comparison of the impact on the first transverse moment of the Siverson function. Labels are the same as those in Figure 18.

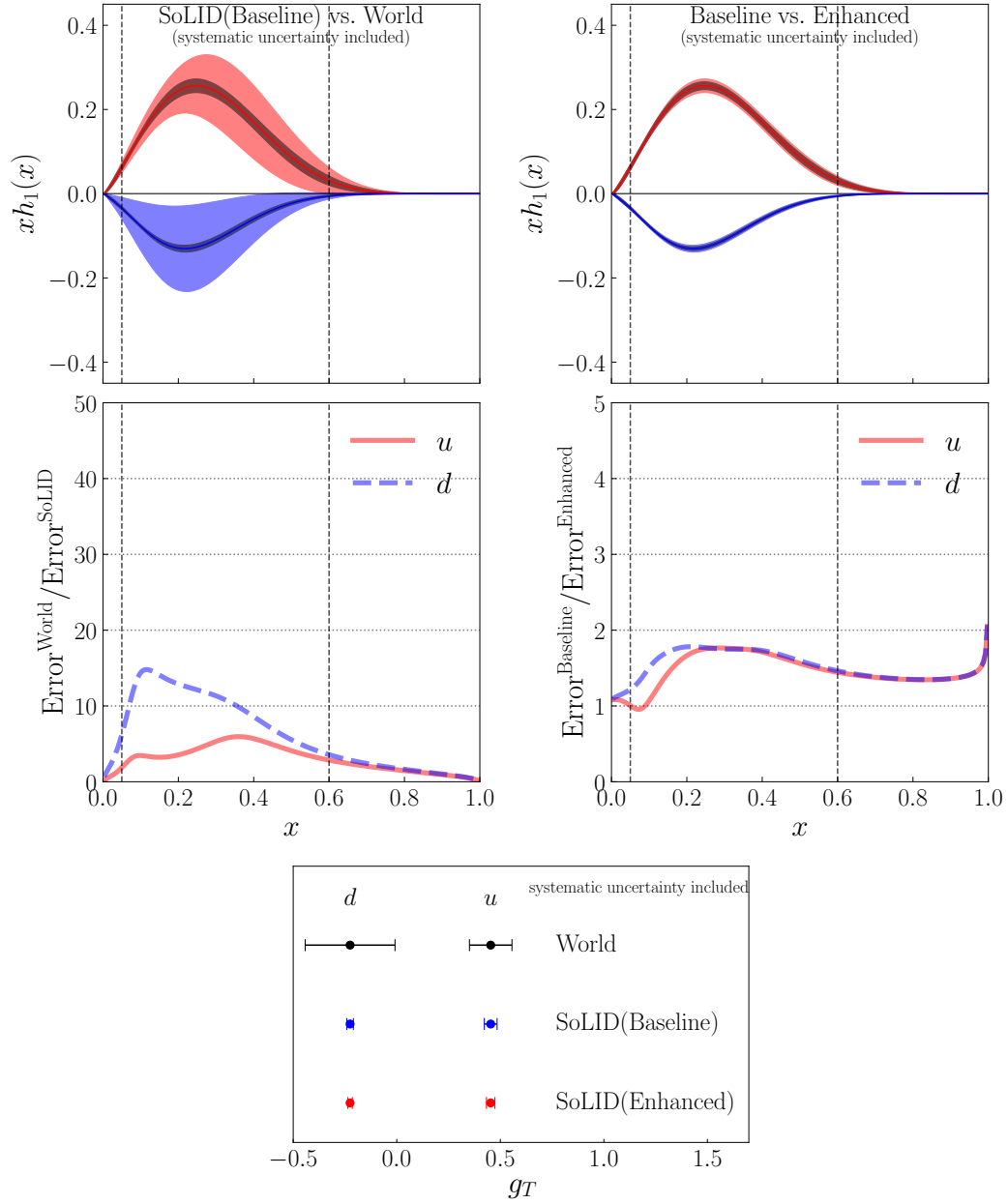


Figure 20: Upper left panel: the impact on transversity extractions for up (red) and the down (blue) quarks by SoLID baseline configuration; the outer light shaded bands show the uncertainties from the world data, and the inner dark shaded bands show the uncertainties expected from SoLID baseline configuration. Upper right panel: the comparison of the impacts between the baseline and enhanced baseline configurations; the outer light shaded bands show the uncertainties expected from the baseline configuration, and the dark shaded bands show the uncertainties expected from the enhanced baseline configuration. The uncertainty ratios curves are shown in bottom plots. Lower panel: the tensor charge extraction uncertainty from the current world data (black), SoLID with the baseline configuration (blue), and SoLID with the enhanced baseline configuration (red). All results are plotted at a typical JLab 12 GeV scale $Q^2 = 2.4 \text{ GeV}^2$.

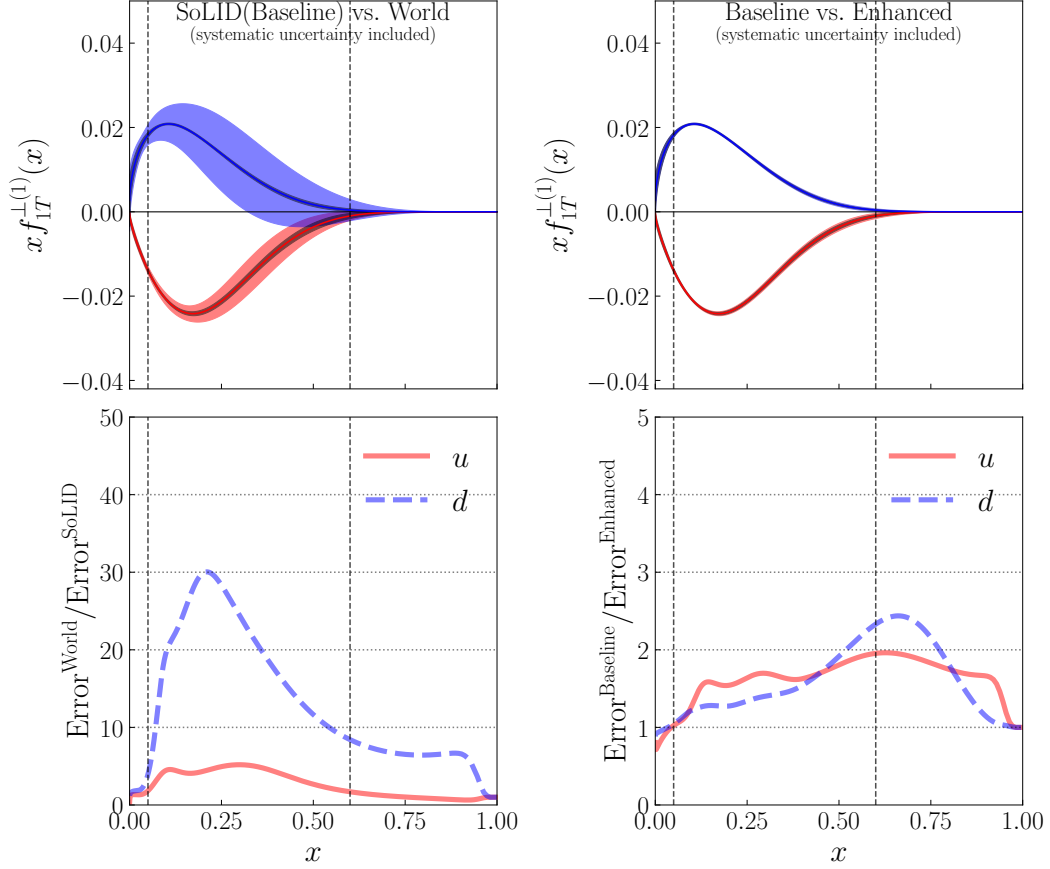


Figure 21: Left panel: the impact on Sivers extractions for up (red) and the down (blue) quarks by SoLID baseline configuration; the outer light shaded bands show the uncertainties from the world data, and the inner dark shaded bands show the uncertainties expected from SoLID baseline configuration. Right panel: the comparison of the impacts between the baseline and enhanced baseline configurations; the outer light shaded bands show the uncertainties expected from the baseline configuration, and the dark shaded bands show the uncertainties expected from the enhanced baseline configuration. The uncertainty ratios curves are shown in bottom plots. All results are plotted at a typical JLab 12 GeV scale $Q^2 = 2.4 \text{ GeV}^2$.

2.3 PVDIS Program

2.3.1 Motivation for PVDIS

The unique opportunities for experiments on parity violation at JLab with the 12 GeV upgrade were recognized in the NSAC long-range planning exercises. The SoLID PVDIS experiment was approved by PAC 35. Quoting the PAC 35 report, “the PAC believes the mission of this and future experiments using SoLID are sufficiently important that the Laboratory should make every effort to assist in securing the necessary funding.”

We reiterate here the physics topics that become accessible with the advent of a longitudinally polarized 11 GeV electron beam via measurements of the parity-violating asymmetry A_{PV} in deep inelastic scattering (DIS) off an unpolarized target in the kinematic region of large Bjorken $x = Q^2/2M\nu$. A_{PV} is defined to be:

$$A_{PV} = \frac{\sigma_R - \sigma_L}{\sigma_R + \sigma_L} \quad (1)$$

where $\sigma_R(\sigma_L)$ is the cross section for incident right-(left-) handed electrons.

The primary motivation of PVDIS is to search for new interactions beyond the Standard Model (SM). PVDIS is unique in that it is sensitive to fundamental axial-hadronic currents but does not have large radiative corrections involving soft hadronic physics that are impossible to make reliably.

We propose to obtain data over a broad kinematic range, with $x > 0.2$, $2 < Q^2 < 10$ (GeV/c)². With a deuterium target, the asymmetry is approximately directly proportional to electron-quark electroweak couplings, and is independent of kinematics and insensitive to the structure function. However, it is possible that the following physics could be observed in our data:

1. Charge Symmetry violation (CSV) at the quark level.
2. Higher-twist effects in the parity-violating asymmetry. Significant higher-twist effects are observed in DIS cross sections. In PVDIS, large higher-twist contributions can only be due to quark-quark correlations.

If these effects are large, they will constitute an important discovery. If they are small, our test of the SM will be quite reliable.

It has been suggested that there is additional CSV in heavier nuclei. By obtaining data with a lead target, we could test this hypothesis. Such an effect would have profound implications for our understanding of the EMC effect.

By switching the target to hydrogen, we can extract from the asymmetry the d/u ratio in the proton without requiring any nuclear corrections.

2.3.2 Review of the Theory

The general expression for A_{PV} for $Q^2 \ll M_Z^2$ is [96]

$$A^{PV} = - \left(\frac{G_F Q^2}{4\sqrt{2}\pi\alpha} \right) \left[g_A^e Y_1 \frac{F_1^{\gamma Z}}{F_1^\gamma} + \frac{g_V^e}{2} Y_3 \frac{F_3^{\gamma Z}}{F_1^\gamma} \right] = - \left(\frac{G_F Q^2}{4\sqrt{2}\pi\alpha} \right) (Y_1 a_1 + Y_3 a_3). \quad (2)$$

Here the F_i^γ are the electromagnetic structure functions and the $F_i^{\gamma Z}$ are structure functions for the parity-violating interference term. The Y_i are functions of the kinematic variable $y = \nu/E$ and the ratios of structure functions $R^j(x, Q^2)$:

$$Y_1(x, y, Q^2) = \frac{1 + (1-y)^2 - y^2(1-r^2/(1+R^{\gamma Z})) - 2xyM/E}{1 + (1-y)^2 - y^2(1-r^2/(1+R^\gamma)) - 2xyM/E} \left(\frac{1+R^{\gamma Z}}{1+R^\gamma} \right) \quad (3)$$

$$Y_3(x, y, Q^2) = \frac{1 - (1 - y)^2}{1 + (1 - y)^2 - y^2(1 - r^2/(1 + R^\gamma)) - 2xyM/E} \left(\frac{r^2}{1 + R^\gamma} \right), \quad (4)$$

with $r = 1 + Q^2/\nu^2$. The above expressions are quite general.

In order to account for possible violations of the Standard Model, it is essential to express the parity-violating part of the electron-hadron interaction in terms of general phenomenological four-fermion contact interactions

$$\mathcal{L}^{PV} = \frac{G_F}{\sqrt{2}} [\bar{e}\gamma^\mu\gamma_5 e (C_{1u}\bar{u}\gamma_\mu u + C_{1d}\bar{d}\gamma_\mu d) + \bar{e}\gamma^\mu e (C_{2u}\bar{u}\gamma_\mu\gamma_5 u + C_{2d}\bar{d}\gamma_\mu\gamma_5 d)]$$

with additional terms as required for the heavy quarks. Here C_{1j} (C_{2j}) gives the vector (axial-vector) coupling to the j^{th} quark. For the Standard Model:

$$C_{1u} = g_A^e g_V^u \approx -\frac{1}{2} + \frac{4}{3} \sin^2 \theta_W \approx -0.19 \quad (5)$$

$$C_{1d} = g_A^e g_V^d \approx \frac{1}{2} - \frac{2}{3} \sin^2 \theta_W \approx 0.34 \quad (6)$$

$$C_{2u} = g_V^e g_A^u \approx -\frac{1}{2} + 2 \sin^2 \theta_W \approx -0.030 \quad (7)$$

$$C_{2d} = g_V^e g_A^d \approx \frac{1}{2} - 2 \sin^2 \theta_W \approx 0.025 \quad (8)$$

The numerical values include electroweak radiative corrections. The key point is that the C_{1i} are about an order of magnitude larger than the C_{2i} , which makes the a_1 term dominant in Eq. 2. Recently, the JLab PVDIS collaboration published in the journal Nature [3] the result from a 6 GeV measurement that the C_{2i} 's are indeed nonzero. The results are shown in Figure 22.

As pointed out by Mantry, et al., [98] for the deuteron where $I = 0$, $Y_1 = 1$ and

$$a_1^D(x) = g_A^e \frac{F_1^{D\gamma Z}}{F_1^{D\gamma}} = a_1^D(x) = \frac{6}{5} (2C_{1u} - C_{1d}) \left(1 + \frac{2s^+}{u^+ + d^+} \right).$$

The only corrections to these formulae are physics beyond the Standard Model, CSV and quark-quark correlations, which form the motivation for the SoLID PVDIS experiment, and known corrections including strange quarks and target mass corrections.

For the a_3 term, we use the quark-parton model (QPM), which describes the structure functions in terms of parton distribution functions (PDF's) functions $f_i(x)$ ($\bar{f}_i(x)$), which are the probabilities that the i^{th} quark (antiquark) carries a fraction x of the nucleon momentum. With the definitions $f_i^\pm = f_i \pm \bar{f}_i$, $y = \nu/E$, the structure functions are given by

$$F_1^\gamma = \frac{1}{2} \sum_i e_i^2 (f_i(x) + \bar{f}_i(x)),$$

$$F_1^{\gamma Z} = \sum_i e_i g_V^i (f_i(x) + \bar{f}_i(x)),$$

$$F_3^{\gamma Z} = 2 \sum_i e_i g_A^i (f_i(x) - \bar{f}_i(x)),$$

where e_i is the electromagnetic charge of the i^{th} quark. Then

$$a_3^D(x) = \frac{g_V^e}{2} \frac{F_3^{\gamma Z}}{F_1^\gamma} = 2 \frac{\sum_i C_{2i} e_i f_i^-(x)}{\sum_i e_i^2 f_i^+(x)} = \frac{6}{5} (2C_{2u} - C_{2d}) \left(\frac{u^+ - d^+}{u^+ + d^+} \right) + \dots$$

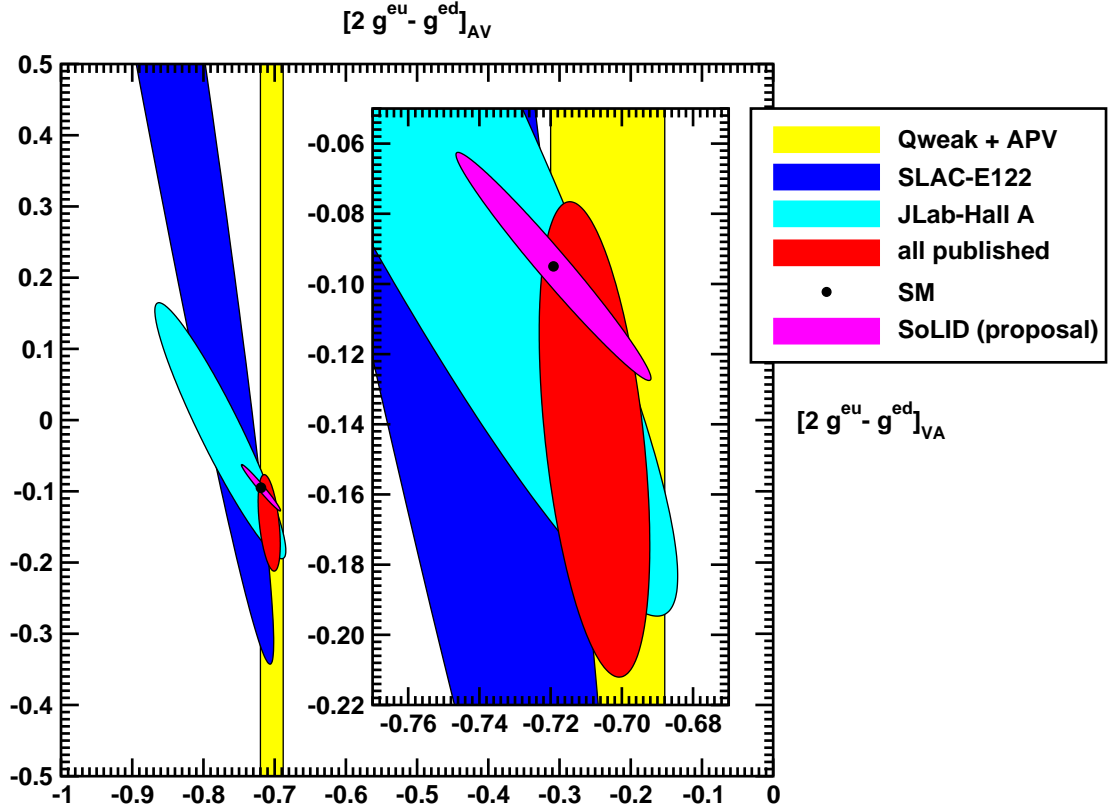


Figure 22: Results from the JLab PVDIS collaboration together with the projected results from the SoLID PVDIS experiment.

where contributions from heavy quark flavors are represented by the \dots . Contributions due to higher twist to this term can be obtained from neutrino scattering. The contribution of R^γ to A_{PV} is given in the Y_3 factor.

The key is that since $(2C_{2u} - C_{2d})$ is small, there is less sensitivity to the hadronic physics, whereas $(u^+ - d^-)(u^+ + d^+) \sim 1$ so that we are sensitive to new physics contributions to the C_{2i} . The main goal of the SoLID PVDIS experiment is to place a narrow error band on the C_{2i} as shown in Figs. 22 and 23. An example of new physics that can contribute to the C_{2i} , but not to the C_{1i} which have been precisely measured by Qweak and atomic parity violation in Cs, is a leptophobic Z' [99] as illustrated in Fig. 24. Searches for these particles is ongoing at the LHC [citeAaboud:2017buh] but the experiments are hampered by backgrounds and are limited to particular final states. The proposed data will also improve the mass limits for generic models for compositeness of quarks and leptons [4] as shown in Figure 25. SoLID has sensitivity for its particular Lorentz structure at the 20 TeV level. Recent limits from ATLAS [100] and CMS [102] set somewhat higher limits but are sensitive to different, higher-dimensional operators [103].

2.3.3 Charge Symmetry Violation

The subtle violation of fundamental symmetries in hadronic systems can often provide important insights into the dynamics at work in those systems. The famous Nolen-Schiffer anomaly has played a significant role in nuclear structure for decades. When it comes to hadron structure charge

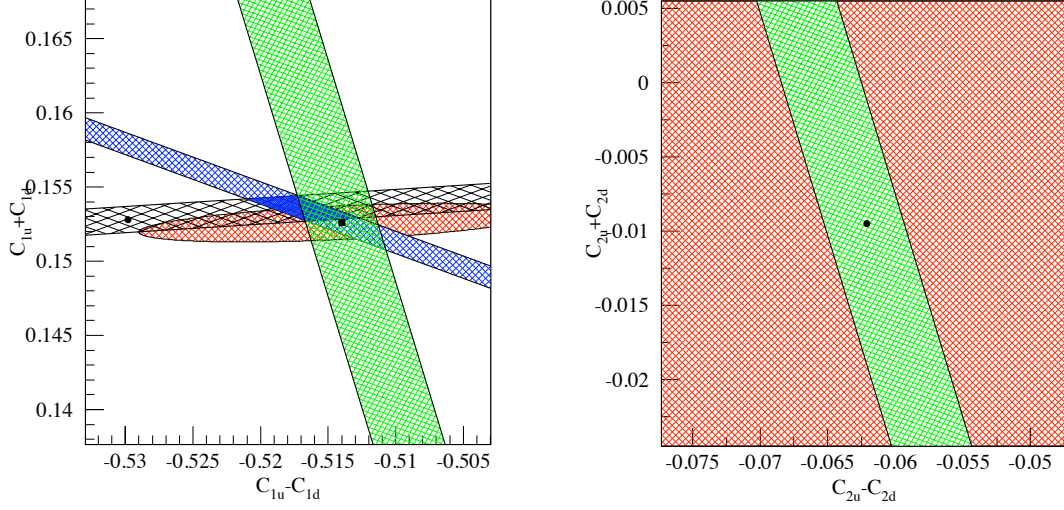


Figure 23: Current world knowledge on the isoscalar and isovector combinations of C_{1i} (left) and C_{2i} (right). Green band: limits projected for this experiment. The blue band is the Qweak experiment and the black is the Cs APV.

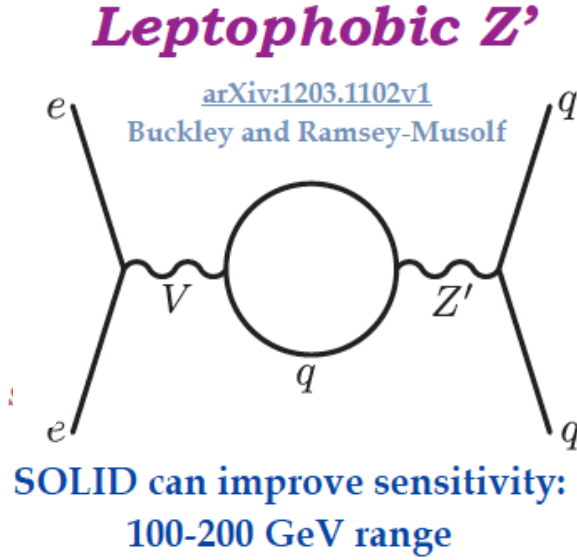


Figure 24: Diagram of a leptophobic Z' that can contribute to the C_{2i} and few other observables.

symmetry violation is of great interest because of its link to the role of di-quarks in non-perturbative parton distribution functions [105–107].

The NuTeV experiment published a discrepancy with the Standard Model [108] with a significance of about three sigma. The result stirred a lot of controversy, resulting in a serious re-evaluation of the work. Additional corrections, including changes in the Cabibbo angle, strange sea, and improved radiative corrections, have recently been made, but have changed the result very little.

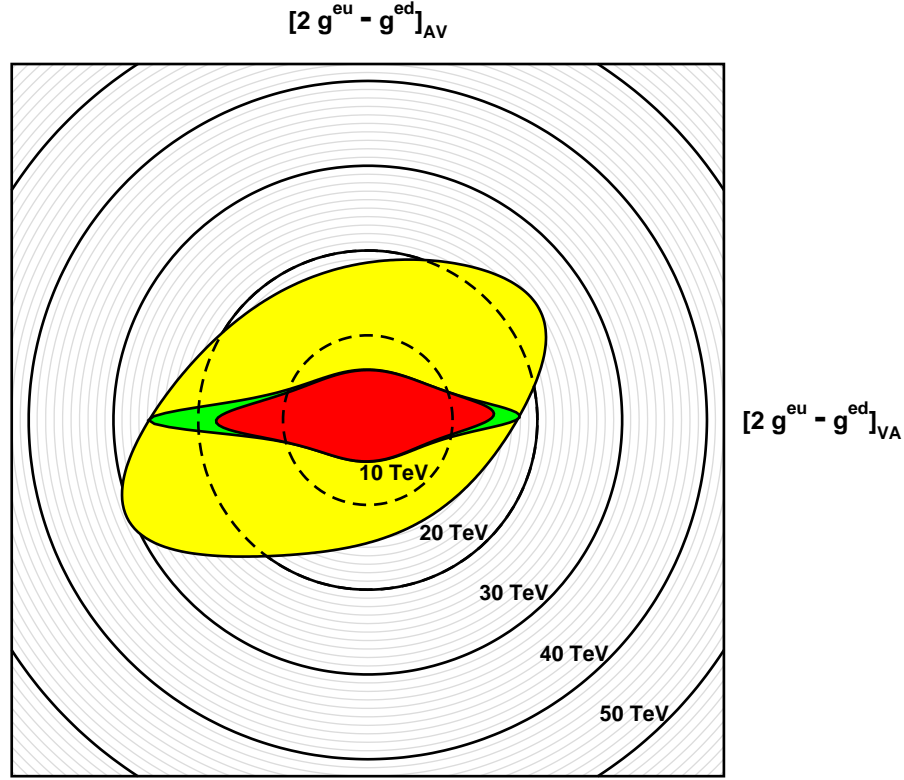


Figure 25: Polar plot for limits on composite models. The red region includes all published results. The green region gives the projected limits with the Proposed P2 experiment at Mainz[104]. The yellow are represents the improvement for the projected SoLID results.

One possible explanation of the NuTeV result is charge symmetry violation (CSV) in the PDF's. This was overlooked in the NuTeV analysis, even though estimates which suggested how important it could be had existed in the literature for almost a decade [106, 107]. Various authors [109–111] have also presented the case that this is a reasonable explanation.

Our experiment is also sensitive to CSV. If the x -dependence of the CSV falls slower than the PDF's as suggested by the curves in Figure 26 our asymmetry should display a clear x -dependence. Moreover, these results will provide an important test of the CSV explanation for NuTeV.

Another interesting possible contribution to the NuTeV anomaly is the isovector EMC effect [113], which occurs for heavy nuclei. Measuring PVDIS in a target such as Pb would be able to demonstrate this effect.

2.3.4 Higher Twist

Higher twist effects originate from quark-quark or quark-gluon corrections. A representative plot on the higher twist effect in the unpolarized electromagnetic cross sections is shown in Figure 27, with D_{HT} defined by $F_{1,2}^{HT} = F_{1,2}^{LT} \left(1 + \frac{D_{1,2}^{HT}}{Q^2} \right)$. Extraction of HT coefficients D_i were extracted from global fits such as MRST [97].

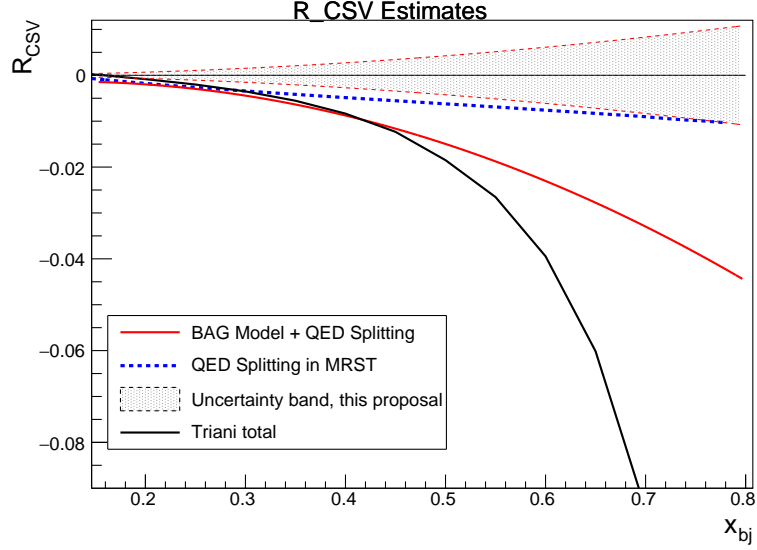


Figure 26: Possible contribution to A_{PV} due to CSV. The largest prediction comes from Ref. [112]

A recent paper has examined possible contribution of higher twist (HT) effects to the dominant $Y_1 a_1$ term in A_{PV} [98]. The correction can be parameterized as a fractional contribution $R_1(HT)$ by

$$Y_1 a_1 \approx Y_1 a_1 (1 + R_1(HT) + \dots)$$

where the ellipsis refers to other corrections including CSV. It turns out that the only contribution comes from the operator

$$\mathcal{O}_{ud}^{\mu\nu} = \frac{1}{2} [\bar{u}(x) \gamma^\mu u(x) d(0) \gamma^\nu d(0) + (u \leftrightarrow d)]$$

which arises only from quark-quark correlations, or in other words, di-quarks in the nucleon. Higher twist contributions involving gluons cancel in the ratio. The special feature of A_{PV} is that it is the only practical experiment that can isolate higher twist due to four quarks.

The result is

$$R_1(HT) = -\frac{4}{5} \frac{[(9 - 20 \sin^2 \theta_W) F_1^{\gamma;4q} - 5 F_1^{\gamma Z;4q}]}{(1 - \frac{20}{9} \sin^2 \theta_W) [u_p(x) + d_p(x)]}$$

where $F_1^{\gamma;4q}$ and $F_1^{\gamma Z;4q}$ are the four-quark higher twist contributions to the structure functions.

2.3.5 Data Sample and analysis

The observation of CSV is possible with our apparatus if the effect varies with x . An x -independent CSV effect would be indistinguishable from a change in the C_{1q} 's. In the absence of existing CSV data, it is quite natural, however, to expect that the x -dependence is similar to that shown in Figure 27, and we will make that assumption in our further discussion. From observations of higher-twist contributions to DIS cross sections, it is also natural to assume that Q^2 -dependent effects will also depend on x and increase with increasing x .

If indeed either higher twist effects or CSV are clearly seen, the experiment will be a success. If they are absent, we plan to untangle the effects of hadronic and electroweak physics by fitting the

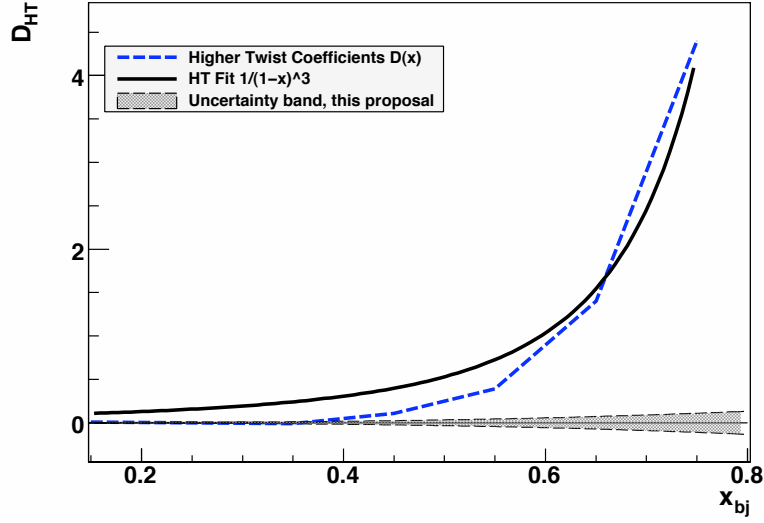


Figure 27: Possible contribution to A_{PV} due to higher twist contributions.

asymmetries to a function of the form

$$A_{PV}^D = A_{PV}^{EW} \left(1 + \beta_{HT} \frac{1}{(1-x)^3 Q^2} + \beta_{CSV} x^2 \right). \quad (9)$$

Since the size of the hadronic effects is small, the sensitivity to the exact form is not important. The resulting statistical errors on the fit parameters are:

$$\delta A_{PV}^{EW} / A_{PV}^{EW} = 0.3\%; \quad \delta \beta_{HT} = 0.0026; \quad \delta \beta_{CSV} = 0.017.$$

With this method, we use the full statistical power of the data set. However, the result has some sensitivity to the exact form of the chosen fitting functions. Under the scenario where the hadronic effects are small, these errors are negligible as long as we assume that CSV and higher twist effects depend strongly on x , as expected. The one-sigma band for the CSV term is plotted in Figure 27.

If the pattern of higher twist effects is the same for A_{PV} as it is for the cross sections, then at $x = 0.6$ the asymmetries at the different Q^2 values will differ by 15%. In that scenario, the rapid x -dependence of the higher-twist coefficients for the cross section would imply that higher twist effects would still be negligible at $x = 0.4$. With a comparable x -dependence, a Q^2 -dependent effect as small as $\sim 3\%$ of the effect seen in cross-section measurements would be easily identifiable given our statistical precision.

Measuring d/u at high x Although the ratio of the structure functions d/u in the nucleon has been of great interest for many years [114–117, 123], reliable measurements of this quantity have proven to be elusive [118]. The traditional method to measure d/u is to compare DIS cross sections for protons and neutrons. However, since there are no free neutron targets, light nuclei must be employed, which requires nuclear physics corrections. The MARATHON [119] experiment has recently taken DIS data comparing ^3H and ^3He to use mirror symmetry to reduce the corrections, but issues may remain such as isospin dependence in off-shell effects [120]. The BONUS [121, 122] experiment will reduce nuclear corrections by measuring the spectator proton.

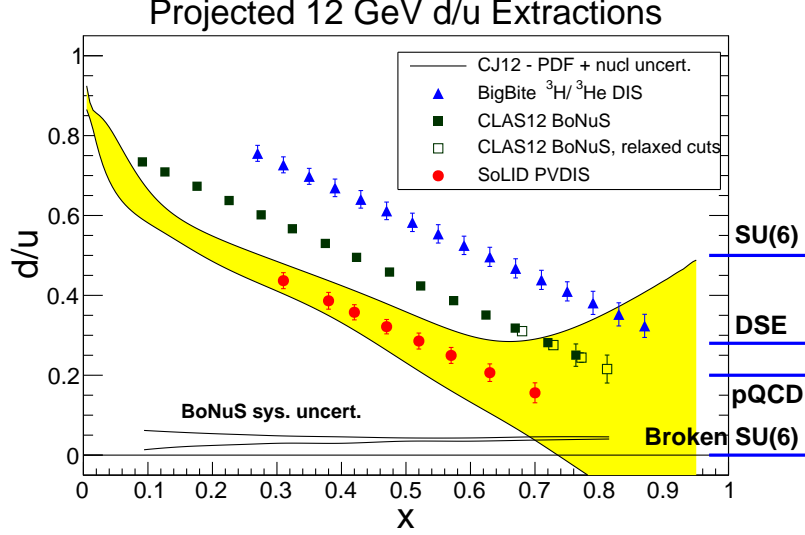


Figure 28: Anticipated precision for d/u measurement with SoLID as well as other proposed experiments.

By using SoLID with a hydrogen target, which is not isoscalar, the structure functions do not cancel in the expression for $a(x)$. In particular,

$$a(x) \approx \frac{3}{4} \left[\frac{6C_{1u}u(x) - 3C_{1d}d(x)}{u(x) + \frac{1}{4}d(x)} \right] \sim \left[\frac{u(x) + 0.912d(x)}{u(x) + 0.25d(x)} \right]$$

and we see that $a(x)$ is sensitive to the ratio d/u . There are no nuclear corrections. By comparing the results of all of these experiments when completed, it should be possible to untangle all of the interesting nuclear physics and also produce a reliable value of d/u at large x . Projected errors for all three approaches are shown in Fig. 28.

2.3.6 Beam Time and Projections

For the deuterium data, we have based our sensitivity on 180 days of production running at $50 \mu\text{A}$ on a 20-cm liquid deuterium target, with 1/3 of the data at 6.6 GeV and the rest at 11 GeV. Approximately 27 additional days, run at various currents, will be required for checkout and calibrations. An additional 18 days will be required at 4.4 GeV and $50 \mu\text{A}$ for radiative correction measurements. The total beam request at all energies for the deuterium measurement is 225 days, with about 25 of those days run mostly at reduced beam currents. Projected statistical uncertainties in A_{PV} are shown in Fig. 29.

For the hydrogen measurement, 90 days are needed for production data at 11 GeV, about 9 days are required at 4.4 GeV to control radiative corrections and another 14 days will be required for calibration. The running time requested for hydrogen totals to 113 days. We have been approved for 180 days total. The plan is to first take half the deuterium data. If nothing exciting appears, we will switch to hydrogen. In the future, we would also anticipate requesting an additional comparable run for a heavy nucleus such as Pb.

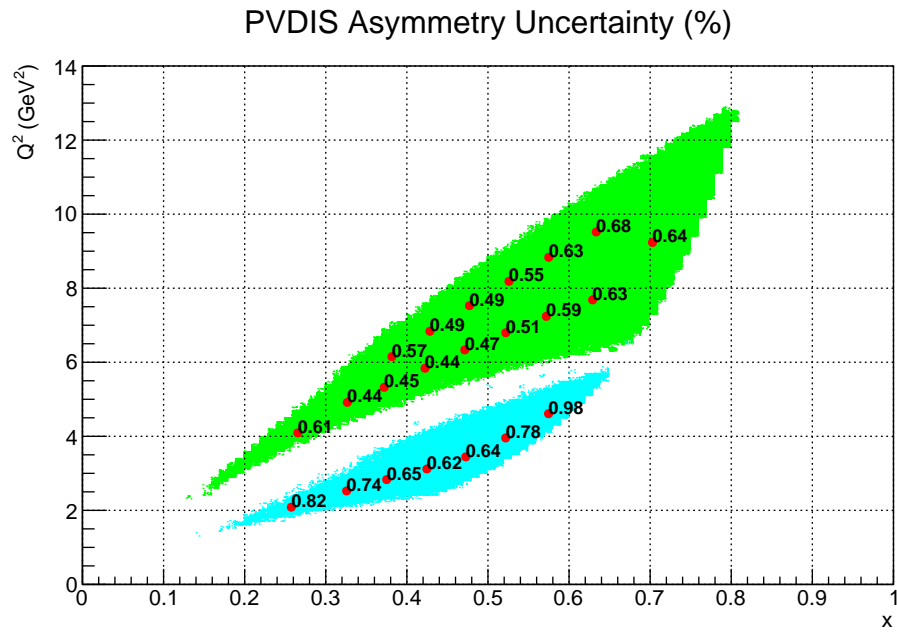


Figure 29: Anticipated statistical precision for A_{PV} in percent versus Q^2 and x . 11 GeV data (green region) are based on a simulation including the electron calorimeter trigger. For the 6.6 GeV data the effect of the trigger is estimated.

2.4 J/ψ Program

2.4.1 Introduction

One of the fundamental goals of modern nuclear physics is to understand hadrons and nuclei starting with Quantum Chromodynamics (QCD), the theory of strong interactions. Nucleons are the fundamental building blocks of all atomic nuclei and make up almost all visible mass in the universe, including the stars, the planets, and us. The nucleon is not static but has a complex internal structure, the dynamics of which we are only beginning to reveal in modern experiments. In QCD, nucleons emerge as strongly interacting, relativistic bound states of quarks and gluons. One of the fundamental goals of modern nuclear physics is to understand the emergence of nucleons, or hadrons in general, their fundamental properties, such as their mass and spin and the forces between them, from the constituent quarks and gluons, and their interactions within QCD.

Hadrons are emergent phenomena of QCD, a realm of the strong interaction where much remains to be understood. While significant progress has been achieved in exploring QCD in its asymptotic and perturbative regime, the theory in the strong interaction regime is hardly tractable without numerical techniques. Here lattice QCD, offers real hope towards an unraveling of hadronic structure. For example, an impressive success was achieved with the recent lattice QCD determination of the low-lying levels of the baryon spectrum [6]. However, there is still a long road ahead to fully grasp the implications of QCD in this regime. The measurement of the elastic production of J/ψ near the threshold at Jefferson Lab could provide the unique and much needed information on the pure gluonic component of the QCD interaction, as well as the nature and the verification of the recently observed charmed pentaquark states.

2.4.2 Color Van der Waals forces

One aspect of the pure gluonic component of the QCD interaction is described by multiple gluon exchange between two color neutral hadrons, such as charmonium and nucleons or nuclei, which do not share common valence quarks. It has long been argued that the force acting between nucleon/nucleus and J/ψ is an attractive force, with negligible mesonic ($D\bar{D}$) or multi-mesonic ($\rho\pi$) exchange contributions at low energies [125]. Since the nucleon/nucleus and J/ψ are color neutral, this force is dubbed ‘color Van der Waals force’ in analogy with physical chemistry.

A direct consequence of such a nucleon- $J\psi$ attractive force is the possible existence of a nuclear bound quarkonium state which was proposed more than 25 years ago [126], but has yet to be observed. At that time a follow up calculation using the operator product expansion (OPE) [127] to describe the low energy interaction of quarkonium with nuclei, in the limit where the mass of the charm quark is infinite, found that the J/ψ binds in nuclear matter with about 10 MeV but the authors caution about possible large corrections due to confinement effects. Over the years with limited available data in kinematic regions sensitive to binding effects, theoretical interest in the subject has been strong nonetheless [128–135].

More recently the NLQCD collaboration [183] showed that in nuclear matter the J/ψ is bound by an energy of the order of 40 MeV or less depending on the light quarks extrapolation in their lattice results. While a phenomenological analysis of the forward J/ψ -p scattering amplitude within a dispersive framework [157] resulted in a ψ binding energy in nuclear matter of 2.7 ± 0.3 MeV. The latter number uncertainty would be dramatically improved with more accurate cross section data in the threshold region. Furthermore, in the same reference a path towards unraveling the ratio of real to imaginary part of the J/ψ -nucleon scattering amplitude is described through the measurement of the $\gamma p \rightarrow e^+ e^- p$ forward-backward asymmetry in the vicinity of the J/ψ resonant amplitude. This

forward-backward asymmetry is sizable due to the interference of the Bethe-Heitler amplitude with the J/ψ production amplitude.

2.4.3 Emergence of hadron mass

The emergence of the proton mass, and hadronic mass in general, from its constituents and their interactions is a fundamental question of interest in the strong regime of the QCD color forces. This mechanism is especially puzzling as the constituent mass plays only a minor role in the accounting for the total proton mass. This is unlike more familiar system such as atoms or nuclei, where the mass can be readily described by its constituents (electrons, nucleons). The expectation value of the trace of QCD energy-momentum tensor in the proton state of momentum p , $\langle p|T^\alpha_\alpha|p\rangle$, which is proportional to the proton mass square in any frame, can be expressed in terms of a sum of two distinct sources of contribution to the proton mass: the conformal (trace) anomaly term plus the chiral symmetry breaking quark mass term. Owing to the color confinement, a defining property of QCD, even the most advanced detector cannot see quarks and gluons in isolation as they are forever bound inside hadrons. Neither terms are direct physical observables, such as the cross sections of hadrons and leptons. To understand the origin of the proton mass, and to disentangle the relative roles of the pure gluonic trace anomaly contribution from the quark mass effect, we will need lattice QCD calculations of individual source contributions, or identify the experimental connections of these two terms to independent measurements with theoretical controllable approximations.

In two important papers [184, 185] Ji offers a more detailed decomposition of the proton mass by providing what he called “A QCD analysis of the mass structure of the nucleon”. By decomposing the expectation value of QCD hamiltonian between the proton state of momentum p , $\langle p|H_{\text{QCD}}|p\rangle$, when the proton is at rest, it was shown that one can partition the mass of the nucleon among four terms identified as the kinetic and potential energy of the quarks, the kinetic and potential energy of the gluons, the quark masses and the conformal (trace) anomaly. The wealth of deep inelastic scattering data was used to estimate the first three terms at a scale of 1 GeV^2 within the $\overline{\text{MS}}$ renormalization scheme, while the fourth (conformal anomaly) term was estimated assuming the nucleon mass sum rule, to contribute roughly 20% to the total proton mass. This first indirect estimation of the conformal anomaly contribution to the nucleon mass was an important step, however, neither direct measurements nor lattice calculations of this term have been attempted yet. It appears that the size of the anomaly term can be accessed through a detailed measurement of the electro- and photo-production cross section at threshold with the extraction of the real part of the forward scattering amplitude all the way to threshold.

Accessing the trace anomaly through the measurement of electro-production of the J/ψ near threshold opens a host of important questions related to the gluonic structure of the nucleon. What is the strength of the J/ψ -nucleon interaction near threshold? What is the production mechanism of quarkonium (J/ψ , Υ) on a nucleon? Are there special states in the threshold region? Both the absolute cross sections and the left-right asymmetry will be measured in the Jefferson Lab SoLID experiment (E12-12-006) [161] described below. These measurements will go a long way to help answer these important questions.

2.4.4 LHCb charmed pentaquark

A renewed interest in the near threshold region of J/ψ photo-production was prompted more recently by the discovery of LHCb peaks in the decay channel $\Lambda_b \rightarrow pJ/\psi K^-$ where the decay rate is plotted against the invariant mass of the J/ψ -proton system. These peaks were interpreted as possible charm pentaquark resonances. However, to confirm or refute this possible explanation direct

photo-production of these resonances in the s-channel was suggested by several authors [7, 187–189]. Such experiments have been recently carried out at Jefferson Lab in three different halls, hall D, B and C. The GlueX collaboration at Jefferson Lab measured photo-production of J/ψ near threshold using the GlueX detector in Hall D and published its results [182]. Experiment E12-16-007 [190] was designed to perform a direct search of the higher mass narrow width $P_c^+(4450)$. It ran during the Spring of 2019 and the analysis will soon be completed. CLAS12 has taken also the relevant data on a hydrogen target and the analysis is underway.

2.4.5 Overview of the J/ψ Program

The high luminosity and large acceptance offered by the JLab 12 GeV energy upgrade combined with SoLID in Hall A is a unique tool to start an investigation program of the J/ψ -nucleon interaction.

Measurements of the cross section of electro- and photo-production of J/ψ on a nucleon near threshold will be performed during experiment E12-12-006 [161] using SoLID. These measurements with the SoLID detector will provide unprecedented precision, even beyond the expected capabilities of the EIC, to probe the possible enhancement of the cross section due to the contribution of the conformal anomaly very close to the threshold photon energy of J/ψ production. Threshold enhancements due to on-shell rescattering or quasi-bound states around threshold have been observed in several processes such as $e^+e^- \rightarrow p\bar{p}, \Lambda\bar{\Lambda}, \Sigma^0\bar{\Sigma}_0, \Lambda\bar{\Sigma}_0$ [155] as well as in the J/ψ radiative decays, e.g. $J/\psi \rightarrow p\bar{p}\gamma$ [156]. Experiment E12-12-006 aims at observing such an enhancement in the J/ψ -proton system and offers the capability to explore the region below threshold if there are hints of an enhancement of the cross section just above threshold. Furthermore, the proposed cross section measurement could also shed light on the existence of predicted super-heavy N^* with hidden charm with a mass around 4.3 GeV [158].

Additionally, we shall explore the interference of the Bethe-Heitler amplitude with that of the J/ψ electro-production to attempt a determination of the relative contribution of the real and the imaginary part of the scattering amplitude. A study of the angular distribution of the J/ψ decay can reveal whether the J/ψ was originally produced from an octet or singlet state. Recently a phenomenological analysis of the forward $J/\psi - p$ scattering amplitude within a dispersive framework [157] resulted in a J/ψ binding energy in nuclear matter of 2.7 ± 0.3 MeV. The latter number uncertainty would be dramatically improved with more accurate cross section data in the threshold region. Furthermore, in the same reference a path towards unraveling the ratio of real to imaginary part of the J/ψ -nucleon scattering amplitude is described through the measurement of the $\gamma p \rightarrow e^+e^-p$ forward-backward asymmetry in the vicinity of the J/ψ resonant amplitude. This forward-backward asymmetry is sizable due to the interference of the Bethe-Heitler amplitude with the J/ψ production amplitude.

Finally, studies of J/ψ production and propagation in the nuclear medium is the natural extension of the proposed measurements on a nucleon. The study of multi-gluon QCD Van der Waals forces in nuclei is believed to shed new light on their possible role in J/ψ -nuclear bound states [126, 126–133]. Another related challenge is the in-medium properties of charmonia as well as the possible restoration of the chiral symmetry in the nuclear medium, which is closely connected to the modifications of masses and widths of mesons when embedded in the nuclear environment [134]. For these studies, it is important to find the appropriate kinematic conditions to produce J/ψ near rest, or with small momentum relative to the nucleus. Therefore, measurements near threshold and even sub-threshold look promising [159].

Experiment E12-12-006 [161] could be seen as a first phase of the SoLID J/ψ program. It will utilize the SoLID spectrometer to measure the cross section of the elastic electro- and photo-

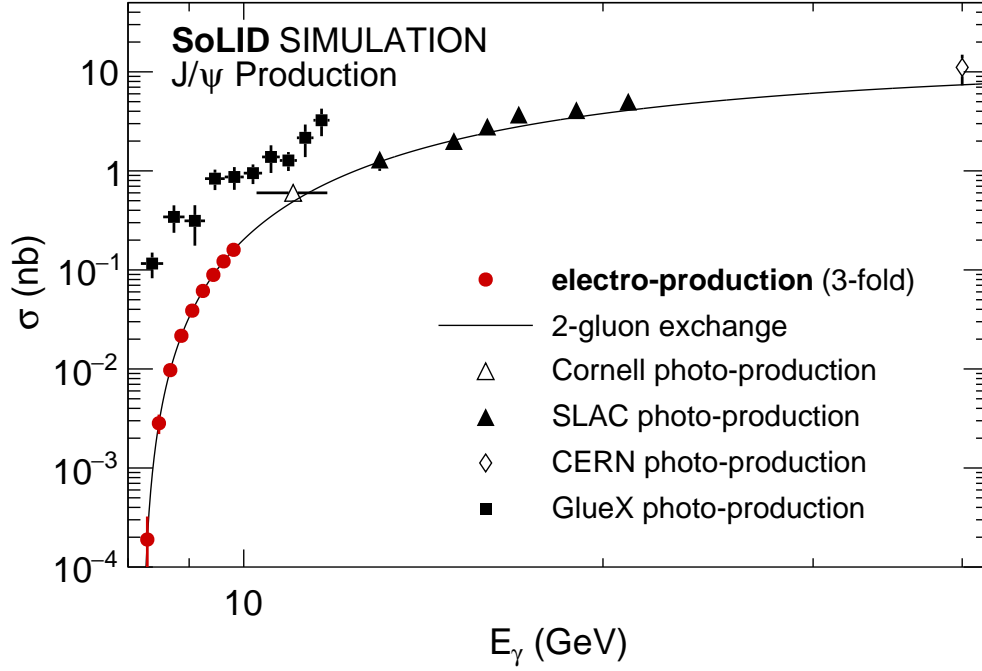


Figure 30: Projected uncertainties on the total elastic J/ψ electro-production cross section, compared to the existing world data. The solid line is the result of a 2-gluon fit to the world data excluding the recent GlueX results.

production of J/ψ near threshold ($4.05 \text{ GeV} < W < 4.45 \text{ GeV}$ and $|t - t_{min}| < 2.5 \text{ GeV}^2$) to study QCD in the non-perturbative regime with luminosity of $10^{37} \text{ cm}^{-2} \text{ s}^{-1}$.

2.4.6 Beam Time and Projections

The J/ψ experiment E12-12-006 was approved by JLab PAC39 for 60 PAC days [161]. The production run itself consists of a $3 \mu\text{A}$ 11 GeV electron beam incident on a 15 cm liquid hydrogen target. The other 10 days will be shared among several activities, such as detector calibration, data taking with an Al dummy target, and dedicated luminosity scans required for the absolute cross section measurement.

E12-12-006 will be the first measurement of the J/ψ production cross section in exclusive electro-production, as well as the first high-precision measurement of the 2-dimensional photo-production cross section in the threshold region. The projected results for near-threshold electro-production as a function of effective photon energy are shown in Fig. 30. The projections are based on a 2-gluon fit to the world data, excluding the new GlueX [182] results. This was done to provide a realistic lower bound on the precision of the experiment, and to showcase the sensitivity to cross sections below 10^{-3} nb . In fact, assuming the GlueX results truly supersede the previous measurement, the projected count rate would be almost an order of magnitude larger.

The electro-production channel has several advantages over the photo-production channel. The photon virtuality Q^2 provides for an additional degree of freedom over the real photon kinematics, which enables the experiment to measure much closer to the J/ψ threshold than would be possible in pure photo-production. This can be clearly seen when comparing the projected electro-production

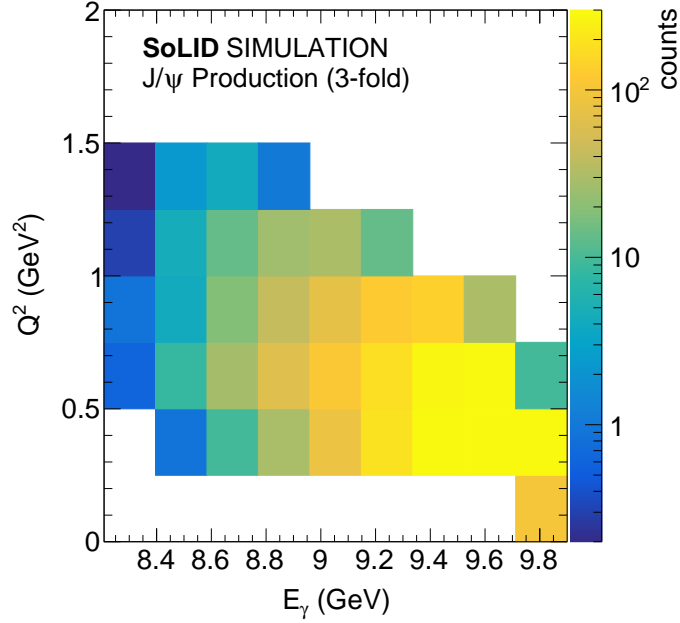


Figure 31: Q^2 coverage for the SoLID electro-production measurement as a function of E_γ . Around threshold, the average Q^2 is approximately 1 GeV^2

results in Fig. 30 to the projections for the photo-production channel in Fig. 33. Furthermore, as the scale for J/ψ production is given by $Q^2 + M_{J/\psi}^2$, the reach in Q^2 will provide for a crucial metric in the understanding of the near-threshold results. The projected sensitivity in Q^2 as a function of the effective photon energy E_γ is shown in Fig. 31. Note that a larger near-threshold cross section, as indicated by the GlueX results, would increase the Q^2 reach at threshold for E12-12-006 even further.

A change in the functional dependence and slope of the t -distribution as a function of photon energy is the true experimental signature of a binding force between the J/ψ and the nucleon. The t -distributions are also crucial to constrain the contribution from the trace anomaly itself. The SoLID J/ψ experiment will be the first truly 2-dimensional measurement E_γ and t for both electro- and photo-production. Fig. 32 shows the projected results on the t -dependence for a kinematic point close to the threshold (left), and at higher photon energy (right), assuming a 2-gluon model for the cross section. The experiment will have excellent coverage of the available phase-space in t , with good sensitivity up to very large values of $|t|$ (4 GeV^2 and larger).

The photo-production measurement will be based around a 2-fold coincidence trigger between the J/ψ decay electrons. The energy reach for the photo-production channel is higher than that for the electro-production channels, starting further from threshold and going all the way to the beam energy for 11 GeV. The expected count rate for the photo-production channel is two orders of magnitude larger than that for the electro-production channel. This makes the photo-production channel especially suited for a high-precision study of the 2-dimensional J/ψ production cross section around the region of the LHCb charmed pentaquarks. Fig. 33 showcases the projected results for this channel using the same assumptions as the projections for the electro-production channel. Contributing to this channel are both quasi-real production as well as production through

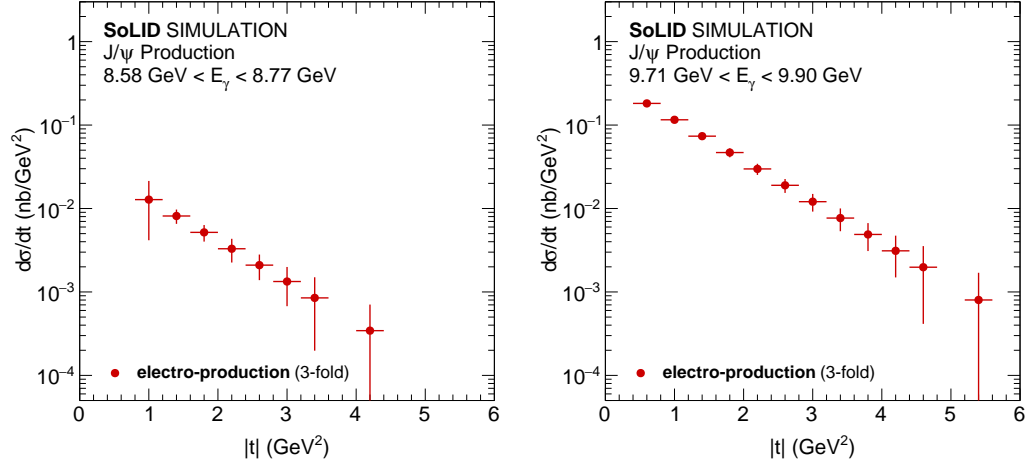


Figure 32: Projected results for the t -dependence in electro-production for a near-threshold point (left), and a point at higher-energies (right).

bremsstrahlung photons inside of the liquid hydrogen target.

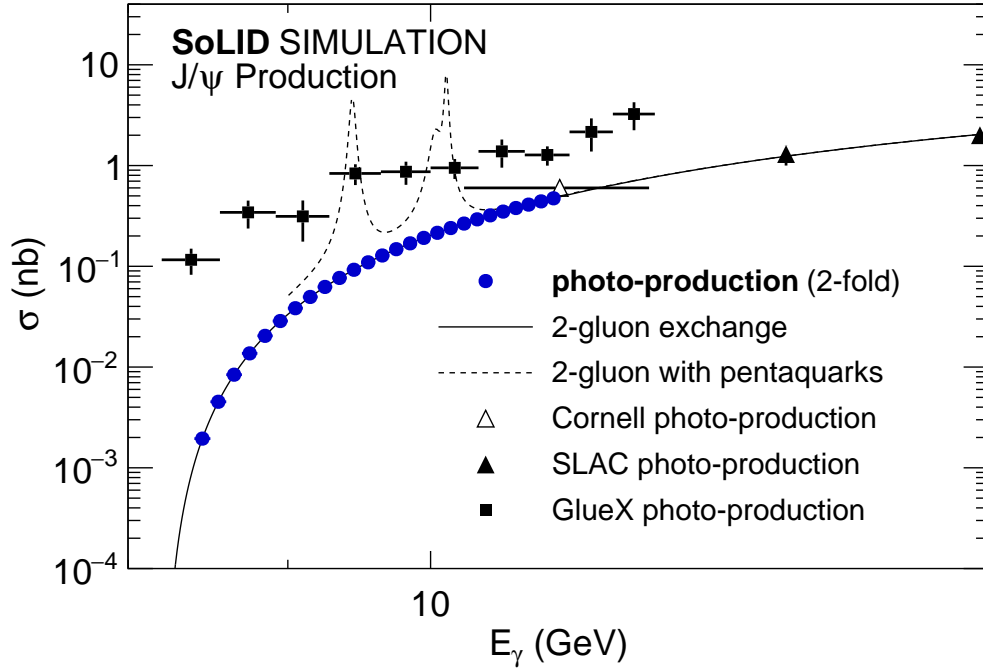


Figure 33: Projected results on the total elastic J/ψ photo-production cross section, compared to the existing world data. Also shown is the upper limit on the LHCb pentaquarks $P_c(4312)$, $P_c(4440)$ and $P_c(4457)$ as constrained by the recent GlueX results (dashed line).

Finally, the photo-production channel has the required statistical precision to study the interference between exclusive J/ψ photo-production and Bethe-Heitler pair production. This interference

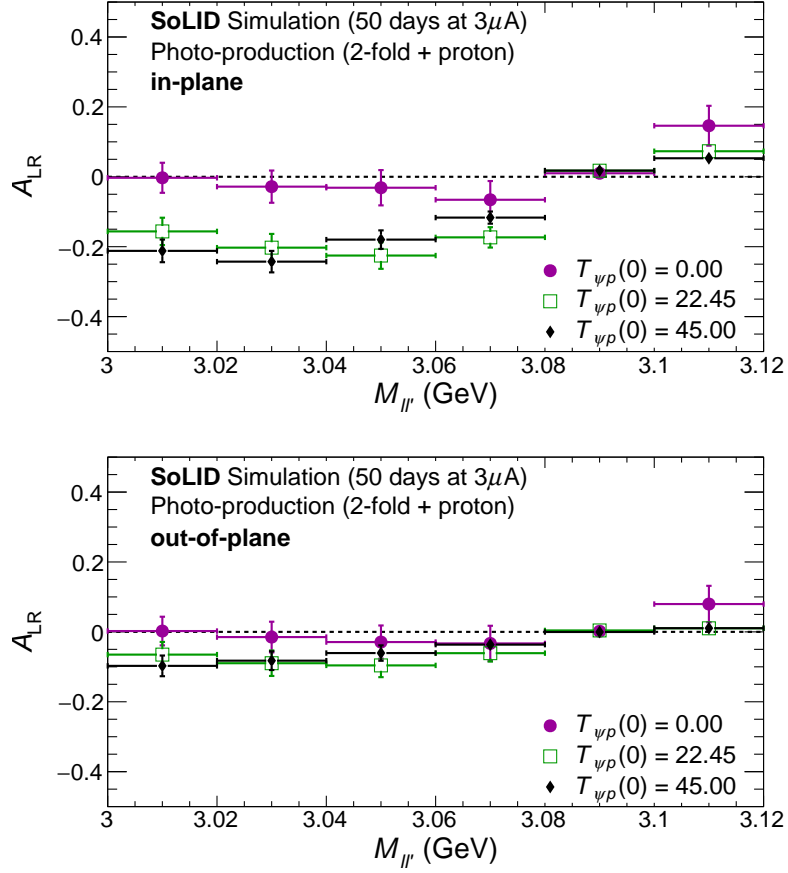


Figure 34: Projected sensitivity to the left-right asymmetry in the pair-production cross section caused by the interference between J/ψ photo-production and Bethe-Heitler pair production, for in-plane production (top) and out-of-plane production (bottom). The different colors correspond to different assumptions for the binding force between J/ψ and proton, ranging from no binding (purple circles) to large binding (black diamonds).

gives rise to a forward-backward asymmetry in the e^+e^- pair close to the J/ψ invariant mass peak, which provides for an independent channel to study the binding force between the J/ψ and nucleon [157]. This forward-backward asymmetry can be translated to a left-right asymmetry that will be measured during the SoLID J/ψ experiment. The forward-backward asymmetry is maximal for pair production that occurs in the photon-proton plane, while it is suppressed for out-of-plane production. The projected results for this asymmetry are shown in Fig. 34 as a function of the invariant mass of the lepton pair $M_{ll'}$. The in-plane asymmetry will have good sensitivity to the size of the binding force between the J/ψ and nucleon. This measurement requires a very high luminosity, and can only be accomplished at SoLID.

2.5 Possible Expansion in Physics Reach

2.5.1 GPD Program

There are several GPD experiments in different stages of study/approval. As has been remarked elsewhere, a variety of hard exclusive measurements are needed to disentangle the contributions of the different GPDs, with the general Compton processes (DVCS, TCS, DDVCS) sensitive to various real and imaginary combinations of all four leading twist GPDs (Fig. 35), vector-meson Deep Exclusive Meson Production (DEMP) sensitive to the spin-average H and E GPDs and pseudoscalar-meson DEMF sensitive to the spin-difference \tilde{H} and \tilde{E} GPDs. The SoLID GPD program under investigation includes many of these reactions, and has the potential to improve greatly our understanding of nucleon structure.

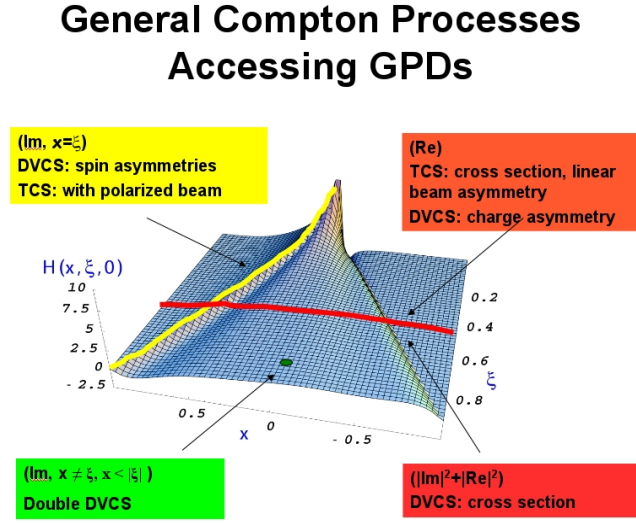


Figure 35: General Compton processes accessing GPDs.

Timelike Compton Scattering (TCS) from an unpolarized LH_2 target can provide information on the real (imaginary) parts of the Compton amplitude using unpolarized (circularly polarized) photons. In this case, the produced lepton pair sets the hard scale ($Q^2 > 4 \text{ GeV}^2$) and the azimuthal asymmetry of the $\ell^+\ell^-$ plane with respect to the q -vector allows the separation of the GPD and Bethe-Heitler contributions. This has been approved as a run group experiment with the J/ψ experiment (E12-12-006A).

Double Deeply Virtual Compton Scattering (DDVCS) in the di-lepton channel on an unpolarized LH_2 target has been reviewed by PAC43 as LOI12-12-005. The solenoidal configuration is ideal for high luminosity, with a fully parasitic proposal (as part of the J/ψ run group) for the e^+e^- channel under preparation. Once this experiment has run, a later phase of measurements might include the $\mu^+\mu^-$ channel. A workshop at ECT Trento to refine the TCS and DDVCS physics program was held for October 24-28, 2016.

A possible Deeply Virtual Compton Scattering (DVCS) experiment on polarized ^3He is also under study. The 12 GeV polarized DVCS experiments to date utilize longitudinally (E12-06-119) and transversely (C12-12-010) polarized proton targets. No polarized neutron-DVCS experiment has been proposed at JLab to date, and SoLID could make a unique contribution here once the

reaction exclusivity requirements and possible backgrounds are better understood. A complete set of SoLID DVCS data with both proton and neutron targets at varied polarization would be essential to control systematic uncertainties, perform flavor decomposition, and disentangle the different GPDs.

Deep Exclusive Meson (π^-) Production (DEMP) using a transversely polarized ^3He (neutron) target looks very promising. The transverse single-spin asymmetry in exclusive charged π production has been identified as the most sensitive observable to probe \tilde{E} . In this case, one fits the $\sin(\phi - \phi_S)$ dependence, where $(\phi - \phi_S)$ is the azimuthal difference between the π^- reaction plane and the polarized target. Theoretical calculations suggest higher twist corrections likely cancel in the asymmetry, allowing access to GPDs at much lower value of Q^2 than typically required in DEMP reactions. This measurement has been approved as a run group experiment with the transversely polarized ^3He SIDIS experiment (E12-10-006B), and detailed studies on the expected uncertainties are underway.

This summary makes clear that the SoLID-SIDIS setup is indeed very attractive in terms of acceptance and luminosity, and will allow a Phase 1 GPD program to be initiated with minimal impact on the approved SoLID program. Once this has been executed, one could envision a later Phase 2 suite of GPD experiments with additional recoil detectors near the target (such as low momentum proton tagging for DEMP), dedicated configurations (for DDVCS), or improved EC resolution (to allow exclusive vector meson and π^0 measurements). These would require much more study, and are clearly beyond the scope of the present proposals.

2.5.2 SIDIS Production of Charged Kaons

The extension of the SIDIS production of charged pion to the SIDIS production of charged kaons is under study. Because the kaon contains a valence strange/antistrange quark, the SIDIS production of charged kaons is more sensitive to the strange distributions. Compared to the pion data, the kaon data are very limited. Lacking the knowledge of the strange quark distributions will prevent us from fully understanding the spin structures of the nucleon. Taking advantage of high luminosities and large acceptance, SoLID could be ideal to measure the SIDIS production of charged kaons with high statistics. The combination of the proton and the neutron (^3He) targets, and the detection of charged pions and charged kaons in a similar kinematic region helps us to have flavor separations of all light quark distributions, *i.e.*, u , \bar{u} , d , \bar{d} , s , and \bar{s} . As kaon is heavier than pion, the SoLID kinematics covers a intermediate region from target-fragmentation to current-fragmentation. A precise measurement in this region will allow us to understand how the factorization breaks down.

A full RICH detector for kaon detection is likely to be too costly to consider. A high resolution TOF is a more practical solution. SoLID needs to do kaon identification over a momentum range of 1 GeV/c to 7 GeV/c. Given the 8 m flight distance, a TOF time resolution of 20 ps is required to obtain a 3-sigma separation between pions and kaons, as shown in Figure 36. Two detector technologies that could give high resolution TOF are being investigated.

The Large Area Picosecond Photodetector (LAPPD) collaboration [194] is developing large area detectors capable of time resolutions in the picosecond range. Such detectors use Micro Channel Plate photomultipliers, which have small paths for electrons, achieving better timing resolution than traditional PMTs. Resolutions of 20 ps for a single photoelectron have been achieved and resolutions of under 10 ps could be obtained for multiple photoelectrons. The main drawback of Micro Channel Plate PMTs is the high cost per area. The LAPPD project is aiming to producing large area MCP PMTs with a cheaper microchannel plate, significantly reducing the cost for large area of detectors. Depending on the ultimate costs, this could be an option for SoLID.

A second TOF option is improving the timing performance of the MRPC detector in SoLID. The baseline MRPC is designed to reach 80 ps. Improvement of the MRPC timing resolution would

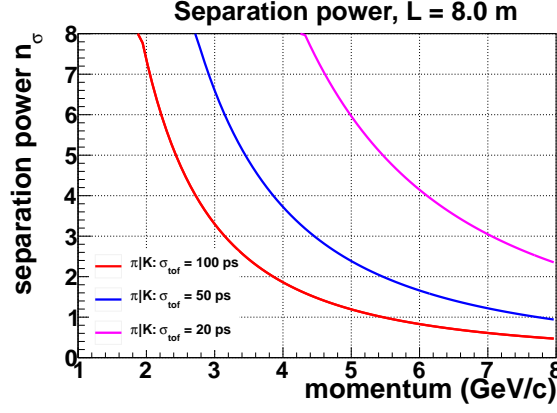


Figure 36: Kaon identification by TOF.

extend the momentum range of π/K identification to the full momentum range. Beam tests showed that current MRPC designs can reach 50 ps with test beam and 80 ps in high background area. There is ongoing EIC R&D [195] on Multi Gap Resistive Plate to improve the timing resolution. A thin gap MRPC prototype has been built and tested by BNL and University of Illinois, achieving a resolution of 20 ps. The R&D plan is described in the MRPC section. As mentioned in the Executive Summary section, the SoLID-Chinese collaboration has developed a prototype and readout electronics system already and has achieved a resolution of 17 ps from bench tests. The next steps are to carry out beam tests and finalize the detector and electronics design in a year.

3 Technical Requirements and Experimental Setup

The key parameters of the approved SoLID physics programs are in Table 6. The proposed SoLID base configuration described below will meet these requirements.

3.1 Summary of Requirements

The minimum requirements of the base equipment for SoLID are summarized below and also listed in Table 7,

- **Magnet:** Outer diameter is 3 meters (to fit in Hall A), inner diameter is 1 meter and length is greater than 3 meters. Field strength is greater than 1.35 tesla and integrated BdL is 5 tesla-meters. Acceptance in azimuthal angle (ϕ) is 2π , in polar angle (θ) is 8° to 24° for the SIDIS configuration and 22° to 35° for the PVDIS configuration. Momentum range is 1–7 GeV, and momentum resolution (combined with 100-micron tracking resolution) is 2 – 3%. Fringe field at the front end after endcap (shielding) is less than 5 gauss (for polarized target operation).
- **GEM Tracking Chambers:** Six planes for SIDIS and five for PVDIS. Total area is 37 m^2 , total number of channels 165K. Tracking efficiency is greater than 90%. Radial position resolution reaches 0.1 mm. Works in high rate environment.
- **EM Calorimeter:** Total 1800 modules of pre-shower (2 radiation length) and 1800 shower (18 radiation length), with a lateral area of 100 cm^2 for each module. Preshower modules are scintillators embedded with WLS fibers. Shower modules are based on Shashlyk sampling design (lead-scintillator and WLS fiber). Radiation hard up to 400 kRad. Energy resolution is $10\%/\sqrt{E}$. Reaches $50 : 1 \pi$ suppression with electron efficiency better than 90%. For PVDIS, combined EC and Cherenkov trigger rate below 600 KHz (20 KHz/sector). For SIDIS, EC, Cherenkov and SPD combined trigger rate to be below DAQ limitation of 100 KHz.
- **Scintillator Pad Detectors (SPD, used for SIDIS only):** 240 pieces 5-mm thick scintillator at forward angle, 5:1 photon rejection; and 60 pieces of 20-mm thick scintillators at large angle, 10:1 photon rejection and $\approx 150 \text{ ps}$ timing resolution for pion identification when combined with MRPC in the forward angle.
- **Light Gas Cherenkov:** 2 meters long with 1 atm CO_2 gas for SIDIS and 1 meter long with 1 atm CO_2 for PVDIS. Contains 60 mirrors and 270 PMTs. Provides number of photo-electrons larger than 10 and electron efficiency greater than 90%. π suppression is greater than 500 for momentum less than 4 GeV (SIDIS) or less than 3.2 GeV (PVDIS). Works in moderate field up to 130 gauss (< 50 gauss after mu-metal shielding). Combined EC and Cherenkov for PVDIS trigger rate to be below 600 kHz (20 KHz/sector).
- **Heavy Gas Cherenkov:** 1 meter long 1.7-atm (abs) C_4F_8 gas, with 30 mirrors and 480 PMTs. The number of photo-electrons is greater than 10. With an efficiency for π better than 90%, kaon suppression is greater than 10:1, from 2.5 to 7.5 GeV. Works in moderate field up to 100 gauss with shielding.
- **DAQ:** 282 FADC sampling at 250 MHz. 32 high-speed pipeline VME switched Series (VXS) system. 30 GEM Scalable-read-out system (SRS). Can handle trigger rate of 100 KHz for SIDIS with event size of 2.6 KBytes and trigger rate of 600 KHz (20 KHz per sector) for PVDIS with event size of 48 KBytes.

- Baffles: Eleven planes of lead blocks, 30 sectors in each plane, thickness of 9 cm, with azimuthal angle opening for each block to be more than 4° out of 12° ($360^\circ/30$). One additional plane of lead blocks with thickness of 5 cm is placed in front of the EM Calorimeter at the small radius region ($110 \text{ cm} < r < 200 \text{ cm}$). The design is optimized to block low energy particle, photon and hadron backgrounds to an acceptable level (total trigger rate below 600 kHz (20 KHz/sector) for the PVDIS configuration).

The requirements for enhancement baseline are listed below:

- MRPC for pion identification: 50 super-modules, each of which contains 3 MRPC modules. There are totally 1650 strips and 3300 readout channels, covering an area of 10 m^2 . Timing resolution is better than 100 ps. Kaon suppression is about 20:1 for momentum $< 2.5 \text{ GeV}$ and photon suppression is as high as 10:1. Works at a high rate up to 10 KHz/cm^2 .
- MRPC for kaon identification: Same as above but with better than 30 ps resolution.

A summary of the detector requirements of all approved experimental programs is given in Table 8. The experimental setup of PVDIS, SIDIS- ^3He , SIDIS-proton and J/ψ are described and shown in the next few subsections.

Table 6: Summary of Key Parameters for Approved Programs

Experiments	PVDIS	SIDIS- ^3He ($e, e'\pi^\pm$)	SIDIS-Proton ($e, e'\pi^\pm$)	J/ψ $e + p \rightarrow e' + J/\Psi(e^-, e^+) + p$
Reaction channel	$p(\vec{e}, e')X$			
Approved number of days	169	125	120	60
Target	LH_2/LD_2	^3He	NH_3	LH_2
Unpolarized luminosity ($\text{cm}^{-2}\text{s}^{-1}$)	$0.5 \times 10^{39}/1.3 \times 10^{39}$	$\sim 10^{37}$	$\sim 10^{36}$	$\sim 10^{37}$
Momentum coverage (GeV/c)	2.3-5.0	1.0-7.0	1.0-7.0	0.6-7.0
Momentum resolution	$\sim 2\%$	$\sim 2\%$	$\sim 3\%$	$\sim 2\%$
Polar angular coverage (degrees)	22-35	8-24	8-24	8-24
Polar angular resolution	1 mr	2 mr	3 mr	2 mr
Azimuthal angular resolution	-	6 mr	6 mr	6 mr
PID (e^-)	detection eff. $\geq 90\%$ pion contam. < 0.001	detection eff. $\geq 90\%$ pion contam. $< 1\%$	detection eff. $\geq 90\%$ pion contam. $< 1\%$	detection eff. $\geq 90\%$ pion contam. $< 1\%$
PID (π^\pm)		detection eff. $\geq 90\%$ kaon contam. $< 1\%$	detection eff. $\geq 90\%$ kaon contam. $< 1\%$	
Trigger type	Single e^-	Coincidence $e^- + \pi^\pm$	Coincidence $e^- + \pi^\pm$	Triple coincidence $e^- e^- e^+$
Expected DAQ rates	$< 20 \text{ kHz} \times 30$	$< 100 \text{ kHz}$	$< 100 \text{ kHz}$	$< 30 \text{ kHz}$
Backgrounds	Negative pions, photons	($e, \pi^- \pi^\pm$) ($e, e' K^\pm$)	($e, \pi^- \pi^\pm$) ($e, e' K^\pm$)	BH process Random coincidence
Major requirements	Radiation hardness 0.4% Polarimetry π^- contamination Q^2 calibration	Radiation hardness Detector resolution Kaon contamination DAQ	Shielding of <i>sheet-of-flame</i> Target spin flip Kaon contamination	Radiation hardness Detector resolution

Table 7: Summary of Minimum Requirements of SoLID Base Equipment. Items listed in parentheses are the SoLID-PVDIS requirements.

Equipment	dimension/description	performance, eff	performance, rej	conditions
Magnet	OD 3m, ID 1m, L > 3m	2π , 8 to 24° (22 to 35°)	P: 1-7 GeV, Res 2 – 3%	Fringe field < 5 G
GEMs	6 planes (5 planes)	Total 37 m ² , Chan 165K	Posi res 100 μ m	high rate
SPD	240 modules (forward); 60 modules (large angle)	150 ps (LA)	5:1 γ (FA); 10:1 γ (LA),	readout in magnet (LA)
EM Calorimeter	1800 \times 100 cm ²	E res 10%, eff > 90%	50:1 π	rad hard
Light Cherenkov	2m CO2 (1m CO2)	$N_{p.e.} > 10$, Eff > 90%	π 500:1 < 4.5 GeV	130 G field
Heavy Cherenkov	1m 1.7 atm C4F8	$N_{p.e.} > 10$, Eff > 90%	K 10:1 2.5-7.5 GeV	100 G field
DAQ	282 FADC @ 250 MHz	Trig 100 KHz \times 2.6 KB	Trig 30 \times 20 KHz \times 48 KB	high noise
Baffle	11 \times 30 blocks, 9 cm	area open $\phi > 4^\circ$ out of 12°	reduce background	

Table 8: Detector Summary for Approved Experiments

Experiments	PVDIS	SIDIS- ^3He	SIDIS-Proton	J/ψ
Target Length	LH ₂ /LD ₂ 40 cm	^3He 40 cm	NH ₃ 3 cm	LH ₂ 15 cm
Target Polarization	N/A	$\sim 60\%$	$\sim 70\%$	N/A
Target Spin Flip	N/A	≤ 20 mins	≤ 4 hours	N/A
GEM Tracking Chambers	5 chambers	6 chambers	6 chambers	6 chambers
SPD	N/A	Forward+Large angle	Forward+Large angle	Forward+Large angle
E&M Calorimeter	Forward angle	Forward + Large angle	Forward + Large angle	Forward + Large angle
Light Gas Cherenkov	1 m long	2 m long	2 m long	2 m long
Baffles	Yes	N/A	N/A	N/A
Heavy Gas Cherenkov	N/A	1 m long	1 m long	N/A
Beam Polarimetry	0.4% determination	$< 3\%$	$< 3\%$	N/A
Target Polarimetry	N/A	$\sim 3\%$	$\sim 3\%$	N/A
DAQ	Single trigger	Coincidence trigger	Coincidence trigger	Coincidence trigger

3.2 SIDIS- ^3He Experiments

Experiment E12-10-006 [87] (E12-11-007 [88]) is designed to measure the single/double spin asymmetries through the semi-inclusive deep-inelastic scattering (SIDIS) ($e, e'\pi^\pm$) with the SoLID spectrometer and the transversely (longitudinally) polarized ^3He target. The layout of the experiment is shown in Fig. 37 and Fig. 38. The entire detector system consists of two parts: the forward-angle (FA) detectors and the large-angle (LA) detectors.

At forward angle, there are five layers of GEM detectors inside the coils to provide the forward-angle tracking, and the first three of them are shared with the large-angle detectors. A 2 m long light gas Cherenkov counter is installed after the GEM detectors to discriminate the scattered electrons from the produced pions. A 1 m long heavy gas Cherenkov counter right after the light gas Cherenkov counter can separate kaons and protons from the pions at momenta larger than 2.5 GeV/c. A “Shashlyk”-type forward-angle Electromagnetic calorimeter (FAEC) will be used for electron/pion separation. One layer of scintillator pad detector (SPD) is placed in front of the FAEC to reject photons and reduce the calorimeter-based trigger rates. In the enhanced configuration, one layer of Multi-gap Resistive Plate Chamber (MRPC) is placed after the heavy gas Cherenkov counter to provide timing information and particle identification of hadrons at low momentum (< 2.5 GeV/c), as well as to suppress photon background. The polar angular coverage for the forward-angle detectors ranges from 8° to 14.8° and the momentum coverage extends from 1 GeV/c to 7.0 GeV/c. A combination of the FAEC and the gas Cherenkov counter (and the MRPC in the enhanced configuration) will be used for electron and pion identifications.

To cover the large electron scattering angles, there are four layers of GEM detectors placed inside the coils, with the last three layers shared with the forward angle detectors. Following a layer of SPD, another “Shashlyk”-type large-angle Electromagnetic calorimeter (LAEC) will be placed inside the coils to separate electrons and hadrons. The large-angle detectors are mainly used for electron detection in a momentum range of 3.5-6.0 GeV/c where the π^-/e ratio is expected to be smaller than 1.5. The polar angle coverage ranges from 15.7° to 24° .

The standard Hall A polarized ^3He target will be used in its transverse mode. A higher than 60% target polarization with a faster than 20 minutes target spin flip is expected at the full polarized luminosity of 10^{36} N cm $^{-2}$ s $^{-1}$, which is corresponding to the unpolarized luminosity of 10^{37} N cm $^{-2}$ s $^{-1}$ at an electron beam current of $15\mu\text{A}$. The target polarization is expected to be limited by the magnetic field gradient in the target region, which is dominated by the leakage field from the SoLID magnet. Therefore, the design of the magnet yokes is important to achieve the required target polarization. As shown in Fig. 37 and Fig. 38, the target will be located about 70 cm upstream of the front yoke. Two target collimators will be placed close to two windows of the 40 cm long target in order to reduce backgrounds generated from both windows. The expected kinematic coverage includes: i) $0.05 < x < 0.6$ which comprises the majority of the valence quark region; ii) $0.3 < z < 0.7$ in which the leading order $x - z$ factorization is expected to hold; iii) maximum pion transverse momentum P_T up to 1 GeV/c, where the TMD framework is valid; and iv) $1 \text{ GeV}^2 < Q^2 < 8 \text{ GeV}^2$ with about 2 GeV^2 coverage in ΔQ^2 at fixed x . These kinematic coverages can be achieved by combining data with incident electron energies of 11 and 8.8 GeV.

In order to achieve the proposed precision in asymmetries, the negative pion contamination in the electron sample needs to be controlled to below 1%. At forward angles, it is achieved by a combination of the FAEC and the light gas Cherenkov detector. For large angles, the LAEC alone will be sufficient to provide the required pion rejection, since the expected pion to electron ratio is small. Furthermore, the coincidence detection of electron and leading pion in the SIDIS kinematics would further reduce the pion contamination in the electron sample.

The particle identification of the leading pion (forward angle detector only) will be achieved by

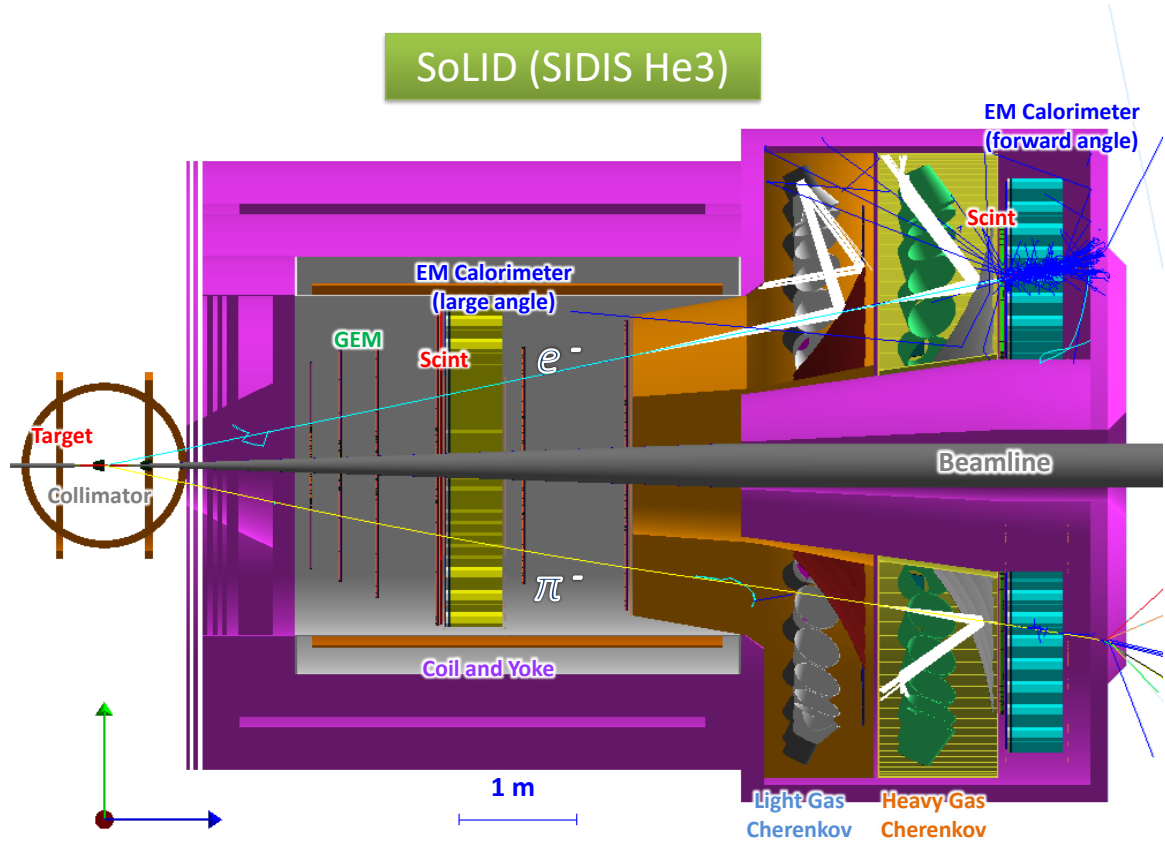


Figure 37: The experimental layout of the SoLID SIDIS- ^3He setup based on the CLEO magnet. The scattered electrons are detected by both forward-angle and large-angle detectors. The leading pions are detected by the forward-angle detector only. The polarized ^3He target will be placed upstream in front of the spectrometer entrance.

the heavy gas Cherenkov detector from 2.5 GeV/c to 7.5 GeV/c in the baseline configuration. The kaon contamination in the pion samples is required to be below the 1% level. Since the kaon to pion ratio is expected to be about 0.1, a kaon rejection factor of 10 provided by the heavy gas Cherenkov detector can satisfy the requirement. For the enhanced baseline configuration, the additional MRPC detector with a time resolution of 100ps will contribute to pion identification by the time-of-flight (TOF) method. It can distinguish pions and kaons from 1 GeV/c to 2.5 GeV/c.

The extraction of various TMD asymmetries relies on the ϕ_S and ϕ_h angular dependence of the measured single/double spin azimuthal asymmetries in each kinematic bin of the 4-D (x , Q^2 , z , and P_T) phase space. Since the kinematics of interests are in the deep-inelastic-scattering (DIS) region, the requirements on the resolution of the reconstructed kinematic variables are modest. For example, a better than a few percent momentum resolution, a better than a few mrad polar angular resolution, a better than 10 mrad azimuthal angular resolution, and a 1-2 cm reconstructed vertex resolution would satisfy the needs of these experiments.

With similar reaction channels, E12-10-006 [87], E12-11-007 [88], and E12-11-108 [89] (see next section) will share the same design of the DAQ system. The required overall luminosity of E12-10-006 and E12-11-007 is $10^{37} \text{ N/cm}^2\text{s}^{-1}$, which is an order of magnitude higher than that of

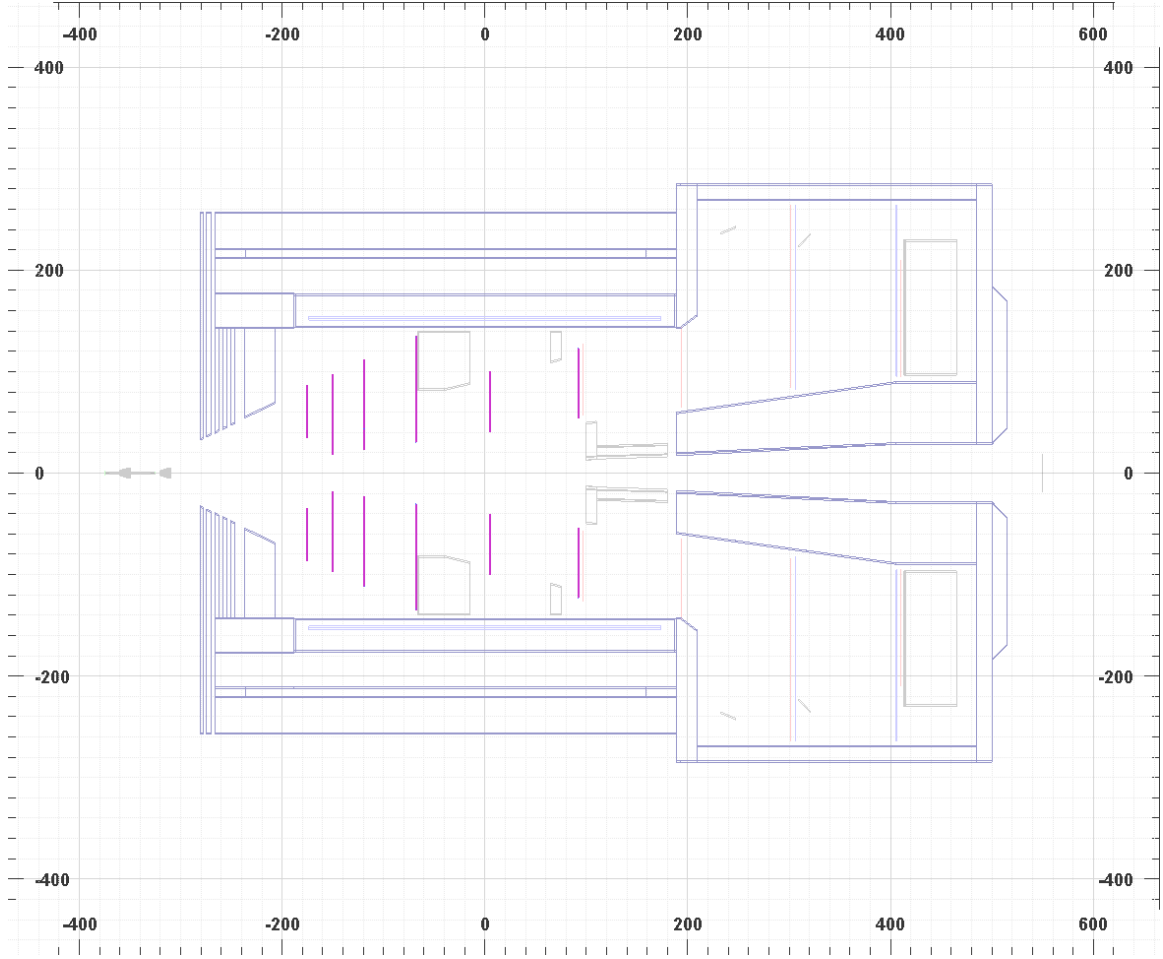


Figure 38: A 2D representation of the experimental layout of SoLID SIDIS- ^3He setup based on the CLEO magnet.

E12-11-108. The goal of the SIDIS DAQ is to satisfy the requirement of ~ 100 kHz trigger rate.

The SIDIS process requires the detection of both the scattered electron and the leading pion. Therefore, a single electron trigger or a coincidence trigger of electron and hadron would satisfy this need. The electron trigger at the large-angle detectors will be provided by the LAEC at an energy threshold of about 3 GeV. Such a trigger would be sensitive to both high energy electrons and high energy photons (mostly from the π^0 decay). With the large angle SPD being incorporated into the trigger, the electron-like triggers can be significantly suppressed. The electron trigger at the forward angle detector will be formed by a coincidence between the light gas Cherenkov detector, the FAEC, and the SPD. Considering the kinematic information of the scattered electrons from the DIS process (e.g. $Q^2 > 1 \text{ GeV}^2$), a position dependent energy threshold with a low limit at 0.8 GeV in FAEC could significantly reduce the trigger rate. The charged hadron trigger at the forward angle will be formed with a coincidence between the FAEC and the SPD (the MRPC will be part of the trigger for the enhanced configuration). The coincidence trigger is given by overlapping the electron trigger and the hadron trigger within a narrow time window. If the single electron trigger can not satisfy the requirement of ~ 100 kHz trigger rate, the coincidence trigger could retain more SIDIS events. Therefore, it is important to include the coincidence trigger in the baseline design of

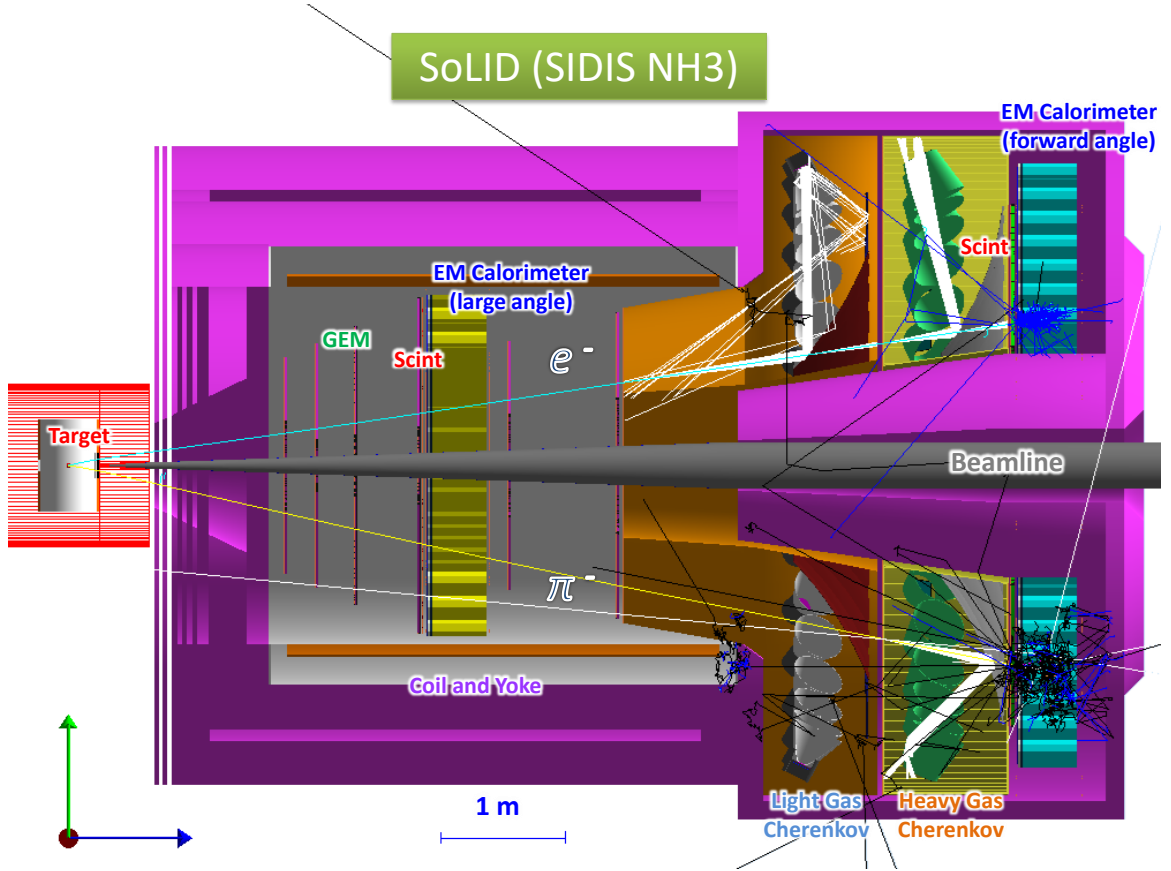


Figure 39: The experimental layout of the SoLID SIDIS-proton setup based on the CLEO-II magnet. It is similar to that of the SIDIS- ^3He setup, except that the ^3He target is replaced by transversely polarized NH_3 target upstream in front of the spectrometer entrance. The scattered electrons will be detected by both forward-angle and large-angle detectors. The leading pions will be detected by the forward-angle detector only.

the SIDIS DAQ system.

3.3 SIDIS-proton Experiment

Experiment E12-11-108 [89] is designed to measure the single/double spin asymmetries through the semi-inclusive deep-inelastic scattering (SIDIS) ($e, e' \pi^\pm$) with the SoLID spectrometer and a transversely polarized proton target. The layout of the experiment is the same as that of the ^3He program except for the target as shown in Fig. 39. The entire detector system consists of two parts: the forward-angle detectors and the large-angle detectors. The overall luminosity in this case is smaller compared to that of the polarized ^3He target with an incident electron beam current of 100 nA.

An improved version of the JLab/UVa/SLAC polarized NH_3 target (shown in Fig. 40) will be used. The main upgrade is to replace the aging Helmholtz-coil magnet with a new magnet and to have a fast spin-flip capability with the AFP technique to minimize the systematic uncertainty in the single spin asymmetry measurement. In order to satisfy the requirements of phase space coverage, the new design will further allow both transverse and longitudinal direction to have a

nominal forward opening of more than $\pm 25^\circ$, while maintaining the same maximum field (5 Tesla) and a uniform field region in the center. The target polarization is required to be higher than 70% with the spin flip every few hours.

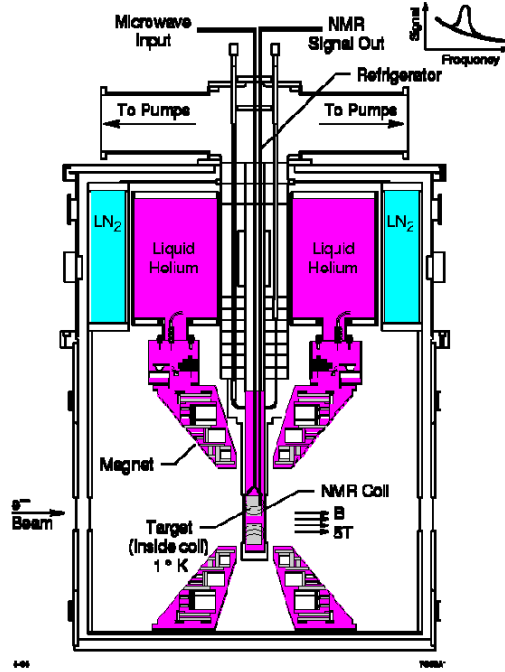


Figure 40: Polarized NH_3 target system.

Due to the large magnetic field in the transverse direction, this experiment will suffer from a different kind of background compared to the low field polarized ^3He experiment, known as *sheet-of-flame*. The main feature of such a background is that a very high rate of charged particles with a momentum range between 1-2 GeV will be localized in a very narrow region of the acceptance. Fig 41 shows this background on all six GEM planes in the SoLID. The GEM chambers in regions outside of the *sheet-of-flame* location see a background rate of less than 1.0 KHz/mm^2 , whereas the regions inside have much higher rates. In order to handle this background and avoid damage to the apparatus, detector sectors in the direct line-of-sight of this *sheet of flame* will be removed or turned off during the proton experiment.

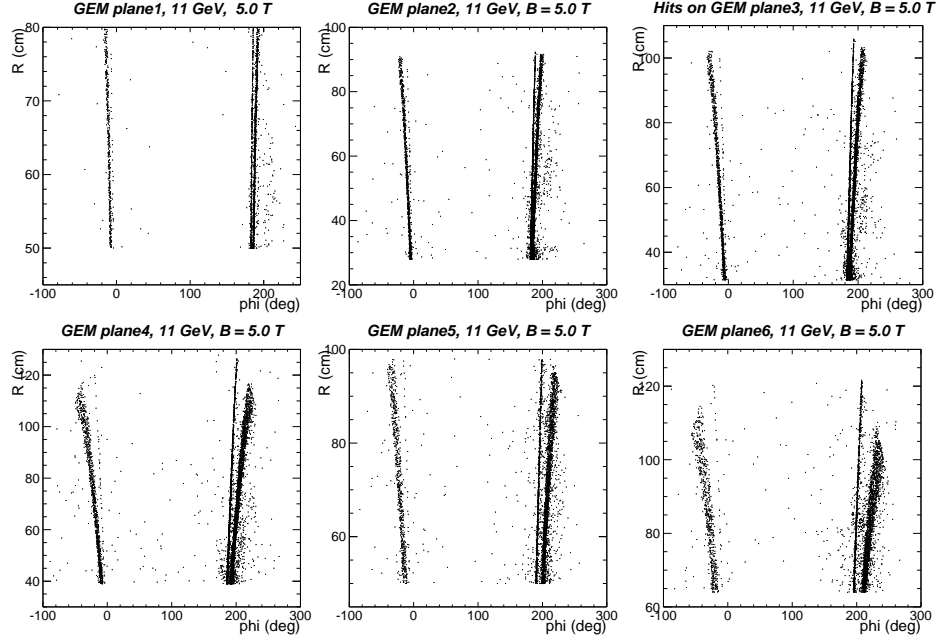


Figure 41: GEANT3 simulation results of background with NH_3 target field ON. The x -axis is the azimuthal angle in lab frame. The y -axis is the radius of GEM chambers (1-6). Narrow regions of high rate (compared to rest of the acceptance) are clearly seen as a function of azimuthal angle ϕ .

3.4 PVDIS Experiment

Experiment E12-10-007 [196] is designed to measure the parity violating asymmetries (A_{PV}) through the inclusive deep-inelastic scattering (DIS) with the SoLID spectrometer. The layout of the experiment is shown in Fig. 42 and Fig. 43. In order to eliminate high energy ($\sim \text{GeV}$) photons, a lead baffle will be placed downstream of the target to block direct lines of sight to the detector system. The detector system consists of four layers of GEM chambers for particle tracking, a 1 m long light gas Cherenkov counter for electron/pion separation, and a “shashlyk”-type electromagnetic calorimeter system for the trigger and additional electron/pion separation. The GEM chambers will be divided into two groups, with one group placed in front of the gas Cherenkov counter and the other group behind it. This configuration will maximize the detector resolution, leading to about 2% momentum and 1 mr polar angle resolutions. The entire detector system will be divided into 30 independent sectors in the azimuthal angle.

The polar angle and momentum coverage of the detector system are from 22° to 35° on an extended (40 cm) target and from 2 GeV/c to 6 GeV/c, respectively. This coverage transforms into kinematic coverages of $0.2 < x < 0.8$ and $2 (\text{GeV}/c)^2 < Q^2 < 12 (\text{GeV}/c)^2$. The overall luminosity is required to be larger than $5 \times 10^{38} \text{ N cm}^{-2} \text{ s}^{-1}$ in order to reach about 0.5% relative statistical uncertainties on the parity violating asymmetries A_{PV} in each of the kinematic bins (see. Fig. 29). Such a high luminosity places specific requirements on the radiation hardness of the detector system.

To leading order, the physics asymmetry A_{PV}^{phys} is related to the measured asymmetry A_{PV}^{measured}

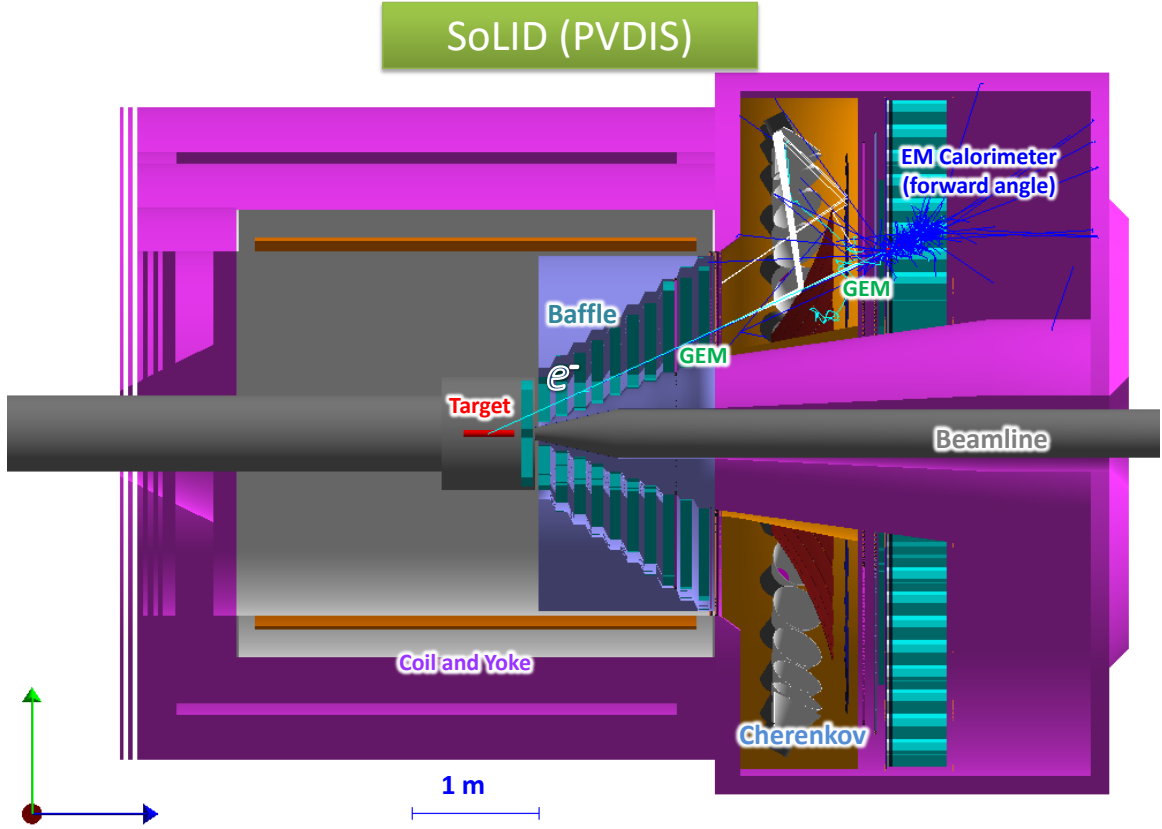


Figure 42: The experimental layout of SoLID PVDIS setup based on the CLEO-II magnet.

by

$$A_{PV}^{\text{phys}} \sim \frac{1}{Q^2 \cdot P_{\text{beam}}} \cdot \frac{A_{PV}^{\text{measured}} - f \cdot A_{PV}^{\pi^-}}{1 - f} \quad (10)$$

where P_{beam} is the polarization of the electron beam, and f and $A_{PV}^{\pi^-}$ are the pion contamination and the parity violating asymmetry of pions, respectively. The proposed high precision measurement of A_{PV} (about 0.5% in each kinematic bin) requires high accuracy. The uncertainty of the electron beam polarization is required to be smaller than 0.4%. Since A_{PV} for produced pions is expected to be similar to that of scattered electrons, the contamination of negative pions in the electron sample needs to be determined to about a 10^{-3} level. Furthermore, the uncertainty in Q^2 also must be controlled to below 0.1% using a precise and comprehensive optics calibration program.

Since only the scattered electrons are detected in this experiment, each sector of the detector system can employ an independent DAQ system. Thus the requirement on the DAQ system for this experiment is modest. The average trigger rate for each sector is estimated to be less than 20 kHz, leading to a total trigger rate less than 600 kHz.

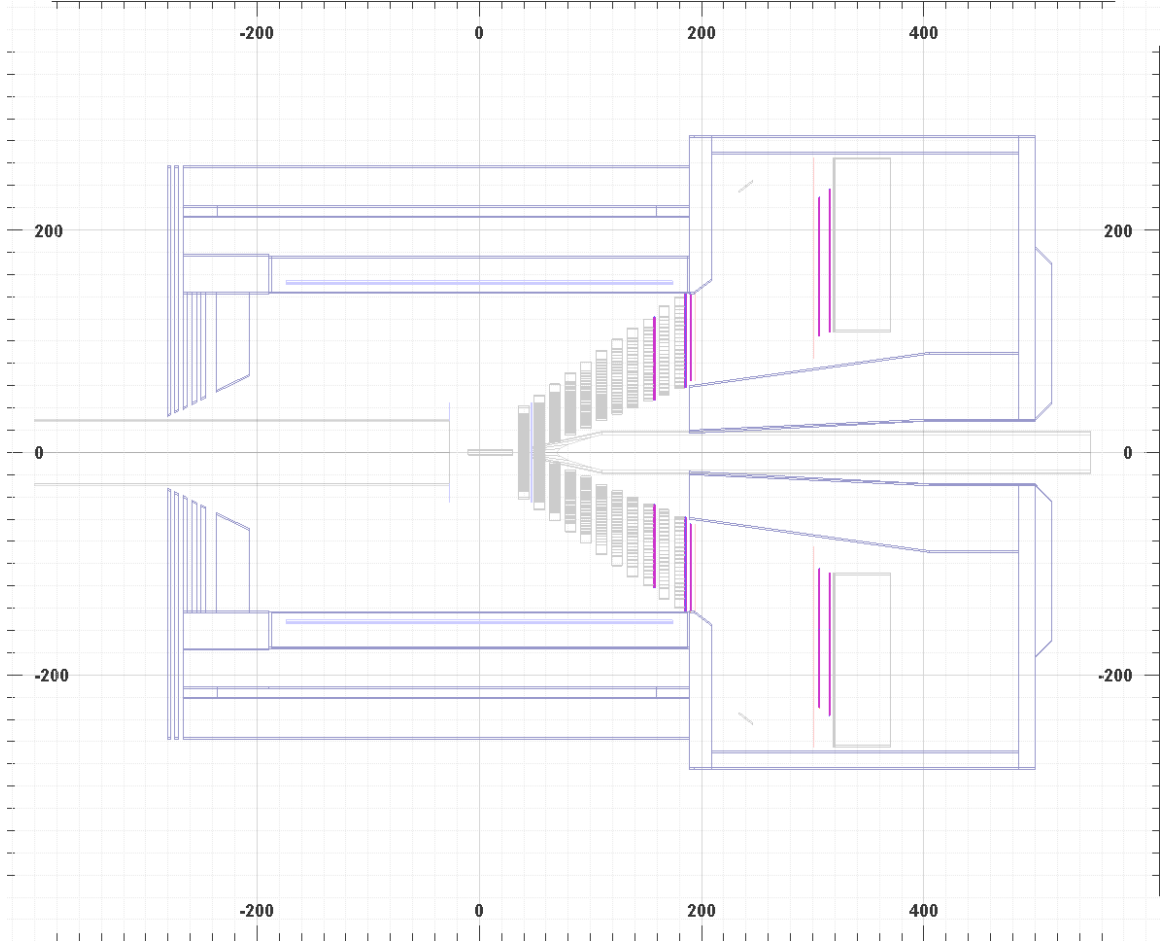


Figure 43: A 2D representation of the experimental layout of SoLID PVDIS.

3.5 J/ψ Experiment

The E12-12-006 experiment [186] is designed to measure the cross section of J/ψ electro-production near threshold. The main reaction of interest is $e + p \rightarrow e' + J/\Psi(e^-, e^+) + p$ where the J/ψ is detected through its decay into a lepton pair (e^+, e^-) with a branching ratio of 5.97%. The primary detection channel for electro-production will be the 3-fold coincidence between the scattered electron and the J/ψ decay electron-positron pair. Additionally, a 2-fold coincidence between the decay electron-positron pair can be used to measure J/ψ photo-production, using the tracking and calorimetry systems to tag the recoil proton. In the 3-fold coincidence channel, the full kinematics of the recoil proton can be reconstructed through energy and momentum conservation.

Because of the requirement to detect electrons and positrons in coincidence, the configuration will be similar to that of SIDIS. Fig. 44 and Fig. 45 illustrate the layout of the experiment. The scattered electron and recoil proton will be detected by the forward-angle detector, while the electron-positron pair from the J/ψ decay will be detected by both the forward and large-angle detectors. Compared to the SoLID-SIDIS setup, the polarized target will be replaced with the standard Hall A 15 cm liquid hydrogen target, located located about 35cm downstream compared to the target center of the SIDIS setup for optimal acceptance.

An optional enhanced-baseline configuration including MRPC for time-of-flight would further

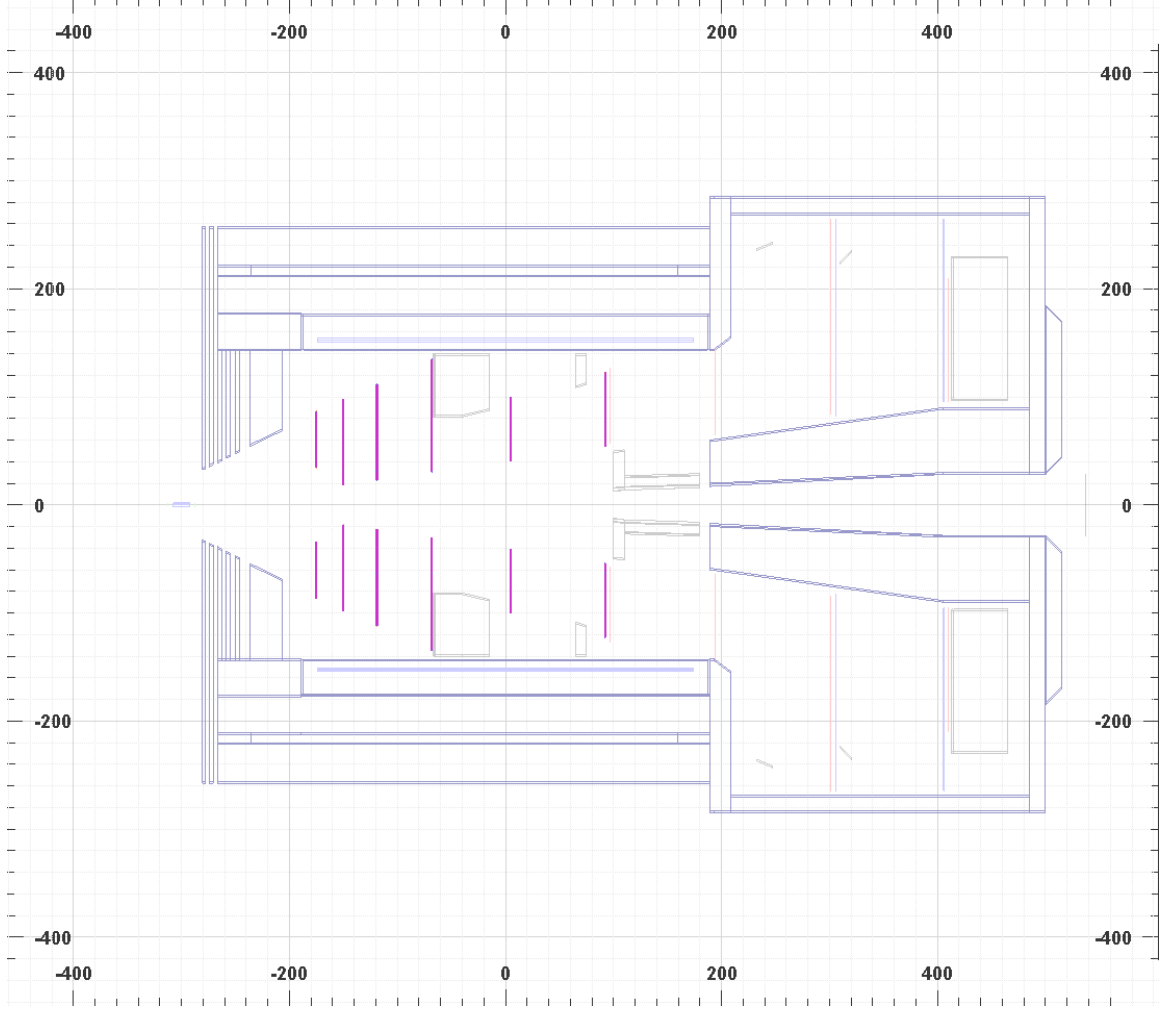


Figure 45: A 2D representation of the experimental layout of SoLID J/ψ setup.

setup is important in rejecting different backgrounds. The expected resolution for the J/ψ setup is similar to those for the SIDIS setup, sufficient for a 2-dimensional high-precision measurement of the J/ψ cross section.

As mentioned before, the optional upgraded baseline including MRPC for time-of-flight (TOF) would allow for the MRPC to be used for particle identification of the recoil proton. The highest momentum of the recoil proton is about 3 GeV/c. With the designed 100 ps resolution in TOF, protons can be separated from kaons at 2 standard deviations (4 standard deviations from peak to peak). In addition, protons can be separated from pions at 6 standard deviations (12 standard deviations from peak to peak). The requirement on the exclusive kinematics in the off-line data analysis would further strengthen the particle identification of protons.

There are two major types of backgrounds. The main physics background originates from the Bethe-Heitler (BH) process. At the proposed kinematics, the BH background is expected to be smaller than the physics J/ψ events by 1-2 orders of magnitude on average ¹. The cross section

¹Due to the rapid decrease of the cross section near threshold for the physics J/ψ events, the BH background becomes comparable at low W .

associated with the BH background can be directly measured by choosing the invariant mass of the electron-positron pair to be away from the J/ψ peak. The other major background is the random coincidence of a J/ψ (normally photo-produced) and a scattered electron, where the event is incorrectly classified as electro-production. This random coincidence background is expected to be 1-2 orders of magnitude smaller than the physics events with the proposed setup. In addition, the random coincidence backgrounds can also be directly measured/subtracted through the commonly used off-window method.

4 Magnet

4.1 Requirements

The SoLID spectrometer is designed to have large acceptance in polar angle, azimuthal angle, and momentum acceptance, and also operate at high luminosity. A solenoid magnet is a natural choice in this case. The magnetic field is symmetric around the beamline, confining the copious low energy charged background particles to the beam pipe region. The detectors are placed symmetrically around the beamline, both within the solenoid and in the end cap region. The approved experiments all place some requirements on the magnet. They are summarized below:

- The PVDIS experiment requires polar angle coverage for the center of the target from 22° to 35° . Its hydrogen and deuterium targets can operate in the magnetic field. To operate the detectors at the design luminosity of $10^{39}/\text{cm}^2/\text{s}$, a set of baffles is required to block unwanted photons and hadrons originating in the target. The magnetic field must then be strong enough to spiral the several GeV DIS electrons through the gaps in the baffles and also provide sufficient curvature in the tracks so that their momentum can be reconstructed. Both requirements can be met with a field integral along the flight path on order of 2.5 T-m.

- Both SIDIS proton and neutron experiments need polar angle coverage from 8° to 24° . The ^3He and NH_3 targets must be located just upstream of the solenoid where the fringe fields before additional shielding are on the order of 5 G. The NH_3 targets require a uniform 5 T field and the ^3He targets require uniform fields of around 25 Gauss. There are two sets of detectors. The forward detectors, located in the end cap, cover particles with angles below 15° . This requires the solenoid to be on the order of 3-4 m long. The large angle detectors are located near the center of the magnet, requiring a diameter on the order of 3 m. The field integral needs to be on the order of 5 T-m in order to provide a sufficient momentum resolution from the GEM tracking system.

- The J/ψ experiment must detect the electron-positron pair from the J/Ψ decay as well as the scattered electron. With a liquid hydrogen target placed upstream of the magnet, the configuration for the SIDIS experiment meets the requirements.

Overall, the ideal SoLID solenoid needs to have an outer radius < 3 m to fit in the experimental hall, an inner radius > 1 m, a length of 3–4 m, and a field integral on the order of 5 T-m.

4.2 SoLID magnet

We have chosen the CLEO II magnet for the SoLID spectrometer. It is a solenoidal magnet with a uniform axial central field of 1.5 T, a large inner space with a clear bore diameter of 2.9 m and a coil of 3.1 m diameter. With a coil length of 3.5 m, its magnetic field uniformity is $\pm 0.2\%$. It was built in the 1980s by Oxford in England and installed for CLEO II in 1989 [207, 208].

The coil is made of 5 mm x 16 mm aluminum stabilized superconductor and run at 3266 A with an average current density of 1.2 MA/m. The large conductor size provides simpler construction and ease of protection. A 3.8 m long cryostat encloses the coil and cools it with a thermosyphon system. The return yoke has 3 layers with 36 cm thickness each and is octagonally divided. There are 2 coil collars, 60 cm thick, supporting not only the return yokes but also the coil. The magnet has good stability, low cryogenic heat load, passive cooling, and passive protection. This gave it the flexibility to be frequently de-energized for maintenance and accelerator studies. After completion of experimental runs the CLEO II magnet remained in the beamline, sealed and under vacuum, until its removal in 2016. The coils and cryostat of the CLEO-II magnet arrived at JLab in 2016 and the return steel was delivered to JLab during the summer of 2019. To use the CLEO magnet for SoLID, the coil and upstream coil collar will be reused as-is but the downstream coil collar and return yoke

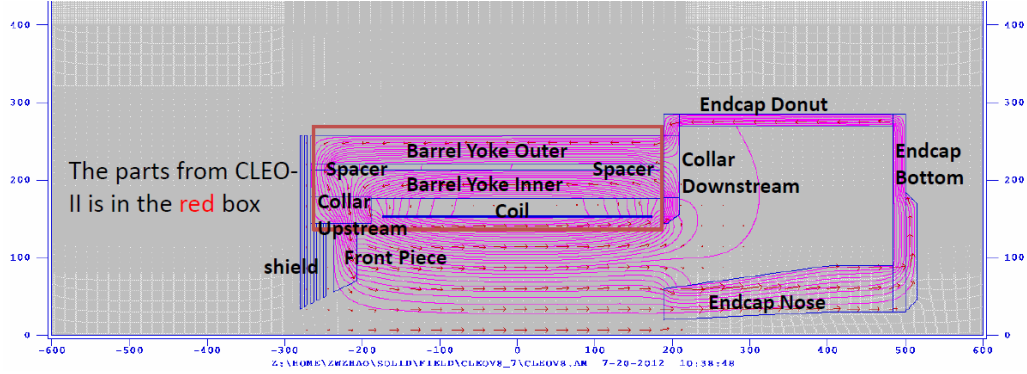


Figure 46: Design of the CLEO II magnet yoke for SoLID.

will be modified to allow the PVDIS acceptance up to 35° . A new detector endcap and front pieces will be fabricated.

The design of the yoke for SoLID using the CLEO II magnet plus new detector endcap is shown in Figure 46. There are two layers of barrel flux return and an upstream collar which are kept from the original CLEO-II magnet. The simulation has shown that the original third layer of barrel flux return is not needed for SoLID and the field in the rest of two layers is well below saturation. The downstream collar will either be modified or new steel will be used. All other parts including the endcap, the front piece and the target shielding need to be built.

The B field for the CLEO II magnet with the SoLID yoke is shown in Figure 47. The strongest field is within the solenoid and drops sharply in the endcap and upstream opening. The magnetic field was calculated using the 2D Poisson Superfish program.

The B_z and B_r fields along the beamline are shown in Figure 48. The B_z field at the center is about 1.4 T, dropping to 0.8 T at the exit of the coil.

The axial force for the 3 sections of coils and all parts of yoke are shown in Figure 49. There are two strong forces compressing the coil. These forces can be balanced so that the net force on the coil is small. It can be adjusted by moving the location of the front piece, where the force varies by 3–5 t/cm.

4.3 Planned Modifications

The CLEO magnet will require some modifications to its design for use in the SoLID experiments. Much of the CLEO magnet will be reused in its original condition. However, SoLID will not use the outermost muon ring. It will use the inner two rings, each consisting of 8 slabs of iron to make up the 8-sided ring. Each of these slabs will have to be shortened to allow the proper position of the endcap. The original upstream coil collar will be reused. Spacers between the slabs will also be reused. The downstream coil collar will be modified if an economical way of reducing its thickness can be found without wasting a majority of its unwanted material. If a solution is not found then a new downstream coil collar will be created. Additional pieces of iron will need to be fabricated to allow for the proper mating of the endcap with the barrel yoke. The existing outer and inner shower counters that mount inside of the coil collars do not appear to be reusable as the upstream coil cup that will reside inside the upstream coil collar. All supporting structure for the magnet barrel yoke and detector endcap will be new fabrications. Please refer to the study in Ref. [206].

The endcap, which consists of the outer cylindrical ring, the backplate, and endcap nose, will all be made from new material. The endcap is designed to be part of the magnetic flux return yoke

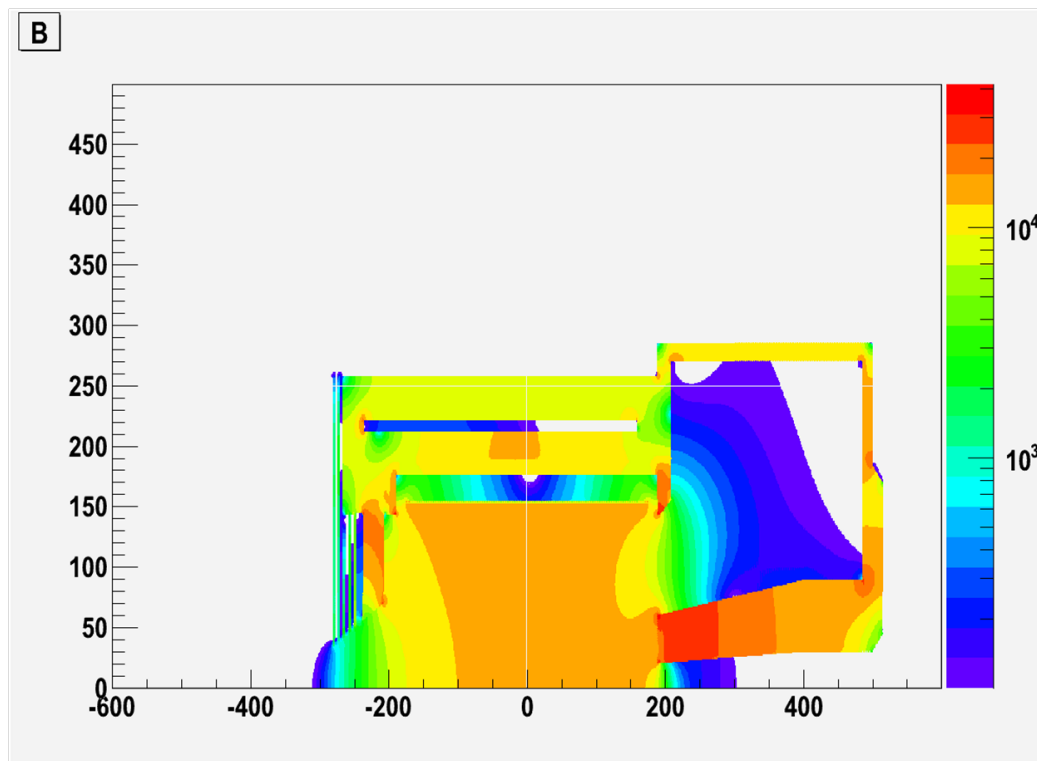


Figure 47: SoLID CLEO magnet field $B > 100\text{G}$.

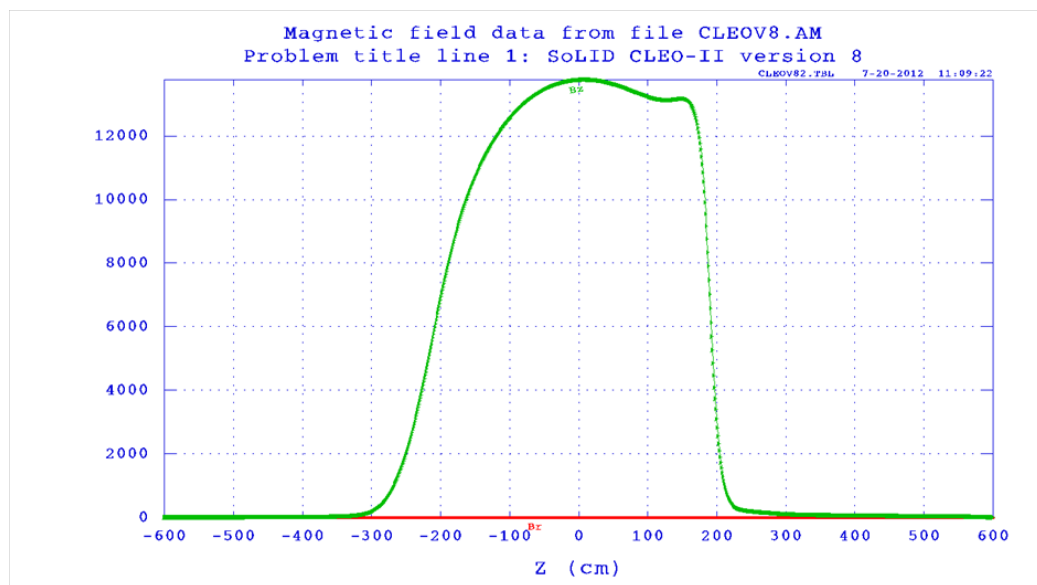


Figure 48: SoLID CLEO magnet field along beamline.

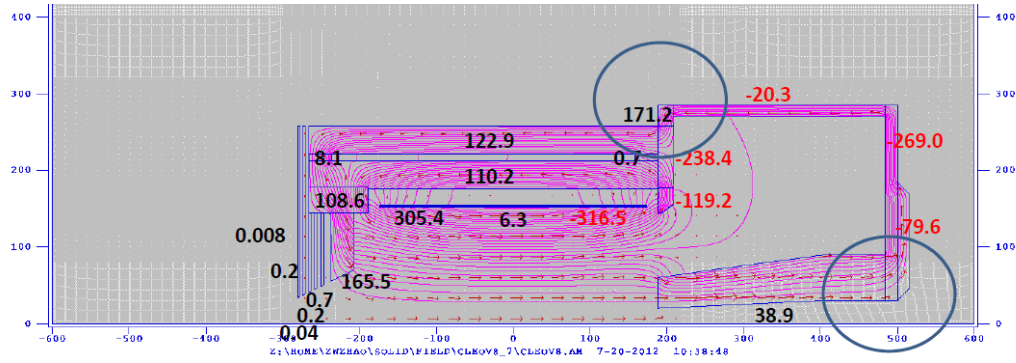


Figure 49: SoLID CLEO axial force in metric t. The two circles show where the force changes direction.

and house the downstream forward angle detector package. The endcap will be split vertically into halves and capable of separation to allow for access to the detector package, see Figure 50. The endcap nose with a secondary backing plate will be a cast two piece design to allow for separation. Each section of the nose will bolt to the main backplate which consists of a two piece round disk. The two halves of the cylindrical outer ring will bolt to the corresponding backplate. The structural support and motion mechanism for the endcap will be discussed in Section 18.

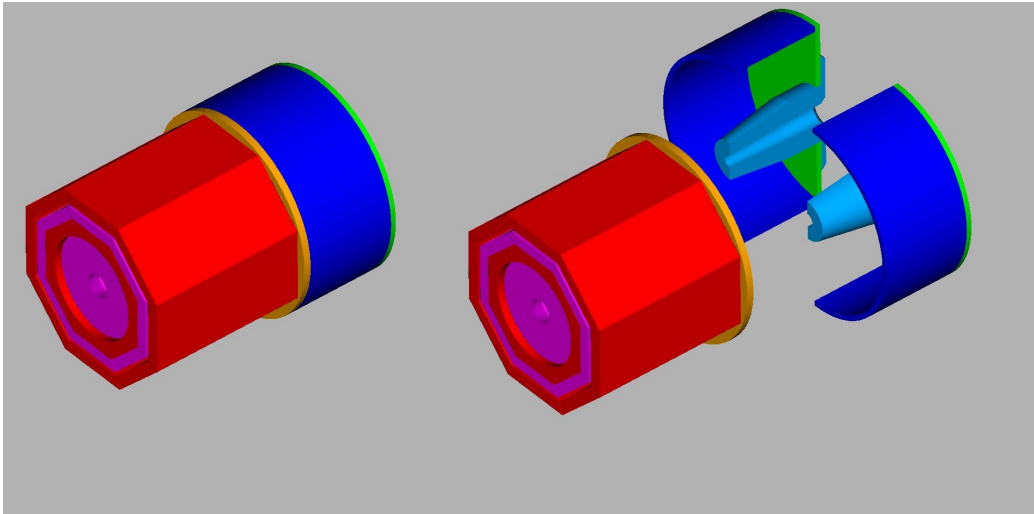


Figure 50: The endcap will be split vertically and also have the capability of separating in the lateral direction

4.4 Current Status

Work on the dismantling of the CLEO II magnet was started by Cornell University in the summer of 2015 with the disconnection of power, cryogen and control lines for the magnet from the building infrastructure. Several of the large return iron blocks were also removed to provide practical experience for the Cornell rigging crew and the project management team to develop a comprehensive schedule for the 2016 removal.

The 2016 summer down period at Cornell started with the removal of the 700 liter helium dewar and outer steel cladding. The leads, cooling supply and return lines as well as instrumentation cables needed to be severed at the top of the service turret to allow the dewar to be lifted away. Next, the beamline and detectors that resided in the bore of the magnet were uninstalled and the return iron was removed layer by layer.

Upon completion of the iron removal, including the coil collars, the axial transport brackets were installed to protect the coils during movement. The cryostat housing the coils could then be moved to the transport frame. The service turret and neck could then be removed from the top of the cryostat. The neck required disassembly to separate the continuous leads from the thermal shielding and cooling lines. The above mentioned disassembly steps adhered to the recommendations of the Oxford Operating Manual for the CLEO II Magnet. The leads were packaged for protection and secured to the side of the cryostat for safe transport. A stainless steel cover was fabricated and attached to the flange on the top of the cryostat providing protection for the ends of the cryo lines and leads. Any remaining openings were sealed to prevent contaminants from entering the vacuum space. Prior to loading on a flatbed truck the entire cryostat was wrapped in fire retardant marine grade shrink wrap to keep the unit weather-tight for the trip to JLAB.

After arrival at JLAB the cryostat was rolled into the high bay area of the Test Lab for climate controlled storage until future use. Inspection indicated the cryostat remained sealed through transport. Loads on the magnet were monitored during transport using (2) three-axis accelerometers and remained under the maximum safe threshold indicated in the Oxford Manual. The two coil collars accompanied the cryostat in the November 2016 delivery and were stored in the Test Lab, as shown in Figure 51.

The existing CLEO II power supply and Instrumentation & Control (I&C) system are 30 years old and will be replaced. The CLEO II 700 liter dewar and cryogenic interface are not compatible with the JLAB End Station Refrigerator (ESR) system. A new Cryo Control Reservoir (CCR) and I&C system based on existing Hall C designs will be adapted for use for SoLID. A new magnet power supply has been added to the SoLID costs.



Figure 51: CLEO II magnet at JLab.

4.5 Planned Magnet Testing

Jefferson Lab has developed a two phase refurbishment/cold test plan to establish the health of the magnet after delivery as well as commissioning after installation in Hall A. Phase 1 will consist of static tests and a low current cold test to confirm the condition of the magnet. Phase 2 will be a full

current test and will be conducted after installation in Hall A.

Phase 1 (JLAB funded) was started in the Fall of 2019 and has a duration of approximately 26 months. This phase will be conducted in the JLAB Test Lab. The initial first step will include static tests of the magnet to establish the post delivery condition. These tests will consist of electrical tests of all sensors and wiring, a hipot test in dry air of the coil, leak and pressure testing of the internal LHe and LN2 circuits and evacuation and vacuum leak test of the cryostat. After establishing the magnet's worthiness for future use, a low current cold test will be conducted without the return iron. Low currents are necessary in the Test Lab to avoid interfering with adjacent equipment. This portion of Phase 1 testing will include the design and procurement of new CCR and I&C system. An existing JLAB DC power supply will be used for Phase 1. Other tasks for the cold test include solenoid neck and service turret assembly, installation of new CCR and I&C systems, leak and pressure testing, cryogenic purification, cool down, controls checkout, calibration and commissioning and low current (approx. 500 amps) testing of the solenoid. All new SoLID magnet systems are clones of existing Physics Division equipment in current use on numerous SC magnets.

Phase 2 (SoLID Project funded) contains all of the Hall A specific items and SoLID Experiment specific items not already included in Phase 1. A new DC power supply with integral energy dump and quench detection is included in this phase. Also included is a new cryogenic transfer line from the cryo source in Hall A to the SoLID magnet. Phase 2 testing will occur during the installation portion of the SoLID Project. Phase 2 tasks include assembly of the solenoid with return iron, installation of new systems including the CCR and cryo transfer lines, I&C system, and DC power supply. Evacuation of the vacuum space, leak and pressure testing, purification of internal cryo circuits, controls checkout and calibration, cool down and controls calibration at 4k, low current and full current SC magnet testing will follow. Including design and procurement of new items Phase 2 is estimated to take 2.5 years to complete.

Other testing will include mapping the magnetic field. This task will require an additional 4–6 weeks in the schedule with use of 2 technicians and 1 scientist/engineer for the duration. \$200k in funding will be required for the mapping apparatus.

The CLEO-II magnet was in excellent condition prior to its disassembling at Cornell. With great care taken in disassembling, packing and transportation from Cornell to Jefferson Lab, and its storage in a climate controlled area at Jefferson Lab, the risk for this magnet is not that different from any potential risk associated with a new magnet. It is realistic to expect that the magnet will be ready for PED without R&D process by completing the aforementioned comprehensive magnet testing plan including a new power supply and new control prior.

As part of the packet of information developed for the Magnet Testing Plan, a risk registry was generated with many of the possible risks to the magnet. Schedule and cost risk consequences are noted along with risk probability in the table that is used as a risk contingency in the updated cost estimation.

5 Targets

There are five approved SoLID experiments. Two semi-inclusive DIS experiments (E12-10-006 and E12-11-007) use a polarized ^3He target with the achieved performance. One SIDIS experiment (E12-11-108) uses a transversely polarized proton (NH_3) target. The parity-violating DIS experiment (E12-10-007) uses a 40-cm cryogenic liquid deuterium (hydrogen) target system. The J/Psi experiment uses the standard cryogenic liquid hydrogen target. The following subsections will describe the polarized ^3He target, the polarized proton (NH_3) target and the PVDIS cryotargets.

5.1 Polarized ^3He Target

The polarized ^3He target is based on the technique of spin-exchange optical pumping of hybrid Rb-K alkali atoms. Such a target was used successfully in the completed SIDIS experiment [209] with a 6-GeV electron beam at JLab. Three sets of Helmholtz coils provide a 25 Gauss holding field for any direction, supporting polarization in transverse (for E12-10-006) or longitudinal (for E12-11-007) direction. Target cells were 40-cm long with density of about 10 amg (10 atm at 0°). The luminosity was about 10^{36} nuclei/s/cm with a beam current of 15 μA . An in-beam polarization of up to 60% was achieved. Both the achieved luminosity and figure-of-merit are the best in the world so far. Two kinds of polarimetry, NMR and EPR (Electron Paramagnetic-Resonance), were used to measure the polarization of the target. The precision for each method was about 5% (relative) and the methods agreed well within uncertainties. It is expected to reach 3% with the planned improvements.

Frequent target polarization direction reversal is needed to minimize target-spin-correlated systematic uncertainties. The fast target spin reversal was achieved in a few seconds for the 6 GeV SIDIS experiment by using RF AFP technique. The frequency of the spin reversal was kept to 20 minutes to minimize the polarization loss due to AFP. The additional polarization loss due to frequent spin reversal was kept at $< 10\%$ (relative). The above quoted maximum in-beam polarization achieved for the 6 GeV experiment (up to 60%) included the loss due to spin reversal. A new method using field rotation for spin reversal was tested and a nearly no polarization-loss result was achieved and will result in an improved performance. It will allow to have more frequent (a few minutes instead of 20 minutes) spin reversal to help further reduce the target-spin-correlated systematic uncertainties.

The upstream endcap plate will keep the magnetic field and its gradients under control in the target region. In this design, the absolute magnetic field strength in the target region is about a few Gauss with field gradients ~ 50 mG/cm. Correction coils around the target will further reduce field gradients to the desired level of 30 mG/cm.

A pair of collimators, similar to the ones used in the 6-GeV experiment, will be placed next to the target cell windows to minimize the target window contribution to the total events.

In addition to the polarized ^3He target, the current target system has a multi-foil ^{12}C target for spectrometer optics study, a BeO target for beam tuning and a reference target cell system, which allows to have different target gases, hydrogen, deuterium, ^3He and nitrogen, be used to measure unpolarized cross sections, for calibration and dilution studies.

Upgrades are planned for other polarized ^3He experiments before the SoLID experiments. These upgrades are not required for the SoLID experiments but will benefit them.

5.2 Transversely Polarized Proton Target

The SoLID collaboration proposes to measure single spin asymmetries in the semi-inclusive, deep-inelastic ($e, e'\pi^\pm$) reaction using a transversely polarized proton target. The target to be used is the

dynamically polarized ammonia target that has been used at SLAC and at JLab in numerous experiments [210]. Its last use was in 2012 for the g2p/Gep experiments, which took place in Hall A [211]. Proton luminosities of $10^{35} \text{ cm}^{-2}\text{s}^{-1}$ have been achieved with this target, in conjunction with electron beam currents up to 100 nA. In order to meet the requirements of the SoLID measurements, however, a new superconducting magnet must be procured, as discussed below.

Dynamic nuclear polarization (DNP) has been used to polarize solid targets for nuclear and particle experiments for more than four decades. To realize DNP, a paramagnetic species is implanted into the target material, either by dissolving a stable radical into the material (if the latter is liquid at room temperature), or by producing radicals directly within the material using ionizing radiation. The unpaired electrons of these radicals are highly polarized by cooling the sample to a low temperature and exposing it to a high magnetic field. For example, at the 1 K and 5 T operating condition of the JLab target, the electron polarization is -99.8%. Under these conditions, the spin-lattice relaxation time of nuclear spins is quite long (hundreds of seconds), while that of the electron spins is much shorter (tens of milliseconds). Microwaves are then used to induce hyperfine transitions in which both the nuclear and electron spins flip, either in the same or opposite directions, depending on the microwave frequency that is chosen. Because the electron relaxes quickly back to its equilibrium state, it can be utilized to flip another nucleus into the desired spin state. In this manner, the nuclei surrounding each paramagnetic radical become polarized, and this polarization spreads throughout the sample via spin diffusion. In well-designed systems, proton polarizations exceeding 95% [90] and deuteron polarizations approaching 90% [212] have been achieved.

Frozen ammonia (NH_3) has been the target material of choice for electron beam experiments at Jefferson Lab. Proton polarizations in excess of 90% are routinely achieved in ammonia, and it has a relatively high ratio of polarizable-to-nonpolarizable nucleons (17.6%). Additionally, ammonia displays a very high resistance to radiation damage, and simply warming the material to about 100 K for a few minutes can largely repair the damage that does occur. Prior to the experiment, paramagnetic radicals (chiefly NH_2) are created within the ammonia by irradiating the material (under liquid argon) with an electron beam. For convenience, this irradiation is typically done off site, and the material is then stored inside liquid nitrogen until required for the experiment. The JLab target system, as utilized in Hall A, is shown in Fig 52. It consists of a 5 T split-coil superconducting magnet, a ^4He evaporation refrigerator with a cooling power of about 1 W at 1 K, and a target insert containing two samples of frozen ammonia along with additional targets for background and dilution studies. These reside in an evacuated scattering chamber specifically built with thin windows around its perimeter for beam entrance and exit. Equipment outside the chamber includes a large set of vacuum pumps for the evaporation refrigerator, microwave electronics for polarizing the target sample, and a NMR system for measuring its polarization. Liquid helium is provided to the target from a nearby 500 L dewar.

Before its use in the g2p/Gep experiments, numerous upgrades were made to the polarized target in order to improve its performance, reliability, and safety:

- An entirely new refrigerator was constructed at JLab according to the safety regulations dictated by 10 CFR 851;
- The quench-relief piping system for the superconducting magnet was upgraded to replace leaking rubber seals with copper gaskets, and also made compliant to 10 CFR 851;
- The pumping system and controls were overhauled;
- A more robust sample insert and motion mechanism were constructed to address problems that were encountered in previous experiments;

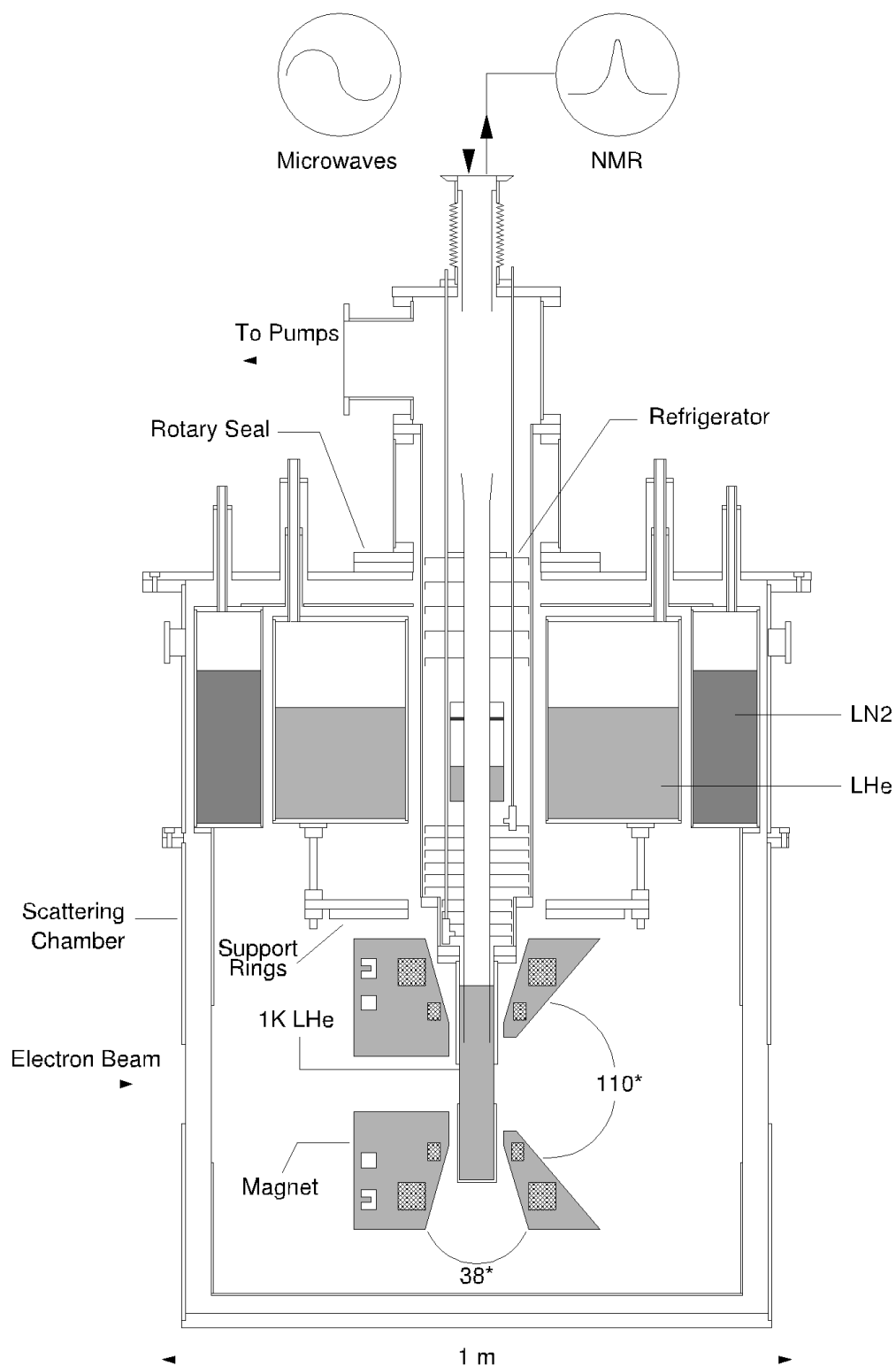


Figure 52: The dynamically polarized target, as utilized in Hall A. The cryostat can rotate 90° about the vertical axis, thus providing either longitudinal or transverse polarization with respect to the electron beam. The longitudinal orientation is shown.

- A new rotary vacuum seal was implemented that significantly reduces the time required to rotate the magnet between its longitudinal and transverse orientations. With the new seal, there is no longer a need to disconnect the refrigerator pumping line, nor to remove and replace the sample insert;
- The 5 T magnet suffered irreparable damage during the final systems tests, and was replaced with a similar magnet removed from the Hall B polarized target [213].

It should be noted that both the original and Hall B magnets were primarily designed to provide longitudinal polarization, while still permitting limited use for transverse polarization. As such, each magnet possesses an “opening angle” of 110° ($\pm 55^\circ$) in the direction parallel to the magnetic field, compared to only $\pm 17^\circ$ perpendicular to it (see Fig. 52). Because the SoLID proposal requests transverse polarization with an opening angle $\pm 25^\circ$ or greater, a new magnet will be necessary.

Oxford Instruments (manufacturer of both the Hall B and the original magnet) has performed a detailed feasibility study and concludes that they can build a 5 T split-coil magnet with both a $\pm 25^\circ$ split angle and the homogeneity required for DNP [214]. The SoLID collaboration and JLab Target Group will work alongside the eventual vendor to ensure the magnet can be easily incorporated into the existing JLab cryostat. This will greatly reduce the time and cost required to field a transversely polarized target for SoLID.

5.3 Cryogenic Target for PVDIS

The proposed target consists of 40 cm liquid hydrogen/deuterium cell. This cell will be filled with either hydrogen or deuterium as needed. The heat load on this target will be much more modest than the Qweak target that was employed from 2010 to 2012 at JLAB. A conceptual design of the target is shown in the figure. The current concept allows for remote placement of a single cryogenic cell and a dummy cell with several solid targets necessary for calibrations. Such a target has the following basic elements:

1. Heat exchanger (HX)
2. Insulating vacuum chamber (IVC)
3. Target stack
 - (a) Cell
 - (b) Dummy target
 - (c) Solid targets
4. Recirculating pump
5. Cryostat
6. Temperature stabilizing heater
7. Positioning system
8. Gas handling system and gas storage
9. Instrumentation
10. Depolarizer

All components in the system must comply with 10 CFR 851 with regard to pressure, electrical, and fire safety. The majority of these components will remain outside the high magnetic field of the solenoid. The cell and connecting piping together with the rest of the target stack are necessarily placed in the magnetic field of the solenoid. Selection of materials for these components shall consider this.

The insulating vacuum chamber will consist of two main sections. One section will be inside the bore of the solenoid and a section similar to the IVC for the standard Hall A cryogenic target will be upstream of the magnet. This latter section will contain the motion system, heat exchanger, etc. The section in the magnet will only contain the target stack and connecting piping. Materials for the chamber section inside the solenoid must be compatible with the magnetic field inside the solenoid. The exit of the chamber will be compatible with the acceptance of the detector.

Careful attention must be given to the design of the cell. While the requirements of this target regarding density fluctuations are much less stringent than those imposed on either the Qweak or G0 targets, it is of some concern. Analysis of the cell design using computational fluid dynamics (CFD) will be employed to ensure an acceptable cell design. Based on experience with previous targets at JLAB, noise associated with density fluctuations is not expected to be significant compared to counting statistics. To reduce the background from Al-e- asymmetries, the sections of the cell upon which the beam impinges will be thin. Thicknesses of 120 μm are commonly available and are adequate for the needs of the experiment. The remainder of the cell will be designed to optimize boiling performance, detector acceptance, and pressure safety. High strength aluminum alloys such as AL-7075 and AL-2219 (used on welded components) shall be used on critical parts of the cell. Through extensive experience it has been shown that cell and cell block assemblies are much more reliable when welds and mechanical joints such as conflat (CF) are employed. This avoids the issues with solder and other sealing techniques. This approach also accelerates the design and prototyping phase and simplifies testing and assembly.

To avoid interference between the exiting particles at maximum scattering angle of 35° and the upper and lower target components, the cell and dummy target must be separated by a minimum of 28 cm plus half the width of the cell and dummy target. Similarly the dummy and the solid targets (positioned at $Z = 0$) will require 14 cm of separation plus half the width of the dummy target and first solid target frame. A total stack height of more than 70 cm is expected. The motion system must accommodate this height and allow for some alignment adjustments. The standard Hall A cryogenic target has over 70 cm of travel, thus a similar mechanism will be suitable.

Dummy and solid targets can be selected and installed as needed. The thickness of the dummy target will be chosen to match the radiation length of the liquid cell. Solid targets required for optics studies, background measurements and alignment checks will also be installed.

The cryogenic liquid hydrogen and deuterium target must accommodate a beam current of 50 μA on a 40 cm long cell. The estimated beam heat load for this is $\sim 800\text{W}$. The pump, heater overhead, transfer line and other losses require an additional estimated $\sim 250\text{W}$. During the Qweak experiment, more than 3 kW of power at 20K was dissipated by the heat exchanger. This design made use of both 15K and 4K refrigerant from the End Station Refrigerator (ESR) and the Central Helium Liquefier (CHL). A careful study of the target heat load and ESR/CHL refrigerators will be necessary to design the heat exchanger. However, it is expected that the heat exchanger will not need to dissipate more than 1500 W which includes a comfortable operating margin. Operationally, only $\sim 1\text{kW}$ of refrigeration will be required by one or more refrigerator.

The hydrogen and deuterium target fluids may become slightly polarized in the magnetic field of the solenoid. This would result in an asymmetry unrelated to the physics of interest. This effect can be mitigated in the case of deuterium with an RF-depolarizer. In the case of hydrogen, pure para-hydrogen would reduce this effect. A catalyst (such as an iron oxide bed) would enhance the

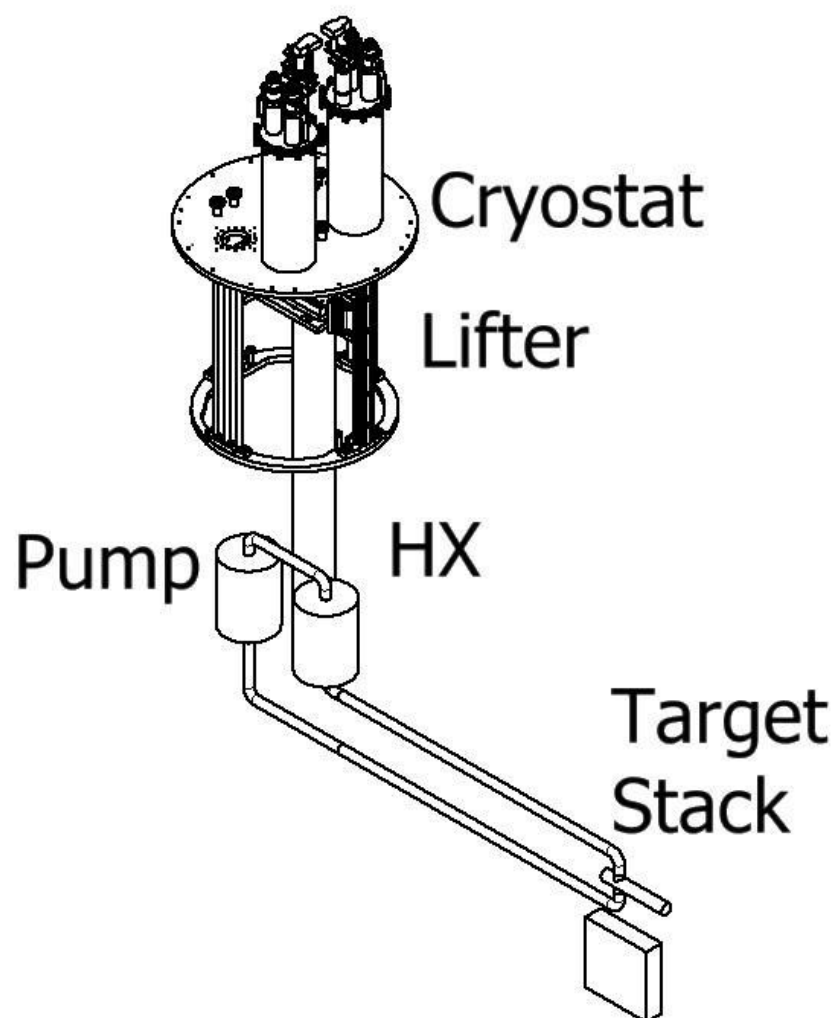


Figure 53: Cryogenic Target for PVDIS

para to ortho fraction.

6 Baffles

In order for the detectors in the PVDIS experiment to operate at the design luminosity, a set of baffles is required that passes a reasonable fraction of the DIS electrons while blocking as much of the background as possible. The baffles provide curved channels through which only the spiraling high energy negative particles can pass. Most line-of-sight photons and positively charged hadrons are blocked.

The design of the baffles requires careful optimization since there are many sources of background and the different detectors respond differently to the different backgrounds. The dominant background in the GEMs is soft photons, especially those between 1 and 2 MeV. The GEMs are relatively inefficient for lower energy photons. Sources of these photons include beam bremsstrahlung, forward radiation from wide-angle 30-100 MeV Møller electrons generated in the target, and photons from showers in the baffles induced by neutral pions. The light gas Cherenkov is sensitive to pair production from photons above 20 MeV or so which can come from neutral pions produced in the target to bremsstrahlung from the wide-angle Møller electrons. The ECal is sensitive to the positive hadron punch-through and high energy photons from neutral pion decay.

To design the baffles for a specific magnetic field and detector configuration, ray-tracing of simulated DIS electrons is performed for the desired momentum range. For a uniform solenoidal field, high momentum electrons have a trajectory in $\phi - z$ space that is linear and the $\theta - z$ trajectory is independent of the field. The design process takes simulated electrons in a realistic field and exploits this approximate behavior to define pathways for ranges of electron momenta. This allows for a relatively simple design process involving an extended target where one considers radial rings of restricted scattering angle and places blocking material to only allow these trajectories. The number of sectors to be used for this experiment is driven by the azimuthal angle ϕ traversed by the minimum momentum particles, which for these kinematics is about 12° , hence 30 sectors.

To block line-of-sight photons, there must be sufficient material to block line particles that have a constant trajectory in ϕ . Due to the fact that the target is extended, the simple model does not completely hold, allowing some fraction to leak through.

We recently have undertaken studies of our baffle design including evaluation of materials, acceptance, and background reduction. While our baseline baffle design uses lead, other possibilities include copper or tungsten. These materials vary by a factor of four in radiation length. The variation in nuclear interaction length is smaller, as shown in Table 9. Tungsten's high density and short interaction length is advantageous, however its cost is higher, and solid tungsten is difficult to machine. An easier approach to construction would be to use powdered tungsten which can be easily molded and glued.

We have performed studies of trigger rates in the EC, rates of neutrons entering the EC, and rates of photons striking the last GEM with baffles constructed of different materials, but with the same geometry. All show fairly small differences, seen in Table 9. Lead provides a slightly lower photon rate than copper, while copper's hadron rates are slightly better. Powdered tungsten has a density only about 60% of solid tungsten, and consequently provides little or no performance advantage over lead.

An important background is photons from π^0 decay interacting in the baffles. When photons strike the baffles close to the "hot" edge of a slit, shower products can escape into the slit and from there thread through the slits in the remaining baffle plates. A modification we have considered is to remove material amounting to 0.6° in angular width from the hot edges on baffle plates 2, 4, 6, 8 and 10, allowing photons that would have hit near these slits to strike instead further from the hot edges on the next plate. Our simulations show a 16% reduction in photon rates above $p = 1$ GeV/c, and 26% reduction for $p > 10$ GeV/c. Removal of this material would increase the pion background,

	Copper	Lead	Tungsten powder	Solid tungsten
Radiation length (cm)	1.436	0.5612	0.583	0.3504
Nuclear interaction length (cm)	15.32	17.59	16.58	9.946
Machinability	Easy	Soft, needs support	Easy to mold and glue	Hard
Cost	Low	Low	High	High
EC trigger rate (kHz)	4.78×10^3	5.45×10^3	5.25×10^3	4.59×10^3
Neutron rate in EC (kHz)	3.35×10^7	4.7×10^7	4.0×10^7	2.9×10^7
Photon rate in last GEM (GHz/sector)	2.98	2.59	—	—

Table 9: Properties and performance of copper, lead, tungsten powder and solid tungsten as baffle materials.

but by less than 10%.

We have performed detailed studies of track trajectories through the baffles to identify places where improvements in the baffle geometry can be made. One finding was that, for the upstream baffle plates, the solid ring at the inner radius and an angular constriction at small radius interfere with the acceptance for electrons produced at the downstream end of the target. For vertices at the upstream end of the target, acceptance was being lost due to the too-small outer radii of the upstream baffle plates.

Based on these studies we have developed an improved baffle design, shown in Fig. 54. Inner rings and angular constrictions on the first few plates have been removed, and outer radii of these plates have been increased. Shapes of the slits in all the plates were optimized, keeping the overall aperture in polar angle unchanged, but tightening up slits that were slightly too wide. The outcome of this program was a geometrical design, having modest acceptance improvements over our previous baffles while not significantly affecting photon rejection, which we believe to be optimal; see Figures 55 and 56.

A detailed study of the activation of different materials suitable for the baffle has been carried out. Radiation levels for each material were studied for three different durations of beam exposure, and possible shielding configurations were evaluated. The final selection of the baffle material will likely be driven less by performance and more by activation and ease of construction.

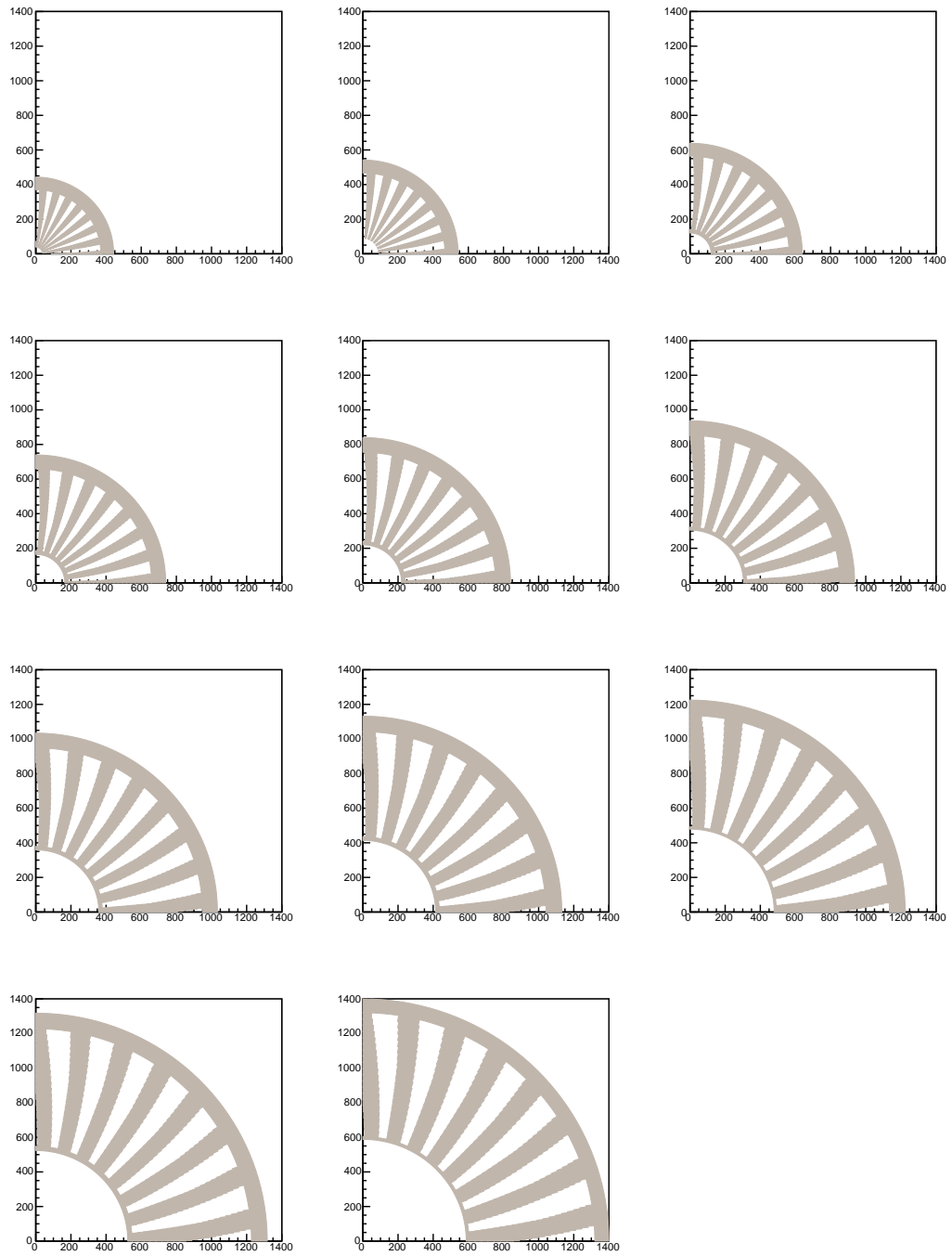


Figure 54: Face on views (first quadrant only) of the 11 plates in the PVDIS baffle system.

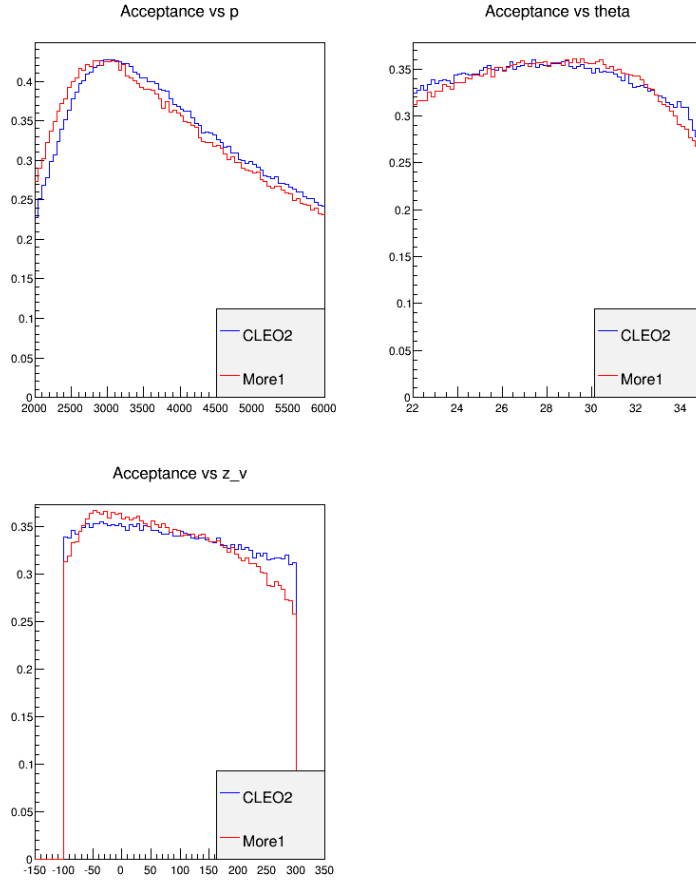


Figure 55: Geometric acceptance of the PVDIS baffles for DIS electrons with $Q^2 > 6 \text{ GeV}^2$, $W > 2 \text{ GeV}$, and $x_{bj} > 0.55$ versus momentum (top left), scattering angle (top right), and vertex position (bottom left). Blue (red) lines are acceptance for the optimized (previous) baffle design.

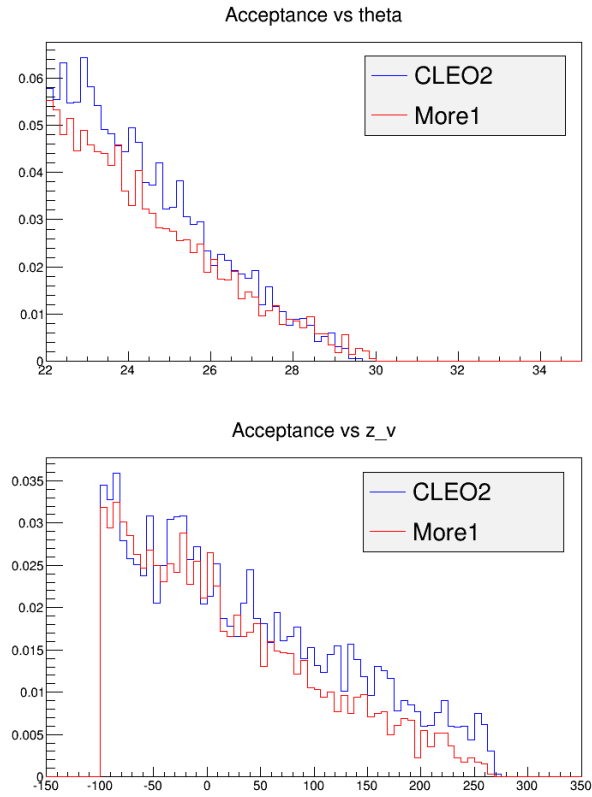


Figure 56: Geometric acceptance of the PVDIS baffles for photons versus scattering angle (top), and vertex position (bottom). Blue (red) lines are acceptance for the optimized (previous) baffle design.

7 GEM Tracker

7.1 Design

The SoLID spectrometer requires high resolution track reconstruction under high rate conditions over a large area. A cost effective solution for such requirements is provided by the Gas Electron Multiplier (GEM) technology invented by F. Sauli [215] in 1997. The GEM is based on gas avalanche multiplication within small holes (on a scale of $100\ \mu\text{m}$), etched in a Kapton foil with a thin layer of copper on both sides. The avalanche is confined in the holes, resulting in fast (about 10 ns rise time) signals. Several GEM foils (amplification stages) can be cascaded to achieve high gain and stability in operation. The relatively small transparency of GEM foils reduces the occurrence of secondary avalanches in cascaded GEM chambers. All these properties result in very high rate capabilities of over 100 MHz per cm^2 and an excellent position resolution of approximately $70\ \mu\text{m}$. Fig. 58 illustrates the principle of operation of a triple (three foil) GEM chamber. Triple GEM chambers have been successfully used in the COMPASS experiment at CERN [216], in the PRad experiment at Jefferson Lab [217] and may other experimental setups around the world.

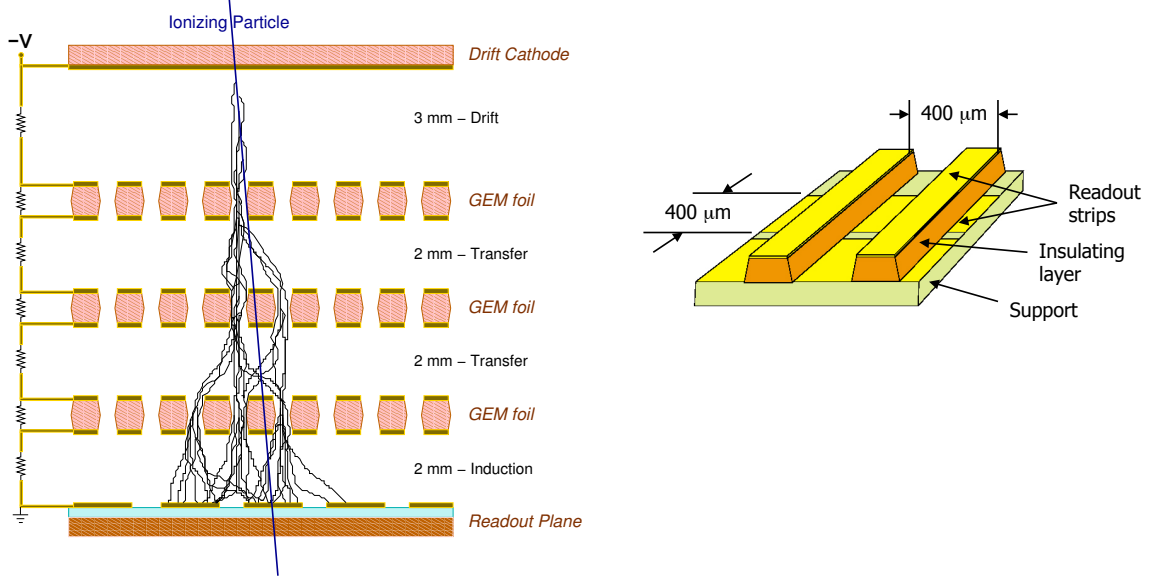


Figure 57: Principle of triple GEM operation.

Figure 58: The 2-D Cartesian (x-y type) readout board used in a GEM detector.

For the PVDIS configuration of SoLID, detector locations 1, 2, 3, 4, and 5 will be instrumented with GEM chambers. Table 10 summarizes the parameters of the SoLID PVDIS GEM chambers. At each detector location there will be 30 trapezoidal GEM chamber modules, one for each sector defined by the baffles. The GEM modules will have an angular width of 12° with the readout stripes parallel to the two edges of the sector, so that the stripes from the two readout layers are at a 12° stereo angle. The readout pitch for locations 1, 2 and 3 will be 0.4 mm while the pitch for locations 4 and 5 will be 0.6 mm. For location 1 each readout strip will be split into two readout channels to reduce occupancy. Figure 59 shows the GEM module arrangement for five the detector locations of the PVDIS configuration. Figures 60 and 61 show the details of the GEM module edges and mounting at the inner and outer radii of the SoLID detector wheel.

The SIDIS configuration of SoLID calls for detector locations 1, 2, 3, 4, 5, and 6 instrumented with GEM modules. Table 11 summarizes the parameters of the SIDIS GEM chambers. While

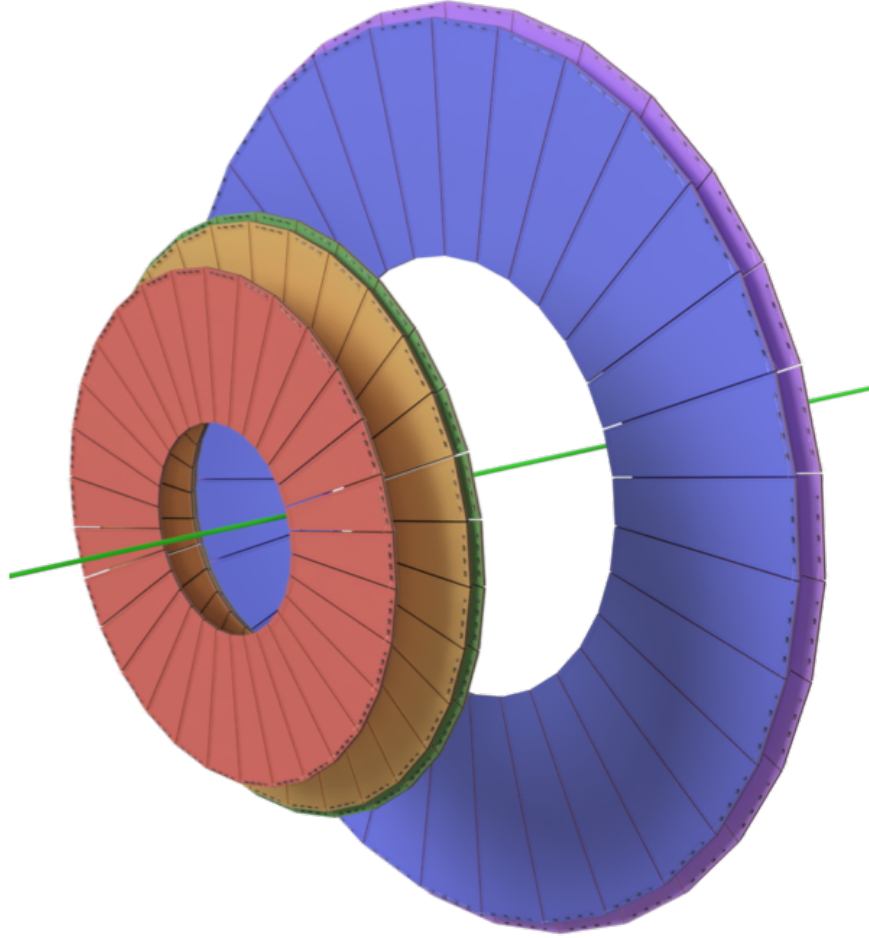


Figure 59: The GEM module arrangement at one of the detector locations of the SoLID PVDIS configuration

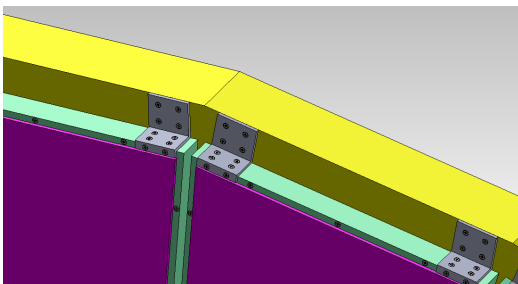


Figure 60: GEM module mounting at the outer edge of a GEM ring in the PVDIS configuration.

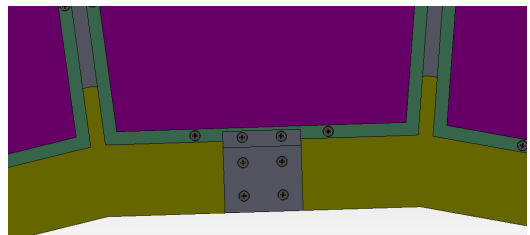


Figure 61: GEM module mounting at the inner edge.

the number of detector stations is higher in the SIDIS configuration, the inner and outer radii of the detector wheels are significantly smaller compared to the PVDIS configuration. Furthermore, since there are no baffles in the SIDIS configuration, the active detection area has to cover the entire surface area of each detector wheel. In order to meet these requirements, the SIDIS detector configuration will be set up by rearranging the GEM modules from the PVDIS configuration in

Layer	Z (cm)	R_{min}^{needed} (cm)	R_{max}^{needed} (cm)	R_{min}^{actual} (cm)	R_{max}^{actual} (cm)	pitch (mm)	# of channels
1	157.5	51	118	50	118	0.4	55.8 k
2	185.5	62	136	61	140	0.6	29.5 k
3	190	65	140	61	140	0.6	29.5 k
4	306	111	221	110	228	0.8	36.0 k
5	315	115	228	110	228	0.8	36.0 k
Total							≈ 187 k

Table 10: The locations, sizes and number of readout channels of GEM detectors for the SoLID PVDIS configuration. The five tracker layers will be assembled using three module sizes: Columns 3 and 4 give the minimum and maximum radii respectively of the acceptance coverage required at each tracker location. Columns 5 and 6 give the minimum and maximum radii of the actual module active areas used for each tracker layer. Column 7 gives the readout strip pitch while column 8 gives the total number of channels, for the 30 modules, at each tracker layer. The the number of readout channels indicated for location 1 is based on the assumption that half the readout strips in the of the GEM modules at this locations will be split into two readout channels to reduce occupancy. The group of split-strips in each module will be in the high exposure area of the sector.

an overlapping two-wheel arrangement at each detector station as indicated in Figure 62. This configuration ensures that there is at least 10% overlap between adjacent GEM modules in the SIDIS case, so that there is no loss of acceptance due to the small dead areas created by the chamber frames; in the PVDIS configuration these frames sit in the shadows of the baffle-ribs and do not contribute to any loss of acceptance either.

Location	Z (cm)	R_{min}^{needed} (cm)	R_{max}^{needed} (cm)	R_{min}^{actual} (cm)	R_{max}^{actual} (cm)	PVDIS layer(s)	# of modules	# of channels
1	-175	36	87	36	87	1	30	55.8 k
2	-150	21	98	36	87	2,3	24	23.6 k
3	-119	25	112	36	87	4,5	21	25.2 k
4	-68	32	135	36	87	4,5	21	25.2 k
5	5	42	100	36	87	2,3	29	28.5 k
6	92	55	123	36	87	2,3,4,5	25	28.5 k
Total							150	≈ 187 k

Table 11: The locations, sizes and number of readout channels of GEM detectors for the SoLID SIDIS configuration: The six GEM tracking layers for SIDIS will be assembled using the same GEM modules used in the PVDIS configuration: Columns 3 and 4 give the minimum and maximum radii respectively of the acceptance coverage required at each tracker location. Columns 5 and 6 give the minimum and maximum radii of the actual module active areas used for each tracker layer. Column 7 indicates the PVDIS tracking layer(s) (as defined in 10) from which the GEM modules will come from for each SIDIS tracking layer. Column 8 gives the total number of GEM modules of the respective size needed to cover the full 2π acceptance of each SIDIS tracking layer with at least 10% overlap between adjacent GEM modules. Note that tracking layer 6 is made of modules of two different sizes (both more than sufficient to cover the full acceptance in the radial direction at this location), with 18 modules from layers 4/5 and 6 modules of layers 2/3 of the PVDIS configuration. Column 9 gives the total number of readout channels needed at each SIDIS tracking layer. Note that this proposed configuration uses all 150 PVDIS modules and the associated readout channels.

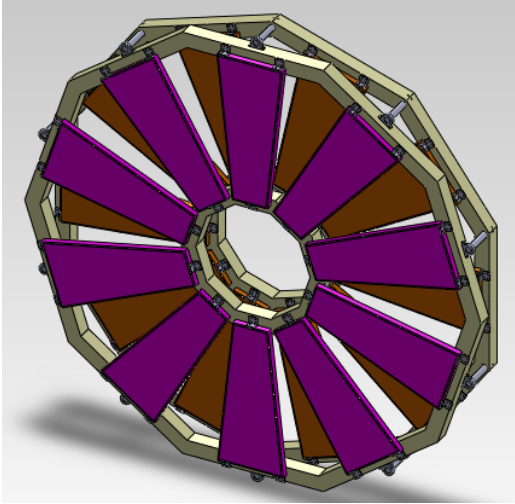


Figure 62: The GEM module arrangement at one of the detector locations of the SoLID SIDIS configuration

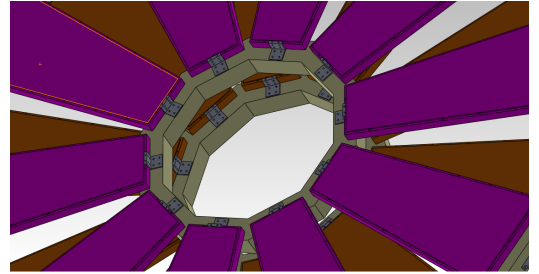


Figure 63: GEM module mounting at the inner edge of the ring in the SIDIS configuration

Figure 64 left shows the detailed design for a GEM module of the size proposed for SoLID. The “wings” shown in the frames are to support the frames during chamber assembly; they will be removed once the chamber is completed. The 2D readout plane will be glued on the bottom plate

(shown in cyan). This plate, made out of a 3 mm thick honeycomb structure material, also provides structural rigidity to the GEM chamber. All other frames are made out of Permaglass² with 8 mm wide sides. The spacers shown within the active area are for keeping the GEM foils from touching each other; these spacers are approximately 300 μm wide and contribute only about 2% reduction to the active area of the chamber. The GEM foils are mounted on the 3 light green frames, while the drift cathode is glued on the red frame. A thin gas window is glued on the orange frame.

Figure 64 right shows 2D readout layer concept for SoLID GEMs; what is shown in the illustration was created from the design files used to manufacture the readout for a prototype GEM chamber built for the EIC program. This readout was fabricated and was used with the latest EIC prototype GEM module (more detail on this and other prototype GEM detectors developed by the UVa group is presented below).

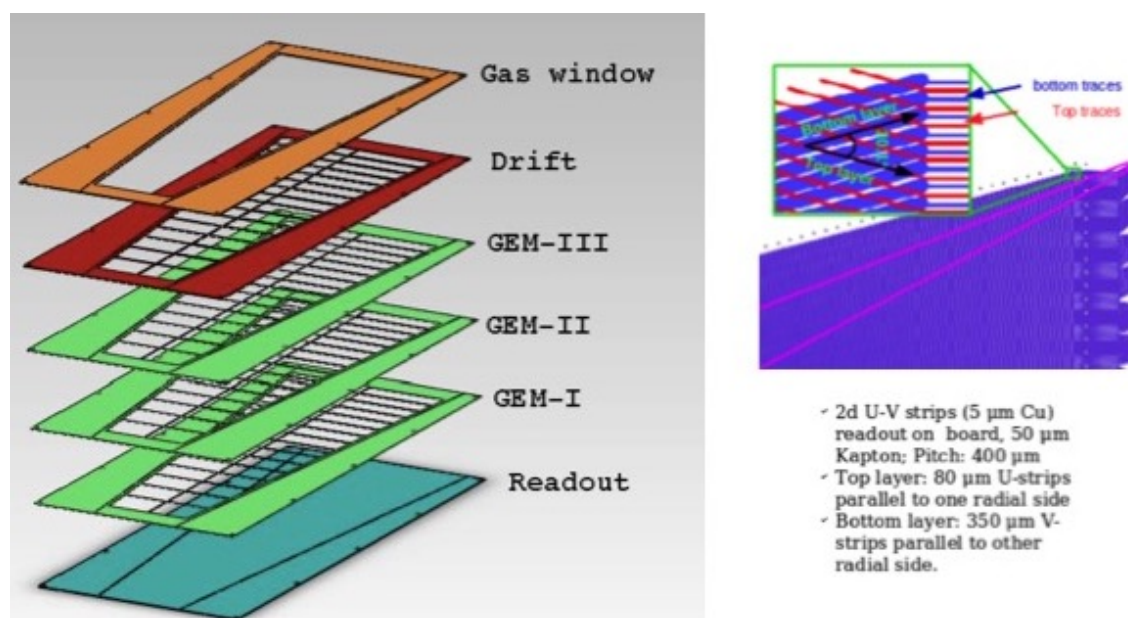


Figure 64: Left: The frame assembly for a GEM module prototype of the size proposed for the largest SoLID GEMs. Right: The concept of the 2D readout plane proposed for SoLID, shown here in a readout layer manufactured for an EIC GEM prototype.

As indicated below, the UVa group will perform the design, prototyping and fabrication of the GEM detectors included in the baseline SoLID project plan. This group has extensive GEM detector design and fabrication experience and has constructed and operated several of the largest GEM detectors in the world. In 2017, the UVa group successfully completed the DOE supported large area GEM detector fabrication project for Jefferson Lab Super Bigbite Spectrometer (SBS) project, on time and on budget, by finishing the construction of 40 GEM modules, each with an active area of $60 \times 50 \text{ cm}^2$, for the two large area GEM trackers of SBS. Since then, the group has also constructed another eight SBS GEM modules to be used as spares. All modules 48 have been tested and demonstrated to work very well meeting or exceeding the design goals of the SBS program. A DOE review panel for the SBS project noted: “We commend the UVa group for excellent progress on chamber construction, and for uncovering and solving a number of sticky experimental issues through their careful analysis.”

Figures 65 and 66 show results obtained during the testing of SBS GEM modules built by the

²Permaglass is a glass fiber material, with randomly oriented fibers, which can be machined with very high precision.

UVa group. Figure 65 is the absolute efficiency, measured at several locations by using electrons from a beta source, as a function of the high voltage. An efficiency of $\approx 97\%$ was achieved. Figure 66 is the ratio of cluster charge for x and y hits. The development and prototyping details of SBS GEM modules as well as results from test runs were published in NIMA in 2015 [218].

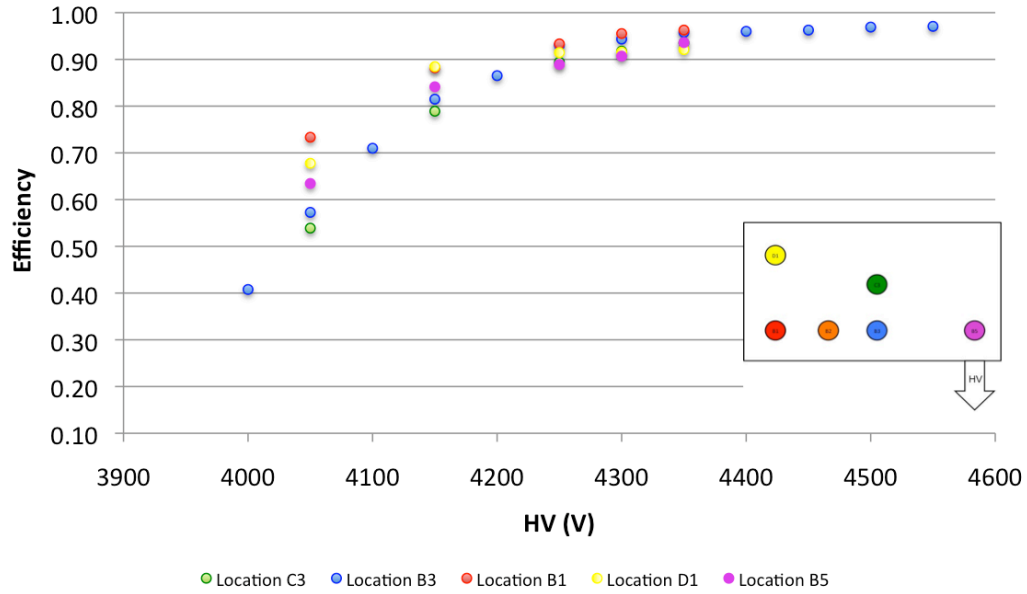


Figure 65: Efficiency of the $40 \times 50 \text{ cm}^2$ GEM chamber

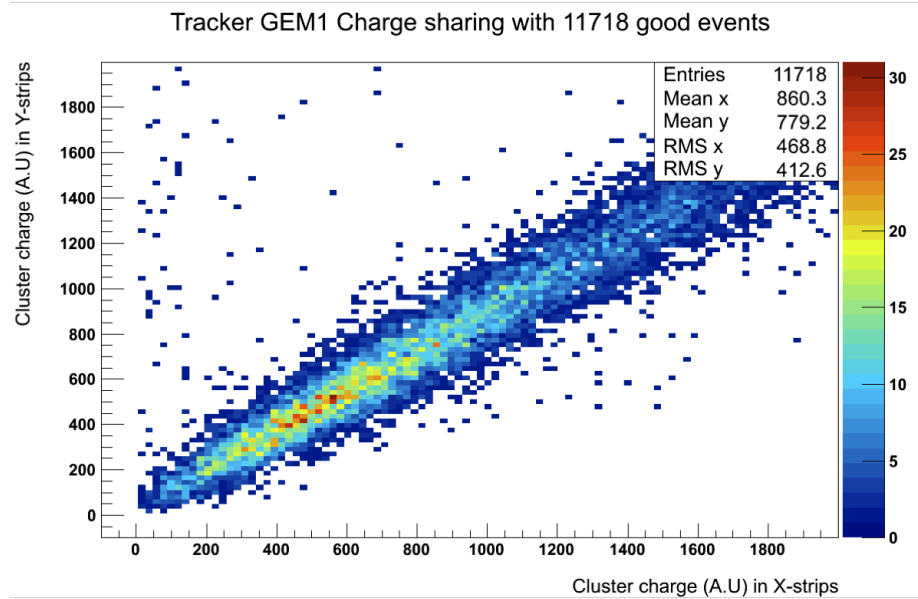


Figure 66: The charge division between x and y stripes for the $40 \times 50 \text{ cm}^2$ GEM chamber.

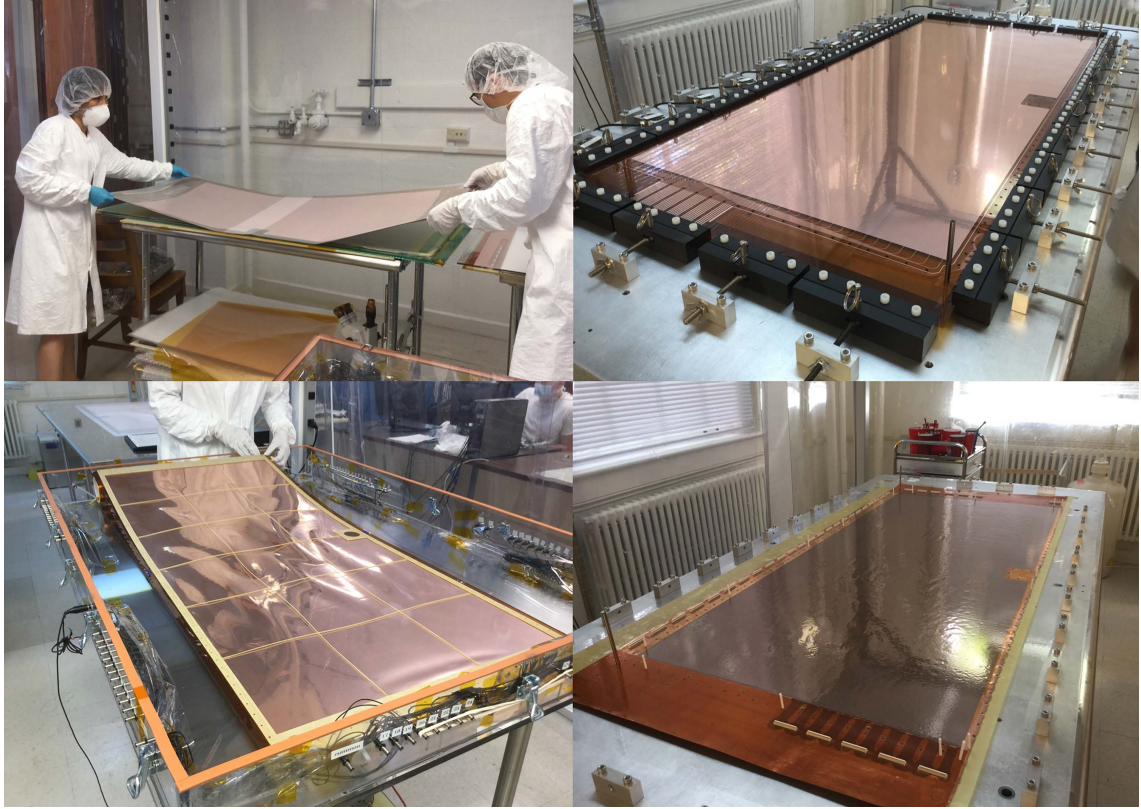


Figure 67: Making of the world's largest GEM detector: (top left) A raw GEM foil from CERN being prepared for visual inspection. Note the the active area of the foil has been covered by a protective foil. Research scientist Dr. Huong Nguyen is the one holding the left end of the foil. She has successfully constructed close to 50 large area GEM detectors for SBS, PRad and EIC R&D projects. (top right) The GEM foil stretched on the stretcher to the required uniform tension. The left and far rows of tensioning blocks are mounted on accurate tension monitoring devices (the cables could be seen in the picture). (bottom left) A GEM foil goes through three High-voltage-testing-and-cleansing cycles (testing the GEM foil under high voltage and foil cleansing by burning any dust particles under high voltage) at the raw foil stage, after the foil is stretched and glued onto its holding frame, and after the foil has been assembled into the GEM detector. This picture shows a framed foil being installed in the large dry-nitrogen GEM foil testing box. The wrinkles seen on the foil are due the holding frame buckling under the tension on the foil. Once the framed foil is dowel-pinned on to the assembly jig and then glued together with all the other frames, the combined tension of the glued together frames prevents this type of buckling in the assembled detector. (bottom right) The 2-D x-y readout board, glued on to the base window, aligned on the assembly jig with dowel pins, waiting for the other frames to be installed over it.

Until a few years ago, one challenge regarding the SoLID GEM tracker had been the large active area of the GEM modules required for SoLID; the active area of the largest GEM modules needed will be approximately $115 \times (21-44) \text{ cm}^2$. However, this is not an issue anymore: the UVa GEM group now has extensive expertise in the design, fabrication and operation of GEM detectors with even larger active area than what is needed for SoLID. In 2015-2016 this group successfully designed and fabricated the world's largest GEM detector pair with an active area of $123 \text{ cm} \times 55 \text{ cm}$ for Jefferson lab PRad experiment. The active area of these detectors were more than a factor of

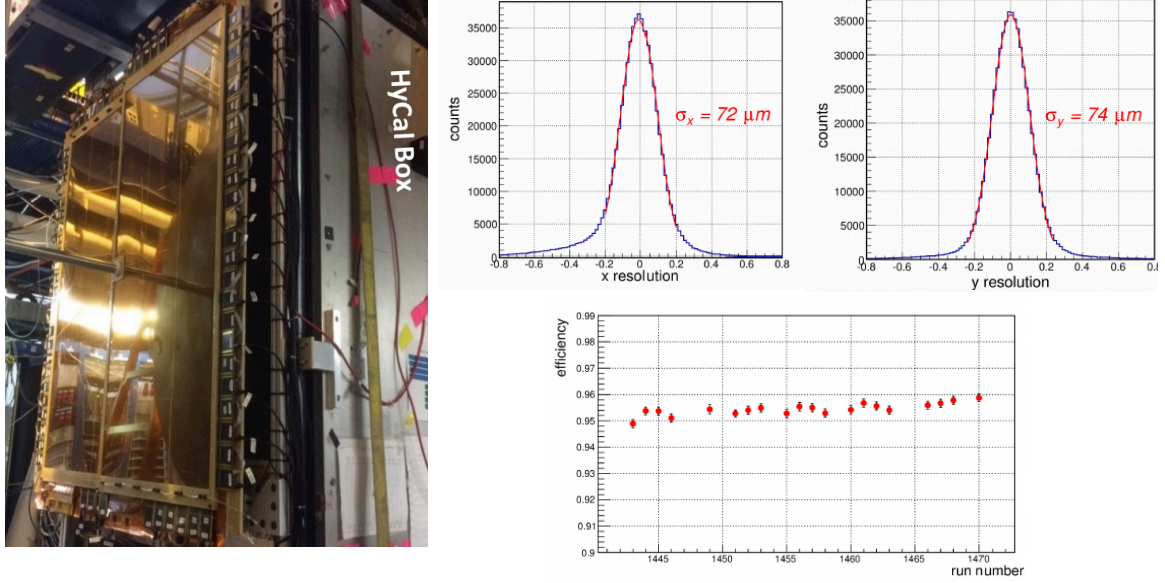


Figure 68: (Left:) The large area GEM detector pair developed by the UVa group in PRad experiment setup next to HyCal. The beam-line can be seen passing through the especially designed through-hole in the middle of the GEM layer. (Top-right) The position resolution (approximately 72 (74) μm) for x (y) direction readout of GEM detectors achieved during PRad experiment. A previous review committee for the SoLID project had raised the concern about a possible deterioration of the position resolution for SoLID GEMs due to the increased capacitance of longer than 1 m readout strips. The PRad result presented here showing excellent, in-beam position resolution for PRad GEMs with 123 cm long readout strips in the x-direction (10 cm longer than the longest SoLID readout strips) shows that this is not an issue. (Bottom-right) the GEM detection efficiency over a period of two weeks during the PRad experiment. This plot shows that the average GEM efficiency is over 95% and is stable to within 1% over long periods of time. The small periodic variations are due to gas cylinder changes which introduce very small amounts of air and humidity into the gas supply line. The small upward trend in the efficiency could be due to the long term purging of the detector, with small pockets of air and humidity trapped in the corners of the detector being cleaned out.

two larger than any other GEM chamber built before that. Both PRad GEM modules performed extremely well during the entire experiment. They yielded highly stable operation, high resolution (of approximately 70 μm as shown in Figure 68-right-top), and efficiency ($\sim 95\%$ averaged over the active area). The efficiency was stable over the duration of the whole experiment, as shown in Figure 68-right-bottom.

Figure 67 shows some of the fabrication steps of one of the PRad GEM modules in the UVa group clean room. All specialised equipment used in this process, like the large area foil stretcher and the foil high-voltage testing enclosure, were developed, designed, prototyped and built by the UVa group. Figure 68-left shows the PRad GEM detector pair installed in hall B, next to HyCal electro-magnetic calorimeter, ready for taking data during the experiment.

The PRad GEM detector project allowed the UVa group to gain expertise in the construction of large area GEMs and to demonstrate the feasibility of the GEMs with the dimensions required for SoLID. The EIC GEM R&D program carried out by the UVa group allowed the development of several other features crucial for SoLID as well as for EIC GEMs. These features include U-V

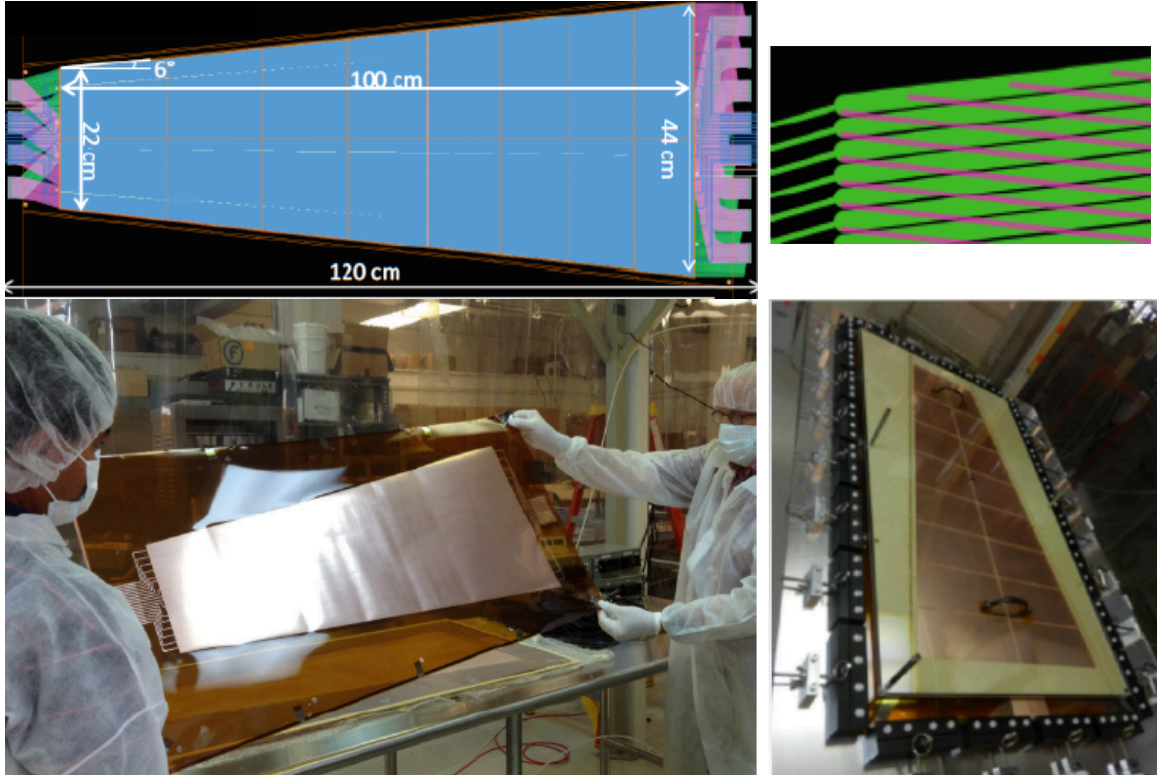


Figure 69: (Top left:) The photolithographic design for the 2D readout board of UVa EIC GEM prototype I. As the highly zoomed-in figure on the top-right shows, the U-V readout strips in this readout structure were arranged with a 12° stereo angle between U and V, just as needed for SoLID GEMs. The zoomed in section comes from the left-top corner of the readout board; as could be seen from the full readout board shown on the left, the purple (U) strips ending up on the top-left corner of the board are read out from the opposite edge of the detectors (away from the beam-line edge), while the green (V) strips and some of the U-strips are read out from the inner (close to the beam-line) edge of the detector in this prototype. (Bottom left:) A raw GEM foil used for UVa EIC GEM prototype-I. Note that in the case of this foil, the protective film has been removed to expose the active GEM area for visual inspection. (Bop right) A EIC prototype-I GEM foil stretched with the and the GEM holding frame glued on the foil. Some of the precision dowel pins which ensure the relative alignment between different GEM foils, holding frames and the readout could also be seen in the picture. A thick, heavy plastic "weight-plate" (the one with the black handles) has been placed the stretcher to the required uniform tension. Note the side "wings" on the trapezoidal frame; these wings are removed after the framed foil is glued into the rest of the chamber.

type 2D readout with a shallow angle between U and V strips (for SoLID, this angle needs to be 12° , as opposed to 90° in the SBS and PRad GEMs), and locating all readout electronics at the outer circumference side of the detector to avoid exposure to the high radiation levels close to the beam-line in the cylindrical geometry of both SoLID and EIC detectors.

The first EIC prototype GEM developed by the UVa group in 2013-2014 had dimensions of $100 \times (22-44) \text{ cm}^2$, approaching the size of the largest SoLID GEM modules, and with 12° opening angle trapezoidal shape required for SoLID. Figure 69 shows the fabrication details for this GEM module. It was extensively tested with cosmic ray data and in a long beam test at Fermilab; the results from these tests showed that large GEM detectors of the sizes and the shape required for

SoLID are feasible and the UV readout proposed for SoLID delivers the required position resolution. The development and fabrication details of this prototype detector as well as results from test runs were published in NIMA in 2016 [219].

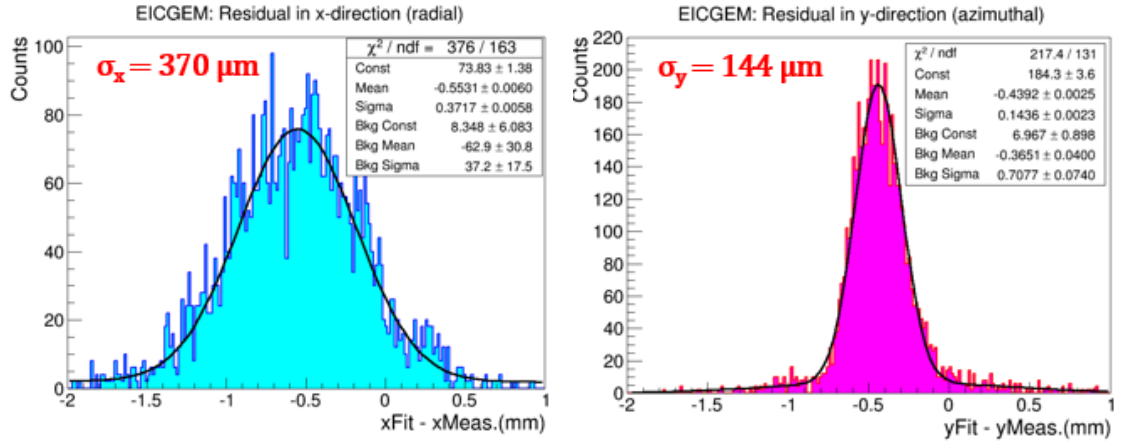
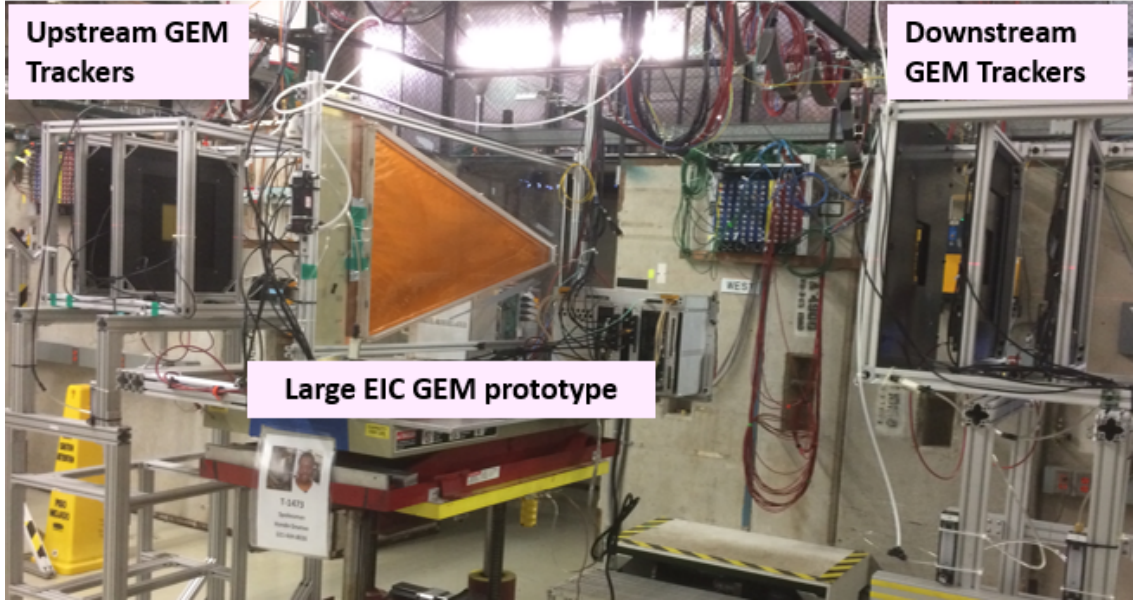


Figure 70: (Top) EIC GEM prototype installed in test beam area at Fermilab (June-July 2018). (Bottom) Preliminary results of spatial resolution performance in both radial (x) and azimuthal (y) directions of the large GEM prototype with stereo-angle (U-V) strip readout structure

Using the lessons learned with the first prototype, a second trapezoidal (EIC and SoLID style) prototype with new design ideas was designed, built and characterized. The the U-V strip readout includes in its design a double-sided zebra connection technique that the UVa group developed to allow the connection of all readout strips to the front-end-electronics at the outer radius side of the wedge-shaped large detector. This new connection scheme drastically minimizes the exposure of the electronics to radiation damage, eliminates the multiple scattering caused by the electronics mechanics and optimizes the dead-to-active area ratio of the detector, by moving readout electronics away from the beam-line. The prototype was successfully tested with cosmic in the Detector Lab at

UVa and later with a high energy proton beam at the Fermilab Test Beam Facility (FTBF) in June and July 2018 (see Fig. 70-right). The analysis of the FTBF data is currently ongoing. The results will be published in NIMA in 2020.

As part of SBS GEM tracker development activities, the UVa group has also carried out an aggressive R&D campaign to ensure proper readout of the GEM data and accurate track reconstruction under very high background conditions. The background hit rate in the SBS front tracker is expected to be up to 500 kHz/cm², similar to the highest hit rates expected at the location of SoLID GEM trackers. Correctly reconstructing the particle tracks of interest in this very high background environment is achieved by using especially adapted high rate techniques at every step of the tracking process: optimizing the GEM module and tracker design at the hardware level, using high bandwidth electronics and real time Field Programmable Gate Array (FPGA) based background suppression techniques at the Data Acquisition (DAQ) level, and developing highly specialized tracking algorithms to pick out the signal hits from among the vast amount of background hits. As part of SBS R&D, these techniques were developed, implemented, and tested under realistic conditions. A detailed Geant4 simulation of the SBS setup was combined with a digitization package to generate the detector level pseudo-data similar to what is expected in the actual experiments. The digitization procedures were calibrated against actual GEM data from cosmic-ray runs, X-ray tests, beam test runs in experimental Hall-A, and the PRad experiment in Hall B. Then, optimized tracking algorithms were developed and implemented in an analysis program used to analyze these pseudo-data and to extract expected high-level parameters. These extracted quantities were then compared with the input parameters from the simulation to verify and determine the performance characteristics for the SBS tracker. This work has demonstrated that the already developed techniques are adequate for the high rate operation under SBS conditions. This work also has laid a firm foundation to further improve the tracking performance for the SBS experiments as well as for the SoLID program. A detailed description of this work could be found in [220].

7.2 GEM tracker Design Activities

The design and optimization activities towards the SoLID GEM tracker is currently being led and conducted in the United States at the University of Virginia (UVa). According to the current plan, the UVa group, which has an ongoing large area GEM module production program, will do the designs and prototyping of the SoLID GEM chambers, and the construction for the SoLID baseline configuration. Within the SoLID collaboration, five institutions in China including the China Institute of Atomic Energy (CIAE), Lanzhou University (LZU), Tsinghua University (THU), the University of Science and Technology of China (USTC) and the Institute of Modern Physics (IMP), have various GEM related research activities. The plan is for these efforts to contribute towards the enhancement to the baseline configuration such as upgrade to the GEM readout.

7.2.1 GEM chamber construction facilities at UVa

The UVa group's **UVa Micro-Pattern Gas Detector Lab** is a 15 x 15 m², well equipped nuclear physics detector development lab that has been used for the development, construction, and testing of many large area GEM detectors. The lab consists of a 8 x 4 m², level 1,000 clean room, especially set up for the GEM chamber construction. The lab contains specialized GEM construction equipment worth over \$ 200,000, purchased mostly using capital equipment funding from the University of Virginia.

The facilities in the the lab include:

- Equipment needed for GEM detector fabrication.

- Mechanical Stretching systems with tension load monitoring for large area GEM foil foils.
 - High power optical microscope for GEM foil inspection.
 - Picoammeters for GEM foil testing and characterization.
 - Large volume dry N₂ boxes for GEM foil testing.
 - Large capacity ultra-sonic bath for GEM frame cleaning.
 - Laminar flow racks for GEM foil storage.
 - Particle counter for clean room monitoring.
- GEM readout system based on APV25-S1 electronics: a state of the art, 10,000 channel GEM readout system based on APV25-S1 electronics (this is the readout system used for GEM R&D activities in the lab; new separate new readout system with 127,000 channels is being set up for SBS). APV25-S1 is a fast pipeline readout chip used for COMPASS GEM trackers, CMS silicon stripe detectors, and STAR FGT GEM chambers [7]. The capacity of this system is sufficient to readout the prototype GEM trackers.
 - Wiener-Iseg multi-channel High Voltage system: The UVa GEM group owns a Wiener-Iseg2 multi-channel High Voltage system that is especially suited to provide high voltage to sensitive tracking chambers. This system currently has 16 channels and can be expanded to 40 channels.
 - A GEM detector testing station equipped with a high-flux x-ray tube and radioactive sources. This setup is located within a large, walk in cabinet shielded with lead.
 - A cosmic ray test stand equipped with large area scintillators for trigger.
 - A CODA (Jefferson lab DAQ architecture) based Data Acquisition system.

7.2.2 GEM chamber programs in China

The aforementioned five Chinese institutions all have worked on gas detectors for many years, including development and test activities on MWPC, MRPC, GEM, Micromegas, THGEM, TPC, and applications of these detectors. These institutions have well-equipped facilities that include clean rooms for GEM detector assembling, front-end readout electronics based on APV25-S1 (developed by the INFN group), and Multi-channel HV power supply systems and DAQ systems.

CIAE, which has over 20 years of experience in nuclear pore foil production and Kapton etching, signed a license agreement for manufacturing and commercialization of GEM foils and GEM based products with CERN, and has been working with CERN and Chinese manufacturers to develop large area GEM foil production capabilities in China in recent years. LZU has been building a Micromegas+AFTER chip system for fast neutron (14 MeV) imaging in the past few years. The experience gained from this R&D work is useful to their GEM project. For instance, several designs of neutron converters with different parameters were tried in a simulation based on MCNP4 and GEANT4 (for both Micromegas and GEM), and different conversion efficiencies were compared. THU has experience with GEM detectors by developing the electronics, such as a GEM-based TPC readout, a 16-channel CSA and shaping amplifier for GEM.

The USTC group started the GEM detector R&D work in 2000. Following the initial success with the construction and testing of small GEM detectors, the USTC group has since been focusing on the R&D of large area GEM detectors, especially on further developing the self-stretching

technique, which was initially developed at CERN, to better suit the need of fabricating large-area GEM detectors with high quality. The USTC group has been able to build multiple $100 \times 50 \text{ cm}^2$ GEM detectors with good gain uniformity ($\sim 5\%$). It's worth pointing out that in principle, the sliding self-stretching technique would allow for the building of super-large GEM detectors (multiple square meters) as long as GEM foils are available in such sizes. In parallel with the GEM detector R&D, the USTC group has worked intensively on GEM readout electronics, and has developed a MPGD readout system based on the VMM chip and achieved a time resolution of 0.5 ns with equivalent noise of 0.6 fC at a shaping time of 25 ns. These effort will contribute towards the enhanced SoLID baseline configuration.

8 Light Gas Cherenkov

8.1 Design

The light gas Cherenkov detector for SoLID is divided into 30 identical sectors to match the 30 sector symmetry of the PVDIS baffle system. Many elements of the light gas Cherenkov remain identical between the PVDIS and SIDIS/ J/Ψ experimental configurations, but some elements are adjusted or added/removed. Beyond the criteria dictated by the experimental physics requirements, the design of the Cherenkov detector was optimized with the goal of reducing the costs of construction and maintenance over the detector's lifetime including the switch over between experiments. The specifications of the tank and each major element per sector for each configuration are described below:

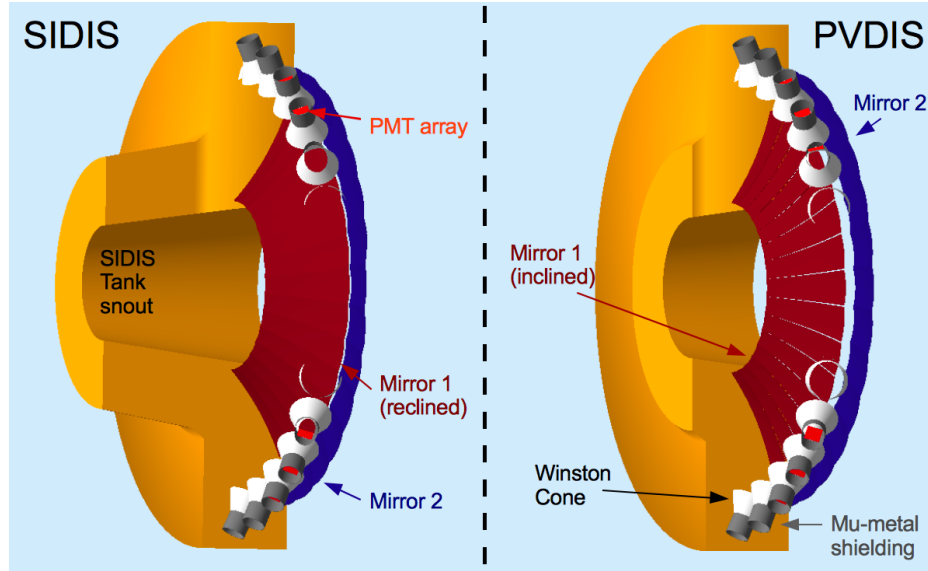


Figure 71: A side by side cross-section comparison of the light gas Cherenkov detector for both the SIDIS and PVDIS configuration with all major components labeled.

8.1.1 Tank and Cherenkov Gas

The main body of the tank remains identical between PVDIS and SIDIS configurations, and has a length roughly 105 cm with an inner radius of 71 to 85 cm, and an outer radius of 265 cm. With the PVDIS baffles removed for SIDIS, an additional tank ‘snout’ is attached upstream of the main tank inside the additional space evacuated by the baffle system. This tank snout adds an additional 107 cm of length to the tank with an inner radius of 58 to 71 cm, and an outer radius of 127 to 144 cm. In both configurations, the windows will be constructed from polyvinyl fluoride (PVF or Tedlar) at a thickness of 0.05 mm and 0.1 mm for the entrance and exit windows respectively. PVF provides a strong and gas-tight seal at minimal density (1.45 g/cm^3). The radiator gas in both configurations will be CO_2 or N_2 pressurized at slightly over atmospheric pressure to maintain gas purity.

8.1.2 Mirrors

Each sector will consist of two spherical mirror segments with dimensions listed in Tab. 12. Radially outward from the beam line, the inner most segment we will refer to as mirror 1 (red in Fig. 71)

and the outermost segment as mirror 2 (blue in Fig. 71). In order to accommodate two different incident particle angles between PVDIS (22° to 35° from a central Z-vertex 270 cm away) and SIDIS (8.0° to 15.0° from a vertex 520 cm away), mirror 1 must be adjusted between experiments such that the reflected Cherenkov light in both configurations falls into the PMT detector acceptance. This is achieved by rotating mirror 1 by an angle of approximately 8° inward about the mirror's inner-most edge (or edge closest to the beam-line). In Fig. 71 we see a cross section of the light gas Cherenkov, sliced along the beam or Z-direction, with the mirrors in both the reclined and inclined positions. Mirror 2 is fixed in position and rotation and non-contributing to the SIDIS configuration; however, mirror 2 is necessary to cover the larger angular range in the PVDIS configuration. The mirrors will be crafted to minimize areal density while maintaining good rigidity and keeping fabrication costs reasonable. A low radiation-length strong spherical mirror blank will be fabricated from carbon fiber. A reflectively coated Lexan plastic film will cover the blank surface and provide high reflectance ($\geq 85\%$ for $\lambda = 200$ nm to 620 nm) aluminum with a protective coating of MgF_2 .

Mirror	inner-edge W (cm)	outer-edge W (cm)	L (cm)	R of curv. (cm)
Mirror 1	16.26	36.03	114.53	277.51
Mirror 2	37.06	45.95	59.26	157.99

Table 12: The dimensions of the two mirror segments in the light gas Cherenkov.

8.1.3 PMTs

The light gas Cherenkov will use Hamamatsu flat panel multianode photomultiplier tube assemblies: H12700 [234]. These PMT assemblies are an 8×8 pixel square array with a total active surface area of $49 \text{ mm} \times 49 \text{ mm}$ with a UV-glass window, Bialkali photocathode material producing an average quantum efficiency around 15%, and a 10-stage dynode structure allowing resolution down to a single photoelectron. A 3×3 array of these PMT assemblies will be mounted in each sector, as shown in the PMT mounting prototype in Fig. 72. The position and orientation of the PMT array will remain fixed between PVDIS and SIDIS configurations. The PMTs will be coated with a wave-length shifting p-Terphenyl coating. This coating is a cost effective method to boost the PMT response of Cherenkov radiation in the UV range. The expected effective increase in photoelectron gain is shown in Fig. 73. Every pixel in the H12700 will be summed together to produce one signal per PMT; a trigger will then be constructed by requiring two PMT assemblies in the same array to fire in the same time window, with a minimum photoelectron discrimination. Simulations show a $>90\%$ average electron detection efficiency, integrated over all angles and momenta, when requiring 2 separate PMTs assemblies in an array to each generate 2 or more photoelectrons in either the PVDIS or SIDIS configuration. This trigger configuration would result in 36 possible coincidences per sector, consequently reducing the single photoelectron rate due to dark current or other backgrounds by at least a factor of 10. Specific filtering of the PMT signals will be tested while prototyping the PMT array and electronics. The pixel summing electronics is being developed by the Jefferson Lab Detector group.

8.1.4 Magnetic Shielding and Winston Cones

The PMTs will be shielded by a mu-metal cylinder/cone construction that doubles as support for a reflective aluminum inner glass cone to direct light onto the PMT array. The cylinders will measure 30 cm in length with an inner radius of 11.28 cm, the cone will have a height of 30 cm with an inner radius of 7.8 cm at the narrow end and an inner radius of 21 cm at the wide end. The

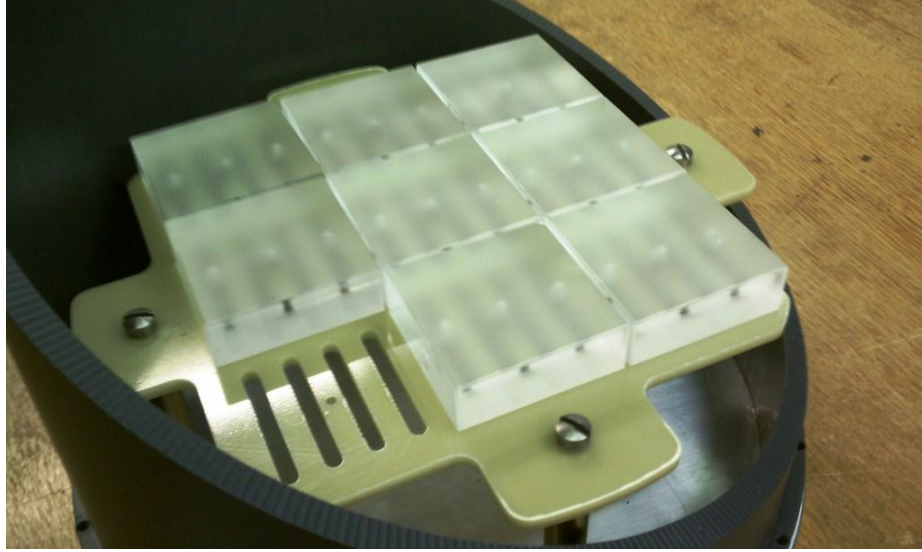


Figure 72: PMT assembly mounting prototype showing 3×3 array of dummy PMTs inside the space restricted by magnetic shielding.

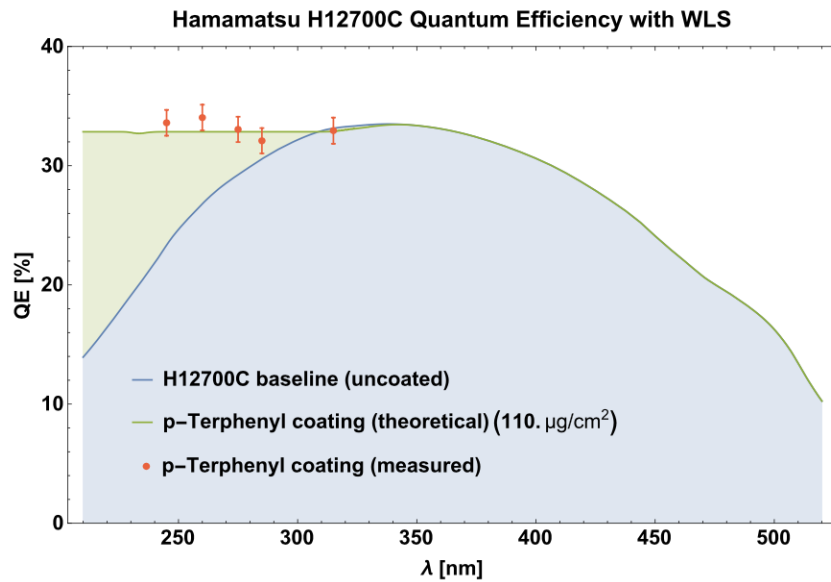


Figure 73: The increase in effective gain resulting from p-Terphenyl coating on H12700 PMTs. Red points are measurements done at Temple University. The curves show the current H12700 quantum efficiency, and the expected effective gain in the quantum efficiency from p-Terphenyl coating as a function of optical photon wavelength.

mu-metal shielding will be 0.04 inch thick reinforced by 0.125 inch thick 1008 carbon steel and manufactured by Amuneal Manufacturing Corp [235] or the Magnetic Shield Corporation [236]. The PMTs are most sensitive to the magnitude of the magnetic field parallel to the photon collection face (transverse direction). We require a reduction of 95 gauss to <50 gauss in the transverse direction, and a reduction of 135 gauss to <50 gauss in the longitudinal direction, to where we expect an output loss <10% as seen in Figure 85

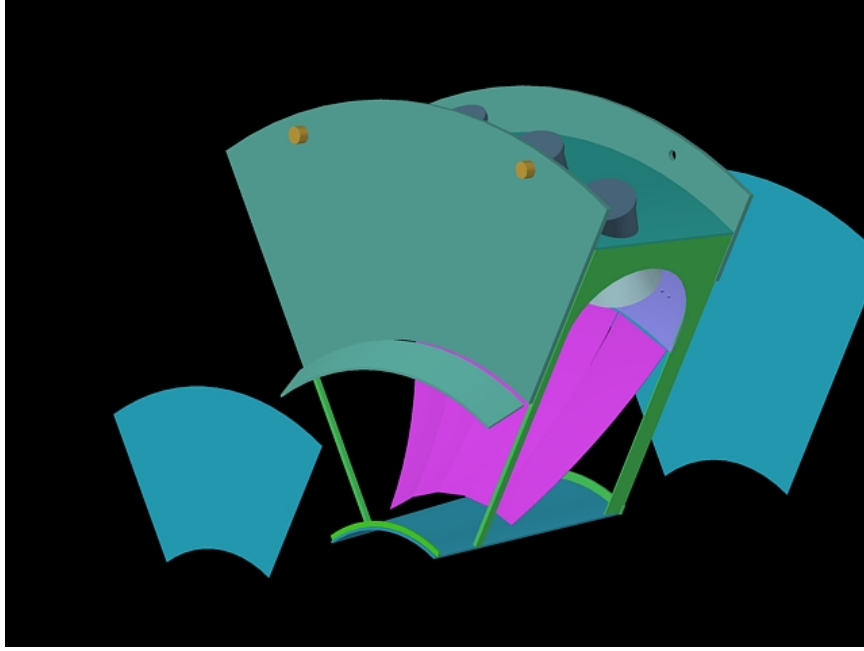


Figure 74: The support frame for one subsection of the light gas Cherenkov. The front and back acceptance windows (blue) are exploded to show the mirrors (pink and purple) and the support frame (green). The mounting points of the tank to the magnet housing are shown in orange.

8.2 Tank Support

The Cherenkov tank front and back windows will be divided into six radial sections. Between each pair of sections will be two thin rectangular aluminum support spokes, one to support and frame the upstream side of the tank and another to support and frame the downstream side (see Fig. 74). Both spokes are positioned and aligned to minimize the probability of tracks passing through the support material. Additionally, both spokes are interconnected at the outer radius of the tank, outside of the desired physics acceptance, by a solid arc-shaped plane to increase the rigidity of the frame and provide additional support for mounting the focusing cones and PMT assemblies. The space between the upstream and downstream spokes will remain open to maximize Cherenkov light collection. The combined frame itself will be mounted to the back wall of the downstream magnet housing, to support the full weight of the Cherenkov detector. This alleviates placing additional stress on the end-cap nose, which other additional downstream detectors will use to support their weight. Each PMT array will be accessible from the outer radial wall of the tank for alignment or maintenance purposes.

8.3 Simulations

All simulations were done with a slightly modified version of the GEMC [237] software developed at Jefferson Lab. GEMC uses a GEANT4.95 [238] backend to simulate all particle tracking through and interaction with materials and geometries. All plots shown in the light gas Cherenkov section of this document use the same simulation dataset. Event generation was performed by the eicRate DIS event generation tool authored by Seamus Riordan. The simulations also have the following features:

- Acceptance through the PVDIS baffle system (PVDIS events only).

- Cherenkov radiation process for creation of optical photons.
- Expected delta ray and pair creation from e^- and π^- particles interacting with the Cherenkov front window using the standard and low energy EM packages for GEANT4.
- Expanded mirror reflection properties in GEMC to be more in line with the latest functionality from GEANT4.
- PMT photoelectron signal simulation which includes the PMT dead area, quantum efficiency pixel-by-pixel, and optical properties of the PMT UV glass window.

8.3.1 Collection Efficiencies

The collection efficiencies for electrons in both the PVDIS and SIDIS configuration can be seen in Figs. 75 and 76. The slight jump in photoelectrons around 32° in the PVDIS figure is a result of the inclined inner mirror, which moderately reduces the number of optical photons produced by reducing the particle's path length through the gas before crossing the mirror.

8.3.2 Background Rates

A low energy inclusive background simulation was performed using GEMC by generating an electron beam on target, including all expected materials between the beam entrance to the Cherenkov back window. Secondaries produced anywhere in the SoLID detector and above the Cherenkov radiation momentum threshold while passing through the Cherenkov gas were considered as a possible source of background. For the PVDIS configuration, lepton production from initial π^0 production at small angle produced the majority of accidental backgrounds. This background was calculated using the same methodology as the modified Hall D generator, which uses a modified version of PYTHIA and SAID input to match known world data. More information on the pion generator can be found in Sec. 12.2.3. The combined background rate is estimated to be ≈ 0.8 MHz per sector for a trigger requiring at least 2 photoelectrons in 2 separate PMTs in the same sector. For the SIDIS configuration, the expected background rate is less than 100 KHz in the same trigger configuration above.

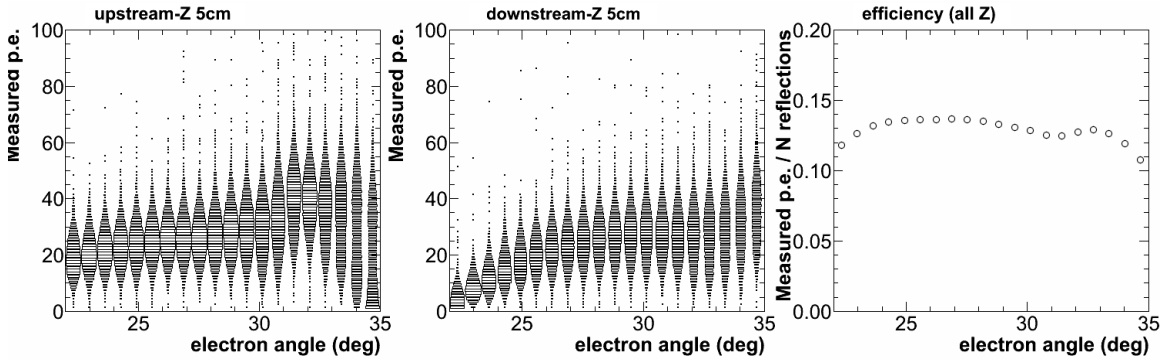


Figure 75: PVDIS configuration: The number of surviving photoelectrons versus theta after losses due to quantum efficiency of the PMTs, PMT dead area, or secondary reflections/absorptions of the cones or PMT UV-glass window for events in the 5 cm of target most upstream (left) and 5 cm of target most downstream (middle). The right plot shows the corresponding collection efficiency versus theta for all 40 cm of the target Z-vertex.

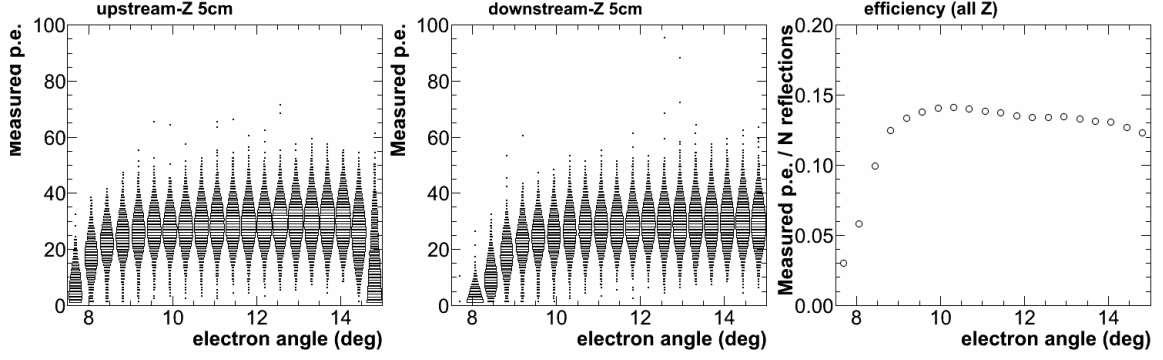


Figure 76: SIDIS configuration: Same as in Fig. 75 but with the SIDIS configuration.

8.3.3 Pion Rejection

The expected pion rejection is shown in Figs. 77 and 78. All pion signal below the pion Cherenkov radiation threshold (4.67 GeV/c CO₂ gas) is produced by knock-ons or (e^+ , e^-) pair creation. The photoelectron signal itself is a poisson distribution convoluted with a gaussian to simulate the PMT 1 photoelectron resolution. The pion-electron photoelectron cut is determined by taking the intersection of the two signal distributions, simultaneously maximizing the electron selection probability while maximizing the pion rejection probability. Additional calculations are shown in Figs. 77 and 78 with a stricter cut on the pion signal, which consequently reduces the electron efficiency (by 10% for the red points and 20% for the blue points). An example of these photoelectron cuts are shown in figure 79 for one bin in momentum in the PVDIS configuration.

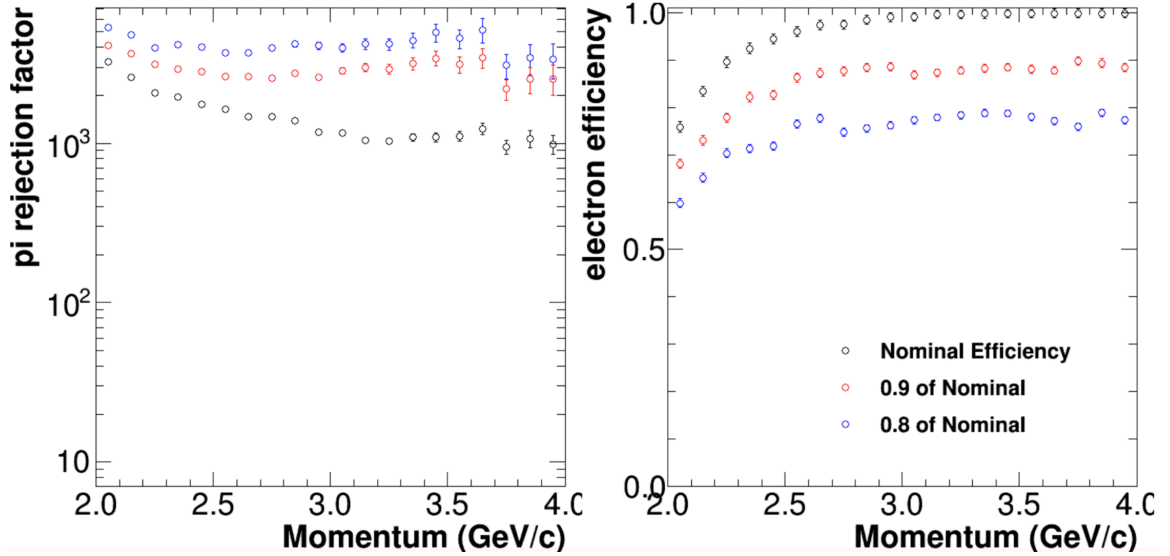


Figure 77: PVDIS configuration: The pion rejection factor versus momentum for 3 electron selection efficiencies: The nominal efficiency maximizes the pion rejection while minimizing loss of electrons, the red points correspond to a stricter pion cut with up to 10% additional loss of electrons, and the blue points allow an additional 20% loss of electrons.

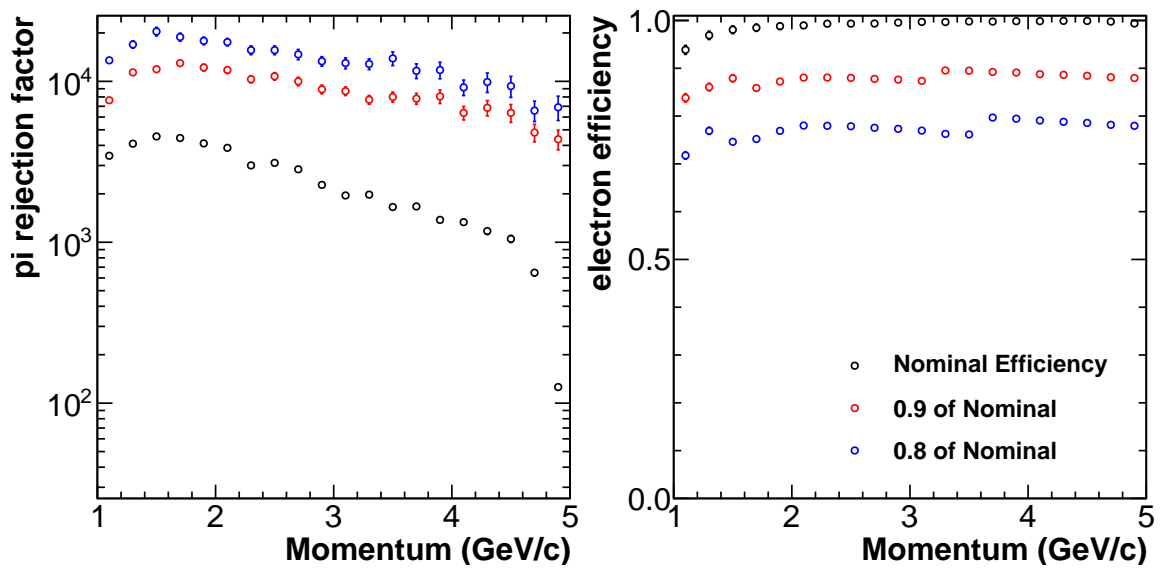


Figure 78: SIDIS configuration: Same as in Fig. 77 but with the SIDIS configuration.

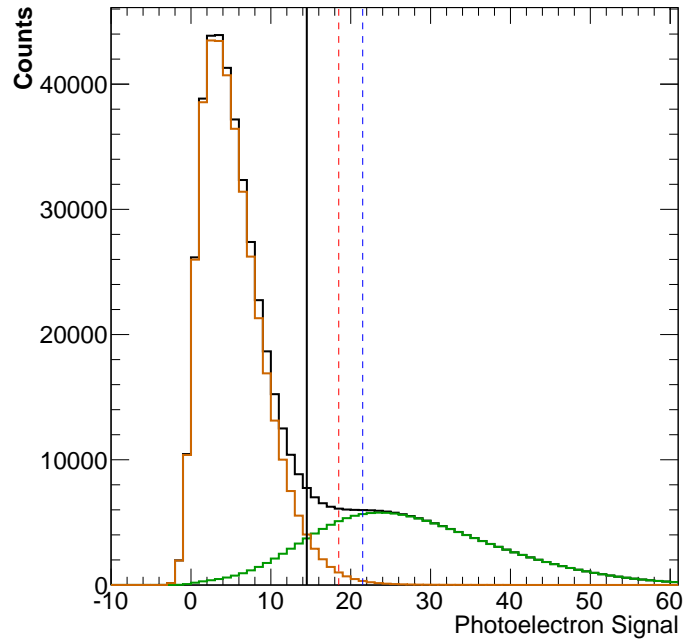


Figure 79: An example of the pion rejection cut made for one arbitrary bin in momentum for the PVDIS configuration. The pion signal is shown in orange and the electron signal is shown in green. The nominal efficiency cut is shown as a solid black line. The 90% and 80% electron efficiency cuts are shown as dashed red and blue lines respectively.

9 Heavy Gas Cherenkov

9.1 Design

9.1.1 Overview

A hadron Cherenkov detector is required for the identification of charged pions for the SoLID SIDIS program at forward angles from 8 to 15 deg. A clear distinction between charged pion and kaon Cherenkov signals is required from a momentum range of 2.5 GeV/c to 7.5 GeV/c. The heavy gas C_4F_8 at 1.7 atm absolute pressure and around 20°C temperature can cover such a momentum range with the number of photoelectrons > 10 for charged pions. Due to geometrical constraints, the gas length available for Cherenkov light production along the electron beam direction is about 1 m. Other requirements on the design are full azimuthal angular coverage and photosensors maintaining a good performance with shielding under the expected external magnetic field of ~ 100 Gauss in the SoLID magnet endcap.

	HGC
z (cm)	(306,406)
Radius (cm)	(90, 260)
Polar angle (degree)	(8,15)
Azimuthal angle	Full coverage
Volume (m ³)	~ 20
Number of PMTs/Channels	480

Table 13: HGC coverage and PMT counts. The z direction is along the electron beam and the origin is at the solenoid center. The range of various dimensions are shown.

9.1.2 Optical System

The optical system consists of three components. A ring of 30 spherical mirrors with radius of curvature of ~ 210 cm will focus Cherenkov lights onto 30 photosensor arrays. The photosensor arrays are positioned outside of particles trajectories and each photosensor array has a size of $\sim 8 \times 8$ inches (i.e. 16 of 2 inch PMTs in 4×4 array) to accept photons. A combined magnetic shielding and light collection cone will encompass each photosensor array to help collect lights and reduce magnetic field. The optical system has good performance for photons above 200 nm.

The mirrors will be made using the same material and technique as those of the Light Gas Cherenkov (LGC) mirrors. For the light collection cones, we will use the Aluminum coated polycarbonate resin thermoplastic (Lexan) films and attach them to the inner sides of the magnetic shielding cones. The same films were used in the JLab CLAS12 Low Threshold Cherenkov as its mirror reflection surface and have good reflectivity.

The photosensor of choice is the same one used for LGC, namely 2 inch multi-anode PMT (MaPMT) H12700-03 from Hamamatsu. It performs well in relatively high magnetic fields, is square shaped, and has good photocathode coverage (87% of its total area), making it ideal for tiling. It will be coated with a layer of wave-length shifting (WLS) p-Terphenyl coating to enhance its response in the UV range near 200 nm. The electronic readout system summing analog signals from all 64 pixels in one MaPMT H12700-03 is similar to what LGC proposes, with the exception that the HGC output will not be in the trigger.

9.1.3 Tank and Window

The conceptual engineering design is shown in Fig. 80. HGC has 30 sectors and each sector has a complete set of optical components. 3 sectors form a supersector with one common front window and one common back window. 10 supersectors are separated into two halves of the detector tank with 5 supersectors in each half tank, to facilitate fabrication and handling. At the tank outer radius, there are mounting structures to be connected to the rail supporting system in the SoLID magnet endcap. The spherical mirrors are fixed with mounts at their outer radius ends and attached to the tank. The combined magnetic shielding and light collection cones are mounted inside the outer shell. The PMT arrays are positioned in the cones, with the possibility for fine position adjustment through the mount tube.

The tank structure and back windows will mostly be made of Aluminum. The front thin windows consist of layers of mylar/carbon-fiber/kevlar with mylar for gas tightness and others for support. As a pressure system of 1.7 atm absolute/0.7 atm relative pressure, the HGC tank and windows design and prototyping will follow the JLab ESH&Q guidelines and are under the supervision of the JLab Design Authority. The tank and back window are required to be designed with a yield safety factor > 3 at the operational pressure and later pneumatically tested to a minimum of 1.15X the operational pressure. As an example, Fig. 81 shows that the current design of 0.25 inch Al curved back window has a yield safety factor > 3 at 1 atm relative pressure which is more than the 0.7 atm relative operational pressure. The front thin window needs to be designed by lesser of 90% yield and be tested to more than $2\times$ operational pressure to qualify design and material batch. As shown in Fig. 82, we have constructed a full size front thin window prototype and tested it up to 1.8 atm relative pressure which is more than the $2\times$ (1.4 atm relative) operational pressure. And the window deflection is stable at ~ 6 cm after multiple tests.

9.2 Simulation

9.2.1 Photoelectron Yield

The optical system for the Cherenkov light production and collection has been optimized using the standard SoLID Geant4 simulation software "SoLID.GEMC". We include wavelength dependent parameters for the gas refraction index, gas transparency, mirror and light collection cone reflectivities and the quantum efficiency of the WLS coated H12700-03 MaPMTs to obtain the photoelectron yields. Both the SoLID magnetic field map and particle decay are also taken into account in the simulation.

Due to the SoLID geometrical acceptance with respect to the target and the constraints on the photosensor positioning, particles with a larger polar angle entering the detector will travel a longer gas length compared to those with a smaller polar angle. Thus, the optimization was done favoring the smaller angle kinematics and by keeping the number of maximum reflections up to 2: one on mirrors and the other on light collection cones. Many photons only need 1 bounce from mirrors before reaching PMT arrays directly. As a consequence, the loss of photons through absorption on the reflective surfaces is kept to a minimum.

The dependence of negative-pion photoelectron yield on momentum is shown in Fig. 83. The result is from the HGC standalone simulation without including any other SoLID subsystem except for the magnetic field. The variation of minimum 8 deg and maximum 14.8 deg in polar angles and the vertex position at the target center and target ends are studied. For a fixed polar angle, the number of photoelectrons increases with momentum as it moves away from the threshold of the pion Cherenkov process and then becomes saturated. There is also an increase of yield with an increasing polar angle due to the detector geometry which allows for pions with larger polar angles

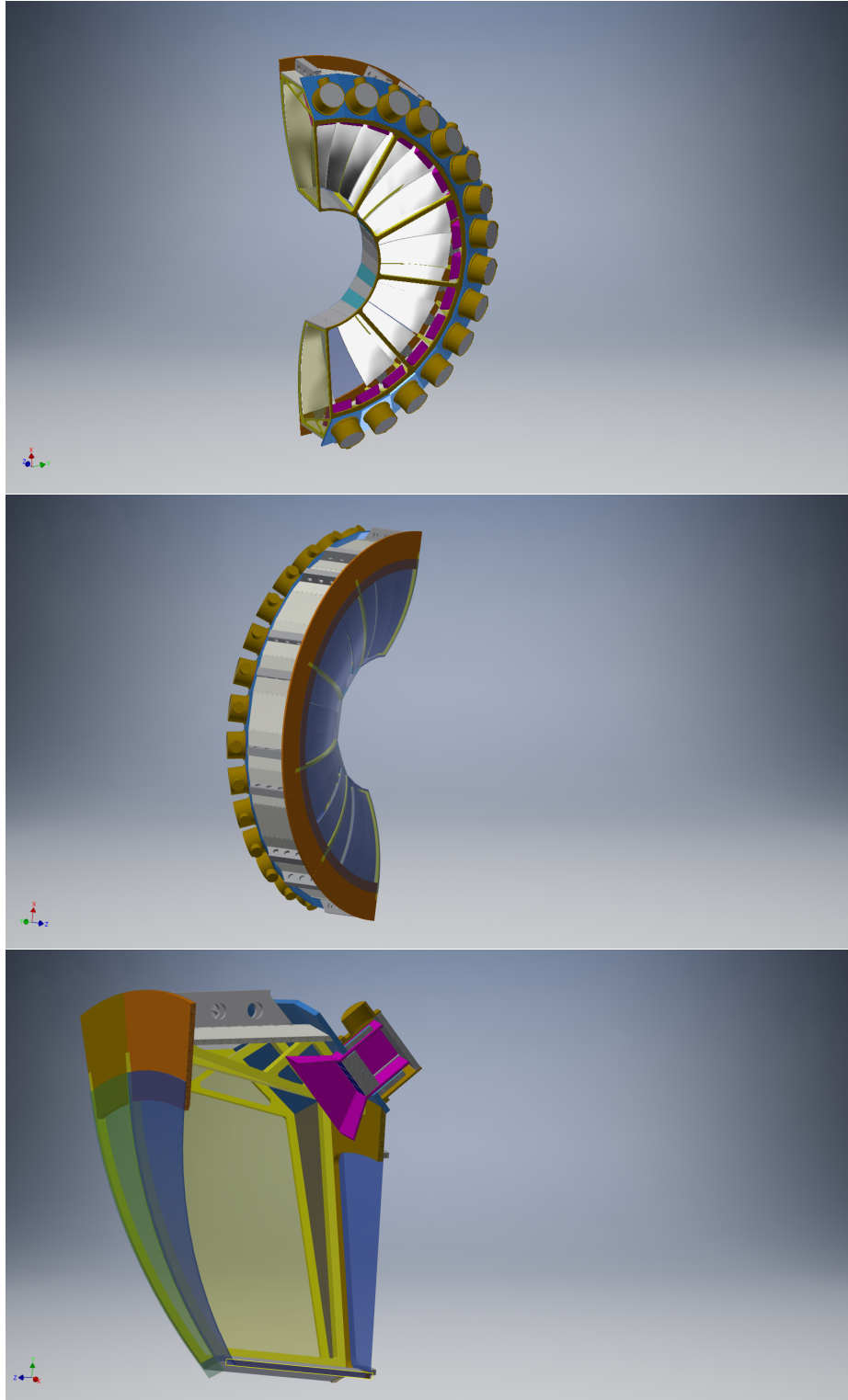


Figure 80: Conceptual engineering design of the heavy gas Cherenkov detector. The front view of one half tank without the front thin windows is shown in the top plot and the back view of one other half tank is shown in the middle plot. The bottom plot shows the side view of a sector.

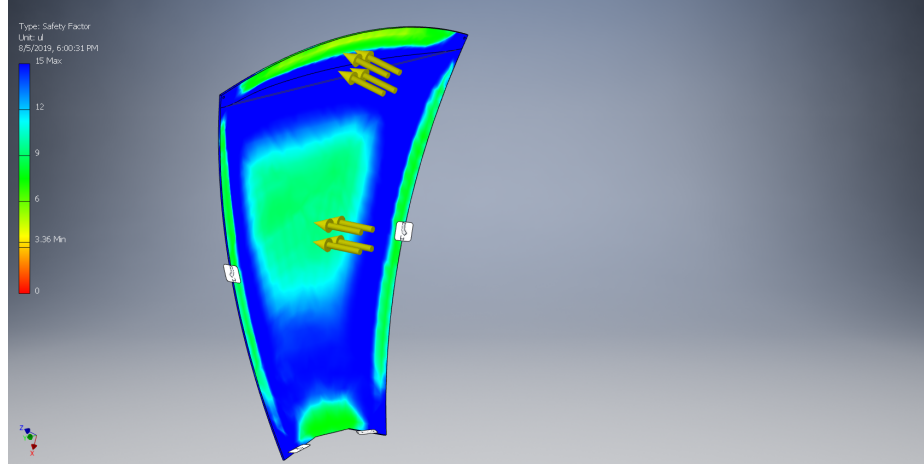


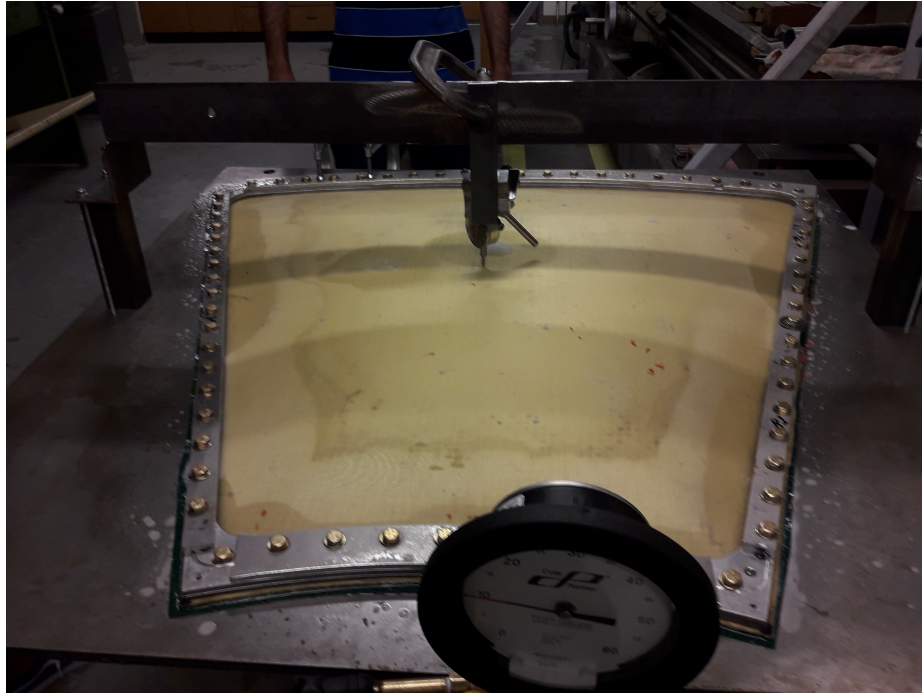
Figure 81: Conceptual engineering design of the HGC curved back window using 0.25 inch Al is shown to have a yield safety factor > 3 at 1 atm relative pressure, more than the 0.7 atm relative operational pressure.

to traverse more gas than those with smaller polar angles. The dependence on the vertex position along a 40-cm target length is small. Overall, we expect photoelectron yield to be > 10 over the entire kinematic range.

9.2.2 Pion Detection Efficiency and Kaon Rejection Factor

Taking advantage of the modular feature of the SoLID simulation program "SoLID_GEMC", the HGC detector can be loaded into the full SoLID SIDIS setup without any modification for detector description and signal processing. The performance of HGC in terms of pion detection efficiency and kaon rejection factor can then be further studied in the complete SoLID SIDIS setup. All materials from the target to HGC along particle trajectories of about 7 meters are included in the simulation. Both charged pions and kaons could decay and produce secondary particles before they reach HGC.

We studied two extreme kinematics. The first configuration is for $2.5 < P < 3.0$ GeV/c and $8^\circ < \theta < 9^\circ$, where the smallest number of photoelectrons is expected and pion detection is most difficult. The second configuration is for $7.0 < P < 7.5$ GeV/c and $14^\circ < \theta < 15^\circ$, where the largest number of photoelectrons is expected and kaon rejection is the hardest. The results are shown in Fig. 84. The photoelectrons generated by charged pions Cherenkov process are mostly distributed in a Gaussian distribution with small tails. But photoelectrons from charged kaons distribute widely because some decay particles like pions, muons and knock-on electrons from the front thin windows can produce signals in HGC. In real experiments, more sophisticated likelihood algorithms can be used for particle identification. For demonstration, here we just use the simple cut on number of photoelectrons. At any given cut, the pion detection efficiency and kaon rejection factor can be obtained simultaneously. By varying the cut values, we can balance the two to satisfy the requirement of pion detection efficiency $> 90\%$ and kaon rejection factor > 10 at the same time over the entire kinematic coverage. Background studies have shown that the expected number of pions to kaons is 10 to 1 [87–89]. The HGC will help keep the kaon contamination in pion samples to be below 1% while maintain a high pion detection efficiency.



HGC Thin Window Test

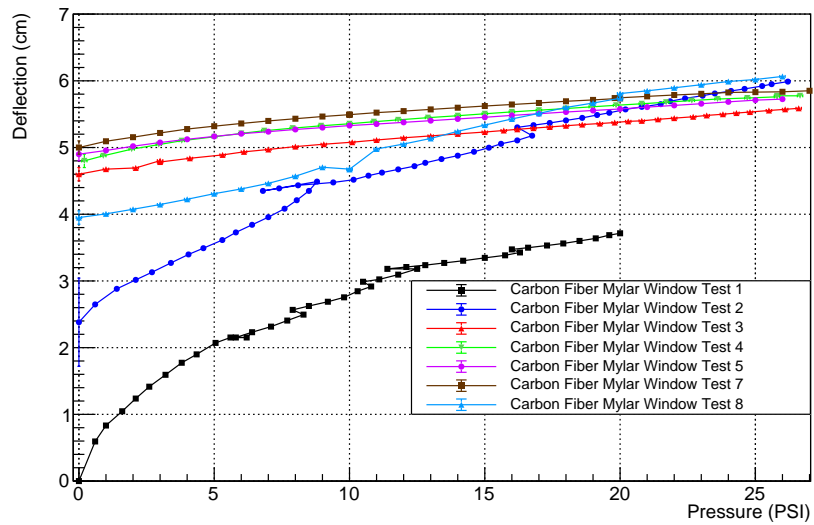


Figure 82: A full size front thin window prototype with layers of mylar/carbon-fiber/kevlar was constructed and tested up to 26.5 psi/1.8 atm relative pressure which is more than the $2 \times (1.4 \text{ atm relative})$ operational pressure. The top plot is a photo of the window on its pressure testing gig. The bottom plot shows the testing results. After multiple tests, the window deflection is stable at ~ 6 cm.

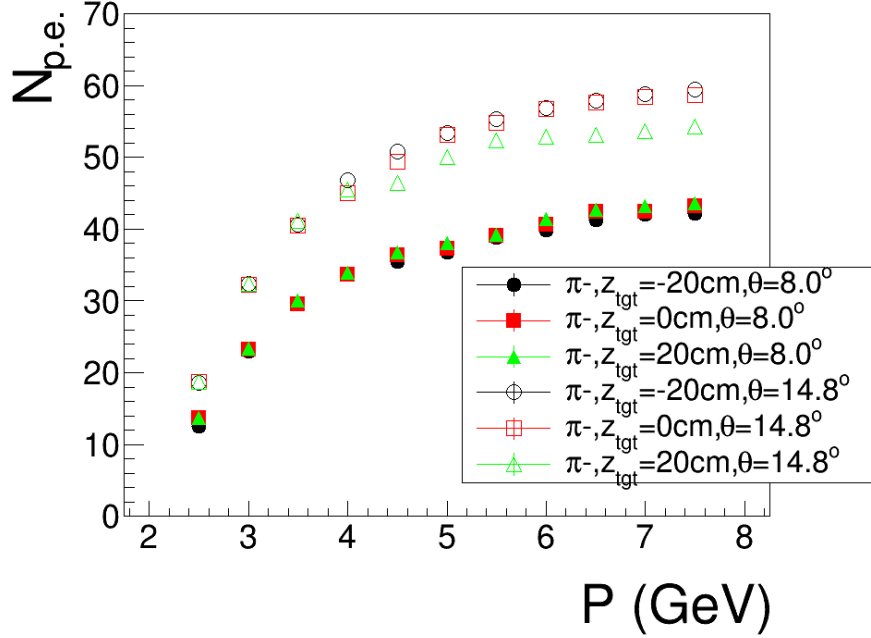


Figure 83: Simulated number of photoelectrons of negative pions as a function of momentum at various polar angles and target vertex positions. A very similar output is obtained for positive pions.

9.3 Performance of the PMTs in Magnetic Field

We performed extensive bench tests of MaPMT H12700-03 and its older model H8500-03 to map their performance in a magnetic field and assessed their capability of resolving single photoelectron signals[231]. The single photoelectron resolution was measured to be 1 photoelectron or better. The magnetic field test results are summarized in Fig. 85. The longitudinal field is perpendicular to the face of the PMT and is labeled as B_z . The transverse field orientations, perpendicular to the sides of the PMT are shown as B_x and B_y . The PMT relative output is reduced by at most 30% when being exposed to a longitudinal magnetic field up to 400 Gauss. Our studies of the single photoelectron response in magnetic fields indicated that these losses happen mostly at the amplification stage on the dynode chain making it possible to compensate for this effect with external amplifications. These results are very encouraging as they suggest that the effect of the magnetic field component which is the hardest to shield, the longitudinal one, could be compensated by simple shielding and additional external amplifications. The degradation of the PMT output in transverse magnetic fields is more pronounced, up to 90% at 180 Gauss but this field component is easier to shield.

The magnetic shield incorporating the light collection cone would reduce the solenoid magnetic field at the PMT location to a few tens of Gauss which would lead to only a few percent of gain loss. We have done some magnetic field simulation and prototype testing with two thin layers of low carbon steel to achieve the shielding results needed. More can be done by adding another thin mu-metal layer and carrying out a proper annealing treatment of materials for further optimization.

9.4 Gas and Gas System

The HGC uses the heavy gas C_4F_8 as its radiator gas. It is stable, non-toxic, non-flammable, non-explosive, odorless and non-reactive except with alkali metal halides. Being a perfluorocarbon

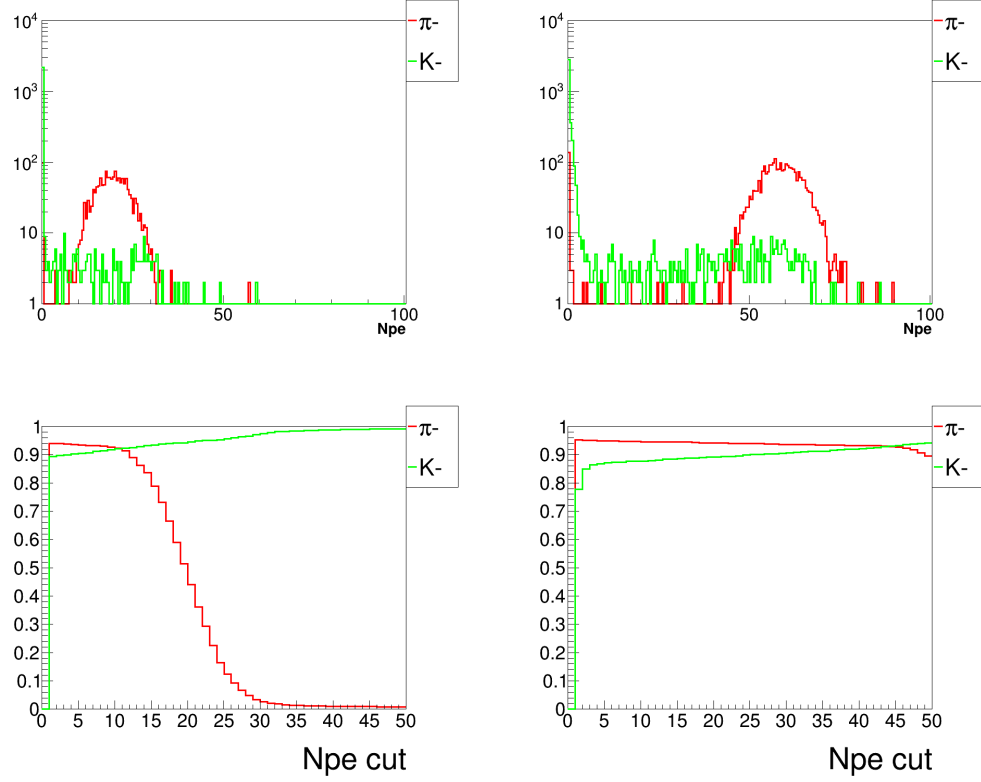


Figure 84: Number of photoelectrons (top) and pion detection efficiency and kaon rejection factor (bottom) are shown in two configurations of $2.5 < P < 3.0$ GeV and $8^\circ < \theta < 9^\circ$ (left) and $7.0 < P < 7.5$ GeV and $14^\circ < \theta < 15^\circ$ (right). Pion results are in red color and kaon results are in green color. For pion efficiency, it's plotted as it is. For kaon rejection, it's plotted as $(1-1/\text{rejection})$ so that the results can be compared together easily.

compound, it is implicated as having a long atmospheric lifetime and high global warming potential. Following the ESH&Q policy, we will minimize its use with a recycling gas system and keep a record of the quantity used. It is relatively inexpensive and commonly available from many suppliers. A recent test in Summer 2019 using the SHMS HGC in Hall C at JLab, which is also sensitive to photons above 200 nm, has shown that the C_4F_8 performance with additional $\sim 10\%$ pressure is comparable to the commonly used heavy gas C_4F_8O .

The total volume of the detector tank is $\sim 20 \text{ m}^3$ and it will be filled with $\sim 350 \text{ kg}$ C_4F_8 gas. With a boiling point of -6°C and a vapor pressure of 2.5 atm at 20°C , C_4F_8 does not require special handling to remain in gas state under the operating condition, namely 1.7 atm absolute pressure and 20°C , which is the JLab Hall A nominal condition. The detector is hermetically sealed to allow for containment of the radiator gas without the need of circulation during operation. A gas system including filling, returning and purifying unit will be used to recycle the gas. It is similar to the existing JLab Hall B heavy gas system, except it can handle the 1.7 atm pressure. During the filling process, the system will initially be purged using nitrogen gas to avoid contamination from the oxygen and water vapor in the air. Then the nitrogen gas will be purged by the radiator gas. The pressure of the gas will be monitored by pressure gauges and a regulation system will be incorporated to maintain the tank at the desired pressure. After use, the gas can be purged out with the nitrogen gas and collected by a buffer tank before being sent into the purifying unit. The purifier

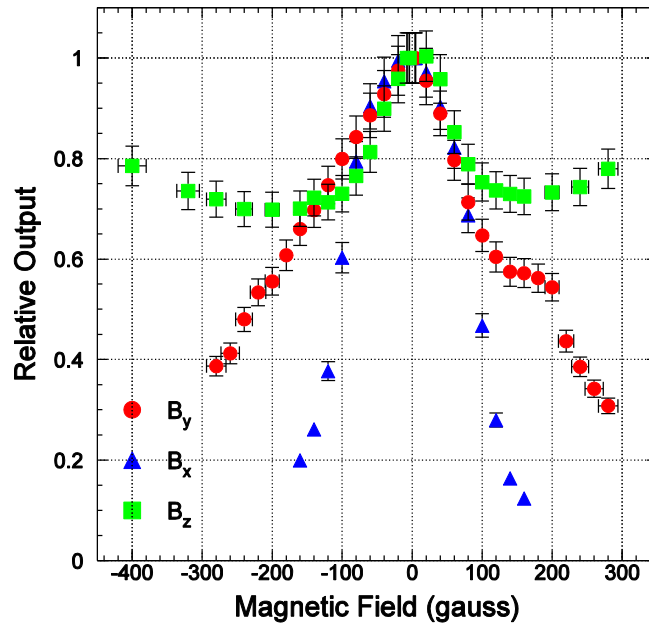


Figure 85: Relative output of the H8500-03 PMT in magnetic fields. The PMT output normalized to the zero magnetic field configuration is shown for a longitudinal field orientation (i.e. perpendicular to the face of the PMT) in squares and for the transverse orientations (i.e. perpendicular to the sides of the PMT) in circles and triangles.

consists of a molecular sieve to remove moisture and particulates from the gas and a liquid nitrogen cooled condenser to separate nitrogen and the heavy gas. The purifying unit of JLab Hall B heavy gas system has been recently upgraded to have recovery efficiency $> 90\%$. It can be shared between Hall A and Hall B because they both operate on demand and have buffer tanks.

10 Electromagnetic Calorimeter

10.1 Overview

Electromagnetic calorimeters (EC) are used in the PVDIS, SIDIS and J/ψ experiments to measure the energy deposition of electrons and hadrons, and to provide particle identification (PID). The SIDIS and J/ψ experiments share similar configurations and is referred to as the SIDIS configuration in this document. The PVDIS experiment uses all modules in the forward angle (PVDIS FAEC) to detect the scattered electrons; in the SIDIS configuration, calorimeter modules are divided into the forward angle (SIDIS FAEC) and the large angle (SIDIS LAEC), both detect the scattered electrons while the FAEC also provides MIP triggers for pions. For electron detection, the dominant background comes from electro- and photo-produced pions. The desired performance is summarized in Table 14 and the EC geometry in Table 15. Please note that the EC geometrical coverage is slightly larger than other detectors because the edges of the EC are expected to have degraded performance due to shower spreading. The total coverage area of the SIDIS FAEC and LAEC is less than that of the PVDIS FAEC. The plan is to share modules between the two configurations, thus all modules need to be rearranged when switching between the PVDIS and SIDIS configurations.

	Desired performance
π^- rejection	$\gtrsim[50:1]$
e^- efficiency	$\gtrsim 90\%$
Energy resolution	$< 10\%/\sqrt{E}$
Radiation resistance	$\gtrsim 400$ kRad
Position resolution	$\lesssim 1$ cm

Table 14: Overview of the SoLID calorimeter desired performance.

	PVDIS FAEC	SIDIS FAEC	SIDIS LAEC
z (cm)	(320, 380)	(415, 475)	(-65, -5)
Polar angle (degrees)	(22,35)	(8,15)	(16.3, 24)
Azimuthal angle	Full coverage		
Radius (cm)	(110, 265)	(98, 230)	(83, 140)
Coverage area (m ²)	18.3	13.6	4.0
Total number of channels	≈ 1830	≈ 1360	≈ 400

Table 15: Geometrical coverage for the SoLID electromagnetic calorimeters. The z direction is along the electron beam and the origin is at the solenoid center. The approximate total numbers of channels are based on 100 cm² lateral granularity per module, see Section 10.2.3 for details.

The design of the SoLID ECs is determined by both the physics goal and the expected running conditions. The design is challenging due to unique constraints including high radiation background (≈ 400 kRad, as in Table 14), strong magnetic field (1.5 T on SIDIS LAEC), large coverage area, and cost. These factors prevent the use of many traditional calorimeter technologies, including NaI (TI), CSI, BGO and lead glass because of their low radiation resistance; PbWO₄, LSO and PbF₂ because of their high cost; and lead/scintillating fiber calorimeter because of the high cost and the large amount of light readout required. We decided to use the so-called shashlyk design [242] that combines relatively high radiation hardness with a reasonable cost. It is a robust technology that

has been used by many experiments such as LHCb and ALICE.

Due to the PID requirement, it is necessary to segment the EC longitudinally into a preshower and a shower detector. We borrowed heavily from the LHCb ECal design, but with geometry and sampling ratio tuned for SoLID: the preshower detector is made of a layer of lead as a passive radiator followed by scintillators, embedded with WLS fibers for readout [243, 244]. The shower section consists of shashlyk modules with a Pb:scintillator ratio of 1:3. Details of the design are summarized in Tables 16 and 17.

Type	passive radiator + sensitive layer
Passive radiator	$2X_0$, Pb
Sensitive layer	2 cm, plastic scintillator 100 cm ² hexagon tile
Light transportation	WLS fiber embedded in the scintillator

Table 16: SoLID electromagnetic calorimeter, preshower design.

Type		Shashlyk sampling calorimeter
Each layer	Absorber	0.5 mm Pb
	Scintillator	1.5 mm plastic scintillator
	Gap	Reflective paper (or other material), 0.12 mm \times 2 sheets
	Radiation Length	$0.093X_0$
Overall	Radiation length (X_0)	2.4 cm
	Molière radius	5 cm
	Length	$18 X_0$, 43.4 cm
	Total number of layers	194
	Lateral granularity	100 cm ² hexagon
	Light transportation	WLS fiber, 100 per module, penetrating layers longitudinally

Table 17: SoLID electromagnetic calorimeter, shower design.

The structure of both the preshower and the shower detector is illustrated in Fig. 86. In the experiment, particles are incident close to perpendicular to the scintillator-lead layers. Scintillation light is absorbed, re-emitted and transported to the photon detector by wave-length shifting (WLS) optical fibers penetrating through the shower modules longitudinally, along the incident particle direction. The cross sectional area of the shower modules was optimized to be 100 cm² (see Section 10.2.3), with a hexagon shape that simplifies the swapping between two configurations. The scintillator tile of preshower modules has the same 100 cm² hexagon shape to match the shower modules, which maximizes PID efficiencies. The lead absorber of the preshower can be made of large sheets.

Simulations were used to study the performance and optimize the design of the key specifications while minimizing the cost. Figure 87 shows the simulated shower of a 3 GeV electron incident on the PVDIS EC. In the following we will present details of the shower and the preshower design, general layout and the support system, light readout, expected radiation dose, PID and trigger performance, and a cost estimate.

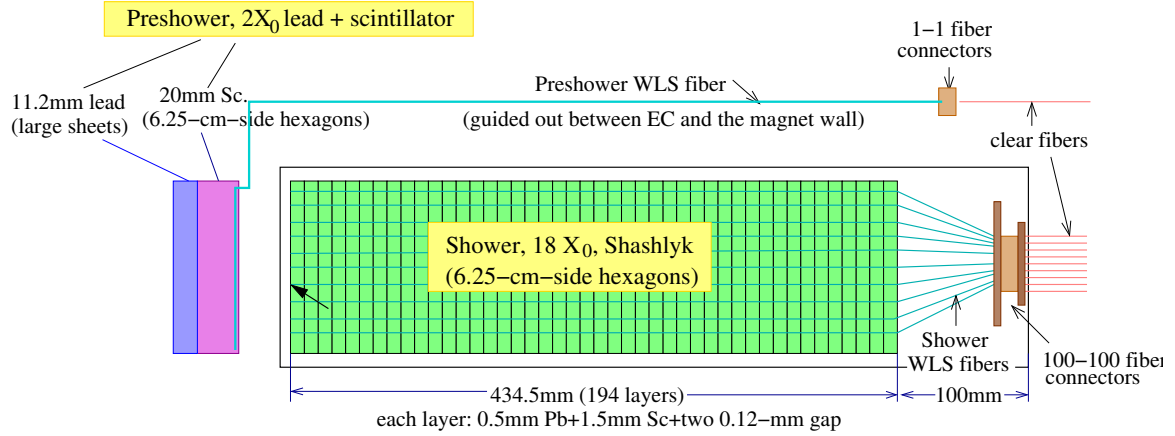


Figure 86: Design diagram of the SoLID electromagnetic calorimeter module. Spacing between the preshower and the shower detectors, and the spacing between the shower module and the 100-100 fiber connectors, need to be kept as small as possible yet still allow for safe routing of the WLS fibers and positioning of the support structure.

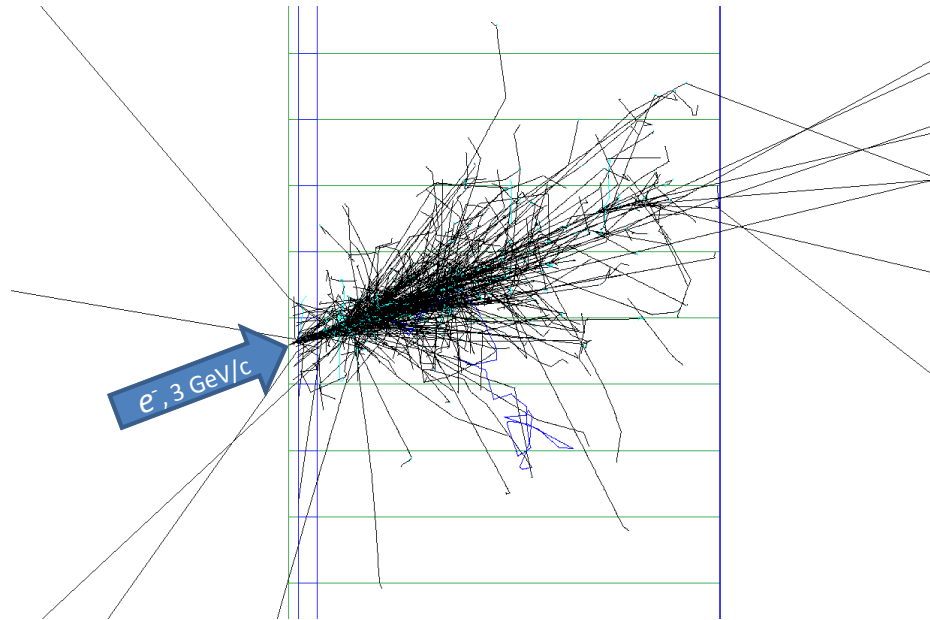


Figure 87: GEANT4 simulation of the shower generated by a 3-GeV electron incident on the PVDIS calorimeter. The black and green tracks are secondary photons and electrons respectively. The green horizontal lines are edges of calorimeter modules. The first two layers of materials are the preshower detector, consisting of $2X_0$ of lead and 2 cm thick of scintillator. The shower maximum is found at a depth about $5-6 X_0$ from the front of the module.

10.2 Shower Detector Design Considerations

10.2.1 Total Length of the Calorimeter

The overall length of calorimeter should be long enough to enclose most of the electromagnetic shower and short enough to maximize the difference in energy deposition between electrons and pions. The fraction of energy leakage for electron showers, averaged inside the acceptance of the SIDIS-Forward calorimeter, was studied for different total lengths of calorimeter. As shown in Fig. 88, a total length of 20 radiation lengths was found to be a good balance, limiting the energy leakage to $(1 - 2)\%$. Considering the 2-radiation-length thickness of preshower, this leads to a shower detector length of 18 radiation lengths or 43.4 cm.

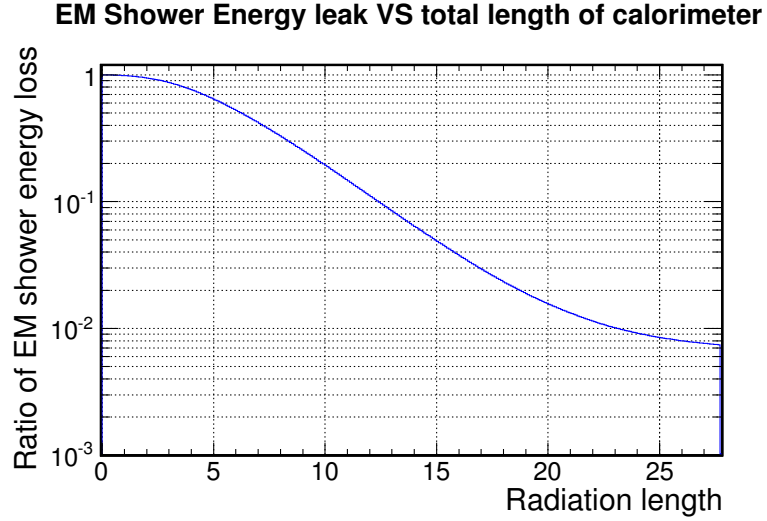


Figure 88: Fractional energy leak for an average SIDIS-Forward electron shower vs. different total length of the calorimeter.

10.2.2 Sampling Ratio

Each layer of the shower module consists of a 1.5 mm-thick scintillator plate and a 0.5-mm absorber plate made of lead. A Pb absorber thickness of 0.5 mm or less is favored to provide a fine sampling and therefore better energy resolution. The thickness of the scintillator plate should be thin enough to ensure fine longitudinal sampling, while thick enough to reduce light attenuation in the lateral direction. A thickness of 1.5 mm was chosen following the experience of previous Shashlyk designs used by the KOPIO experiment [242, 245], the PANDA experiment [246], and the COMPASS-II experiment. The COMPASS module is shown in Fig. 89. A gap of 120 μm is kept between the lead and scintillator plates to accommodate a sheet of high-reflectivity paper, which reduces the loss of scintillation light.

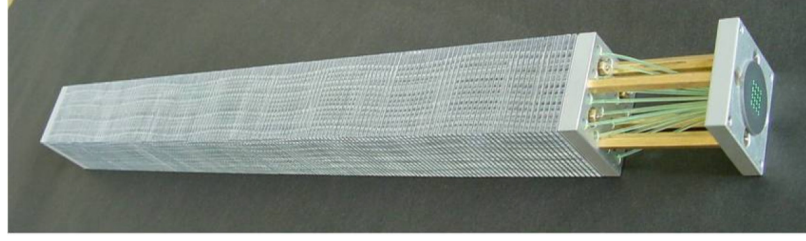


Figure 89: COMPASS-II Shashlyk calorimeter module. This illustrates the basic design of shashlyk modules: each module consists of alternating scintillator and lead (or other absorber material) layers, with WLS fibers penetrating across all layers to guide out the scintillation light signal. Four stainless steel rods are used to fix all layers together and support the whole module.

Figure 90 shows the simulated energy resolution using the chosen configuration of 1.5 mm scintillator and 0.5 mm lead. A resolution of about $4\%/\sqrt{E}$ is achieved.

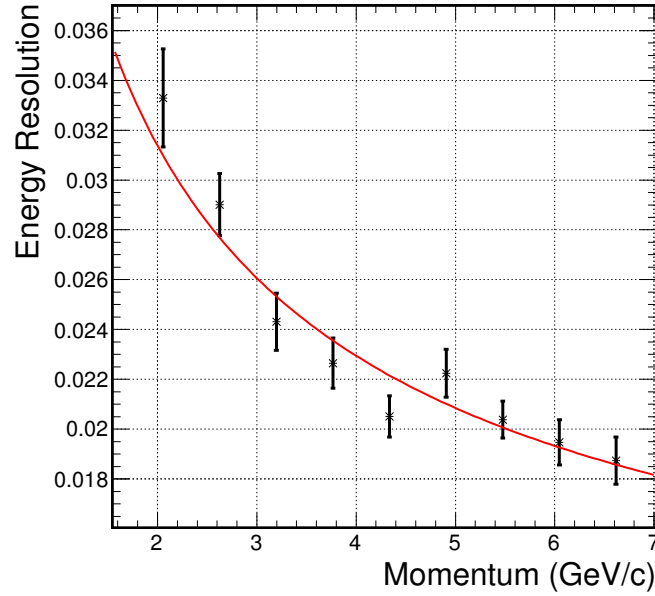


Figure 90: Simulated energy resolution of the SoLID calorimeter using both the Preshower and the Shower. The error bars are statistical error of the simulation. This simulation was performed without background to demonstrate the intrinsic PID performance of the EC. Simulation results including the background will be presented in section 10.7.

10.2.3 Lateral Size

A smaller lateral size for calorimeter modules leads to better position resolution and lower background. However, it will also increase the total number of modules and readout channels, leading to higher overall cost. The study shows that a lateral size of about 100 cm^2 will provide a good balance between position resolution, background and the overall cost as shown in Fig. 91. A hexagon lateral shape is favored by the layout.

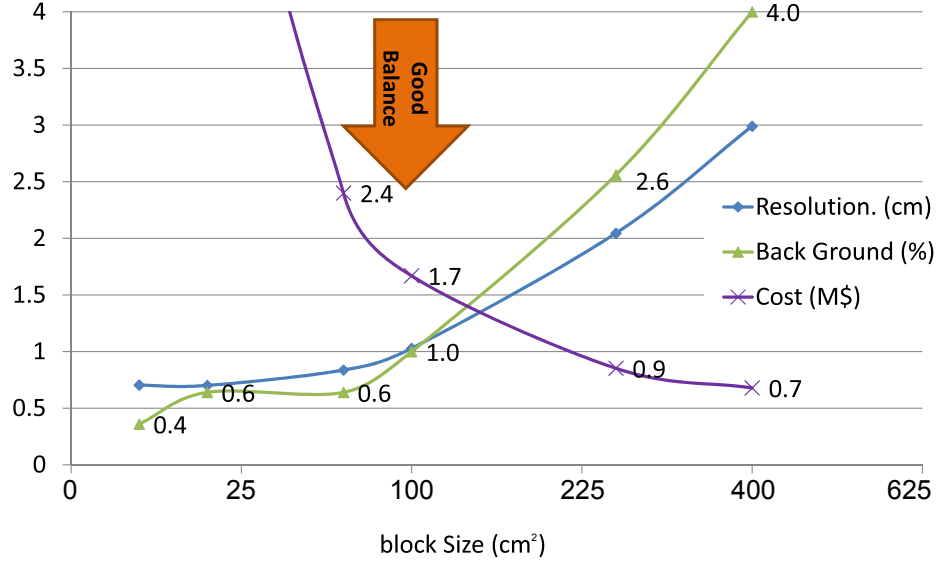


Figure 91: Position resolution and background level from simulation and the cost of the shower detector vs. lateral block size of the module.

10.3 Preshower Detector

Segmenting the EC longitudinally into a preshower and a shower part is essential to reaching the required pion rejection. Two designs were considered for the preshower detector: a full Shashlyk-type design that is optically isolated from the shower detector, and a passive radiator/scintillator pad design as used in the HERMES [243] and LHCb [244] experiments. Comparing to a Shashlyk-type preshower, the passive radiator/scintillator pad design has several advantages including increased radiation hardness, simplicity in construction, and fewer WLS fibers to read out. Separating preshower from shower completely also means one can repair or replace the preshower portion independently of the shower. For a passive radiator of $2X_0$, the impact on overall energy resolution is less than $0.5\%/\sqrt{E}$ for electrons with momentum larger than 2 GeV/c. Therefore, the passive radiator/scintillator pad design was adopted for the preshower detector. Details of the design are as follows:

- The thickness of the preshower radiator was determined by optimizing the overall pion rejection at the desired electron efficiency. As shown in Fig. 92 (top), the preshower-alone pion rejection improves as the radiator thickens up to $3.5X_0$ due to immediate development of the electromagnetic shower. However, the impact on the overall energy resolution degrades with increased thickness of the absorber. A thickness of $2X_0$ for the radiator was found to be an optimal choice for the SoLID application.
- The scintillator and readout design is similar to that of the LHCb experiment [244]: WLS fibers are embedded in one 2 cm-thick scintillator pad to absorb, re-emit and conduct the photons for readout.

With the above configuration and assuming a response of 100 photoelectrons per MIP (see next paragraph), the relation between pion rejection and electron efficiency for preshower alone can be plotted as a function of scintillator energy cuts, as shown in Fig. 92 (bottom right). One can see a pion rejection of better than 5 : 1 can be achieved at an electron efficiency of $> 94\%$.

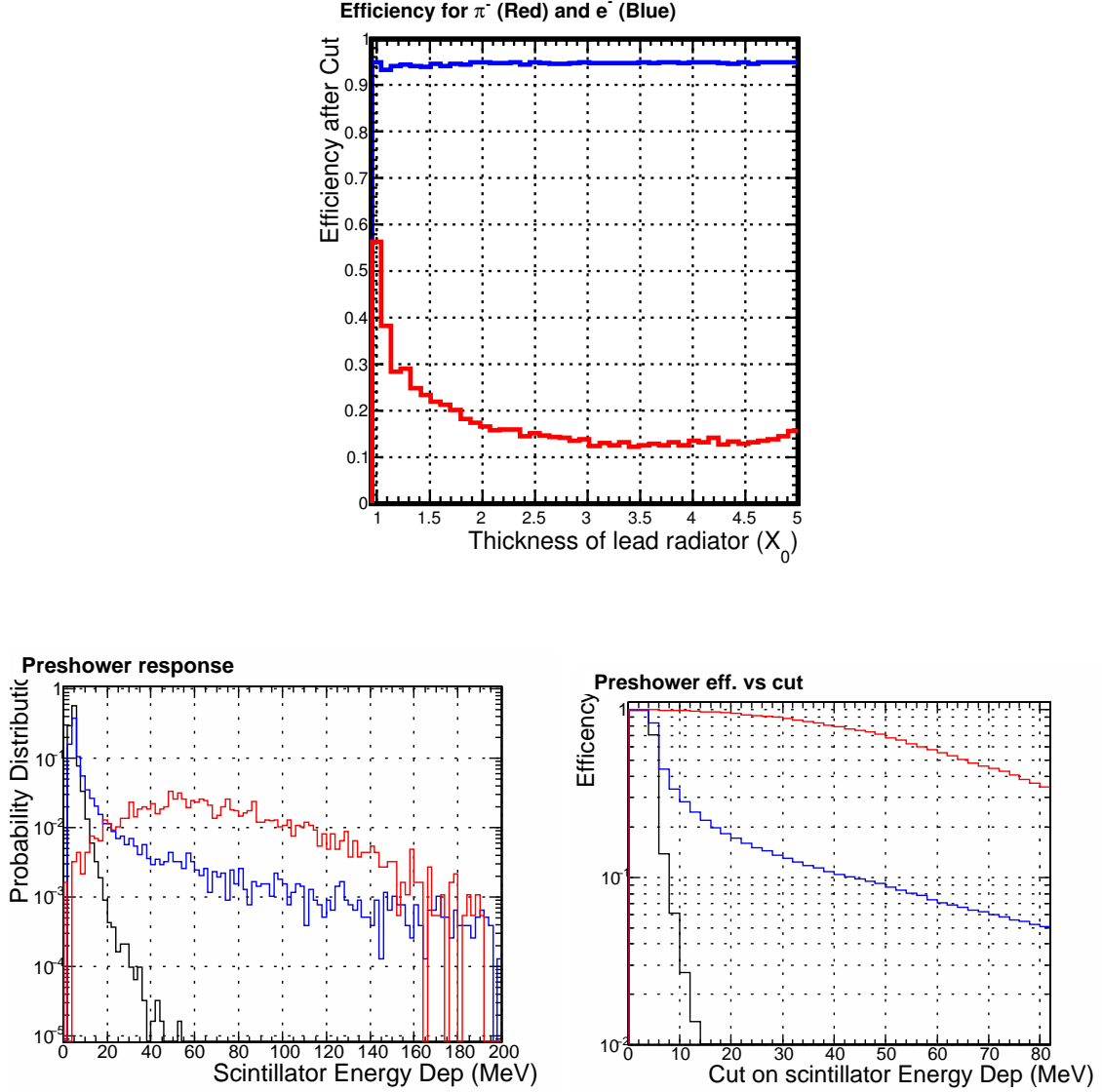


Figure 92: Simulated performance for the preshower detector. Top: $1/(\pi^- \text{ rejection})$ (red curve) at a 95% electron efficiency (blue curve) vs. different thickness of the lead radiator. Bottom: Energy deposition in the scintillator (left) and detector efficiency vs. energy deposition cut (right), for electrons (red), π^- (blue) and μ^- (black), for a preshower consisting of $2X_0$ of lead radiator and 2 cm of scintillator.

Figure 93 shows pictures of the LHCb preshower tile (left) compared to a SoLID preshower prototype made by IHEP (right). Preliminary cosmic tests show that we can achieve up to 50 photoelectrons per MIP by embedding two 1.5-m long, 1-mm diameter Kuraray Y11(200)S WLS fibers in the circular groove on the preshower scintillator. The use of multiple fibers allows minimizing the attenuation due to WLS fiber length. The final number of photoelectrons that reaches the PMT will depend further on loss in the fiber connector and the attenuation in the clear fiber. Current simulation assumes a preshower response of 100 photoelectrons per MIP, and studies of how the number of photoelectrons affects the PID performance are ongoing.

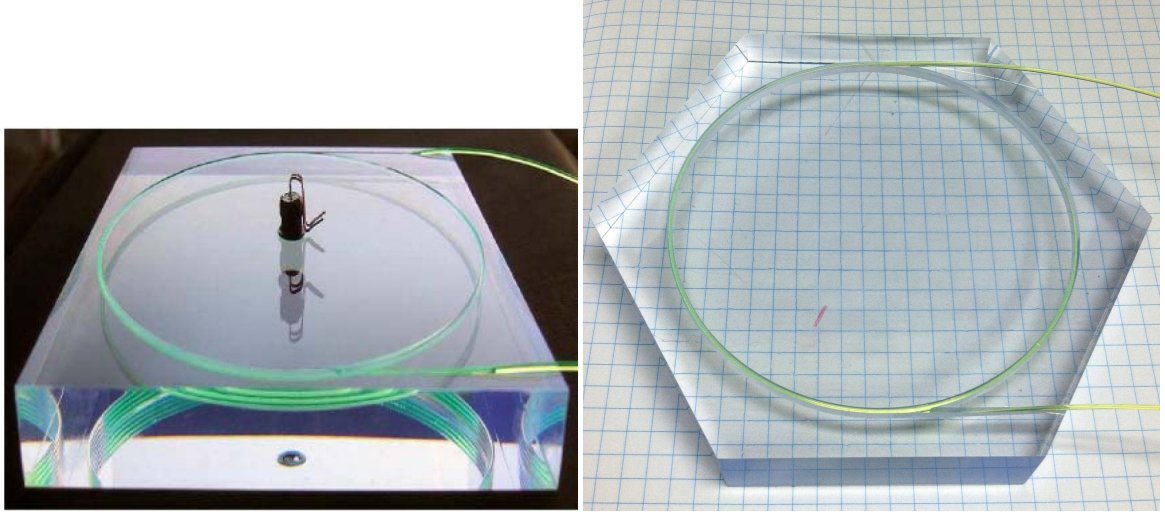


Figure 93: Preshower scintillators. Left: LHCb preshower tile ($12 \times 12 \times 1.5$ cm) [244]. A single WLS fiber is embedded in a circular groove for 3.5 turns. In the middle of the tile is an LED for testing purposes. Right: SoLID preshower prototype made by IHEP. The SoLID prototype has a geometry of 6.25-cm-side hexagon and is 2 cm thick. Shown here are two 1-mm diameter WLS fibers embedded in a 9-cm diameter circular groove, each 2.5 turns.

10.4 Layout and Support

The total area of the PVDIS EC is slightly larger than that of the SIDIS ECs. The modules will be re-arranged between the two configurations, where modules from the PVDIS FAEC will be split and re-arranged into the SIDIS FAEC and LAEC. The SIDIS EC layout must preserve the 2-fold rotation symmetry in the spectrometer, and it is convenient to have the same symmetry for the PVDIS configuration as well. The design layout that meets these requirements is shown in Fig. 94 for the PVDIS configuration. The forward angle support system is shared by PVDIS and SIDIS FAEC, and the SIDIS LAEC will have a separate support system.

The scintillator tiles of the preshower modules will be mounted on an aluminum plate that simultaneously supports also the $2X_0$ lead. For shower modules, the lead and the scintillator layers in each Shashlyk module are held together by six stainless steel rods penetrating longitudinally through the module. The modules are terminated by two aluminum endplates. The six rods protrude from the endplates and are supported by two aluminum support structures, one 2 cm thick plate between preshower and shower, and one 4 cm thick plate behind the shower. The support structure also holds the optical fiber connectors (see next section).

10.5 Light Readout

For both preshower and shower, the blue light from scintillators is converted into green light by WLS fibers embedded in or penetrating through the modules. Each preshower tile will use two WLS fibers with 1 mm diameter, each fiber arranged for two turns and embedded in a groove on the surface of the tile. The preshower WLS fibers will be routed using the space between preshower and shower to the space between EC and the solenoid wall. Each shower module will use 100 1 mm diameter WLS fibers arranged along the direction of the particle trajectory, and the fibers will be guided directly towards the back of EC. To avoid light loss over long distances, WLS fibers will be connected immediately to clear fibers using one-to-one connectors for readout by PMTs.

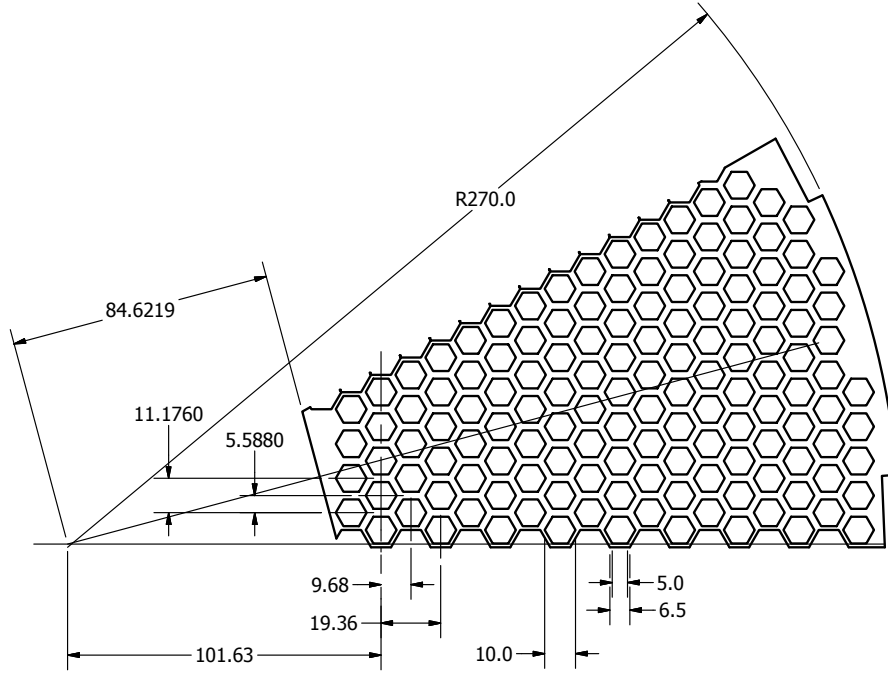


Figure 94: Layout of the hexagon-shaped modules with their support for a 30-degree wedge of the FAEC for the PVDIS configuration. The number of modules is 138 full modules plus 9 half-modules along the horizontal line. If counting 147 modules per 30-degree wedge, the total number of modules needed is 1764. We use 1800 modules for planning purposes at this stage.

LHCb used homemade fiber connectors. For SoLID, homemade connectors is an option but we have tested fiber connectors from the Japanese Fujikura company and found they work well. The Fujikura connectors were used by the Minerva experiment and their tests indicate the light loss in the connector is in an acceptable range of (10-20)% [248].

For the preshower it is essential to achieve a high photoelectron yield such that the best PID performance can be reached. We chose the Kuraray Y11(200) fiber because it has better mechanical properties and further a small minimal bending radius, as shown by the ATLAS Collaboration [247], which is crucial for us because our preshower fiber groove has a bending radius of 4.5cm. Our tests show the Bicron BCF91A fiber has similar light loss to Y11 but the light output is reduced by a factor of two when it is embedded in the preshower groove (compared to nearly zero loss for the Y11). The Y11 fiber has also been tested to higher radiation dose than Bicron BCF91A fibers by ATLAS [249]. For shower modules, the fibers are straight and hence the Bicron BCF91A WLS fiber becomes a more economical choice while still satisfying the requirement on radiation hardness. Bicron BCF92 fiber has faster decay time but gives less yield than BCF91A, and is not being considered here.

The magnetic field reaches about 1.5 T behind the SIDIS LAEC and a few hundred gauss behind both the PVDIS and SIDIS FAECs. For other experiments such as those at JLab Hall D or at LHC, silicon photomultipliers (SiPMs) are used. However, our simulation shows the radiation background behind the calorimeter is at the level of 10^{13} cm^{-2} 1 MeV equivalent neutrons. Studies done by the LHCb on their tracker upgrade [250] reported cooling the SiPM can overcome the radiation damage from a high neutron background. Still, projecting from the LHCb study tells us for SiPM to work for the shower detector, we need to cool to -70 or -80 °C. The space limitation alone imposed

by the SoLID magnet makes such cooling nearly impossible, let alone the necessary electronics for temperature control. Therefore, our current default design is to use PMTs. Long clear fibers (about 1.5 m for the SIDIS FAEC and 3.5 m for the SIDIS LAEC) will be used to guide the light from the WLS fibers to PMTs located outside the solenoid region.

We will use one PMT per shower module to read out the 100 fibers. We plan to design custom PMT bases so that preamplifiers with a $\times(2-5)$ gain can be used and to minimize the aging of the PMTs. For preshower modules we plan to use multi-anode PMT (MaPMTs), with all four fiber ends from each module read out by one pixel of the MaPMT. For MaPMT, the high background of the SoLID running condition constrains us to a relatively low gain in the range of $5E3-2E4$, due to the fact that the total anode current needs to be kept at only a fraction of the maximum specification to reduce the aging of the MaPMT. We plan to design pre-amplifiers with gain up to 50 and 16-channel MaPMTs. Note that LHCb used 64-ch MaPMTs at a gain of $5E3$ combined with a front-end electronic board that provided an intrinsic gain of about 10, and our current design is based on and is consistent with the LHCb readout method.

10.6 Radiation Effects

The ECs for the SoLID spectrometer are designed for high luminosity experiments. The expected luminosity and run time are 169 PAC-days at $10^{39} N \cdot \text{cm}^{-2} \text{s}^{-1}$ in the PVDIS configuration, 245 PAC-days at $10^{37} N \cdot \text{cm}^{-2} \text{s}^{-1}$ for the SIDIS experiments and 60 PAC-days for the J/ψ experiment. In the current design, the maximum radiation dose on the active material — scintillator and WLS fibers — in the calorimeter is significantly reduced by the use of the $2X_0$ lead plate in the preshower, and the lead blocks described in section 6 for the PVDIS configuration. Because of the use of lead blocks, the PVDIS configuration has been divided into higher and lower photon flux regions; each consists of thirty 6-degree azimuthal regions.

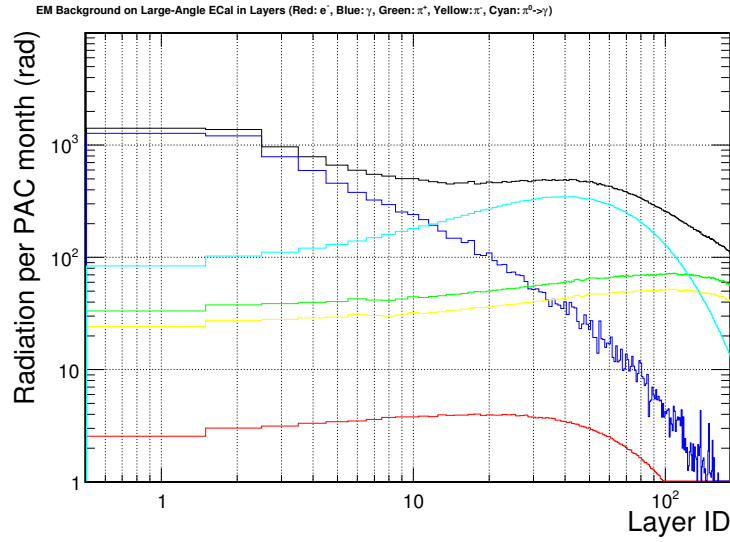
The radiation dose inside the calorimeter was simulated using GEANT4 based simulations considering a wide range of energy and species for the background particles. The dose rates for the active material (scintillators and fibers) are shown in Figs. 95 and 96. The highest radiation region is at the front part of the calorimeter, including the preshower scintillator pad and the front scintillators of the Shashlyk calorimeter modules. The maximum integrated radiation level for the active material reaches 100 kRad for the PVDIS experiment and 20 kRad in the SIDIS and J/ψ experiments, which leads to a total radiation dose of less than 200 kRad for all approved experiments. Experience from LHCb shows light yield of their preshowers reduce by factor two at 200 kRad and factor five at 2 Mrad. Our own irradiation tests of preshower prototypes showed similar results at 200 kRad. While we are confident the current design will last 200 kRad, studies of the effect on the detector performance with reduced light yield is on-going.

10.7 Performance

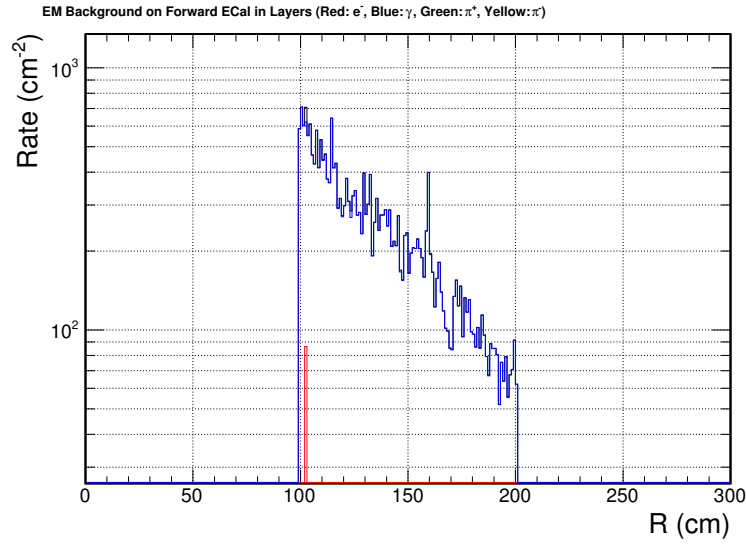
The EC system plays multiple roles in the SoLID spectrometer. Its performance was evaluated in the GEANT4 based simulation and discussed in this section, including PID performance, trigger capability and shower position resolution. A realistic background simulation was set up to evaluate the calorimeter considering a wide range of species and momenta of the background particles.

10.7.1 Intrinsic electron-pion separation

As a baseline, the PID performance was first evaluated without the background. The primary track is propagated through the SoLID magnetic field in GEANT4, then enters the calorimeter. A local cluster which consists of the central calorimeter module and six neighboring hexagon-shaped

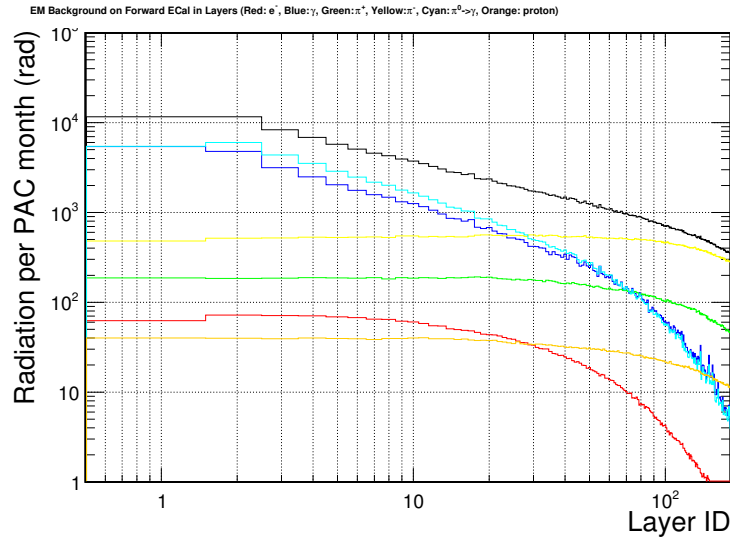


(a) SIDIS large-angle calorimeter

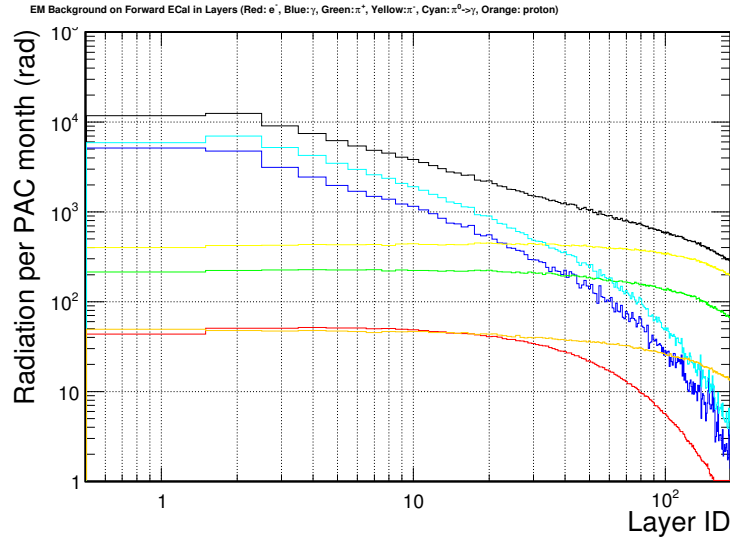


(b) SIDIS forward-angle calorimeter

Figure 95: SIDIS radiation dose rates per PAC month in each layer of the scintillator tiles in the calorimeter. Layer ID 1 is the preshower scintillator. The rest of IDs are assigned for each scintillator layer in the Shashlyk calorimeter in the order of increasing z . The color code stands for different contributions of various particle species at the front surface of the preshower: electrons (red), photons (blue), EM total (magenta), π^+ (green), π^- (yellow). The overall dose is shown by the black curve.



(a) PVDIS calorimeter in higher-photon flux region



(b) PVDIS calorimeter in lower-photon flux region

Figure 96: PVDIS radiation dose rates per PAC month in each layer of the scintillator tiles in the calorimeter. Layer ID 1 is the preshower scintillator. The rest of IDs are assigned for each scintillator layer in the Shashlyk calorimeter in the order of increasing z . The color code stands for different contributions of various particle species at the front surface of the preshower: electrons (red), photons (blue), EM total (magenta), π^+ (green), π^- (yellow), and protons (brown). The overall dose is shown by the black curve.

modules is formed. With a multidimensional cut of the preshower and shower response within the cluster (see Sec. 10.7.5), the overall pion rejection averaged over the acceptance of each calorimeter is shown in Fig. 97. A 100 : 1 pion rejection at 95% electron efficiency is achieved for momentum bins of $p > 2 \text{ GeV}/c$. For the lowest momentum bin $1 < p < 2 \text{ GeV}/c$, which is only needed for the SIDIS FAEC, a better than 50 : 1 pion rejection at 90% electron efficiency is obtained.

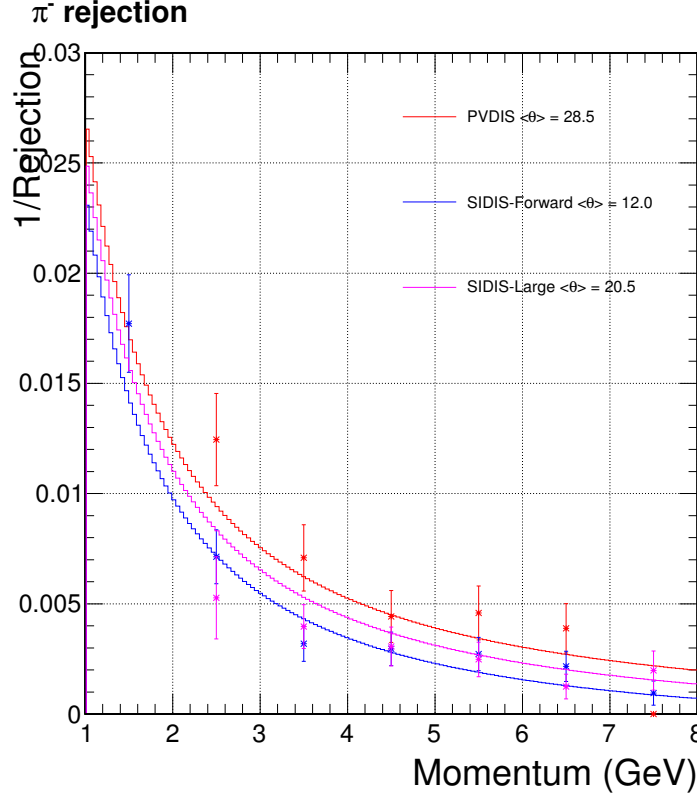


Figure 97: SoLID EC intrinsic (without background) π^- efficiency ($1/\text{rejection}$). From top to bottom: PVDIS with average track polar angle $\langle\theta\rangle = 28.5^\circ$ (red), SIDIS LAEC with $\langle\theta\rangle = 20.5^\circ$ (magenta) and SIDIS FAEC with $\langle\theta\rangle = 12.0^\circ$ (blue). A constant 95% electron detector efficiency is maintained for $p > 2 \text{ GeV}/c$. A 90% electron efficiency is maintained for the lowest momentum bin $1 < p < 2 \text{ GeV}/c$, which is only required for the SIDIS FAEC. The $\langle\theta\rangle$ value is different for the three calorimeter configurations, which leads to slight differences in the pion rejection curves.

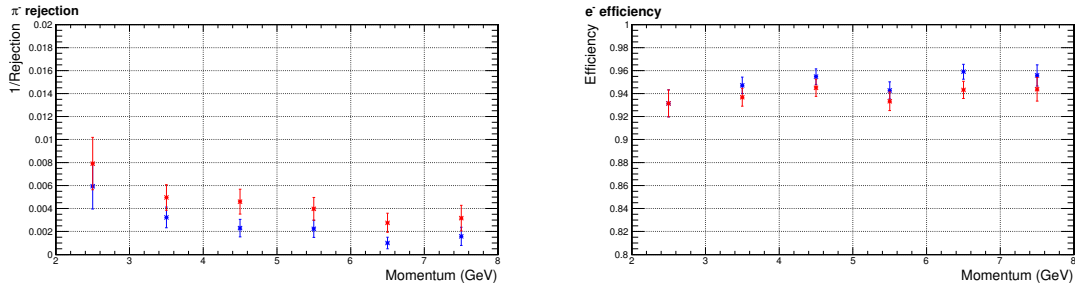
10.7.2 PID performance under realistic background simulation

For a large intensity device, background particles and their influence on the calorimeter performance have to be considered. A full background simulation was implemented to study calorimeter performance. The background simulation procedure is as follows:

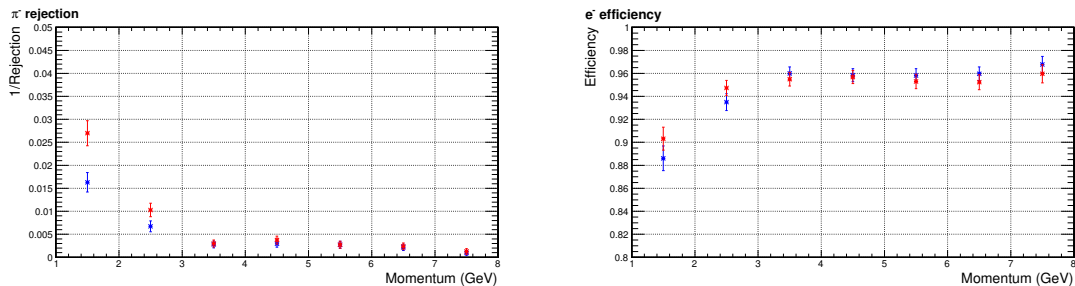
1. Particles are generated at the target including photons and electrons from the low energy EM processes (based on physics in GEANT4), DIS electrons (based on CTEQ6 PDF), and hadrons (based on Pythia, MAID and SAID);

2. Particles are propagated through a SoLID GEANT4 simulation to the front surface of the calorimeter;
3. The EC response is simulated for a wide range of background particles — electrons, photons, pions, and protons — within the momentum range $10 \text{ keV} < p < 11 \text{ GeV}$. A statistical model is used for the correlation between preshower and shower responses;
4. The background contribution to each event is produced by combining the background rate at the EC front surface and the EC response described above for a region of interest on the calorimeter, usually defined by a radius-azimuthal angular bin. A conservative 30 ns coincidence window between background particles and the primary event is assumed.
5. The background contribution is embedded into the raw signal from the simulated primary particles (high energy electrons and pions). The background-embedded data are then analyzed as raw ADC signals. The energy response is calibrated and PID and trigger performance are analyzed.

Typically, background rate is the highest in the inner radius region and drops by approximately one order of magnitude in the outer radius region. Figure 98 shows the EC performance for the SIDIS configuration in the inner radius region. For SIDIS experiments, effects from background particles are visible but not significant: for large-angle EC, the pion rejection remains better than 100:1 for all momentum bins; for forward-angle EC, there is no noticeable change in the PID performance other than for the lowest momentum bin $1 < p < 2 \text{ GeV}/c$ where the pion rejection is a half of the no-background case. However, the Cherenkov detector provides high PID performance in the low momentum range and the overall pion rejection is sufficient for the experiment.



(a) SIDIS large-angle calorimeter



(b) SIDIS forward calorimeter

Figure 98: Calorimeter pion and electron efficiency without (blue) and with (red) the consideration of background particles for the inner radius region (highest background) for the SIDIS configuration.

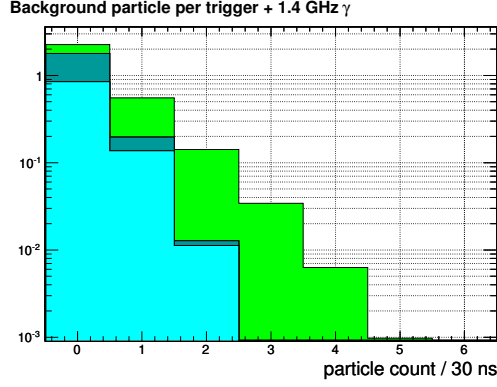
In the PVDIS configuration, the background rate is significantly higher and the performance is affected. The 30-fold structure of the baffle system for the PVDIS experiment causes the background to alternate between high- and low-rate 30 times in the azimuthal direction. Therefore, calorimeter performance is studied for the high- and the low-rate “slices” separately, with each fan-shaped slice covering 6 degrees. Background structure for the inner-radius, high-rate slice is shown in Fig. 99. The PID performance with the background is evaluated for different radius, see Fig. 100. Comparing to the intrinsic performance of Fig. 97, the pion rejection is up to 8 times worse: the pion rejection varies from 25–50 at $p = 2.5 \text{ GeV}/c$ to 50–100 at $p = 6 \text{ GeV}/c$, while keeping the electron efficiency to be in the range (90–95)%. Particle identification for the experiment will need to rely on a full-waveform analysis of the EC, combined with information from the Cherenkov detector.

10.7.3 Trigger capability

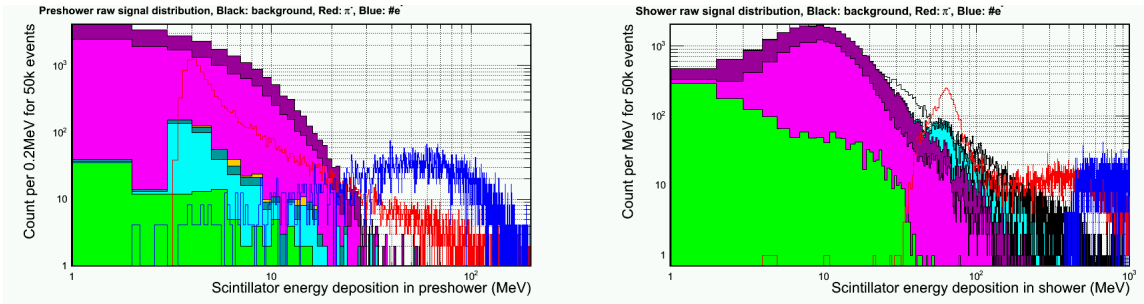
Trigger capability is an important function of the EC. The calorimeter shower energy deposition in all combinations of local 6+1 clusters (central block plus six neighboring hexagon blocks) is first summed after digitization, forming local shower sums. Triggers are then formed by passing the local shower sums through a threshold cut. Electron triggers are formed with a targeted electron threshold, and the efficiency curves for both pions and electrons are studied with the full-background simulation. The following triggering specifications have been studied:

- SIDIS large angle calorimeter: electron triggers of 3 GeV are formed by cutting on local shower sum larger than 2.6 GeV. The trigger turn-on curve is shown in Fig. 101. High electron efficiency is observed for electrons above the threshold. The rejection on few-GeV pion background is high, in the range (20-100):1, which satisfies requirement of the SIDIS experiments.
- SIDIS forward calorimeter: position dependent electron triggers provide high trigger efficiency for electrons of $Q^2 > 1 \text{ GeV}^2$. The pion rejections with 1 GeV threshold is shown on the left plot of Fig. 102. With higher thresholds, pion rejections are better.
- SIDIS forward calorimeter: MIP triggers allow the calorimeter to trigger on hadrons for the SIDIS measurement. The threshold is determined by MIP peak position minus two sigma of the Landau fit of the distribution, which lead to a calibrated local shower sum energy of 220 MeV. The trigger efficiency for pions is high, as shown on the right plot of Fig. 102.
- PVDIS forward calorimeter: electron triggers are formed with radius-dependent trigger thresholds. As shown in Fig. 103, the targeted electron threshold varies from 1.5 GeV at outer radius to 3.8 GeV at inner radius on the calorimeter, which produces high trigger efficiency for DIS electrons with $x > 0.35$. The trigger turn-on curves are evaluated for several regions on the calorimeter as shown in Fig. 103. The efficiency for both electrons and pions are lower for inner radius regions due to the use of high thresholds for background-suppression. Overall the pion rejection at the trigger level is > 2 and varies with the radius.

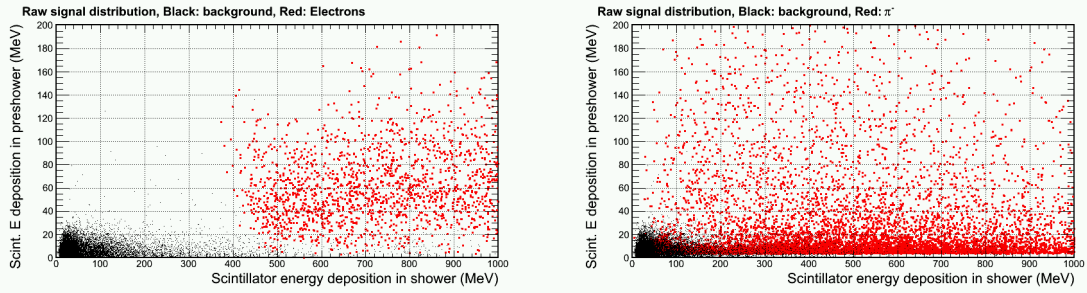
The PVDIS experiment will run with a luminosity up to $10^{39} \text{ cm}^{-2}\text{s}^{-1}$. A baffle system is used to reduce the very high background rate expected at this luminosity. To further reduce the rate from high energy photons from neutron pions and low energy backgrounds, fan-shape lead blocks, each covering 2.5 degrees azimuthally, will be placed in front of the EC. The trigger of PVDIS will be formed by taking the coincidence between the EC and the gas Cherenkov detector. Estimation of the trigger rate from EC can be performed using the realistic background simulation (described



(a) Stacked probability to find the number of background π^- (light blue), π^+ (dark blue) and electrons (green) at the front of the preshower. The photon rate is as high as ~ 1.4 GHz, thus the photon count is off-scale and not shown in this figure.

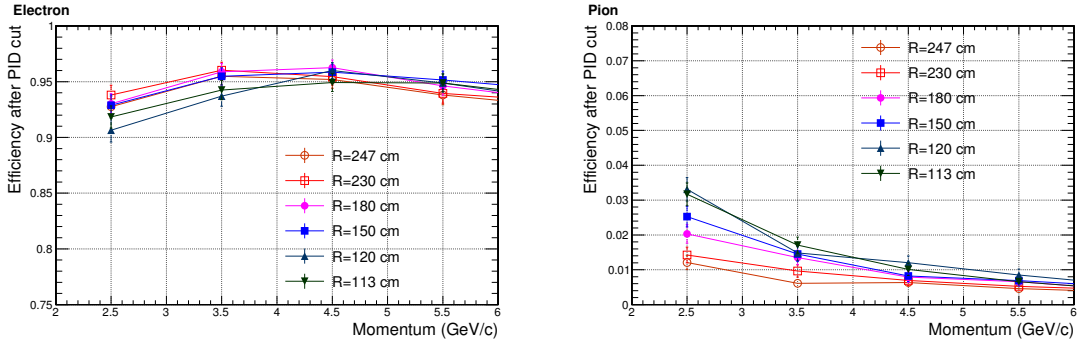


(b) Stacked probability (count per 50k events) vs. Preshower (left) and Shower (right) scintillator energy deposition for incoming background electrons (green), π^- (light blue), π^+ (dark blue), protons (yellow), EM process-originated photons (magenta) and π^0 -originated photons (dark magenta). For comparisons, energy deposition for high energy pion (red) and electrons (blue) are shown as non-filled curves.

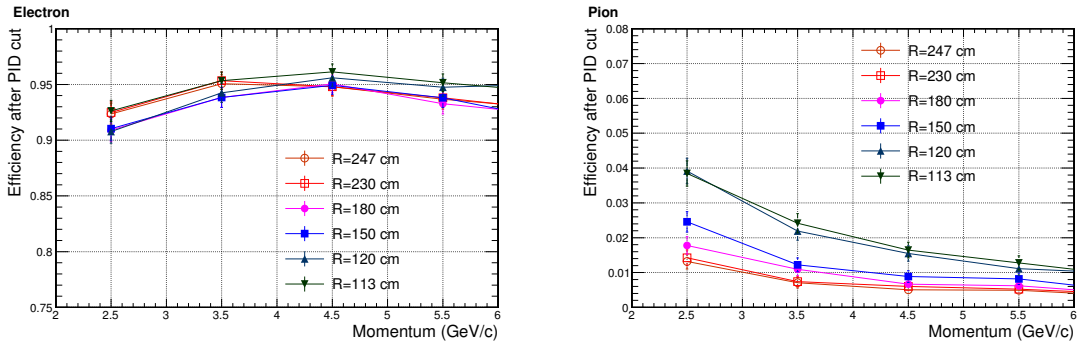


(c) Preshower-shower scintillator energy correlation for background particles (black), compared with high energy electrons (left, red) and pions (right, red)

Figure 99: Background distribution for the PVDIS forward calorimeter at the production luminosity of a liquid deuteron target. Background for the inner radius ($R \sim 1.2$ m) and higher-radiation azimuthal region is shown. The energy deposition originated from background is compatible to that of high energy pions.

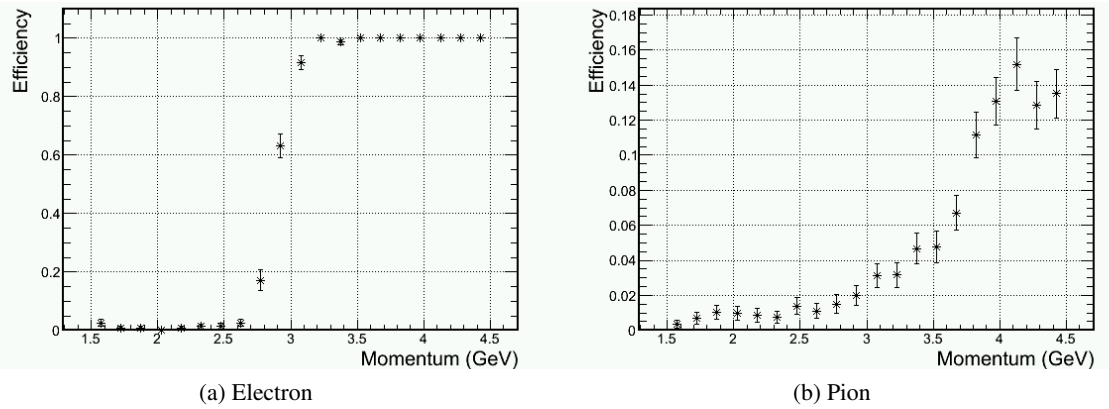


(a) lower-radiation azimuthal region



(b) higher-radiation azimuthal region

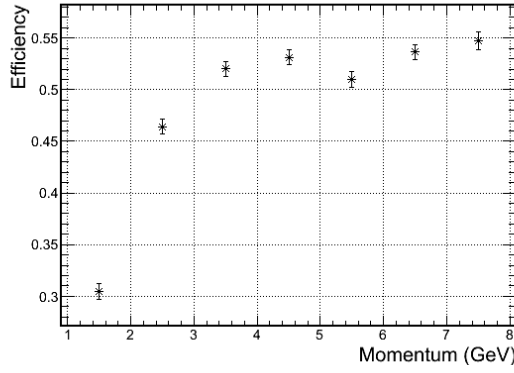
Figure 100: Calorimeter pion and electron efficiency for the PVDIS experiment, evaluated with the presence of background at eight typical regions on the calorimeter.



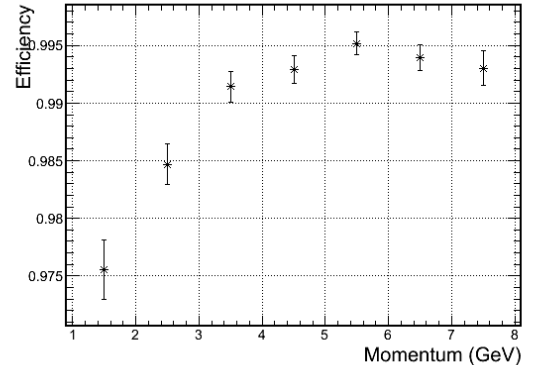
(a) Electron

(b) Pion

Figure 101: Trigger efficiency for electrons (a) and pions (b) for the SIDIS large angle calorimeter. The target trigger threshold is approximately $P_e = 3 \text{ GeV}/c$. Only the (high-background) inner-radius region is shown here.

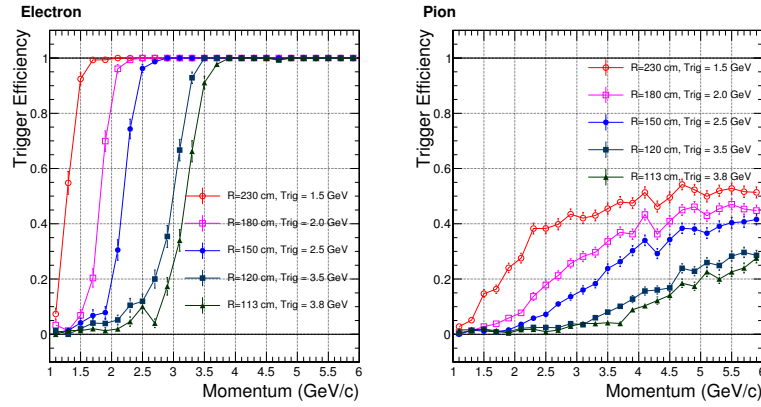


(a) Pion efficiency in electron trigger with a target trigger threshold of ($P_e = 1 \text{ GeV}/c$)

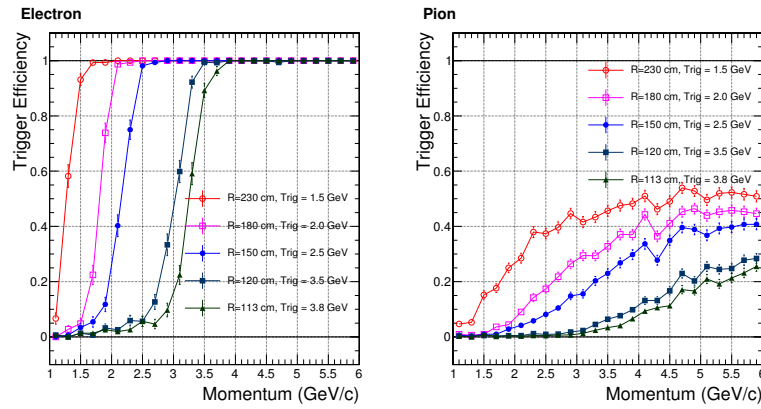


(b) Pion efficiency in the MIP trigger

Figure 102: Trigger efficiency for pions in the SIDIS forward calorimeter for electron triggers (a) and MIP triggers (b). Only the (high-background) inner-radius region is shown here.



(a) Higher-radiation azimuthal region



(b) Lower-radiation azimuthal region

Figure 103: Trigger efficiency curves for the PVDIS configuration.

previously in Section 10.7.2) combined with EC trigger capability results described above. The EC trigger rate will then be combined with gas Cherenkov trigger rate to obtain the expected DAQ trigger rates and to make sure they can be handled by the DAQ system. For SIDIS experiments on ^3He , the luminosity will be up to $3 \times 10^{36} \text{ cm}^{-2}\text{s}^{-1}$ on ^3He target and additional about $3.7 \times 10^{36} \text{ cm}^{-2}\text{s}^{-1}$ on target glass windows. Target collimators (described previously in Section 10.7.2) will be used to reduce backgrounds from the glass windows. The SIDIS triggers are formed from EC in combination with Cherenkov, MRPC (enhanced baseline configuration) and SPD. The FAEC will also provide MIP trigger for hadron detection. Trigger rate estimation for SIDIS is carried out similar to the PVDIS case. Results for both PVDIS and SIDIS trigger rates will be presented in Section 13.

10.7.4 Shower Position Measurement

Position resolution of the shower center was studied for different lateral sizes of the calorimeter modules, as shown in Fig. 104. The radial resolution is in general worse than the azimuthal resolution because the tracks are not perpendicular to the radial direction. As can be seen from Fig. 104, with the use of proper algorithm, a position resolution of better than 1 cm is achieved for both directions at the designed lateral granularity of 100 cm^2 .

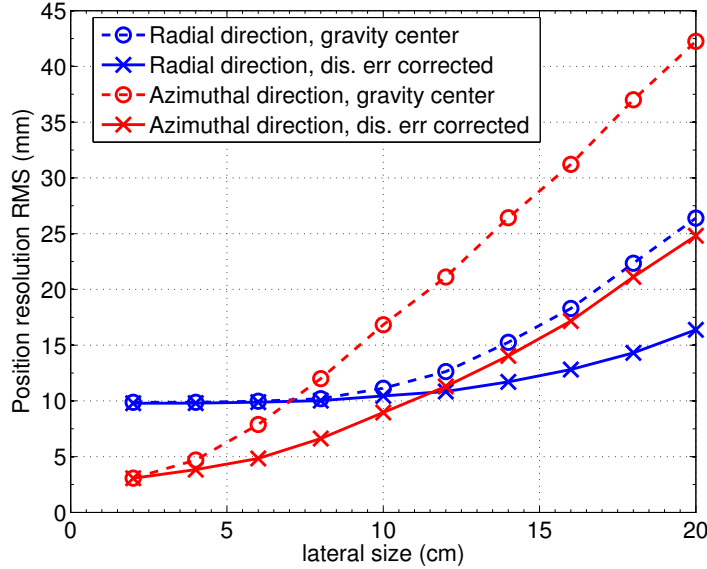
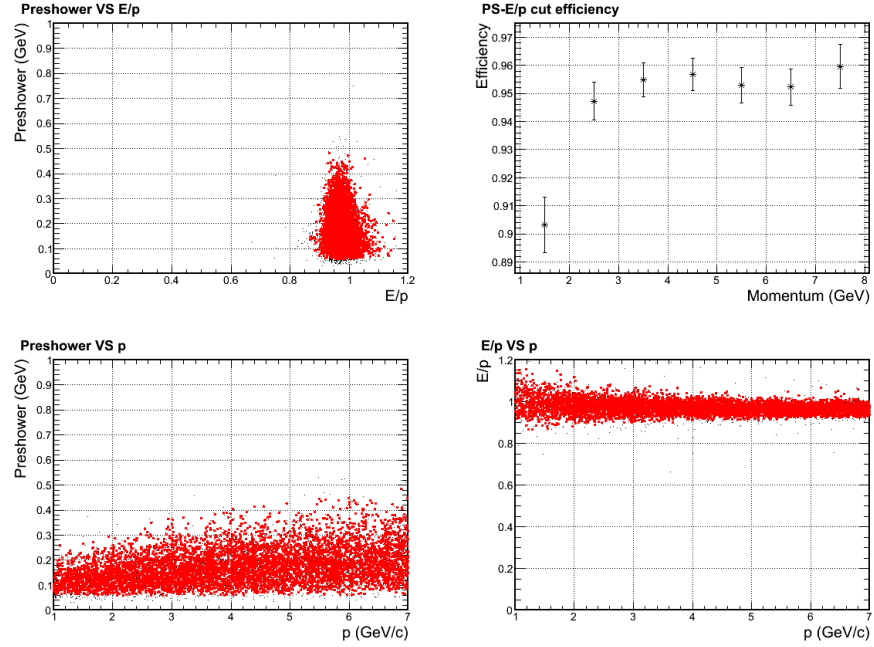


Figure 104: Position resolution for electron showers vs. different lateral size of the calorimeter module. Both azimuthal (red) and radial (blue) resolutions are shown, with the shower center calculated from a simple energy-weighted geometrical center (dashed curves), and those calculated with further corrections using the energy deposition distribution among neighboring modules (solid curves).

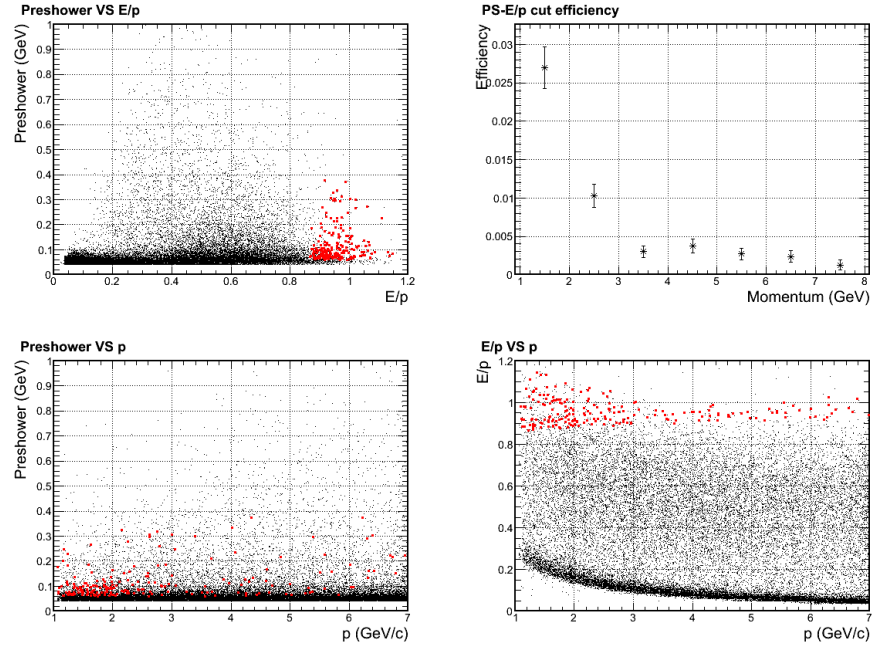
10.7.5 Supplemental Information: PID Selection Cuts

A three dimensional PID cut was used to select the best electron samples with maximal π^- rejection as illustrated in Fig. 105. For each given momentum bin, the cut on E/P and preshower energy roughly follows the contour lines of the ratio of π^- efficiency to e^- efficiency, which is the optimal

cut for the π^-/e^- separation. A momentum dependence is then introduced to the cut to maintain a constant 95% electron efficiency for most of the bins. Events passing the cut are highlighted in red in the plots.



(a)



(b)

Figure 105: Illustration of electron sample cuts as highlighted in red dots, in comparison to simulated electron (a) and π^- (b) samples. The SIDIS forward calorimeter in the high background (small radius) region is studied in these plots.

10.8 Scintillator Pad Detector (SPD) for SIDIS Experiments

The main purpose of the SPD is to reduce calorimeter-based trigger rates for high-energy charged particles (see Section 10.7.3 for calorimeter trigger capability) by rejecting photons through the coincidence between the SPD and the calorimeter. Two SPDs will be used: one in the forward direction between the heavy gas Cherenkov detector and the calorimeter, and the other in the large-angle direction immediately before the calorimeter. Both SPDs consist of fan-shaped scintillator pads arranged perpendicular to the beam direction. The LASPD will also provide time-of-flight for particle identification with a timing resolution goal of 150 ps.

The performance for the scintillator was studied in the GEANT4 simulation. For FASPD, we plan to use 5 mm thickness scintillators based on a balance between the light yield and the radiation length. The 5-mm thickness corresponds to a radiation length of $\approx 0.013X_0$ which directly affects the photon conversion rate. Typical responses of the FASPD to photons and charged particles are shown in Fig. 106. Approximately 20% of the photon background leaves energy in the scintillator due to back splashing from the calorimeter front face. The trigger threshold was set at two standard deviations below the MIP peak to ensure a high efficiency for charged particles. Pile up effects

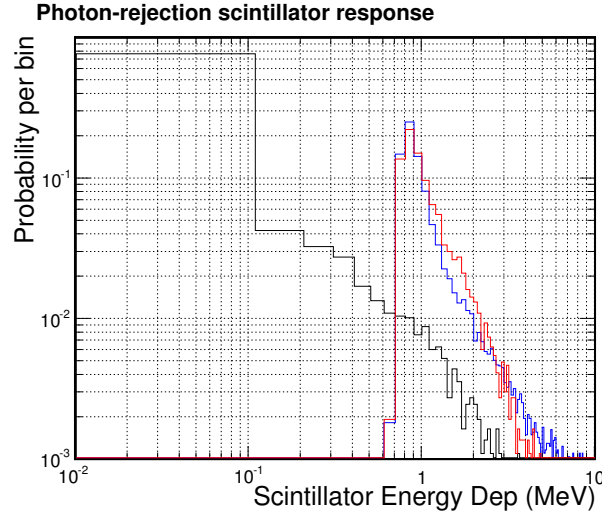


Figure 106: Typical probability for scintillator energy depositions in the SPD, for electrons (blue), pions (red) and high energy photons (black).

were studied for fixed ADC timing windows of 30 and 50 ns. The photon rejection depends not only on the trigger rate per scintillator, but also the scintillator segmentation, see Fig. 107. In addition, photons attenuate significantly in long scintillators and thus the length of the individual segmentation needs to be minimized. The segmentation of FASPD is chosen to be 240 based on Fig. 107 and a desired 5:1 photon rejection, and is arranged as 60 in the azimuthal direction and 4 in the radial direction. The readout of FASPD is by using WLS fibers embedded on the surface of the scintillator, then connected to clear fibers and are readout by MaPMTs. This is similar to the preshowers. Because the threshold is below MIP and is much lower than for preshower, a higher combined gain of PMT and the preamplifier is needed. We currently plan to use preamplifiers with gain ≈ 50 because it's the maximum comfortable gain that can be achieved on a pre-amplifier board. This will allow us to place the threshold around 20 mV, the minimal threshold that is above the noise level.

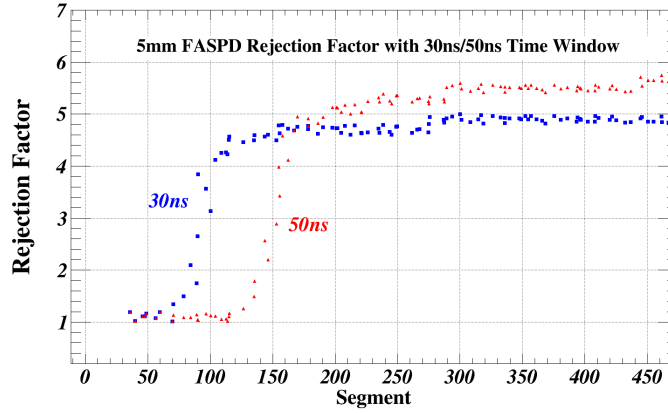


Figure 107: Photon rejection factor for 5-mm thick FASPD as a function of the segmentation, for DAQ windows of 30ns (blue) and 50ns (red), respectively. For the 30-ns timing window, a 240 segmentation is appropriate to reach a photon rejection of 5:1.

For the LASPD, a 10:1 photon rejection is desired to bring the photon-induced calorimeter trigger rate down to below the electron-induced rate. Figure 108 shows the simulated photon rejection factor vs. segmentation. The 10:1 rejection can be achieved by 60 azimuthal segments. Because the radial coverage of the LASPD is small and because of the requirement of high photoelectron statistics to reach the TOF requirement, the LASPD has only azimuthal segmentation, with each covering 6 degrees. For readout, the use of WLS fiber is impossible, again because of high photoelectron statistics. We plan to use field-resistant fine-mesh PMTs on the outer radial edge of the LASPD to readout the scintillating light.

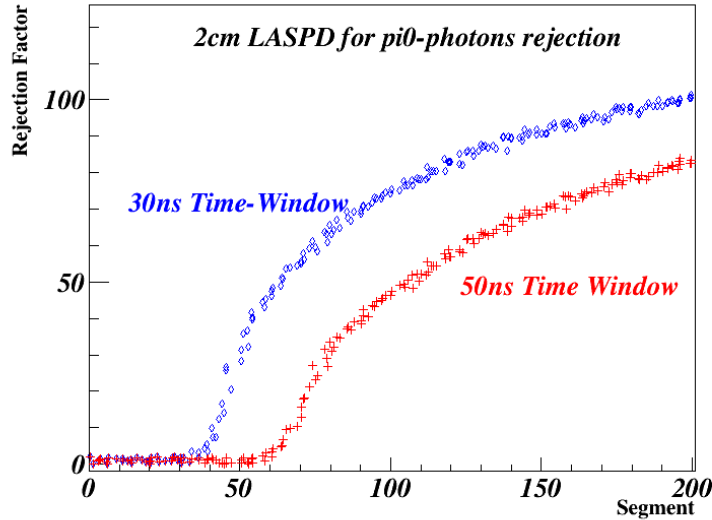


Figure 108: Photon rejection factor for 20-mm thick LASPD as a function of the segmentation, for DAQ windows of 30ns (blue) and 50ns (red), respectively. For the 30-ns timing window, a 60 segmentation is appropriate to reach a photon rejection above 10:1.

10.9 EC Collaboration and Prototyping Status and Construction Outlook

The shashlyk sampling technique adopted by SoLID EC has been used by many experiments, including LHCb, ALICE and ATLAS at the LHC. The LHC/CMS experiment's calorimeter upgrade will use a similar technique. In the R&D for SoLID EC, we studied extensively the calorimeter design and technical details from these experiments. We also learned many useful facts from other experiments and/or collaborations, including Minerva, MINOS, and JLab Hall D.

Our general design for the SPD, the preshower, and the shashlyk shower modules is based heavily on the LHCb's SPD and ECal design. The LHCb and other LHC experiment's detector TDR and associated technical notes provide tremendous knowledge. This includes: readout design for the preshower and the SPD (WLS fiber embedding in grooves on the scintillator surface and the use of MaPMTs) (LHCb); wrapping of the scintillator (LHCb, ATLAS); relative light yield between different scintillator material and WLS fiber types (LHCb); the use of optical grease or glue (LHCb); side treatment and painting of shashlyk modules (LHCb); adding mirror ends to WLS fiber (LHCb); coupling between WLS fiber and MaPMTs (LHCb); Tests of light yield uniformity (LHCb); radiation hardness of the preshower and shashlyk modules (LHCb ECal and HCal) and plastic scintillating fibers (LHCb tracker upgrade, JLab Hall D GlueX barrel ECal); LED monitoring system (LHCb); WLS fiber bending light loss (simulation by LHCb; direct data from ATLAS Tile ECal TDR); performance of SiPM under high neutron radiation background (mainly LHCb tracker upgrade, but also JLab Hall D and CMS); EC commissioning and calibration procedure (LHCb ECal and HCal); tolerance/quality control for the scintillators and fibers (LHCb).

Shashlyk-type calorimeter modules used by most previous experiments were produced by the Russian IHEP group. For some experiments, the scintillators of shashlyk modules were produced at Russian IHEP, and the modules were assembled elsewhere. For example, Wayne State University (WSU) and China Central Normal University (CCNU) both assembled modules for the ALICE experiment (for CCNU, threading WLS fiber was done in Italy, separately from the initial assembling). We contacted the WSU group about their equipment used for ALICE module assembly, but unfortunately their assembly lab was dismantled a long time ago and most equipment could not be recovered. We are also in contact with the U. of Iowa group (Prof. Onel) who is participating in the CMS ECal upgrade, but the CMS Ecal utilizes crystal layers and is very different from SoLID EC in the choice of material and the construction process.

Overall, we could not gain substantial help from groups previously involved in Shashlyk production and assembly, and complete production by the Russian IHEP group can be sensitive to fluctuations in international relationship and economics. Given this status, we are pursuing the possibility of manufacturing scintillators and assembling the Shashlyk modules in China. Two groups, Shandong University (SDU) and Tsinghua University (THU), have already produced several preshower and shashlyk modules and are testing with cosmic rays. Both groups have also developed local contact with CCNU to learn their experience in module assembly. The SDU group has extensive experience with scintillator production in China and cosmic ray testing of the scintillator's light yield, and is in a good position to lead the prototype R&D for SoLID EC. At the moment, cosmic test results show the preshower light yield is comparable to LHCb and is within expectation. Preshower prototypes from Russian IHEP and China all show similar light yield. On the other hand, we do not have a direct light yield comparison of shashlyk prototypes with previous experiments because all published values are for electron yield, while with cosmics we could only measure MIP yield. Beam test with a low energy electron beam at the Beijing IHEP is being planned.

For SPDs, prototypes for both FA and LASPD were manufactured by (US) Eljen and tested with cosmic rays by the UVa group. Results show a MIP light yield of (9-11) photoelectrons for FASPD. Simulation for the effect on SPD performance from the measured light yield is ongoing.

Cosmic results on LASPD show we can reach a ≈ 150 ps timing resolution using regular PMTs, and tests of fine-mesh PMTs up to a 1.9 T field were carried out. The PMT test results showed for Hamamatsu 16-ch MaPMT H6614-70 assembly, there is no degradation in timing resolution up to 1.5 T even though the gain has decreased by nearly a factor 100 [251]. Overall, we are confident we can construct all SPD modules for SoLID.

11 MRPC

An MRPC detector is currently being considered as an enhancement to the SoLID baseline configuration.

11.1 Overview

The Multi-gap Resistive Plate Chamber (MRPC), which will be used as the time of flight (TOF) system, is located in front of the forward-angle calorimeter. Several MRPCs have been recently used in RHIC STAR and LHC ALICE as their TOF systems [252–255] and the typical time resolution for these detectors is better than 80 ps. Most importantly, as a gas chamber, the MRPC does not need PMTs for readout so it can work inside a magnetic field. For the SoLID-SIDIS configuration, the total path length is around 8 meters from the target and the flight time is calculated by comparing the timing signal to the beam RF signal. With a time resolution of 100 ps, we can identify pions from kaons at a rejection factor of 20:1 with momenta up to 2.5 GeV/c. Compared with the MRPCs used at STAR and ALICE, the MRPC for SoLID receives a higher flux rate, approximately 10 kHz/cm². Tsinghua University has developed a new type of low resistivity glass with a bulk resistivity on the order of 10 Ω cm. The rate capability of the high rate MRPC assembled with this type of glass can reach 50 kHz/cm² [256, 257]. We propose to construct the high rate SoLID-MRPCs with this low resistive glass.

11.2 Structure of the MRPC Prototype

The layout of the MRPC is shown in Fig. 109. The inner diameter of the detector plane is about 1 meter and the outer diameter is 2 meters. The area of the disk is about 10 m². The whole detector consists of 50 super modules and each super module consists of 3 MRPC modules. There is overlap between MRPC modules and super modules to avoid blind areas.

A prototype of the MRPC has been assembled and its structure is shown in Fig. 110. This trapezoidal module is assembled with the aforementioned low-resistivity glass. The module has ten gas gaps and the width of each gap is 250 μ m. The outer glass is 1.1 mm thick and the inner glass is 0.7 mm thick. Colloidal graphite is sprayed on the surface of the outer glass and the surface resistivity is about 5M Ω cm. Fig. 111 shows the structure of the readout strips. Each module consists of 11 strips and the width of each strip is 25 mm with a 3 mm gap. The shortest strip is 13 cm and the longest is 17 cm. This prototype will be similar to the smallest module of the three modules in one super module. With this design, the whole detector will consist of 1650 strips, and the total number of readout channels is 3300 since each strip has readouts on both ends.

11.3 Gas system

The MRPC uses a mix of 90% R134 Freon, 5% Isobutane and 5% SF6. The gas mixture is in itself non flammable but since Freon and SF6 are green house gases we are planning for a recycling system for the gas similar to what was used for the PHENIX Hadron Blind Detector.

11.4 Cosmic Ray Test

The cosmic ray test system for the MRPC prototype consists of a cosmic ray telescope and a VME based DAQ system. The telescope consists of three 20 cm \times 5 cm \times 5 cm scintillators and two 4 cm \times 2 cm \times 1 cm scintillators. These five scintillators were used to trigger on cosmic rays. The layout of the cosmic ray telescope and the prototype are shown in Fig. 112. Two of the larger

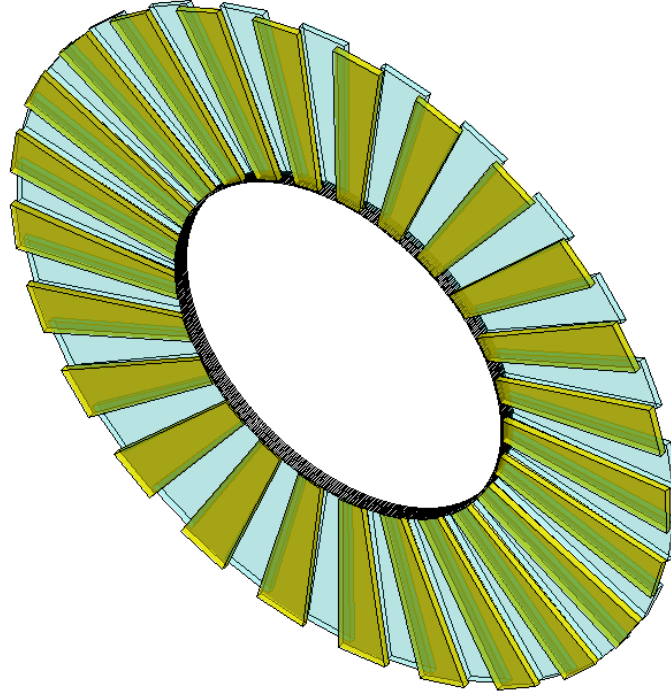


Figure 109: The layout of MRPC TOF

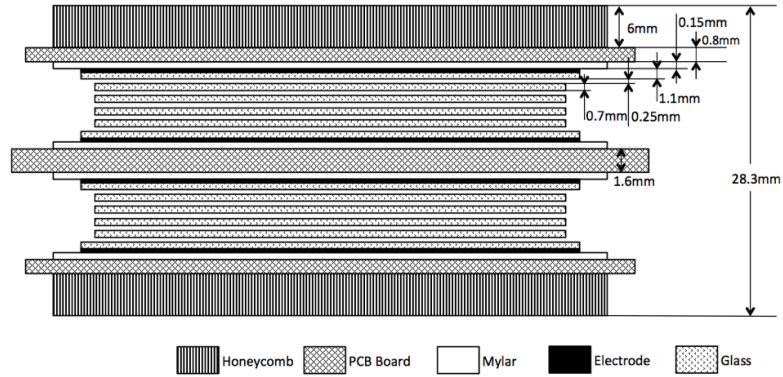


Figure 110: The structure of the MRPC prototype

scintillators and one of the smaller scintillators are above the module, and the rest are below the module. PMT0 through PMT4 were used for basic coincidence triggering and to provide the reference time. The two small scintillators are used to measure the efficiency of the module. The width of the area subtended by the small scintillators is smaller than the width of a MRPC strip. Since this module would be tested with an electron beam at JLab (see later discussion), the cosmic test is only for checking primary performance parameters, such as dark current, noise, efficiency and time resolution. With a high voltage setting of 13.2 kV, the dark current is less than 10 nA and the noise rate is a few Hz/cm². Fig. 113 shows the efficiency plateau. It can be seen that the efficiency can reach 98% and the plateau region is larger than 600 V. Fig. 114 shows the relation between charge and time after slewing correction. The time spectrum after correction is shown in Fig. 115. The

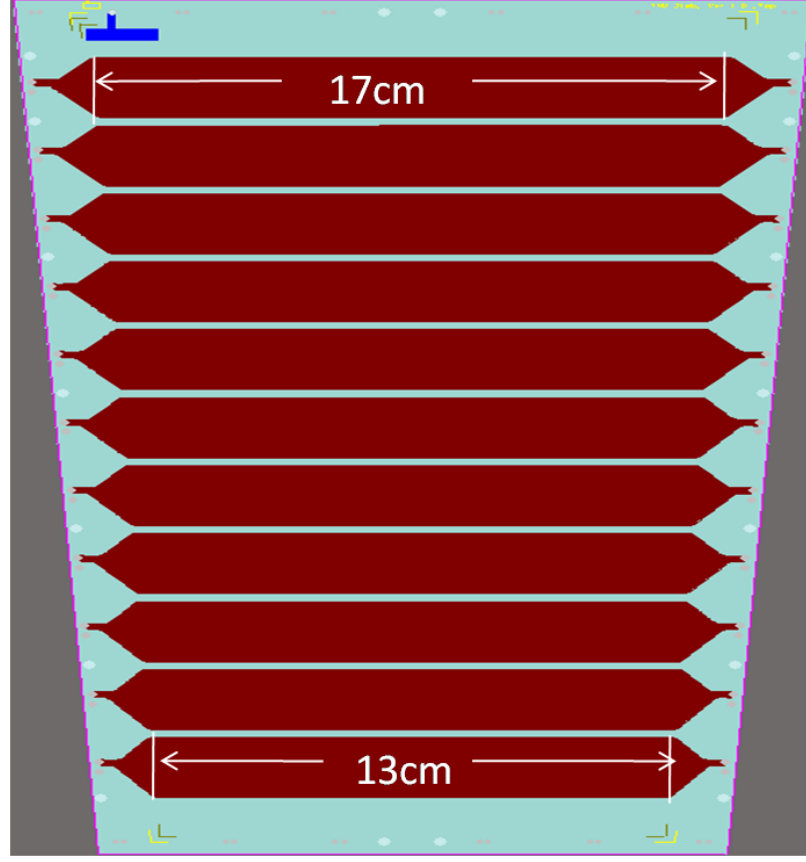


Figure 111: The structure of the readout strips

time jitter of four PMTs is 87 ps, so the resolution of the MRPC can reach 50 ps. All of these show that the MRPC module has good performance.

11.5 Beam Test at Hall A

11.5.1 Test Setup

The setup of the beam test is shown in Fig. 116. The beam was mainly for the JLab g2p experiment [258]. The MRPC test setup stood about 10 m to the side. There was an electron beam passing through the MRPC trigger system and the backgrounds were mainly soft photons, electrons and neutrons. The background intensity was stronger than the main electron beam. A thick concrete shield was used to suppress background particles striking the MRPC. A diagram of the DAQ is shown in Fig. 117. The trigger system was very similar to that of the cosmic test system. One small scintillator ($5\text{ cm} \times 5\text{ cm} \times 1\text{ cm}$) was read out by PMT 0 and each of two long scintillators ($10\text{ cm} \times 5\text{ cm} \times 1\text{ cm}$) was read out on both ends (by PMTs 1–4). The coincidence of PMT0 and PMT4 provided the trigger signal of the system. The delayed coincident signal also acted as the gate signal of the flash ADC and the stop signal of the TDC. PMT1~PMT4 provided the reference time of the system. A CAEN V775 TDC was used to record the time signal and a flash ADC, JLAB FADC 250, was used to record the charge signals. A VME scaler was used to record the time interval between two triggers. From this time interval we can get the signal rate to study the rate

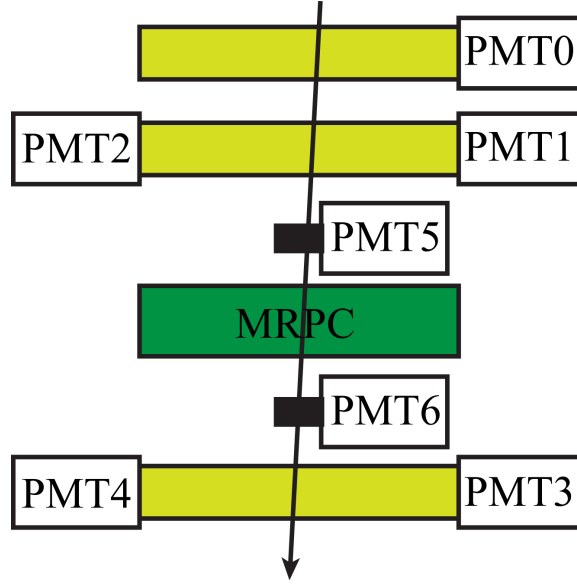


Figure 112: Layout of the test setup

capability of the detector.

11.5.2 HV Scan Result

MRPCs were conditioned under high voltage for a few hours in order to reach a stable, low dark rate working region. The electronics threshold was set to 30 mV. The dark current was less than 8 nA and the rate of the module was less than 10 Hz/cm² at 108 kV/cm. The coincidence of PMT1–PMT4 provided the T0 of the test system, with a time jitter of about 100 ps. In order to find the optimum working voltage of the counters, the efficiency and time resolution were scanned as a function of the applied voltage for a ‘low’ flux of $\bar{\phi} \sim 1\text{--}4$ kHz/cm². The results are summarized in Fig. 118. The counters showed large efficiency plateaus above 600 V, and time resolutions were as good as 75 ps. It can be seen that the time resolution obtained from cosmic rays is better than that from the electron beam test, because the time jitter of T0 in the beam test was larger than that in the cosmic test.

11.5.3 Rate Scan Result

The rate depended on background intensity. From the scaler we can get the signal rate of the MRPC. Fig. 119 shows the signal rate change with time in runs 188 and 193 respectively. The rate was not stable in each run. From these runs, we obtained different rates from 1 to 16 kHz/cm². These two runs were combined to analyze the rate performance. The results are shown in Fig. 120. It can be seen even when the flux rate reaches 16 kHz/cm², the efficiency is still higher than 94% and the time resolution is close to 80 ps. So this module meets the requirement of the SoLID TOF system.

The evolution of the charge distribution can be seen in Fig. 121 for this MRPC. The charge is obtained from the sum of its two ends. It can be seen that, with increasing flux, the average charge decreases and the spectrum shifts down to lower charges as expected.

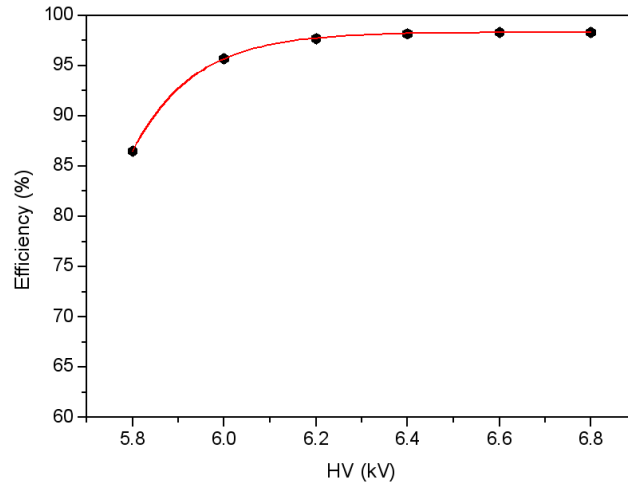


Figure 113: Efficiency plateau of the MRPC

11.6 Radiation hardness and aging

Aging and radiation hardness tests were carried out. For the low conductivity glass, no change in resistivity were seen for neutron fluence up to $10^{14}/cm^2$ as show in Figure 122. The glass was also applied with 1000V for about 32 days with integrated charge of $1C/cm^2$ (about 2 years of continuous running in SIDIS conditions), and its resistivity remained stable. The module was tested using a X-ray source. the chamber was exposed to X-ray for 35 days which corresponded to about $0.1C/cm^2$. No changes in amplitude and efficiency were observed at the end of the test as shown in Figure 123.

11.7 Conclusions

A high rate MRPC was planed to construct the time of flight system for the SoLID-SIDIS program, and a prototype has been designed and constructed. The trapezoidal prototype module assembled with low resistivity glass has 10×0.25 mm gas gaps and 11 readout strips. The width of the strips is 2.5 cm with an interval of 3 mm. This module was tested using cosmic rays and also tested using electron beams in Hall A of JLab. The results show its rate capability of larger than $16 \text{ kHz}/cm^2$. This module has a very promising time resolution. The time resolution can reach 50 ps in cosmic test and is about 75 ps in the beam test. The chambers behaved very stably during the test. A detailed aging study was performed to assure the stability over a long running time. The performance of the prototype meets the requirement of the SoLID-TOF system.

11.8 R&D Plan for Better Time Resolution

A R&D effort by the Chinese collaboration, jointly for SoLID, sPHENIX and EIC, for the next generation MRPC aims at 20 ps resolution. Tsinghua University has developed a prototype and obtained 17 ps results on the bench. Beam tests and design finalization of both the detector and electronics will be done in about a year.

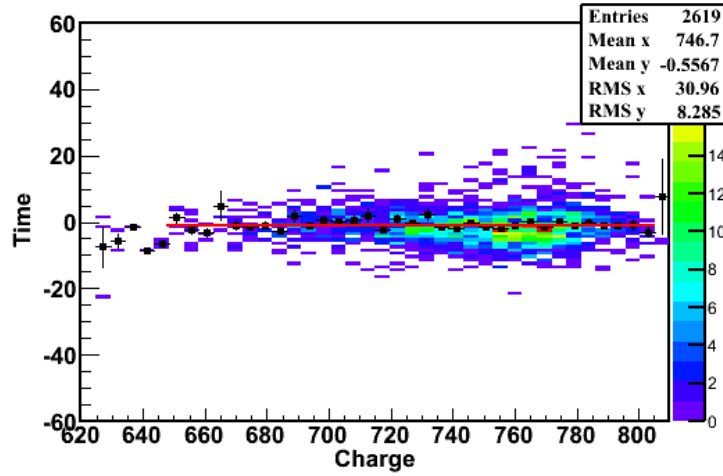


Figure 114: The relation between charge and time after slewing correction

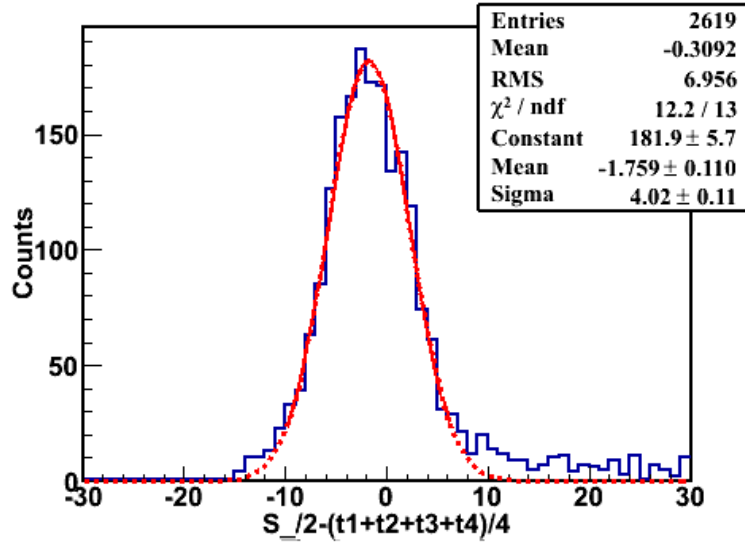


Figure 115: Time spectrum after correction

Obtaining good timing resolution also depends on the electronics including both preamplification of signals and digitization. The EIC R&D at BNL is using 7 GHz bandwidth TI LMH5401 [195] amplifiers for preamplifiers. Tsinghua University is also developing its own amplifier chip which could drive lower costs and allow for a more compact footprint for the electronics with a multichannel amplifier chip.

New sampling electronics, development of which is being motivated by MCP PMTs, can reach picosecond level timing resolution for multi-photons. The system is based on Switched Capacitor Arrays (SCAs), which continuously samples the detector signal on a circular array of capacitors.

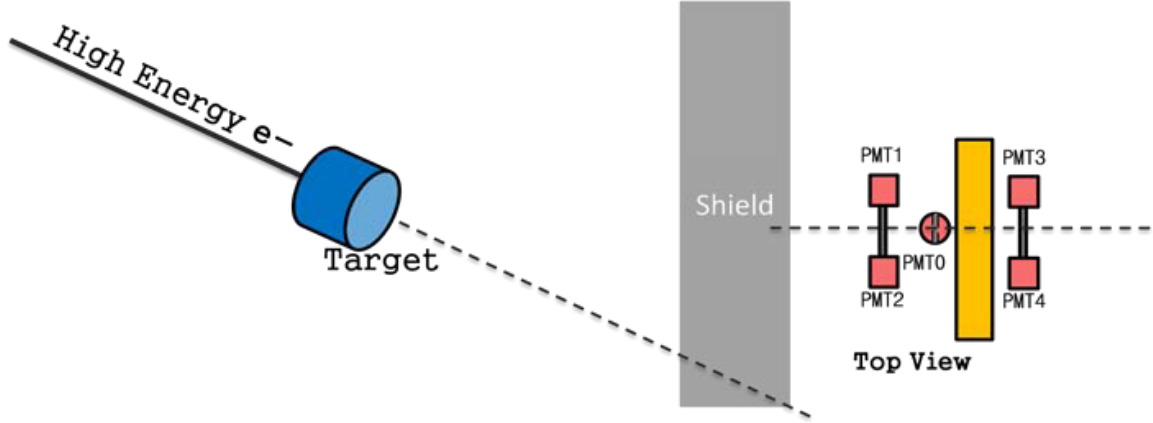


Figure 116: Setup of beam test in Hall A

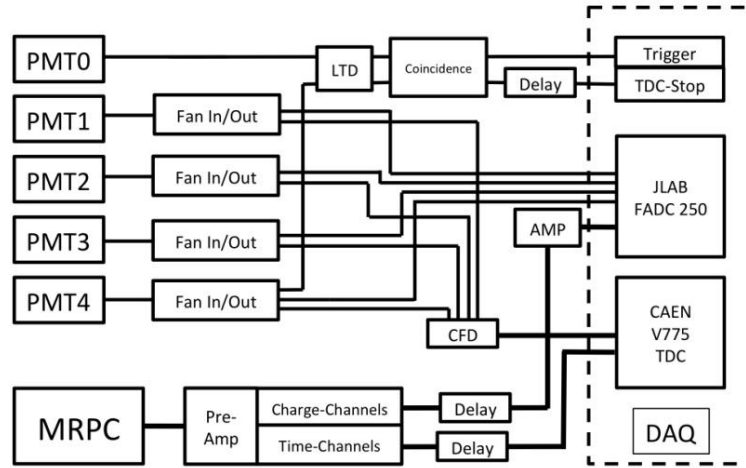


Figure 117: Diagram of the DAQ system

Sampling frequencies up to 10 GSamples/s have been reached. With a good calibration, a timing resolution of 1 ps has been achieved. The following Table 18 summarizes the different available chips.

One of the main drawbacks of the SCA is the inherent dead time to allow readout of all the samples for each trigger. A multi level array design will be implemented in the next generation of chips such as the DRS5 or the successor of PSEC4 called AARDVARC. There is a joint effort from HEP/NP and the NALU commercial company to offer a commercial modular system based on the successor of PSEC4. This is currently the favored option with costs which could go as low as \$15 per channel.

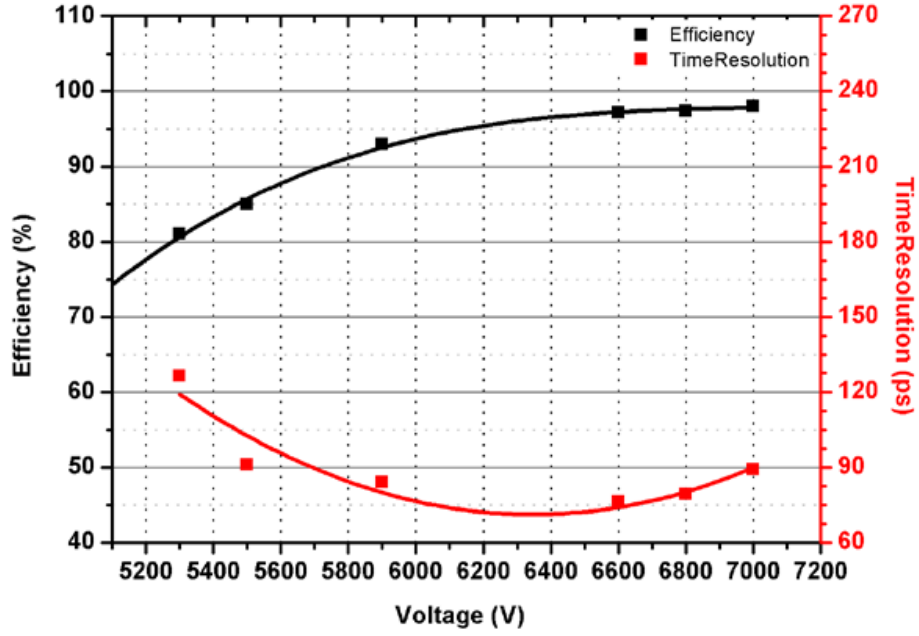


Figure 118: Time resolution and efficiency change versus applied voltage

Chip	Sample Frequency GHz	Bandwidth GHz	Samples	Channels	Readout MHz	Resolution ps
PSEC4	4 to 15	1.5	256	6	40 to 60	9
SAMPIC	3 to 8.2	1.6	64	16 or 8	80	5
DRS4	0.7 to 5 GHz	0.950	1024	9	33	1
DRS5	10	3	4096	32	300 ?	5 ?
PSEC5 (AARDVARC)	10 to 15	1.5 to 2	32768	6 to 8	500?	5?

Table 18: Table summarizing the characteristics of different sampling chips available and future generation ones for DRS5 and PSEC5 (AARDVARC)

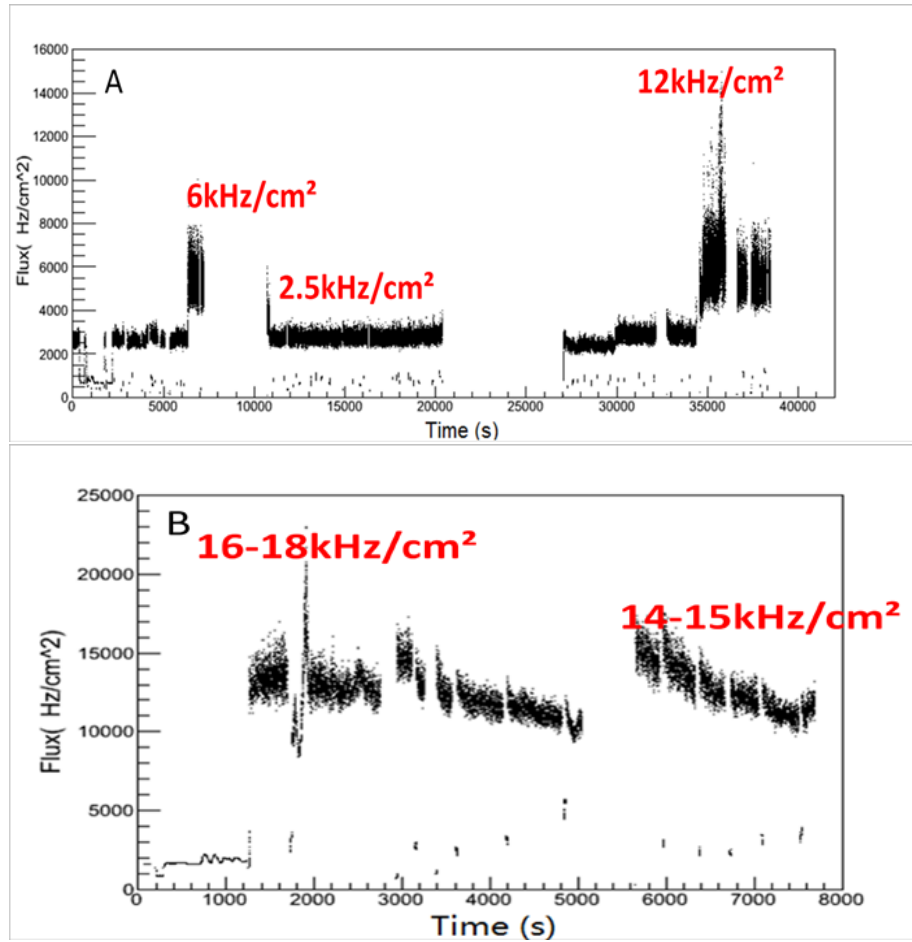


Figure 119: Signal rate changes with time. (A) shows run 188 and (B) shows run 193. The MRPC was located 5 meters from the target. There is shielding in front of the detector in (A), no shielding in front of the detector in (B).

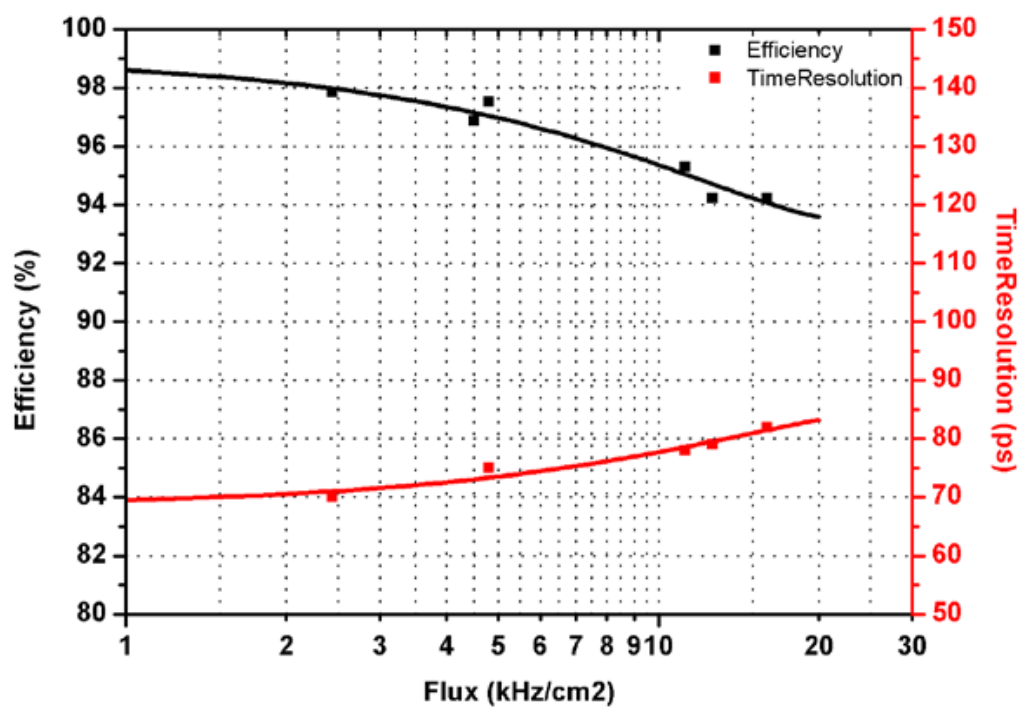


Figure 120: Measured efficiencies and time resolutions as a function of the particle flux.

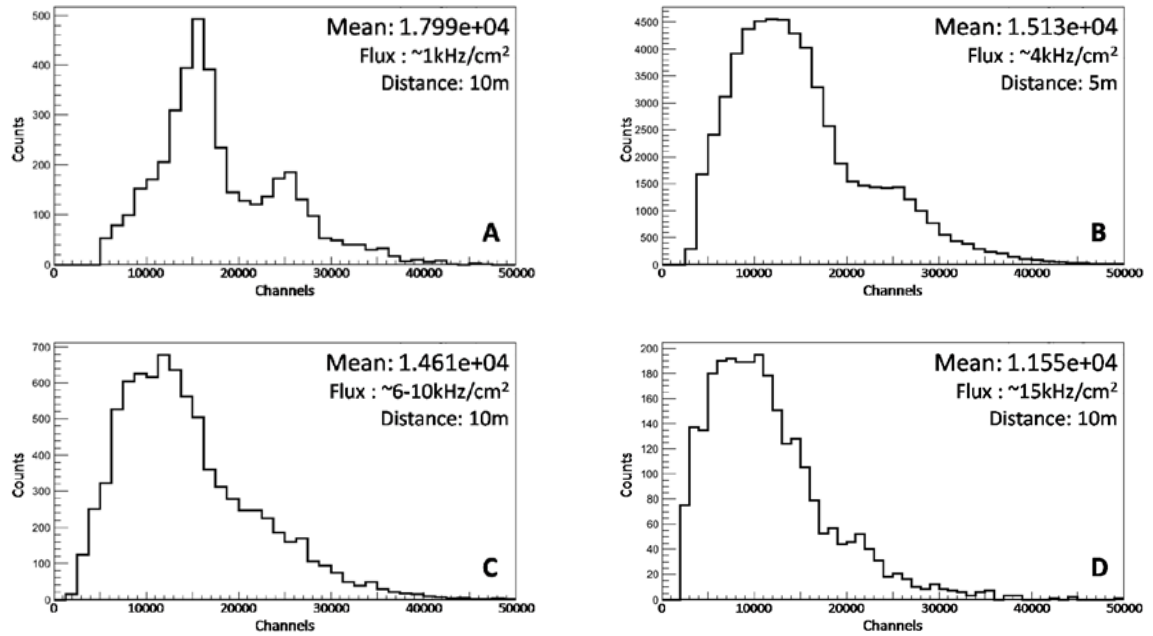


Figure 121: Charge distribution at various fluxes over one readout strip. Flux increases from figure A to D.

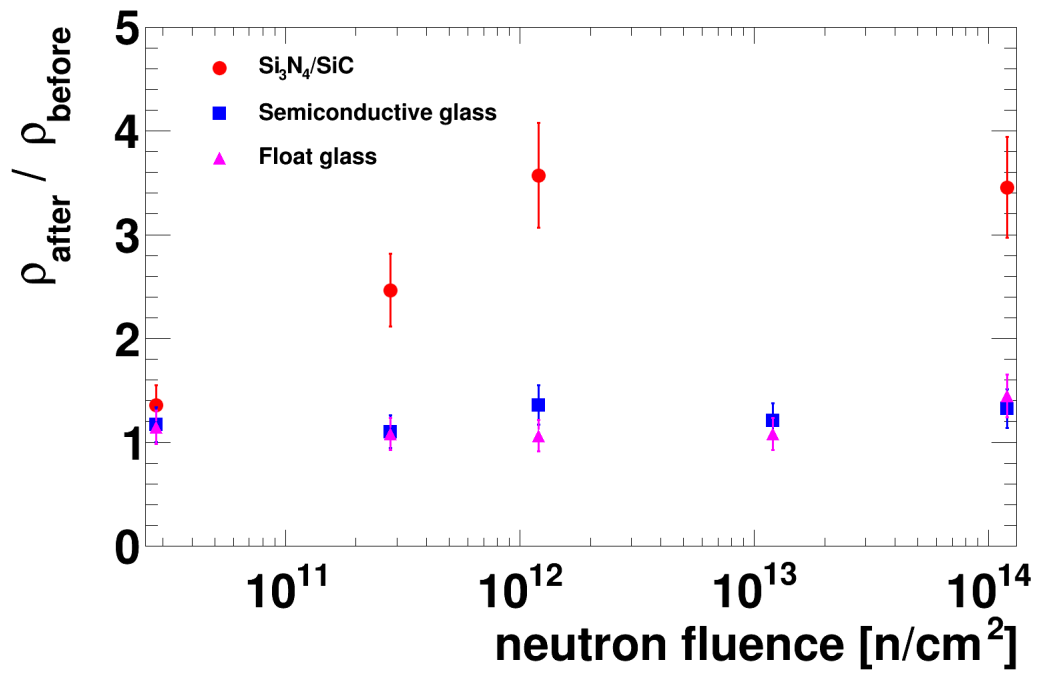


Figure 122: Change in glass resistivity as a function of neutron fluence, where the semiconductive glass is what we used.

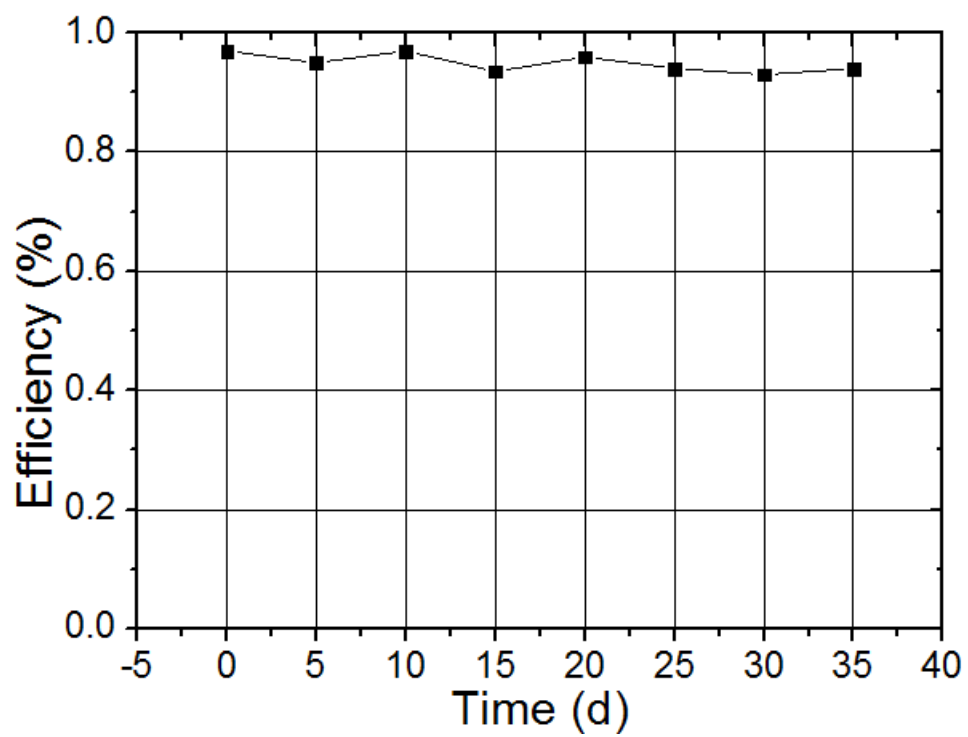


Figure 123: Chamber efficiency as a function of x-ray irradiation days

12 Simulation and Reconstruction

12.1 End-to-End Software Framework

At the time of this writing, research is underway to identify a comprehensive software framework for SoLID. A framework should be chosen early in the software development cycle, where SoLID is now, to provide a common programming interface for all software components. If chosen well, the interface will stay constant, or at least backward compatible, throughout the project’s lifetime so that early investments in code development will continue to pay off. Additionally, it is important at this stage to identify software features and capabilities that will be needed for SoLID data analysis, to the extent foreseeable now. Such feature requirements should be well matched to the specifics of the SoLID experiments, such as data volumes, detector types and configurations, and analysis methods. Retrofitting capabilities that were initially overlooked are often difficult and wasteful because doing so may invalidate original design assumptions, requiring large parts of the first-generation software to be re-written. Conversely, choosing a framework with too many features typically results in overly complex, bloated software that is difficult to learn and faces user resistance.

With these goals in mind, we have developed the following requirements for the SoLID software framework; it should

1. support all major components of the physics data processing chain, *viz.* simulation, digitization, reconstruction and physics analysis, within a *consistent* development and run-time environment (“end-to-end framework”);
2. allow multi-pass data processing, where the output of one analysis pass can be used as the input for the next pass—an essential capability to minimize the need for reprocessing large data sets;³
3. allow multiple processing chains in a single job, for example to run different track fitting, PID or physics analysis algorithms on the same data in a single processing pass;
4. support interactive analysis of reconstructed quantities with ROOT, since ROOT will most likely be the data analysis package best known to and preferred by future SoLID collaborators;
5. save extensive metadata to its output, for example database parameters used in previous analysis stages (if practical) and detailed information about data provenance;
6. support parallel computing, *i.e.* multi-threading and/or distributed processing;
7. be written in C++, as most SoLID collaborators are well-versed in that language; and
8. be readily available at this time, so that development can start without delay.

Given limited staffing, the effort needed to develop a new framework from scratch that satisfies the above set of requirements would be prohibitive. As experiences in other collaborations show [259–262], frameworks with comparable capabilities are invariably complex and may take the better part of a decade to mature. Therefore, it is practically unavoidable, and certainly wise, to build the analysis software for a specific experiment on already existing packages, unless truly unusual or novel requirements arise. Of course, we are not the first to discover this. Motivated by the increasing

³In physics frameworks, this is typically achieved by separation of data and algorithms, where the data objects are persistable and saved to intermediate files. Regarding object persistence, the ROOT streamer model represents the state of the art in the field.

complexity of software in the field, various collaborations worldwide have, over the past decade or two, put considerable effort into developing high-quality, general-purpose frameworks aimed at processing the event-type data prevalent in nuclear and particle physics experiments. The present trend in HEP is a collaborative approach toward software, where already-developed, widely tested frameworks are increasingly shared by similar experiments and re-used for new ones [263]. Practically no modern software in the field does without ROOT [264] in regard to interactive analysis, visualization and object persistency, while a number of choices exist for event processing frameworks that support simulation and reconstruction.

Obviously, we do not expect to find a perfect framework that satisfies all our criteria fully. Generally, however, a good event processing framework should stand out by a superior technical design and reliance on widely adopted, state-of-the-art technologies (*e.g.* support for C++14/17, ROOT object persistency). To minimize development time and maximize user adoption, the right mix of features, excellent documentation and a large body of available example codes would clearly be beneficial.

At present, we are evaluating a number of different NP and HEP data analysis frameworks that are popular and readily available. Specifically, we have been studying Podd (JLab Hall A/C) [265], Clara (JLab Hall B) [259], JANA (JLab Hall D) [260], Fun4All (PHENIX/sPHENIX at BNL) [266], FairRoot (GSI) [261], and *art* (FNAL) [262]. Of these, *art*, the framework developed for and adopted by the Intensity Frontier experiments at Fermilab (DUNE, for example), appears to be a particularly promising candidate for long-term use by SoLID. *art* satisfies all of the SoLID requirements listed above, is mature, sufficiently rich in features, sufficiently flexible for general-purpose simulation and analysis tasks, well supported, and serves a large user community that is unlikely to dissolve over the next decade. As of mid-2018, with version 3, *art* supports task-based multi-threading at the event level.

Also of note, the *art* developers participate in the monthly ROOT planning meetings; as stakeholders, they provide direct input to the ROOT team to help improve compatibility of the framework with ROOT. We interpret this as an additional encouraging sign for the longevity of this framework in particular.

The JANA framework may also be of interest, especially given the recent development of a modernized version, JANA 2.0. However, JANA does not currently meet several of the SoLID software design criteria. For instance, the framework itself has no support for a particular DST file format; such support must be added by experiment-specific plugin libraries. JLab’s Hall D collaboration has developed an extensive repository of add-on code for JANA, including DST input and output modules. However, the chosen file format, HDDM, is non-standard and not used by any other major NP or HEP experiment. Conversion to ROOT format requires a separate analysis step. Additionally, reconfiguration cannot always be done at run time, but may require recompilation. Further limitations exist.

The GSI FAIR experiments are considering moving to a new, concurrent and distributed framework, ALFA [268], which will presumably be in the upgrade path of FairRoot. This option may or may not materialize in time for SoLID. Some components of ALFA could serve as the basis for an extension of SoLID software to distributed computing.

Prototyping and testing of simulation and analysis routines with several frameworks is currently underway to gain experience with the frameworks’ relative benefits. A decision as to which framework to adopt for SoLID will be made at an appropriate time.

An estimate of the effort required for implementing the complete SoLID simulation and reconstruction software can be found in Appendix B.

12.2 Simulation

12.2.1 Simulation Software

Simulations are necessary to guide the detector and DAQ system designs, including quantifying experimental backgrounds to the accuracy required for the design study.

They need to be done in a coherent fashion and validated as well as possible. The simulation software must be flexible enough to be quickly adapted to different configurations.

Initial simulations for SoLID during the proposal stages were done using a GEANT3 based software called COMGEANT. However, these are FORTRAN based and GEANT3 is no longer actively maintained. Since then, we have decided to move to Geant4 [270] to handle particle propagation and interactions. This is a well-supported framework and offers a variety of physics packages, such as simulation of low-energy electromagnetic backgrounds. However, the detector geometries, how magnetic field maps are specified, input parameters, and output formats must all be developed on top of this framework.

To accomplish all these goals, we have adopted a general Geant4 simulation framework, GEMC, which is what the JLab CLAS12 and JLab EIC conceptual detector simulations are based on [271]. GEMC can use external physics event generators and has advanced visualization abilities, which provide a useful debugging tool. GEMC has detector description including geometries and materials with optical properties defined in a tabular structure which can be stored in text files or SQL databases, outside the GEMC binary code. Detector signal processing can also be customized for various kinds of detectors and has output to a compact style similar to those used by JLab data acquisition systems, outside the GEMC binary code.

Using those features, we have built the current SoLID simulation program “SoLID_GEMC” on top of GEMC. This gives access to all of the functionalities within GEMC and allows us to modify and add components as needed. All SoLID detector descriptions and signal processing are outside of GEMC and can be loaded at run time. This allows for easy modification of designs. We can run standalone simulation of a single detector or the whole SoLID simulation with all subsystems without any modifications and ensure consistent results.

A schematic of the current simulation workflow is given in Fig. 124. Geant4 provides the predominant simulation components in modeling secondary physics processes (such as multiple scattering) and particle propagation through a magnetic field. Physics generators provide information on the initial particle type, position, and momentum to the simulation for each event and are described in Sec. 12.2.3. These can take more than one form and we allow for general text file input and internal generators within GEMC. Output from “SoLID_GEMC” is through EVIO, a binary format developed at Jefferson Lab. Libraries are available to provide decoding. These files are converted to ROOT files through available tools and used by higher level analysis packages such as the detector digitization and analysis.

Magnetic field maps for GEMC are described over a grid using text files. It allows various coordinate systems to be used in the grids and handles all interpolation and lookup. As described in Sec. 4, SoLID magnetic field map files are produced using the Poisson Superfish package [272] developed at LANL. The POISSON package allows for the calculation of azimuthally symmetric magnetic fields (relevant for the solenoidal spectrometer). Because both the optics and the fields in the detector regions are relevant, accurate optimization of the iron yoke is important. We also started to use more detailed 3D field maps produced by TOSCA [273].

The entire code, including the production and development version, is kept in a git version control system. Its distribution is by docker containers, which can be used both on JLab computer farm and Open Science Grid.

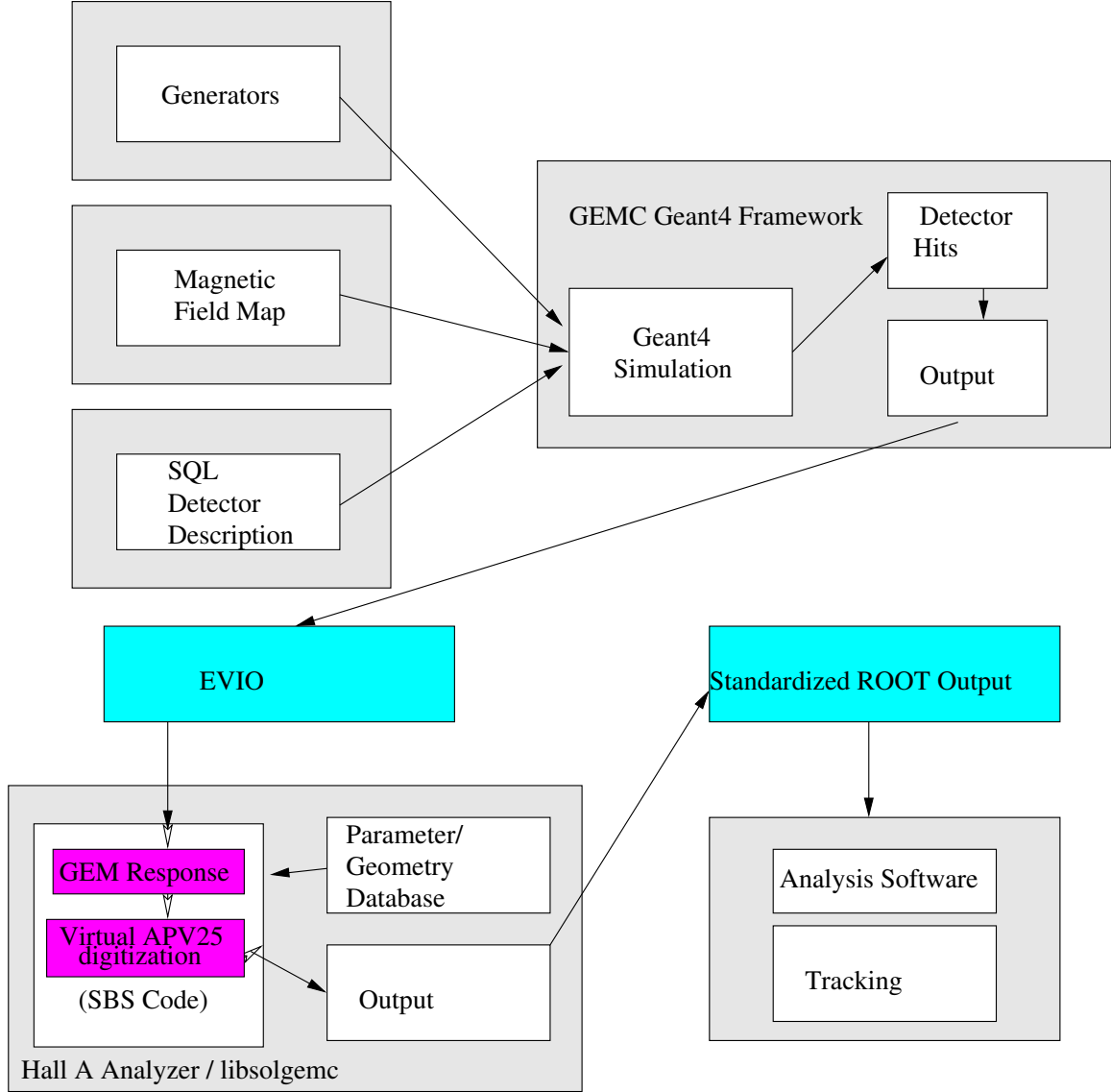


Figure 124: Schematic of the current simulation workflow.

12.2.2 Simulation Status

Significant progress has been made with the 5simulation, which has allowed for realistic performance studies of the core measurements. The simulation of each individual subsystem has been developed by different groups using the same framework, and then all subsystems are combined into the whole SoLID simulation without any code change at run time. We can also choose to turn off a subsystem or replace it with a different version in the whole simulation for testing.

The materials in non-detector subsystems have been implemented. Detector subsystems have materials and responses tailored to themselves. In addition to studies done by different groups for subsystems, we also produce the whole simulation output for various overall studies of characteristics such as acceptance, background rates and trigger performance to ensure consistent results.

The simulation output is stored in ROOT trees. Each detector has a standalone tree, and different trees are linked by the same tree index for one event. Then each tree is analyzed by a standalone

ROOT script. Combining the set of ROOT scripts, we can analyze all SoLID sub-detectors and perform the overall studies mentioned above.

In general, the SoLID simulation is an effort which will last the entire SoLID lifetime. We are still at its early stage. The simulation code will evolve with the Geant4 and GEMC development. SoLID's detector and engineering design will also evolve and they can be easily transferred into the simulation by a CAD model. Detector prototyping and tests will give direct inputs to the simulations and in turn improve the overall SoLID design.

The SoLID collaboration may adopt the *art* event-processing framework as its software framework. *art* currently uses generic Geant4 as its simulation engine and allows for a flexible middle layer. We are exploring the possibility of using GEMC for the simulation layer of *art*.

12.2.3 Physics Event Generators

Beyond the physics included in Geant4, several generators have been implemented to study specific processes. The interface between the generator and GEMC is the LUND format (or an extension of it), which is a text-based file containing event-by-event information of the initial particle configuration. These generators allow for extended targets and randomly sampled beam positions to simulate a fast-rastering system. The generators implemented presently are

- Elastic scattering from protons and neutrons based on dipole parameterizations.
- Deep inelastic scattering cross sections from the CTEQ6 parton distribution fits [275];
- "solid_bggen", charged and neutral pion production based on the modified Hall D background generator which combines Pythia and SAID;
- SIDIS production with cross section based on fit to existing world data and model
- J/ψ production with cross section based on fit to existing data and models

The generator "solid_bggen" is based on the generator "bggen" used by Hall D with adding virtual photon flux. It gives good estimation for pions that matches the existing data. The original Hall D photo-production generator "bggen" uses various experimental data to generate photo-production cross sections on a proton target for photon energies below 3 GeV and uses a modified version of PYTHIA to generate cross sections of photo-production for photon energies above 3 GeV [279, 280]. Hall D "bggen" generator is only a photo-production event generator. SoLID experiment requires an electro-production generator. Hadron production in electron scattering on a nucleon target can originate either from real bremsstrahlung photons radiated in the target or from the interaction of virtual photons with the nucleons. The virtual photon contribution is calculated in the Equivalent Photon Approximation [281]. The bremsstrahlung contribution is implemented following PDG-2012 [282, 283]. A more detailed overview of the hadron generators used for SoLID simulation is available from [278].

Low energy background rates for processes included in Geant4 are evaluated by simulating sufficient numbers of individual electrons passing through the target with the entire SoLID simulation setup.

Additional generators are planned, which include extending the present generators to include initial radiative and multiple-scattering effects. Additionally, self-analyzing hyperon decay processes are a potential systematic and must be evaluated as well.

12.2.4 GEM Digitization

GEM digitization is a crucial aspect in evaluating the tracking reconstruction under realistic conditions. The method implemented is based on an approach developed by the Super-BigBite collaboration, which takes the individual ionization events in the GEM drift region, and produces a charge signal across several readout strips based on a realistic model with parameters tuned to real data.

A track passing through a GEM in Geant4 will initiate energy deposition events caused by ionization which are then amplified through the GEM foils, resulting in a detectable signal over several readout strips, Fig. 125. Within the simulation, the individual ionization events are written into the output and are post-processed through an independent library built upon the Hall A analyzer analysis software [265]. The digitization and track reconstruction can then be developed within a single framework similar to what could be used for analysis of real data.

A full description of the digitization process can be found in Ref [286]. To summarize, from the individual ionization hits, an average number of hole/electron pairs are determined by sampling a Poisson distribution based on the ionization energy W , such that $\bar{n}_{\text{ion}} = \Delta E/W$. The physical spread of the resulting charge cloud is described by a simple diffusion model assuming a constant drift velocity, where the half width at half maximum (HWHM) of the cloud is given by

$$\text{HWHM}(t) = \sqrt{2Dt} \quad (11)$$

where D is the diffusion constant and t is the time from ionization. Variation in the amplification of the GEM signal is described by a Furry distribution

$$f_{\text{Furry}} = \frac{1}{\bar{n}} \exp\left(-\frac{n}{\bar{n}}\right) \quad (12)$$

where \bar{n} is the average number of ionization pairs. The previous formalism provides a realistic (unnormalized) charge distribution over an area which can then be associated with a set of GEM readout strips.

For the strip readout, we have assumed the use of VMM electronics developed at BNL. Instead of sampling the shaped pulse, VMM can seek pulse peak internally and output a peak ADC value. By using the tuned digitization code, we digitized the whole simulation for PVDIS setup with LD2 target, SIDIS setup with ^3He target, and the J/ψ setup with LH2 target. The same set of simulation data are used for acceptance and trigger study including all detector responses. The GEM geometry and material are modeled carefully in simulation and according to the latest design and prototype. The things missing are dead areas by spacers and frames, and the possible overlap over different sectors, which we plan to add in the next round of simulation. Both the simulation and our test have shown that the dominant GEM background is caused by low energy photons which have only a few percent probability to deposit energy and fire GEMs, but with a huge rate. The occupancy is obtained as the average number of readout strips fired within 275 ns time window divided by total number of strips in the readout plane in one of 30 sectors. Both u and v strips are counted. The results are shown in Table 19, 20 and 21. The noise filtering from 3 samples is applied where it's available.

12.3 Reconstruction

12.3.1 Tracking

SoLID tracking reconstruction requires an accurate and efficient track finder that is able to identify signal tracks in a high-noise environment and is sufficiently fast for the level-3 trigger if needed. In

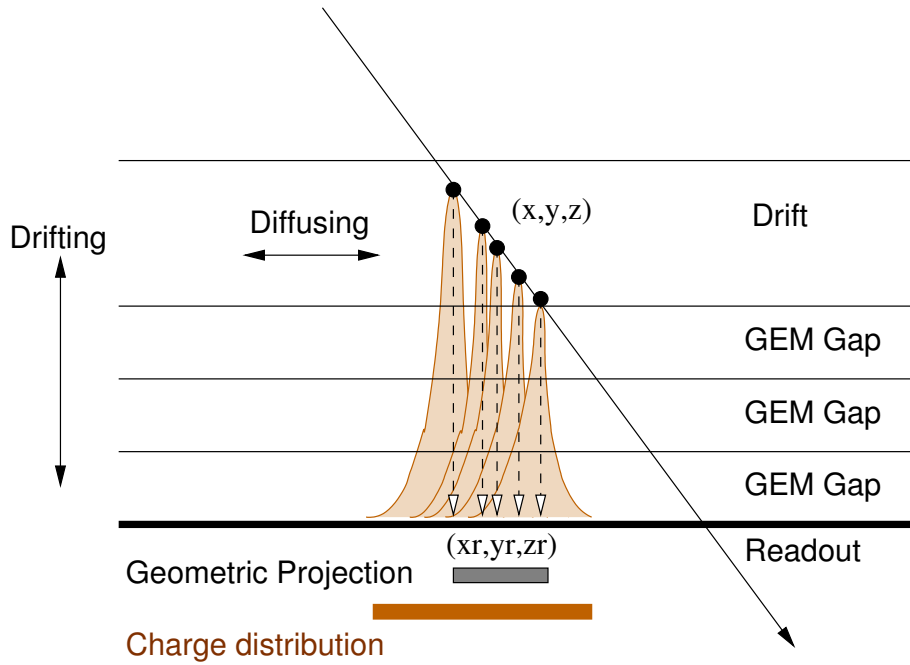


Figure 125: Diagram of the concept behind GEMs using electron avalanching and detection through a set of readout strips.

PVDIS GEM occupancies		
Plane	Total strip number (u+v) per sector	Raw Occupancy (%)
1	1156	4.48
2	1374	2.55
3	1374	2.21
4	2287	0.82
5	2350	0.75

Table 19: PVDIS GEM average occupancies with LD2 target, estimated by digitizing its whole simulation data.

SIDIS ^3He GEM occupancies		
Plane	Total strip number (u+v) per sector	Raw Occupancy (%)
1	906	1.19
2	1020	3.99
3	1166	1.70
4	1404	1.62
5	1040	1.03
6	1280	0.76

Table 20: SIDIS ^3He GEM average occupancies estimated by digitizing its whole simulation data.

J/ψ GEM occupancies		
Plane	Total strip number (u+v) per sector	Raw Occupancy (%)
1	906 2.33	
2	1020	4.64
3	1166	2.85
4	1404	2.15
5	1040	1.89
6	1280	1.48

Table 21: J/ψ GEM average occupancies estimated by digitizing its whole simulation data.

addition, an accurate and robust track fitter is required in order to optimize the resolutions for the vertex variables and other track-related variables.

In order to satisfy the requirements, a Kalman Filter (KF)-based track finding and track fitting algorithm is being developed and tested with digitized GEM simulation data. A Kalman Filter is a recursive fitting algorithm [284]. In contrast to the well-known least-squares fit that provides only one set of parameters after fitting, the track parameters of the KF can evolve along the trajectory. There are three basic steps for the KF. First, it predicts the measurement on the next measurement site by propagating the current track parameters. Second, the covariance matrix of current track parameters is propagated along the trajectory. And last, it filters the next measurement in order to improve the track parameters at the next measurement site. The local field information and errors due to multiple scattering can be collected during the first two steps of the algorithm. Thus, given that particle tracks in the SoLID detector will cross both fringe and uniform field regions, it is expected to perform better than other algorithms that explicitly require a globally uniform magnetic field.

The KF can be easily extended into a track finder as well, achieving concurrent track finding and fitting. This is done by adding two steps to the standard KF algorithm. First, an algorithm is needed to search for seeds, which are track segments that provide initial estimations for track parameters. These seeds are chosen from hits on downstream GEMs, whose occupancy is relatively lower, and at least two hits on two different GEMs are required to initialize the KF. Second, a set of arbitration rules need to be applied before filtering to identify hits belonging to the track. A straightforward rule is to require that the hit on the next measurement site falls within a window around the prediction. The size of the window can be determined based on the covariance matrix elements of the predicted track parameters. In addition, a cut on the χ^2 increment when a candidate hit is added [285] can also be used for the hit selection.

Once all the hits on GEMs are identified and filtered, track parameters on the most upstream GEM is propagated to the target region in order to determine the kinematic variables at the interaction vertex (vertex variables). A beam position monitor (BPM) measurement for the transverse position of the incident electron beam (x_b, y_b) is used, assuming its position resolution is at the level of 300 μm . The z -coordinate of the interaction vertex (z_v) can be determined by finding the closest approach between the track and the electron beam. Finally, the Cartesian coordinate of the interaction vertex (x_b, y_b, z_v) will be filtered by KF in order to further improve the resolution of the vertex variables. This improvement is rather limited for the SIDIS configuration, but it is significant for the momentum resolution for PVDIS as most of its field integral comes from the space between the interaction vertex and the most upstream GEM. The basic steps in this concurrent track finding and fitting algorithm is summarized in Figure 126.

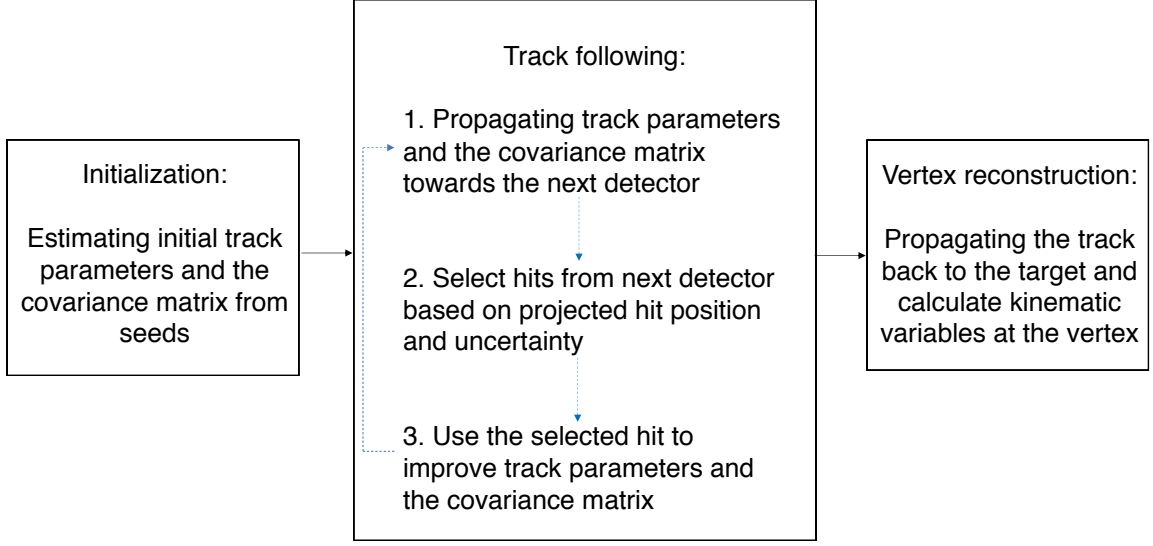


Figure 126: A flow chart for the concurrent track finding and fitting for SoLID tracking reconstruction.

The whole simulation including all SoLID subsystems in their different respective configurations is used for the tracking studies. Both signal tracks from various event generators and background produced by low energy particles, mostly photons, are included in the simulation data.

At present, the track finding algorithm is being developed and tested for the different SoLID configurations. For the SIDIS ^3He configuration, both the efficiency of the track finder and the probability of identifying all correct hits of a track typically exceeds 90% for electron tracks in both the forward angle and the large angle regions. For the PVDIS and J/ψ configurations, the efficiency is about 85% for electron tracks. The track finder also achieves a reasonable execution speed. We will study the possibility of using the current track finding algorithm with looser conditions to improve the reconstruction speed for the planned level-3 data reduction farm.

The track fitting algorithm is also being developed and tested for different SoLID configurations. The kinematic dependence of the reconstruction resolution of the track parameters for the SIDIS ^3He configuration is shown in Figure 127 as an example. Resolution values averaged over the kinematic ranges, obtained for the SIDIS ^3He and PVDIS configurations, are summarized in Table 22. J/ψ results are similar to SIDIS ^3He results. In these studies, energy loss is included for all materials, except for materials in the dead areas of the GEM planes. Low energy photon background in the GEMs is also included. To make our current results conservative, we multiply all values by a safety factor of 1.5 when applying them to various physics studies. All SoLID physics programs are using these track resolutions in their studies by directly applying the full kinematic dependent results. We are continuing the study to have results with all effects included in near future.

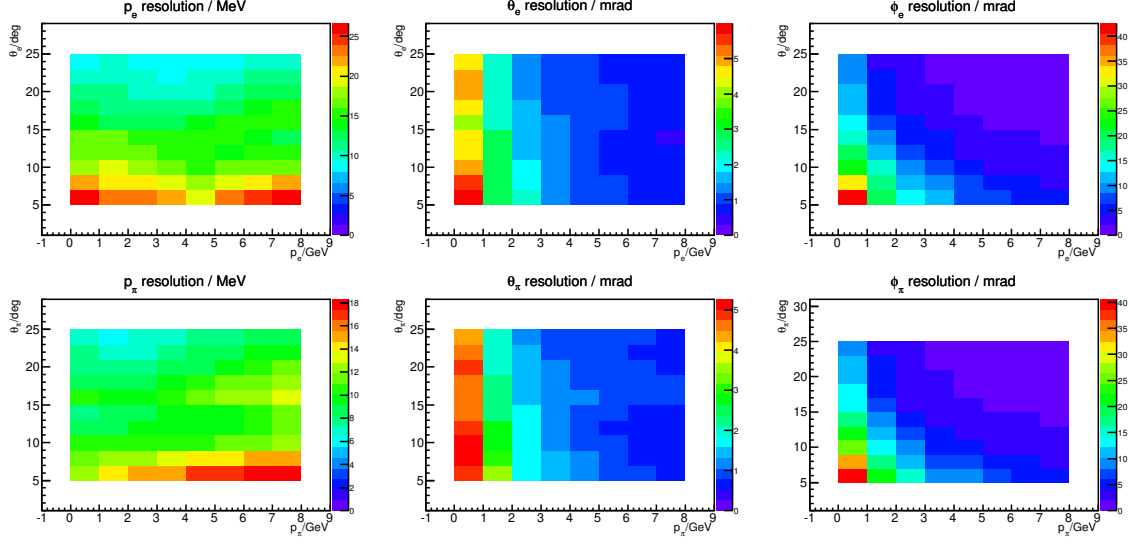


Figure 127: SIDIS ^3He resolutions by track fitting studies with most of material energy loss and without background. The upper panels are the resolution of the electron kinematics. The lower panels are those of the pion kinematics. The variables are defined in lab frame with beam line as the z -axis.

	θ angle (mrad)	ϕ angle (mrad)	Vertex z (cm)	p (%)
SIDIS ^3He fwd angle (e)	1.3	5.7	0.9	1.7
SIDIS ^3He fwd angle (π)	1.2	5.2	0.9	1.1
SIDIS ^3He large angle (e)	1.0	1.7	0.5	1.2
PVDIS (e)	0.8	1.7	0.3	1.2

Table 22: Averaged resolutions by track fitting with most of material energy loss and background

12.3.2 Additional Reconstruction Algorithms

Many existing detector reconstruction algorithms available in the Hall A analyzer [265] or in other packages should be reusable for SoLID, for instance the Cherenkov photoelectron yield analysis and the calorimeter clustering algorithm. While the basic physics algorithms can be adopted without much change, code will have to be developed to support the cylindrical geometry of SoLID as well as the individual local detector geometries. Furthermore, a likelihood-based particle identification scheme or similar should be written. Development of calibration software tuned to the SoLID detectors will be necessary as well.

A high-level overview of the necessary algorithm development tasks can be found in Appendix B, specifically in the spreadsheet referenced in that section [357].

13 Data Acquisition

13.1 Introduction and Requirements

The SoLID detector is a large acceptance detector designed to run at high luminosity. The detector will operate in two basic configurations: the parity-violating electron scattering (PVDIS) configuration and the semi-inclusive deep inelastic scattering (SIDIS) configuration. The experiments planned under these configurations have in common a large number of channels (over 160,000 GEM tracking channels and over 4,000 trigger/particle ID channels), high background rates, and high trigger rates.

We use the whole detector simulation with various experimental configurations to study the trigger as mentioned in Section 12.2. The high energy primary particles are from event generators such as a single electron generator, a SIDIS pion generator and the modified Hall D hadron generator. All secondary particles are generated by Geant4. Low energy particles, primarily from electromagnetic processes, are produced by Geant4 directly from beam electrons on the target. The response in various detectors are examined event by event according to a given trigger configuration. Low energy background and pile up effect are taken into account. The expected trigger rates are shown in Table 23 for different experimental setups. (The trigger simulation will be updated as the simulation tools are improved and additional information becomes available from JLab 12 GeV data and DAQ tests.)

The SIDIS configuration, with an expected trigger (coincidences and accidentals) rate of ~ 100 kHz and total data rate of over 3 GB/s represents the greatest challenge for SoLID data acquisition. For PVDIS, the DAQ requirement is more modest as the ~ 450 kHz rate is divided among 30 parallel DAQ systems, following the segmentation provided by the baffle system. However, there are additional challenges as the DAQ systems for adjacent sectors must communicate trigger information and data for events where calorimeter showers extend into adjacent sectors.

We present here a conceptual design for a DAQ system based on modest evolution of current technology, much of which has been developed at JLab. Considering the large number of channels, the rate requirements and the availability of new electronics developed for the Hall D GlueX detector, a pipelined electronics approach has been chosen. These electronics continuously digitize the detector signals, keeping the data in several microsecond deep buffers which can be retrieved after a trigger is received. With these electronics, the First Level Trigger (L1) is generated primarily from prompt data streams from Flash Analog to Digital Converters (FADC). This gives the ability to reprogram trigger algorithms without the need for re-cabling.

Experiment	PVDIS	SIDIS ^3He	J/ψ
Trigger rate (expected) (kHz)	15×30	100	30
Data rate (GB/s)	0.2×30	3.2	2.5
Running time (days)	169	125	60
Total data (PB)	175	70	25

Table 23: Rates, run times and data total estimates for the PVDIS, SIDIS ^3He and J/ψ experiments. For PVDIS, there are 30 sectors each of which has a separate DAQ.

13.1.1 SIDIS Trigger and Rate Estimate

Three experiments, E12-10-006 [87], E12-11-007 [88], and E12-11-108 [89], have been approved to measure single and double spin asymmetries of semi-inclusive deep-inelastic scattering (SIDIS) ($e, e'\pi^\pm$) with SoLID. As these experiments have similar reaction channels, they can share the same DAQ system design. The required overall luminosity of E12-10-006 and E12-11-007 is $10^{37}/\text{cm}^2/\text{s}$, which is an order of magnitude higher than that of E12-11-108. Therefore, we will use E12-10-006 as an example to illustrate the requirements of the SIDIS DAQ. The goal of the SIDIS DAQ is to satisfy the requirement of ~ 100 kHz trigger rate, see Section 13.2.1 for more information about the limit.

The SIDIS process requires the detection of both the scattered electron and the leading pion. Therefore, a single electron trigger or a coincidence trigger of the electron and the hadron would satisfy this need. The electron trigger for the large angle detector will be provided by the E&M calorimeter at a threshold of about 3 GeV. Such a trigger is sensitive to both high energy electrons and high energy photons (mostly from the π^0 decay). A set of scintillator paddles, added in front of the calorimeter, are incorporated into the trigger in coincidence, significantly suppressing triggers from high energy photons.

The electron trigger at the forward angle detectors will be formed by a coincidence of the gas Cherenkov detector, the E&M calorimeter, the scintillator paddle detector (SPD). Considering the kinematics of the scattered electrons from the DIS process (e.g. $Q^2 > 1 \text{ GeV}^2$), a position dependent energy threshold with a lower limit of 1 GeV in the E&M calorimeter will be used.

The single electron trigger rate was estimated from simulation to be 116 kHz for the forward angle calorimeter in coincidence with the gas Cherenkov, SPD. Adding 32 kHz for the large angle calorimeter in coincidence with the SPD gives a total single electron rate of 148 kHz. In order to keep the Level-1 trigger rate below 100 kHz, we plan to form a coincidence trigger between the electron trigger and the charged hadron trigger with a 20 ns time window. The charged hadron trigger using the calorimeter with the SPD is 20 MHz. The SIDIS processes including charge pions and misidentified neutral pions and protons, has a coincidence trigger rate of 27 kHz. Other multiple hadron processes can also contribute to coincidence rate of 12 kHz. Excluding the true coincidence from SIDIS and multiple hadron processes, we estimate an accidental coincidence rate of 46 kHz with a 20 ns time window. Some single electron triggers will also be acquired. These will be prescaled to about 15 kHz such that the total trigger rate remains below 100 kHz.

13.1.2 J/ψ Trigger and Rate Estimate

The E12-12-006 experiment is designed to measure the cross section of the $p(e, e'J/\psi)p$ reaction at an unpolarized luminosity of $1.2 \times 10^{37} N/\text{cm}^2/\text{s}$ with a proton target. A coincidence trigger between the electron and positron from J/ψ decay will allow both electroproduction and photoproduction reactions to be recorded. By using an electron trigger similar to the SIDIS configuration, with a different radially dependent EC trigger threshold, a rate of 60 kHz is estimated. Adding the scattered electron into trigger to form a triple coincidence will reduce the trigger rate by a factor of 2 to 30 kHz.

13.1.3 PVDIS Trigger and Rate Estimate

The PVDIS measurement is based on the asymmetry of inclusive electron scattering between incident electrons of opposite helicity states. To achieve the needed statistical accuracy of this parity violating asymmetry, high rates will be required in the detector. The rate over the whole detector is expected to be of the order of 500 kHz, above the trigger rates that can be handled by the JLAB

electronics. As the measurement is of singles inclusive electrons, the detector electronics can be divided into 30 sectors (corresponding to the baffle arrangement) each with a separate trigger, giving an acceptable rate for each sector. For each sector, the trigger will be a coincidence between the gas Cherenkov and electromagnetic calorimeter. Based on our simulations of the inclusive electron rate and accidentals (with a 30 ns coincidence window) between singles in the electromagnetic calorimeter and the Cherenkov counter, the estimated trigger rate is 15 kHz per sector.

13.1.4 Detector Rate and Occupancy

We list the maximum rate per unit area in Table 24. For detectors other than Cherenkov, the maximum rate are at their most inner radius. For the two Cherenkov detectors, we choose the maximum within their PMT assemblies. We also list the maximum rate and occupancy per channel in Table 25. For detectors other than GEM, the occupancies are calculated from the corresponding rate and a 50 ns time window. For GEM, the fully digitized rate and occupancy with a 275 ns window are shown. The pile-up effect is already included in the trigger study for EC, SPD and light gas Cherenkov described in pre-CDR.

Rate per unit area (kHz/cm ²)	area(m ²)	SIDIS ³ He	J/ψ	PVDIS	comment
LGC	0.7	16	40	80	Np.e. ≥ 1
HGC	1.2	160			Np.e. ≥ 1
SPD_FA	15.2	0.02	0.06		cut below MIP
SPD_LA	3.7	0.12	0.25		cut below MIP
EC_preshower_FA	15/19	33	77	90	cut below MIP
EC_shower_FA	15/19	10	14	9	cut below MIP
EC_preshower_LA	4.1	45	80		cut below MIP
EC_shower_LA	4.1	5	19		cut below MIP
GEM	21/37	800	1600	500	non-digitized

Table 24: SoLID detector maximum rate per unit area.

Rate (kHz)/Occ per ch.	Num. of ch.	SIDIS ³ He	J/ψ	PVDIS	comment
LGC	270	400/0.02	1000/0.05	2000/0.1	Np.e. ≥ 1
HGC	480	4000/0.2			Np.e. ≥ 1
SPD_FA	240	3200/0.16	8600/0.43		cut below MIP
SPD_LA	60	4500/0.225	9200/0.46		cut below MIP
EC_preshower_FA	$\sim 1300/\sim 1800$	3300/0.17	7650/0.38	9000/0.43	cut below MIP
EC_shower_FA	$\sim 1300/\sim 1800$	920/0.05	2344/0.12	900/0.05	cut below MIP
EC_preshower_LA	~ 500	4533/0.23	8119/0.41		cut below MIP
EC_shower_LA	~ 500	482/0.03	1894/0.1		cut below MIP
GEM	$\sim 161e3/\sim 188e3$	4e3/0.3	5e3/0.4	5e3/0.4	digitized

Table 25: SoLID detector maximum rate and occupancy per channel.

13.2 DAQ Hardware and Trigger

The DAQ system for SoLID will use modules recently developed for Hall D by the JLab Physics Division Fast Electronics and Data Acquisition groups. These include flash ADCs (FADC250), VXS Trigger Processors (VTP) and Global Trigger Processors (GTP), Sub-System Processors (SSP), Trigger Supervisors (TS), Trigger Interface (TI), and Signal Distribution (SD) modules.

Analog signals are digitized by the JLab FADC250, a 16-channel 12-bit flash analog to digital converter sampling at 250 MHz. The input signals are continuously recorded into a memory with a depth of up to 8 μ s with event data latched by a trigger. The system is dead-timeless as long as the latched data can be readout as fast as it is generated.

In addition to making data available for readout when triggered, the FADC250 is capable of sending continuous digitized data over high speed VME switched Serial (VXS) lanes on the back-plane connector. This data, a 16 bit word per module every 4 ns, could be a digital sum of the 16 channels of the ADC or more complex information.

Each crate will have a VXS Trigger Processor (VTP) which receives a 16 bit word from each FADC250 every 4 ns. The VTP processes the data stream from each module in the crate to generate a 32-bit word every 4 ns. This word, which could be, for example, a sum of all the channels in the crate or a bit pattern, is sent upstream via a 10 Gbps optical link to a Sub-System Processor (SSP) board which gathers trigger data from multiple crates. All the SSP boards send their information to the Global Trigger Processor (GTP) which generates the level one (L1) trigger.

The GTP sends the trigger to the Trigger Supervisor (TS) which makes sure the system is ready to accept a trigger and sends the accepted signal to Trigger Distribution boards which are linked to the Trigger Interface (TI) boards in each crate via optical links as represented in Fig. 128. The trigger and synchronization clock signals are then sent back to individual crates and payload modules through Trigger Distribution (TD) boards and Signal Distribution (SD) boards which distribute the signals to electronics such as the FADCs. Once a trigger is generated, the full resolution data which is still in the pipeline, is readout out using a serial VXS link at a data rate of 8 Gbit/s corresponding to 1 GB/s. As this is a point to point connection, the aggregate full crate bandwidth is 16 GB/s, giving plenty of headroom for FADC readout.

13.2.1 GEM readout

The GEM detectors will be readout with the VMM3 chip [304] which was developed for New Small Wheel Micromegas tracker for the ATLAS detector. This 64 channel chip has analog shaping from 25 to 200 ns and includes a built-in ADC and TDC as shown in Fig. 129. The chip has multiple FIFOs (Fig. 130) which allows for deadtimeless operation of each channel up to a 4 MHz trigger rate.

Data is output from the chip at 640 Mbps (effectively 560 Mbps due to 10b/8b encoding). The ADC, TDC and timestamp data is a 38 bits. If all channels fire continuously, the trigger rate is limited to 230 kHz, which exceeds the SoLID requirement. The VMM3 has similar radiation hardness as previously foreseen chip APV25 and has been tested at a 2 Mrad level without showing major degradation.

In the rest of the document most of simulation results were done with the APV25, a GEM readout chip currently in use at JLab. Extensive simulation of the VMM3, similar to what was done for the APV25 chips, will be done. Preliminary simulations of VMM3 with a shaping of 50 ns give similar or better results as the APV25 with the main difference being that the processing is done on the chip improving the data bandwidth thanks to zero suppression. These simulations will be confirmed by bench and beam tests.

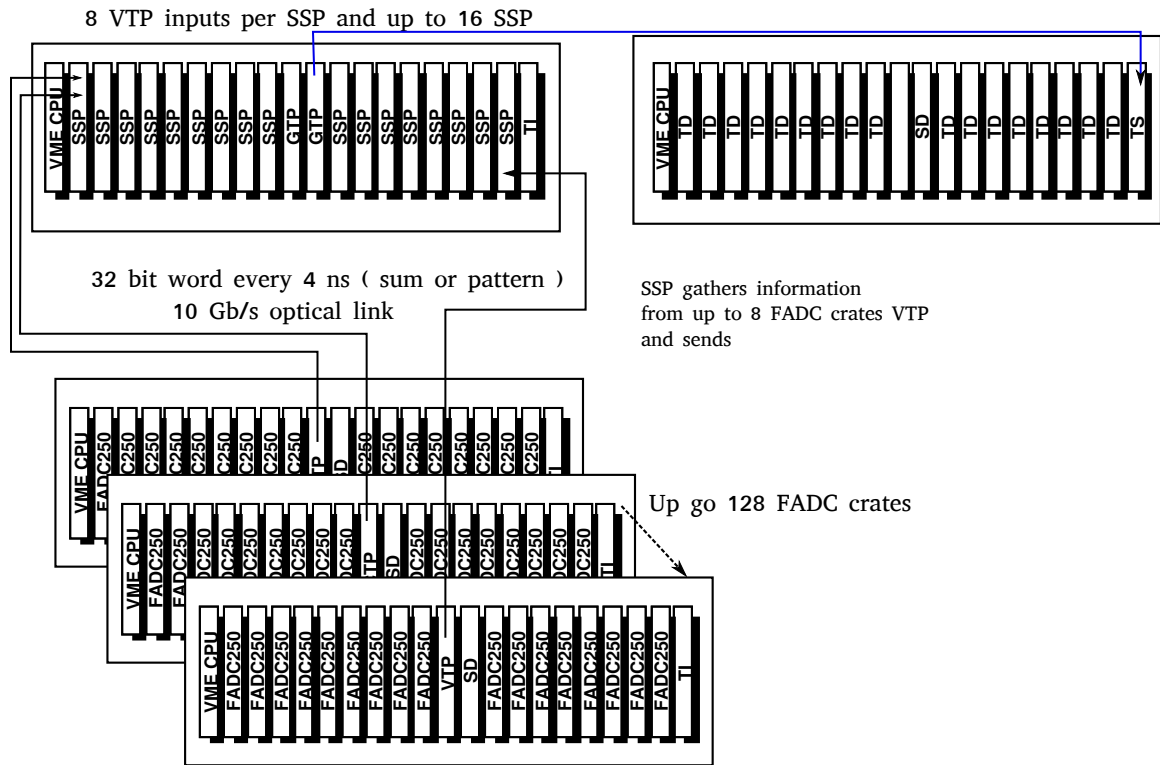


Figure 128: Standard Triggering scheme using the JLAB pipeline electronics

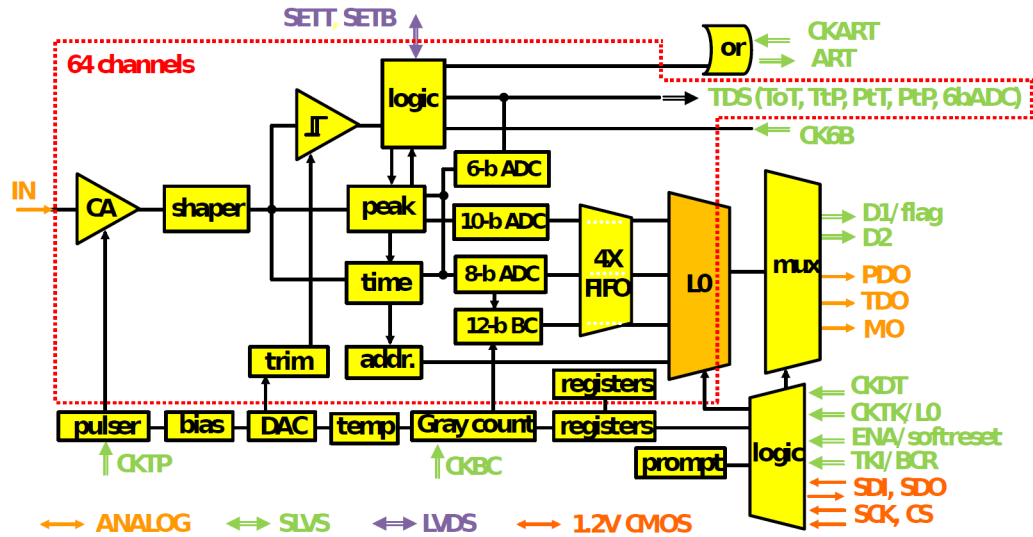


Figure 129: VMM3 functional diagram

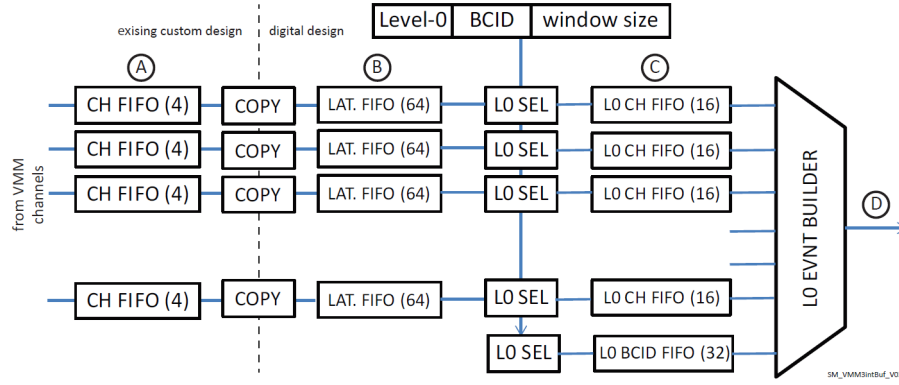


Figure 130: VMM3 multilevel FIFO design

Detector	Channel
EC Shower	1800
EC Preshower	1800
SPD	300
Light Gas Cherenkov	270
Heavy Gas Cherenkov	480

Table 26: Detector channel counts for the SIDIS and J/Ψ experiments, excluding the GEMs.

Implementation of the chip will use a similar design as the MAROC chip design for CLAS12. A front-end board holding the chip mates with the GEM detector. The data from four VMM chips is collected by a FPGA board and the gathered data is sent on a 6.25 gbit optical link to a JLab Sub System Processor (SSP) board for read out. Each SSP will be able to accept data from 128 VMM chips.

13.2.2 SIDIS Configuration

The SIDIS experiment will use a similar detector setup as the PVDIS experiment with the addition of more detectors. Scintillator planes will be used to reduce the photon background as the PVDIS baffles will be removed. A Heavy Gas Cherenkov will be added for π/K separation. The PVDIS crates will serve as the basis of the SIDIS DAQ, but the signals from the VTP will be sent to the SSP and GTP in an additional crate to make a coincidence trigger. The additional detectors will be instrumented with FADCs.

Based on current simulations, the size of each event is expected to be about 31.1 kBytes including signals from all detectors. So for a SIDIS ^3He rate of 100 kHz (coincidences plus prescaled singles) a data rate of 3110 MB/s is expected.

The SIDIS experiment trigger formula is

forward angle electron trigger Forward Angle Calorimeter *AND* Light Gas Cherenkov *AND* SPD

large angle electron trigger Large Angle Calorimeter *AND* SPD

forward angle charged particle trigger Forward Angle Calorimeter *AND* SPD

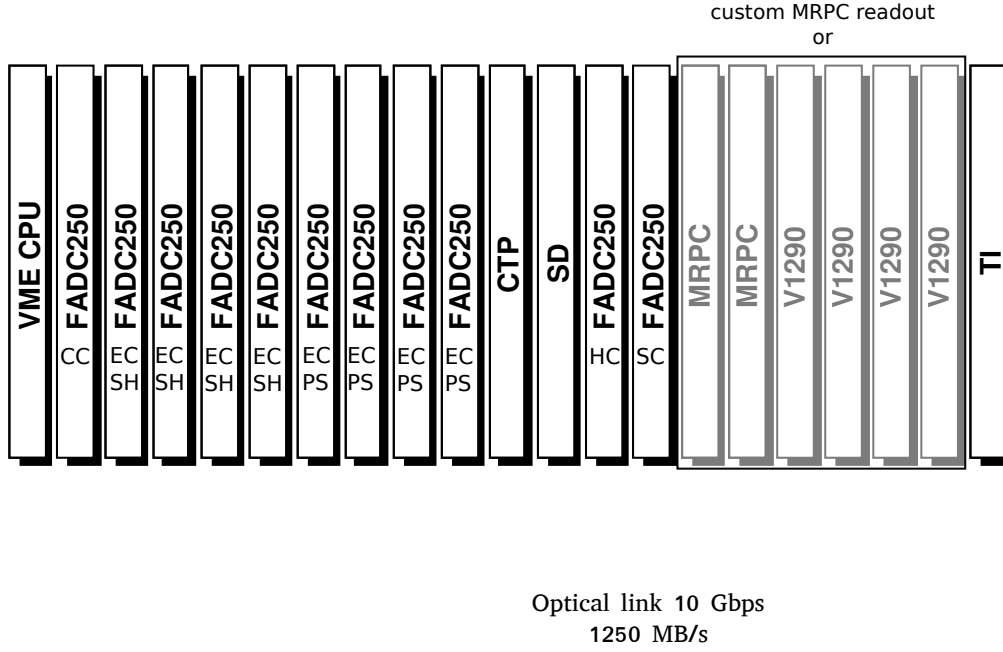


Figure 131: SIDIS FADC crate layout

coincidence electron trigger (large *OR* forward) *AND* forward angle charged particle trigger

The SIDIS experiment and J/Ψ will use the same detector configuration, cabling, DAQ and trigger hardware. The only difference is that the DAQ will be configured to trigger on a high energy electron and a pion for SIDIS while for J/Ψ it will trigger on 2 high energy leptons.

SIDIS GEM rates As the DAQ for the SIDIS experiments can not be segmented into a separate DAQ chain for each sector, the event size is an important factor in keeping the DAQ throughput below limits to the overall data rate that can be recorded. The occupancy of the detector is fairly low compared to PVDIS, we expect the DAQ to handle at least 100 kHz of trigger rate.

13.2.3 PVDIS Configuration

Calorimeter trigger for PVDIS There are currently two options to generate a Level-1 (L1) trigger from the calorimeter. The standard option is to use the sum of the 16 FADC channels which is computed and sent to the VTP every 4 ns. The VTP can add all the FADC sums, generating a global sum for each crate and generating a trigger when that sum exceeds a threshold. Another scheme was devised for the Heavy Photon Search experiment in Hall B. In this scheme 16 bits of data for each of the 16 FADC channels is sent every 32 ns as in Fig. 134. These data contain both the signal amplitude, and the timing (to a 4 ns resolution) of any threshold crossing. With the VTP receiving a signal from all the calorimeter elements, it can compute the signal sum, in parallel, of every possible cluster of one central and 6 surrounding blocks. This approach of triggering on the cluster sum can reduce the number of triggers coming from background and improve online pion rejection.

Chamber	Occupancy	Hits per sector	Hits detector
1	2.37	21.5	644.2
2	7.98	81.4	2441.9
3	3.4	39.6	1189.3
4	2.24	31.5	943.5
5	2.03	21.1	633.4
6	1.52	19.4	583.7
Total hits		6435.9	193076.8
Event size 1 sample (Kbytes)		945.3	28408.4
Data rates 100 kHz (Mb/s)		94.5	2840

Table 27: SIDIS GEM occupancies and event size for GEM

Table 28: Channel counts of individual detectors for PVDIS for one sector

Detector	Module Type	Number of Channels	Number of Modules
Electromagnetic Calorimeter (EC)	FADC	122	8
Light Gas Cherenkov (GC)	FADC	9	1
GEM	MPD	4700	1

Particles near the edge of a sector will likely shower into calorimeter blocks in the adjacent sector. In order to avoid inefficiencies near the edges of sectors, VTPs for neighboring sectors will share information through bidirectional optical links as shown in Fig. 133. Once the VTP receives all the FADC data from its own crate and the two adjacent crates, it either computes the total sum or performs cluster searching to generate trigger. If the cluster trigger method is used, a 64 bit pattern containing the FADC channels to be readout will be generated by the VTP and transferred to the Flash ADC using the trigger data path. A new firmware for the FADC will be developed to take this pattern into account allowing each FADC to only read the channels that are part of a cluster in order to reduce event sizes.

Gas Cherenkov trigger Both Cherenkov detectors are divided into 30 sectors. The most straightforward way to generate a Cherenkov trigger is to put all the channels of a given sector (9 for the light gas and 16 for the heavy gas) into one FADC board and generate the trigger in the VTP by putting a threshold on the sum of the PMT signals. To improve efficiency at the interface between two sectors one can include a threshold on the sum of the two adjacent sectors. If the combinatory background is too large, a clustering scheme similar to that discussed for calorimeter could be used. The efficiency and background of the different schemes has been evaluated in the full simulation of the digitized background. This simulation shows that a simple trigger based on PMTs sums works and has a sufficient efficiency.

PVDIS GEM rates In order to estimate the per event size of data from the GEMs, the GEM signal and the APV25 digitization process were modeled in a simulation. This simulation is detailed in the simulation section 12.2.4 of this document. The total number of GEM strips firing in a 25 ns window was computed without and with deconvolution. The last column are the results coming from the Table 19 in the software GEM digitization Section of this document.

Chamber	Occupancy (%)	Hits	Occupancy with noise cut (%)	Hits after noise cut
1	21.2	244.8	10.0	115.2
2	10.3	142.2	5.1	70.2
3	8.8	121.0	4.4	60.7
4	3.1	70.2	1.6	37.5
5	2.8	65.6	1.5	35.2
Total hits		643.8		159.8
Event size 3 samples (Kbytes)		7.9		3.9
Data rates 20 kHz 3 samples (Mb/s)		159.8		79.2

Table 29: PVDIS GEM occupancies and event size for GEM

For PVDIS, we are interested in the data rate per sector. The numbers in Table 29 are evaluated for 20 kHz (15 kHz rate + 5 KHz of safety margin). Even though occupancies are high, the data rates for PVDIS are reasonable (about 80 MB/s per sector) and simulations show that tracks can be efficiently identified if a 3 sample readout is used. The 3 sample readout will allow for more effective offline rejection of pile up. The deconvolution and filtering are also able to significantly reduce the occupancy and event size. Using the MPD system, each module can transfer up to 1Gbps through its optical link. A fraction of the GEMs will be readout using the VMM3 chip which has a faster integration time and digitizes the signal internally by only sending data for channels with hits. Simulations show that the improved timing resolution of the chip gives similar results to the APV25.

13.3 Event size from FADC

The FADC samples are 12 bits at 250 MHz. In the case of PVDIS, since pile up is going to be significant, we plan to record the entire waveform. As pulses are 40 ns wide, we will record 10 samples for each detector channel. FADC events have a 4 byte block header, a 4 byte block trailer, a 4 byte event header and pack 2 samples into each 4 byte word. For a 10 samples size, the event size per module is thus $(12 + 4 \times (10n/2))$ bytes where n is the number of channels firing.

The FADC simulation with digitization is still being developed. Given the size of a sector, the event size will be estimated with a maximum of 2 clusters of 7 for shower and 2 clusters of 7 preshower and assuming all 9 PMTs of the Cherenkov fire all the time. With this assumption the event size is 1480 bytes per event.

With a trigger rate of 20 kHz, this gives 29.6 MB/s data rate, well under the VXS backplane transfer rate limit of 1.25 GB/s per link.

In the case of SIDIS, the occupancy on the detector is small enough that only pulse integrals need to be recorded. The estimated event size using the occupancies from the simulation is 31.2 KBytes, which gives an aggregate data rate, including GEMs, of 3110 MB/s at 100 kHz for all 30 crates.

13.4 Data rates, event size, and tape storage

A JLab network upgrade, completed in 2014, provided two 10 Gigabit Ethernet links between the Hall A counting house and the computer center. It is expected the transceiver will be able to be

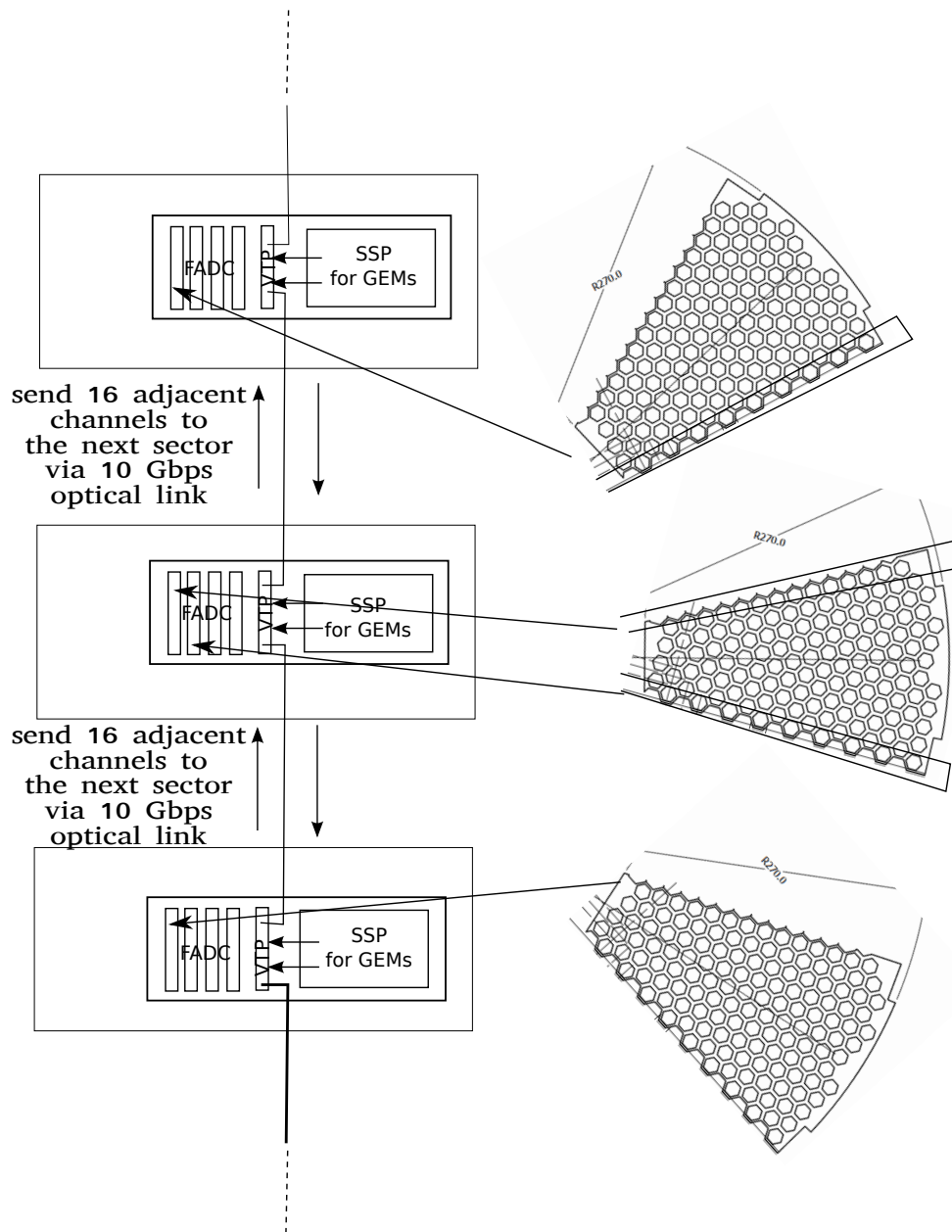


Figure 133: PVDIS specific electron trigger

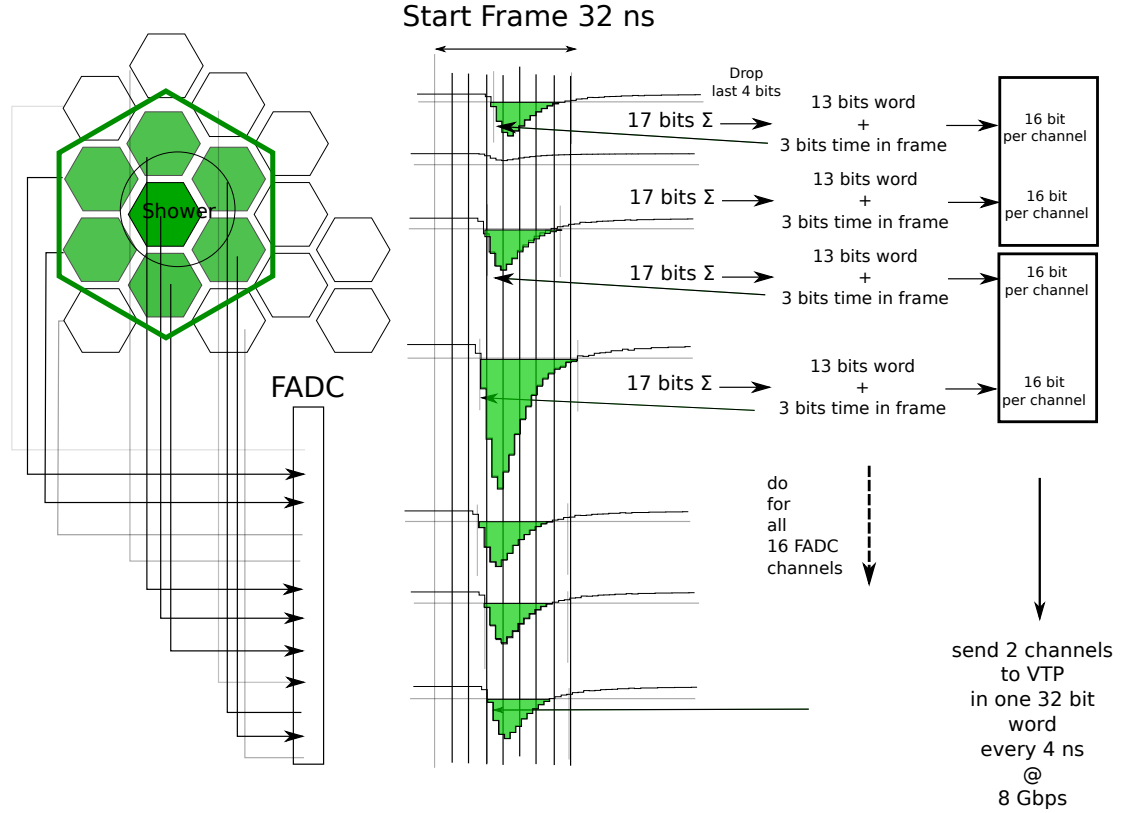


Figure 134: Calorimeter clustering scheme using the HPS algorithm. All calorimeter signals are sent to the FADC.

upgrade to 100 Gigabit Ethernet by the time SoLID runs giving a 12.5 GB/s bandwidth to the counting house. Additional fibers are also available if needed so it is reasonable to expect the link between counting house and computer center to be sufficient for SoLID. Currently the JLab tape silo system can hold up to 11,240 tapes giving, with compression, a current capacity of 47 PB using LTO6 drives. The computer center out year budgets include plans to add a second silo, giving a storage capacity of 22,480 tapes and 48 drives. Assuming the evolution of LTO technology (shown in table 31 below), a fully upgraded silo would hold up to 919 PB of data using LTO10 technology with a 13.2 GB/s data rate per drive frame or 26.4 GB/s for the whole silo. With the planned second two frame silo system (24 drives) the total capacity would be 1840 PB with a data transfer rate of 13.2 GB x 4 = 52.8 GB/s, accommodating the needs of SoLID and the other halls.

LTO version	4	5	6	7	8	9	10
Availability	2008	2010	2012	2015	2018	2020	2023
Capacity/tape (TB)	0.8	1.5	2.5	6.25	12.8	25	48
Data rate/drive (MB/s)	120	140	200	300	472	708	1,100
Compression	2	2	2	2.5	2.5	2.5	2.5

Table 31: LTO tape drive evolution.

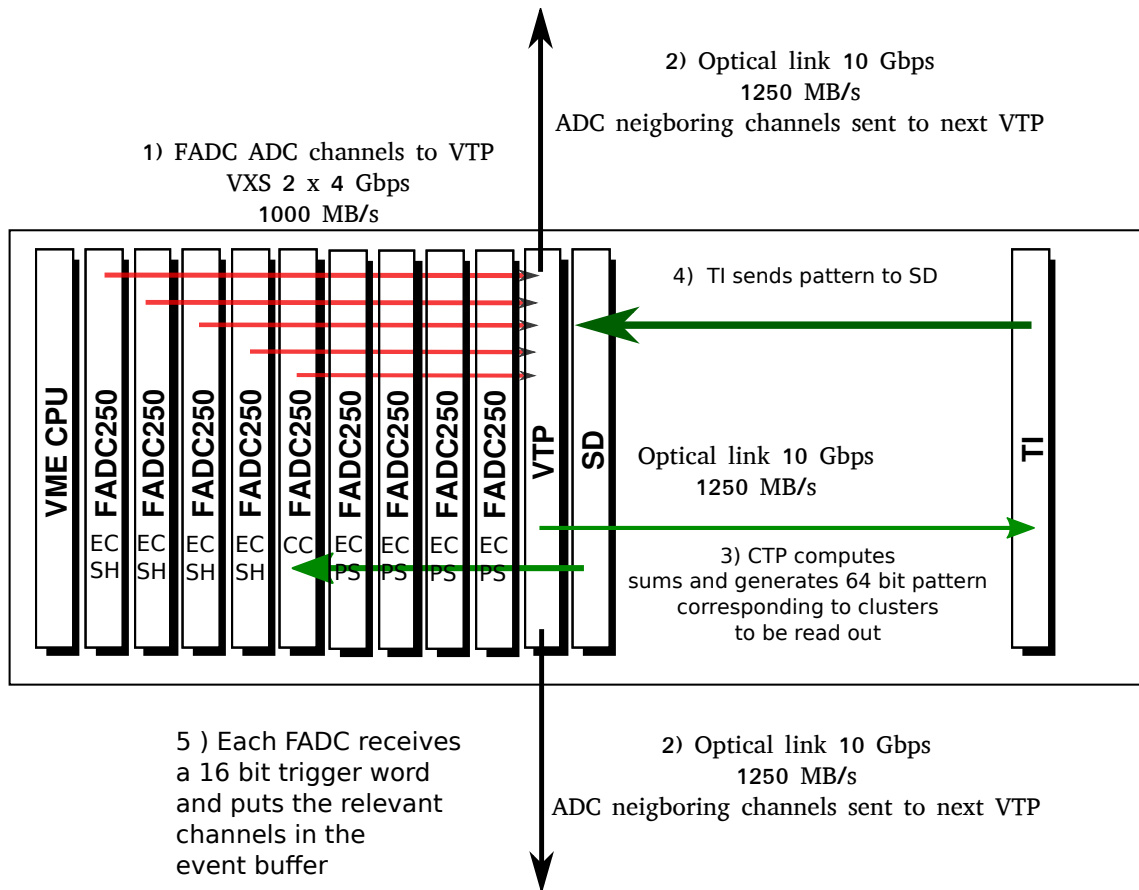


Figure 135: PVDIS FADC crate layout

The total amount of data from all SoLID running will total to about 380 PB representing about 20 % of the future silo size.

13.5 Hall DAQ installation

The DAQ for both the SIDIS and PVDIS configurations will be located in the hall. As is typically done, a shielded bunker will be constructed to house the data acquisition electronics, protecting them from beam induced radiation. This bunker will contain ~ 15 racks hosting 32 VXS crates and the crates containing the GEM front-end cards.

Approximately 4500 coaxial cables (RG58) will connect the PMT based detectors to the ADCs in the bunker. HDMI cables will connect the detector mounted GEM chips to the front end cards.

13.5.1 Experiment switch over

Switch over of the DAQ electronics between the PVDIS and SIDIS setups will be relatively straightforward. Changing to the PVDIS setup, the VTP module in each sector's crate will connect directly to the TI module in that crate to give an L1 trigger signal for that crate and the corresponding GEM electronics. The unused SSP, TD and TS, and VTP modules as well as ADC and TDC modules for detectors not in PVDIS will be removed from the hall to avoid extra radiation dose.

13.6 Managing data rates

Managing total data rates for SoLID will require careful system design to avoid bottlenecks. While the PVDIS configuration has the highest overall trigger and data rate, the segmentation of SoLID into 30 nearly independent sectors allows for natural parallelization. The data rate per sector is a few hundred MB/s. The parallel data paths can be preserved through the event builder (that combines VME and GEM data), to temporary disk storage, through parallel network paths, and through an L3 farm before merging into a smaller number of paths for storage on tape.

The SIDIS configuration is more challenging as the data for each event is spread over 30 VME systems and 30 sectors of GEMs which must be combined to build events. It is presently not feasible to build events from these 60 sources into single data stream of over 3 GB/s. This can be overcome with the option in CODA of multiplexing events to multiple event builders. A possible architecture would have up to 60 ROCs pushing data to several primary event builders so that each event builder handles a more modest data rate. (One event builder for the VME crates and several event builders for the GEM data.) Each of these primary event builders, which contains a fraction of each event, would feed, in round robin fashion, several secondary event builders. Each secondary event builder would build complete events, but only have a fraction of a given run's events saved to its disk cache. This architecture is scalable such that bottlenecks can be mitigated by using a sufficient number of primary and secondary event builders.

13.7 Summary and Pre R&D plans

The conceptual design of the SoLID data acquisition system is based on hardware that has already seen use with beam at JLab. While SoLID's trigger rate and total data rate exceed what has been achieved by detectors such as GlueX and HPS, it is expected that it is feasible to meet the requirements with careful system design, hardware firmware improvements and upgrades to the CODA software.

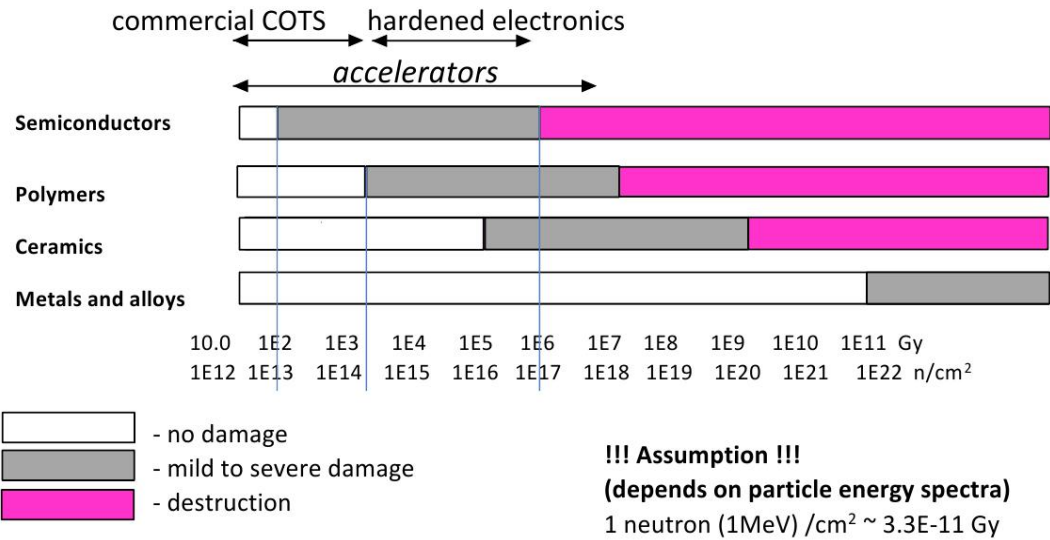
The collaboration has proposed a Pre R&D plan with a DAQ component to understand the capability and limitations of the conceptually designed system.

The goals of the DAQ Pre-R&D plan:

- Prototype new GEM readout (VMM chip based) performance
- Develop fast FADC readout method required for PVDIS DAQ
- Prototype calorimeter trigger algorithms
- Prototype PVDIS and SIDIS overall trigger algorithms, including trigger and data sharing between SoLID detector sectors
- Determine full system deadtime for PVDIS configuration
- Prototype Cherenkov readout and triggering schemes
- Demonstrate required timing resolution for time-of-flight particle ID
- Provide a DAQ system for in beam detector tests

14 Radiation damage estimates and Activation

The simulation and background calculation software for SoLID is using the two simulation packages with independent code base (Geant4 and FLUKA [307] [308]). This allows for independent cross checks both in geometry and in physics modeling. At the same time the two codes each provide unique capabilities expanding the overall reach. FLUKA provides useful tools that simplify the study of radiation damage and estimates, but the physics processes present in the simulation lack of direct electro-nuclear dissociation and fragmentation models. Such electro-nuclear reactions are dominant in the neutron production from the liquid Deuterium target at high energies (see figure 141). If one just considers the neutron photo-production, both codes (GEANT4 and FLUKA) have really good agreement with experimental cross sections, as shown in figure 139 and 140. A full simulation and tests are underway in order to construct a better and common target background generator for both simulation packages (see figure 141). To have a first idea of the tolerance of different materials to radiation damage, see figure 136. As a weighting factor to estimate the effect



© Lockheed Martin

Figure 136: Estimate of the tolerance of different material to different level of radiation exposure given in Gy and $\frac{\text{neutron}(1\text{MeV})}{\text{cm}^2}$. This is just a first order approximation and a detailed analysis of each equipment is needed in order to establish the correct radiation tolerance of each detector/material

of radiation damage on electronics, we used in parallel to the calculation of full Dose estimates, the Displacement damage in silicon, on-line compilation curves by A. Vasilescu (INPE Bucharest) and G. Lindstroem (University of Hamburg). These curves assume that the damage effects by energetic particles in the bulk of any material can be described as being proportional to the so-called Non Ionizing Energy Loss and normalize the damage in Silicon to the one caused by a 1 MeV neutron (more details can be found here [310]).

14.1 Radiation damage to GEM electronics

A simulation in order to test the radiation level on the GEM foils has been done. The comparison to the estimated radiation level of the CMS experiment, which shares the part of the electronics

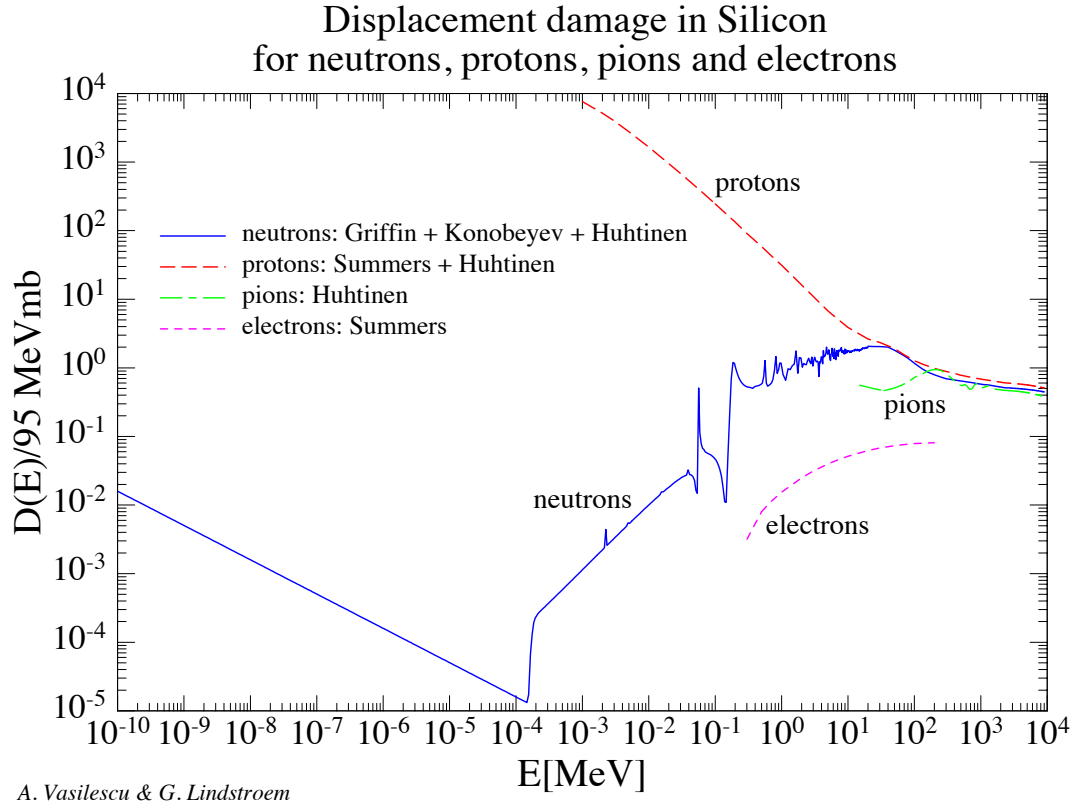


Figure 137: Not Ionizing Energy Loss curves to 1MeV equivalent damage in Silicon for electrons, pions, neutrons and protons

most susceptible to radiation damage for the GEM chambers detectors, permitted us to establish a radiation limit flux for our expected running time. Already with our first conceptual design of the shielding we are able to reach tolerable radiation levels also in the first layer of the GEM chambers (the one that is supposed to sustain the highest radiation fluxes). This result is shown in figure 142.

14.2 Power deposited

A detailed study of the power deposited in the SoLID spectrometer has been done in order to detect areas of possible activation. In these areas, in order to define possible activation, the FLUKA simulation has been used as a tool, and particle fluxes were provided by GEANT4 for areas where the particle fluxes estimated by FLUKA were known to be incorrect. FLUKA in fact provides many good tools for activation and radiation estimates, but it lacks direct electro-nuclear dissociation-fragmentation models and has limitations in producing more complex geometries, like the Baffle design for the PVDIS experiment in SoLID. In the following study of activation, GEANT4 has been used as a common input for an estimate of the background radiation in areas where direct electro-nuclear dissociation-fragmentation models are important.

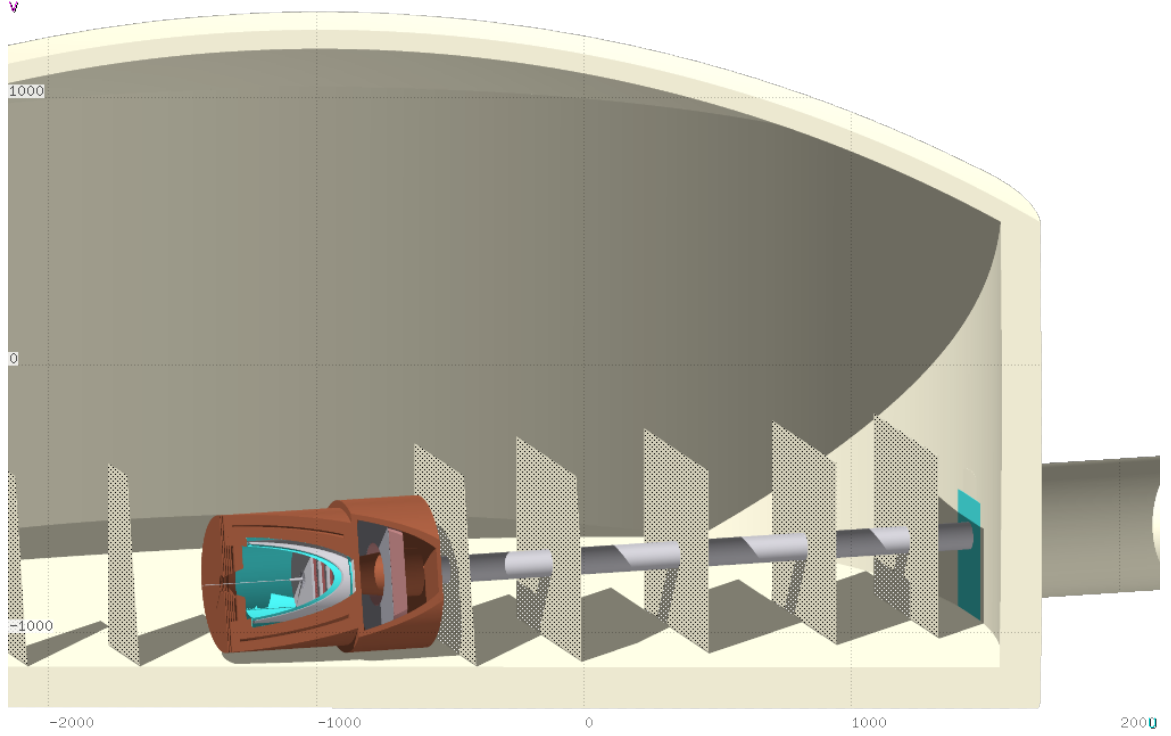


Figure 138: FLUKA simulation for the PVDIS experiment with SoLID.

14.2.1 Power in 1st baffle (due to Möllers), (Cooling, activation)

The first baffle, due to its proximity to the Deuterium target in the PVDIS configuration for SoLID, has a power deposition of $\sim 8W$ for a beam current of $50\mu A$ and an energy of 6.6 GeV. The high production of neutrons from the Deuterium target can be an ulterior source for activation in the baffle. For this reason an investigation of the possible activation has been done. In this study, it has been considered at the same time the radiation coming from the target and from the baffle itself that “self-irradiates” different parts of its structure. The impact of activation due to the utilization of different materials have been directly studied (see 143) for the first baffle. In order to optimize the computing time and avoid issues of pixelization due to the detailed shape of the baffle, a single block of material was used in this study. Using a single block means that the solid angle coverage seen by the main source of radiation (the target) of the baffle is not the same as in the real case: The radiation calculated should be scaled accordingly or used as an extra safety factor since we are relying just on simulations.

These results (see show the Dose equivalent radiation spatial distribution for 3 different cooling times. This study (see figure 143) shows, for example, that, in order to survey the area in proximity of the first baffle, one should wait around 1 day of cooling, in order to reach level of radiation tolerable. The Residual nuclei activated in the Lead baffle are shown for the same cooling time in the bottom plots of figure 144.

14.2.2 Power in exit hole in magnet (elastics) (Cooling, activation)

Another spot for possible activation will be the part close to the exit hole of the magnet. Further investigation will need to be done, after a final design of the magnet will be reached, but it is expected to be less important than the activation on the first baffle, due to the distance to the target and to the

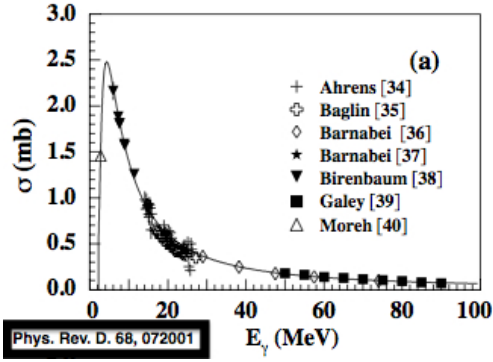


Figure 139: Neutron cross section for photo-production [309]

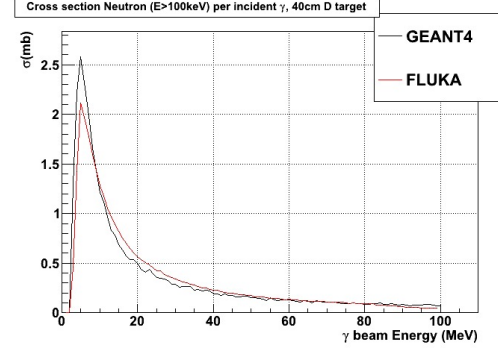


Figure 140: Test for Neutron cross section for photo-production with FLUKA and GEANT4

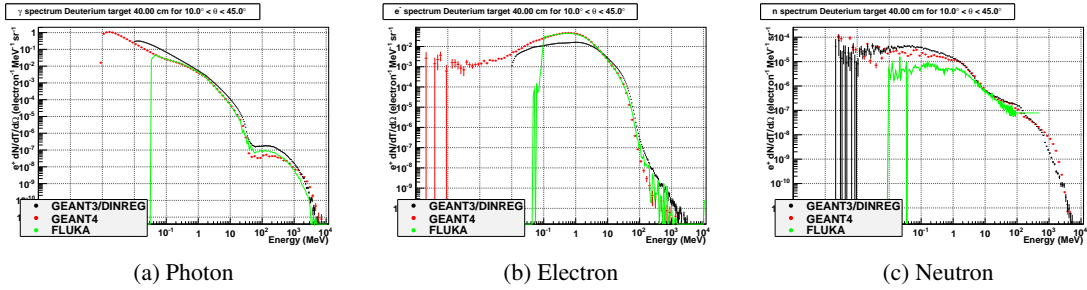
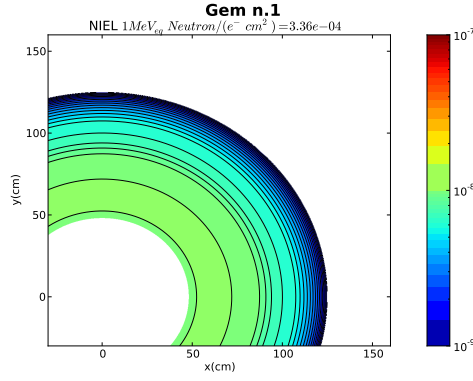


Figure 141: Background comparison produced from GEANT3(DINREG), GEANT4 and FLUKA with 40cm of Liquid Deuterium. What's Plotted here is the $\frac{d^2N}{dT d\Omega}$ per incoming electron in the angle range of $10^\circ < \theta < 45^\circ$ for γ (a), e^- (b) and n (c)

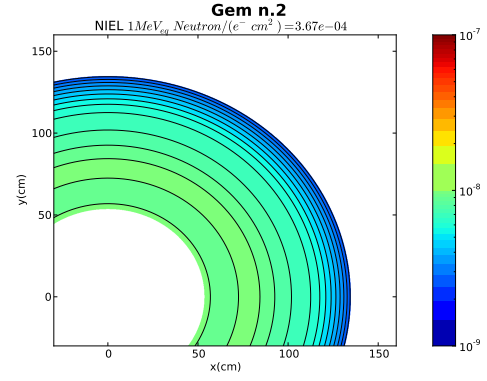
less intense and less localized radiation. This situation has been investigated and compared to the PVDIS design, because it is the one with the expected highest activation of all the configurations with SoLID, with the proximity of the lead baffles to the target (see this section at page 173). This has been done in order to compare power deposition to have a first idea of possible activation areas. The levels of power deposited in the exit hole of the magnet are at least lower by one order of magnitude with respect to the one expected in the first baffle, as shown in figure 145a and 145b. The integrated value (using the cylindrical symmetry) over the higher area of power deposition in the exit hole of the magnet has a maximum of $\sim 0.9W$ per cm in the z direction and is mostly constant over the full internal section of the exit hole with $r_{xy} < 40cm$ (color scale of $\sim 3E-04$ in figure 145a). This compares to a full power deposition on the first baffle of $\sim 20W$, running in the same conditions. A power deposition estimate for the beam-line downstream is shown in figure 145b. As one can see in 146c, the impact of the configurations like SIDIS is considerably smaller on the activation in this area.

14.2.3 Power in the entrance surface of the magnet (Cooling, activation) (external target configurations)

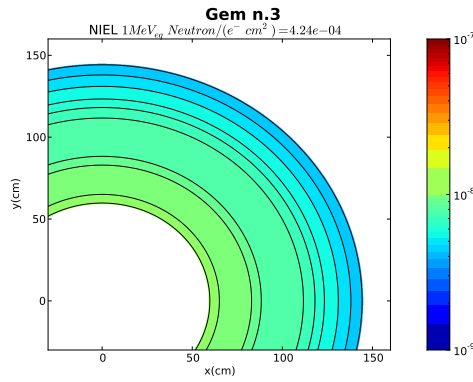
With configurations like SIDIS that have the target positioned outside the magnet, there is a consistent power deposition in the front part of the magnet. Some simulations have been done in order to estimate the possible activation in this area. The results of these studies are presented in figure 146



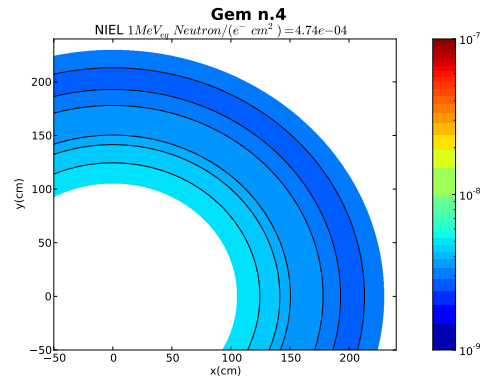
(a) NIEL weighted 1MeV equivalent neutron flux per cm^2 per incident electron on the 1st GEM foil



(c) NIEL weighted 1MeV equivalent neutron flux per cm^2 per incident electron on the 2nd GEM foil



(b) NIEL weighted 1MeV neutron equivalent neutron flux per cm^2 per incident electron on the 3rd GEM foil



(d) NIEL weighted 1MeV equivalent neutron flux per cm^2 per incident electron on the 4th GEM foil

Figure 142: The CMS experiment dose rates are expected to be of the order of 10 MRad(SiO_2) ($5 \times 10^{13} \frac{n}{cm^2}$). This translate for us, assuming 2000 hours of beam at $100\mu A$, into a flux of $\sim 1.1 \times 10^{-8} \frac{1MeVeq n}{e^- cm^2}$. This puts us on the same level of radiation that the APV25 chip was built to tolerate.

and show the areas of power deposition in the magnet and in the front surface of the magnet. As expected the areas of possible activation are the areas more exposed to the target radiation and the collimators positioned in front of the nose-cone of the magnet.

14.2.4 Heat load in magnet cryostat

A detailed design of the cryogenics and coils of the CLEO II solenoid has been obtained and we constructed a detailed model that replicates key components of the magnet (see Fig.147). Particular attention was put in to well represent:

1. the 3-5 mm of stainless steel which is the inner bore of the cryostat
2. the 3-5 mm of aluminum thermal shield 3-5 cm beyond (1)
3. the 6+ mm of stainless steel which is the helium vessel
4. any winding forms left at the inner diameter of the coils

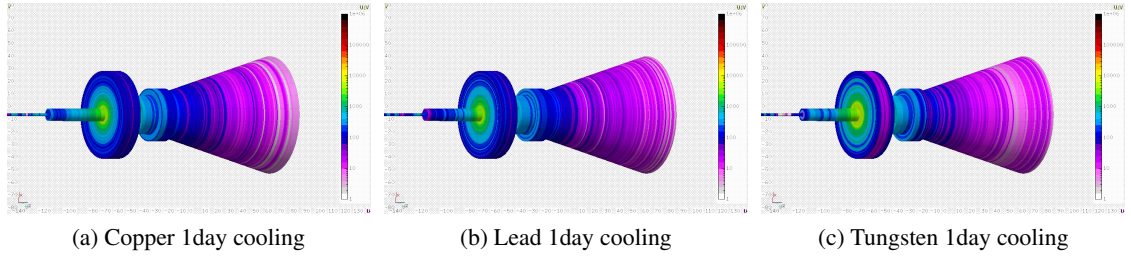


Figure 143: First Baffle: Activation studies have been calculated for 3 different Cooling times (shown here after 1 day), after an assumed exposure to the beam of 3 separate full weeks interleaved by a down time of 4 days. (143a, 143b,143c) The dose is expressed in $mrem/h$ and its spatial distribution is shown.

5. the copper matrix in which the Nb-Ti is embedded. Typical conductors of the era were 66-80% copper with balance Nb-Ti (2:1 to 4:1 Cu:SC).

After updating the design, a detailed calculation was done with the PVDIS configuration with Deuterium as its target. This configuration, with the Deuterium target inside the magnet, is the one among the different SoLID configurations that presents the highest flux of neutrons on the Coils. An integrated dose was calculated and determined using the cylindrical symmetry of the system and the flux calculated per cm^2 on the more susceptible parts of the magnet. An integrated dose of $10^{17} \frac{1MeV_{neutron}}{cm^2}$ is needed in order to start to see some modification on the Critical Current (I_c) of the magnet. A map of the integrated dose for the PVDIS and D_2 case was created and presents peaks for the integrated fluxes around $10^{14} \frac{1MeV_{neutron}}{cm^2}$, well below the tolerance level of the magnet. As a consequence, also even if it is not known what is the current level of exposure reached by the CLEO-II solenoid, the full scientific outreach that is planned at this moment with SoLID does not seem to be going to affect considerably the lifetime of the coils of the magnet (see Fig. 148).

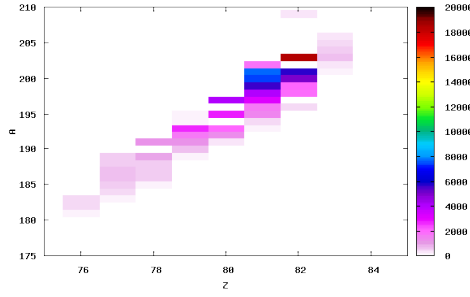
14.3 Estimates for radiation damage in the Hall

A study has been done in order to address possible radiation damage areas with the current SoLID design with no further shielding in place. This work has been done in order to address and pinpoint areas that will need to be further investigated when a final design for the magnet and electronics will be reached.

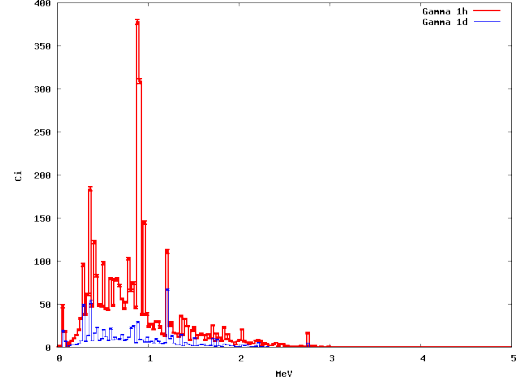
14.3.1 Radiation damage to electronics in Hall

The results of the different simulation runs suggest that the design of a shielding structure to minimize the radiation in the Hall seems not to be a priority, with the different layouts of the multiple configurations possible with the SoLID spectrometer as currently planned. In this study the magnet has been placed in a dome structure of concrete that mimics the presence of the Hall (It is important to consider that the SoLID spectrometer will not be placed in an open environment, but in a Hall full of equipment, with relative reflectivity that could cause an enhancement of the radiation present in the Hall). A few features of these results are in common among the different configurations for SoLID:

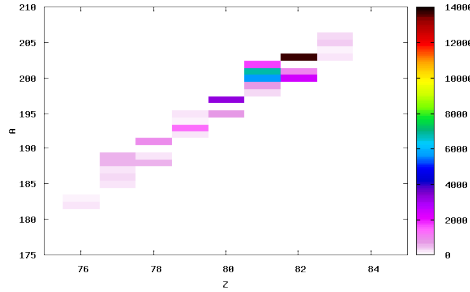
- The radiation damage estimated with the simulation is, as expected, consistently lower in the area outside the SoLID spectrometer with respect to the one inside the magnet.



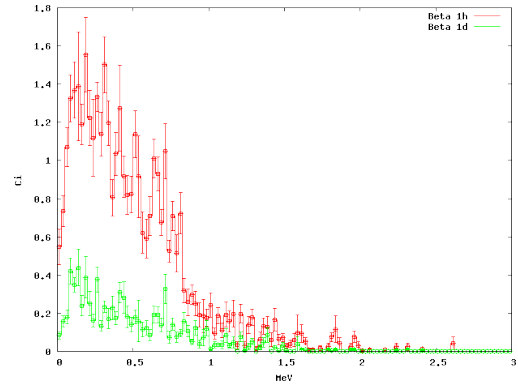
(a) Residual Nuclei for Lead Target after 1hour cooling (Z vs A)



(c) Photon Energy spectrum in Curie due to activation at 2 different cooling times



(b) Residual Nuclei for Lead Target after 1day cooling (Z vs A)



(d) Electron Energy spectrum in Curie due to activation at 2 different cooling times

Figure 144: (144a, 144b) The Residual decaying Nuclei are shown as a function of Z,A in the first baffle assumed it is made of Lead. The Gamma and Beta activities are also shown for the same decay time (144c, 144d). Determining the activity allows for establishing different needs for shielding at different times of the experimental running (repair or decommissioning).

- In the downstream part of the Hall, the predominant part of the radiation that escapes the magnet is present in the last part of the beam-line, enhancing the choice of keeping in the upstream section of the Hall for the existing left and right arm spectrometers.
- The configurations that have the target area external to the solenoid have also an high radiation area in the proximity of the target.

The configuration that gives the highest radiation estimates in this simulation study, is the PVDIS configuration with Deuterium target. The radiation damage estimate in this configuration is investigated in detail in the next section.

14.3.2 Radiation from beam pipe

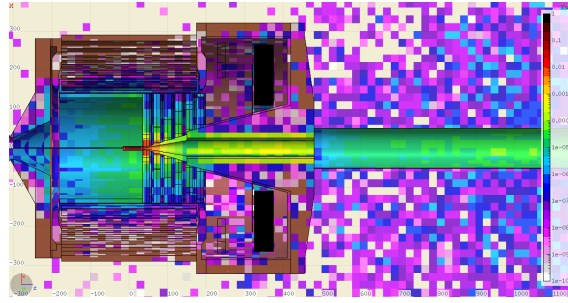
The main source of radiation leaking from the magnet to the Hall is from the downstream beam pipe. In order to quantify the leaking associated with the different SoLID layouts, different simulations have been carried out. The one that presents the biggest impact on possible damage to electronics is

the PVDIS configuration with a 40cm Liquid Deuterium target, but the localization of the leakage (close to the beam-line, see figures [149b](#) ,[149c](#) and [149d](#)), and the low level of radiation present, suggest that a shielding construction is not needed. If an additional factor of 10 reduction is needed, it can probably be reached by placing shielding material around the hot areas and around the beam-line. This shielding will be needed if not rad hard electronics will be placed in this area during the experiment If this area will be used during the experiment.

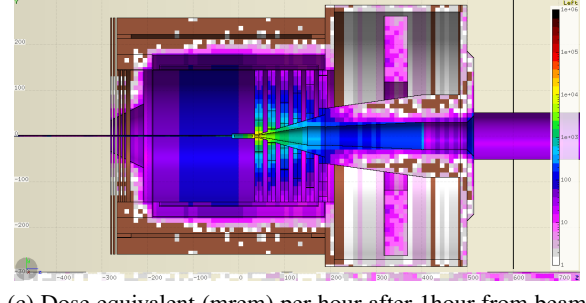
14.3.3 Radiation with external targets

Some of the configuration with the SoLID spectrometer, position their target in the proximity of the entrance of the magnet. Simulations have been done in order to evaluate possible high radiation areas for electronics. An example for the possible areas of high radiation with these layouts for the experiments is shown in figure [150](#) (SIDIS configuration with 3He target) and figure [151](#) (J/Ψ configuration with H_2 target).

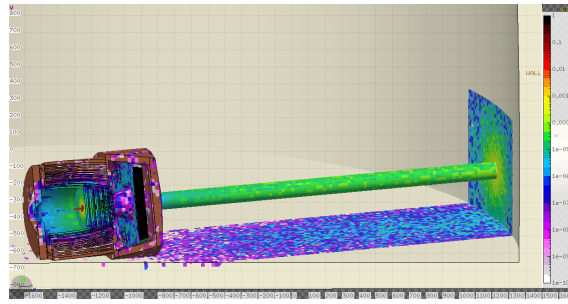
More details and plots on the studies can be found in [\[311\]](#).



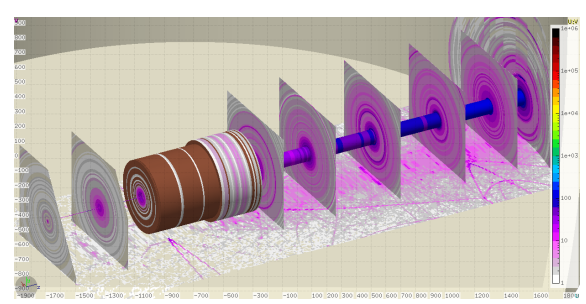
(a) Energy deposited (W) per cm^3 for PVDIS configuration and Liquid Deuterium target



(c) Dose equivalent (mrem) per hour after 1 hour from beam exposure for PVDIS configuration and Liquid Deuterium target

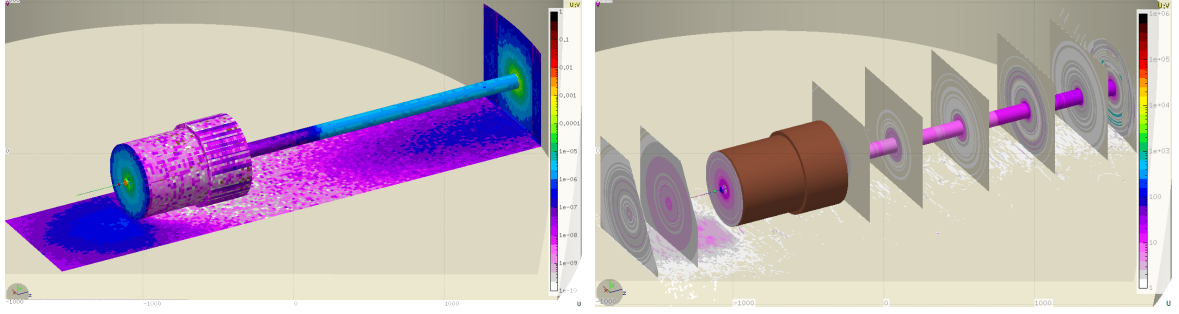


(b) Energy deposited (W) per cm^3 for PVDIS configuration and Liquid Deuterium target (Hall view)

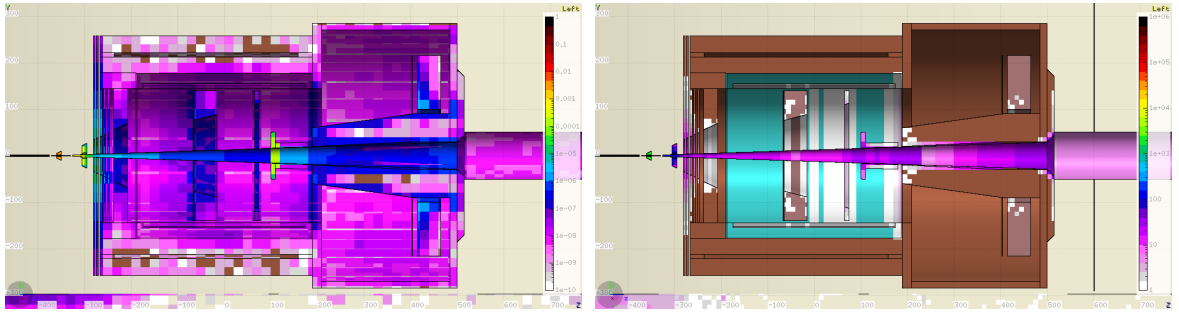


(d) Dose equivalent (mrem) per hour after 1 hour from beam exposure for PVDIS configuration and Liquid Deuterium target (Hall view)

Figure 145: Energy deposited (W) per cm^3 (145a and 145b) considering running condition with Liquid Deuterium target and electron beam current of $100\mu A$. The spectrum is averaged over blocks of size of $20cm \times 20cm \times 20cm$ in order to boost statistics, since this simulation with the complex SoLID design is highly demanding in CPU time. One can see how the power deposited in the first baffle region is considerably higher with respect to the one expected in the exit hole of the magnet. To obtain the integrated power deposition for the expected beam time for the PVDIS configuration (2000h), one multiplies the values of the plots by $7.2E+06$. Activation dose equivalent (mrem) rates per hour expected with the same configuration after 1 hour from beam exposure (a current of $100\mu A$ for a month with an efficiency of 70%) are shown in 145c and 145d. This study has been done in order to simulate the condition in the Hall during running time. For a more accurate description of the activation expected in the baffle area, see figure 143.



(a) Energy deposited (W) per cm^3 considering SIDIS running condition with 3He target and electron beam current of $15\mu A$ exposure for SIDIS configuration and 3He target (Hall view)
(b) Dose equivalent (mrem) per hour after 1 hour from beam exposure for SIDIS configuration and 3He target (Hall view)



(c) Energy deposited (W) per cm^3 considering SIDIS running condition with 3He target and electron beam current of $15\mu A$ exposure for SIDIS configuration and 3He target (Inside the magnet)
(d) Dose equivalent (mrem) per hour after 1 hour from beam exposure for SIDIS configuration and 3He target (Inside the magnet)

Figure 146: Energy deposited (W) per cm^3 (146a 146c) considering running condition with 3He target and electron beam current of $15\mu A$. In order to obtain the integrated power deposition for the expected beam time for the SIDIS configuration (3000h), multiply the values of the plots by $1.08E+07$. The main part of the energy is deposited, as expected, in the target area and in the collimator positioned in front of the nose-cone part of the magnet. The energy deposited in the exit hole of the magnet is considerably lower than the one with the PVDIS configuration. Activation dose equivalent (mrem) rate per hour (146b and 146d) expected with the same configuration after 1 hour from beam exposure ($15\mu A$ for a month with an efficiency of 70%). This study has been done in order to simulate the condition in the Hall during running time.

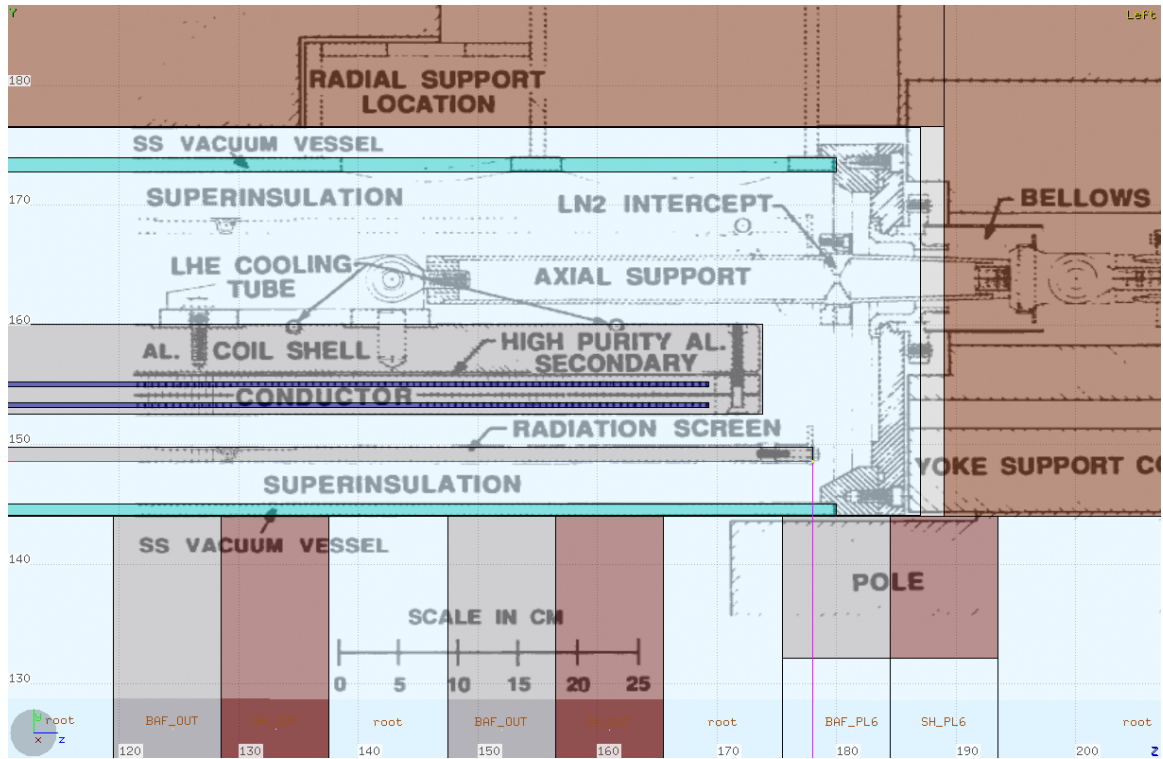


Figure 147: Existing engineering design for the CLEO magnet are put in comparison with the simulation design used for this study.

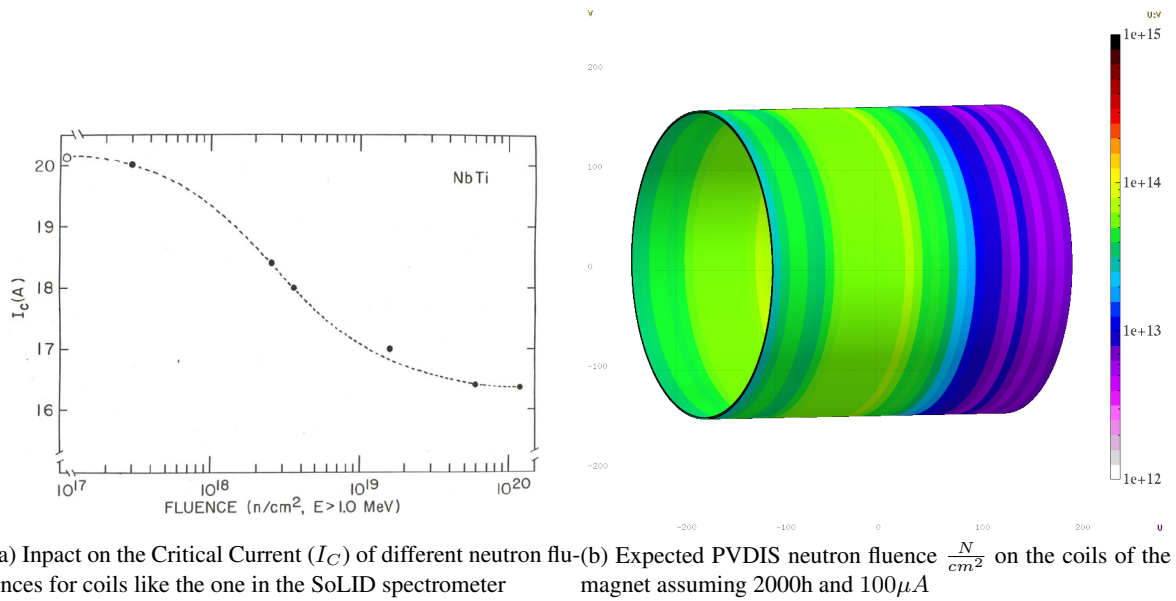
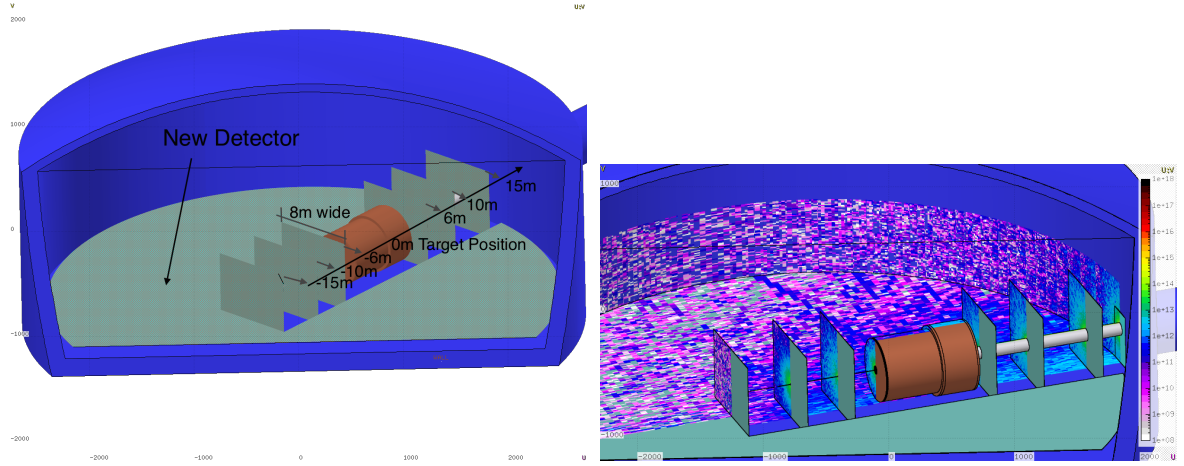
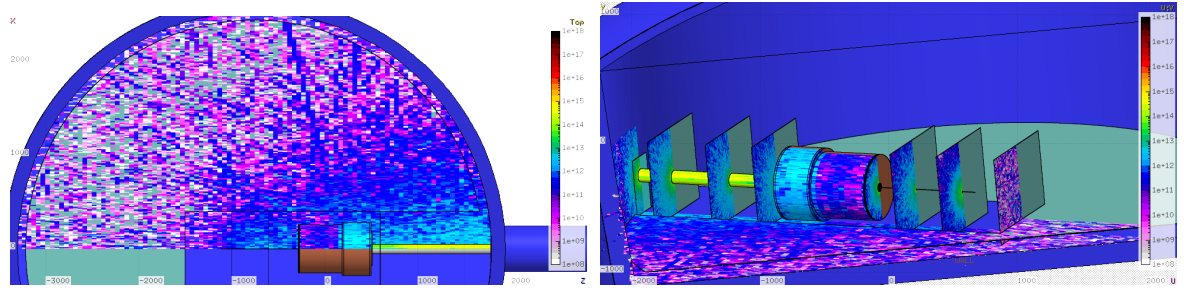


Figure 148: Expected exposure of the Solid magnet coil and expected impact of neutron fluence on Nb-Ti based coil for the Critical Current of the superconducting magnet.



(a) Positions of the different planes are shown, where in the (b) Estimate of radiation damage in the Hall with the SoLID spectrometer and the PVDIS configuration: A different view next plots the expected $\frac{N_{1MeV-eq}}{cm^2}$ integrated flux are shown. Different planes are put at different positions perpendicular to the beamline; A plane is also put parallel to the floor at 1m of height



(c) Estimate of radiation damage in the Hall with the SoLID spectrometer and the PVDIS configuration: A different view (d) Estimate of radiation damage in the Hall with the SoLID spectrometer and the PVDIS configuration: A different view

Figure 149: Estimate of radiation damage in the Hall with the SoLID spectrometer and the PVDIS configuration. The leading part of radiation present in the Hall for the SoLID spectrometer is leaking through the downstream part of the beam-line assembly. The plot shows the 1MeV Neutron equivalent flux per cm^2 on the volume surfaces estimated for 2000h of continuous running with a beam current of $100\mu A$ (This is the expected beam-time with the PVDIS configuration). In order to better show the behavior of the radiation leaking, different planed of observation have been inserted (at a distance from the target of $\Delta z = -15m$, $\Delta z = -10m$, $\Delta z = -6m$, $\Delta z = 6m$, $\Delta z = 10m$, $\Delta z = 15m$ (see Fig. 149a). The level of radiation leaking increases as one moves farther from the target, reaching a maximum $\leq 10^{15} \frac{N_{1MeV}}{cm^2}$. These levels of radiation are on the “mild to severe” damage range for commercial semiconductors (as one can see comparing them with Estimate of the tolerance of different material plots 136). This area is not expected to host any delicate equipment. On the upstream section of the beam-line, the level of radiation leaking is tolerable also for commercial equipment (not rad-hard). A comparable plot of this one, with a projection plane on the zy axis, is show in figure 149c

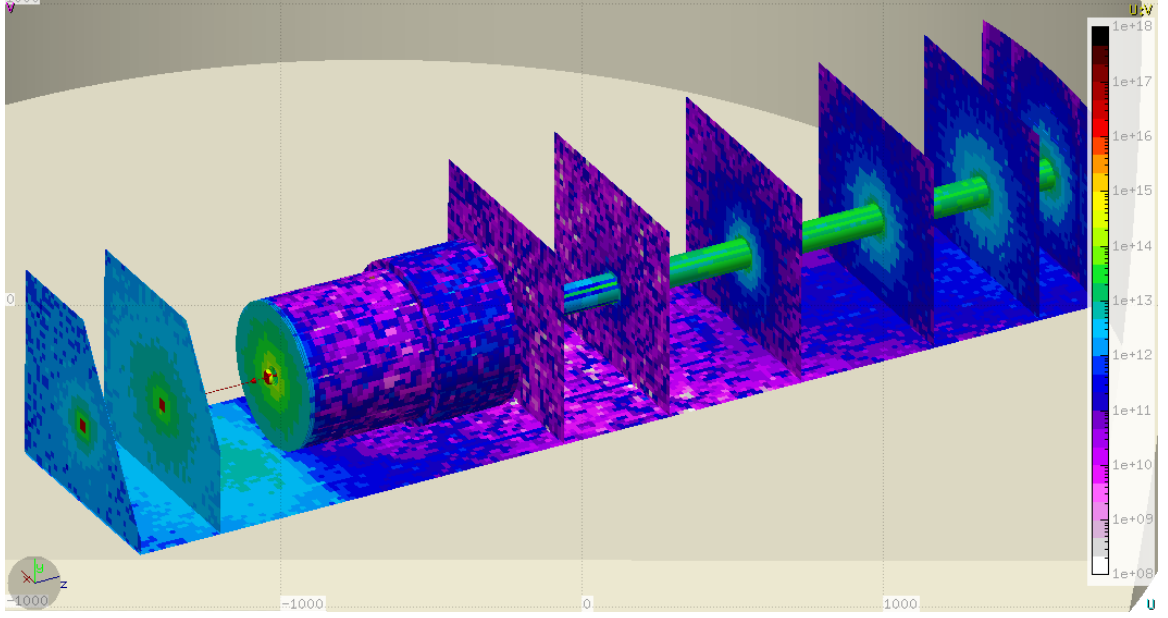


Figure 150: Estimate of radiation damage in the Hall with the SoLID spectrometer and the SIDIS ^3He configuration. The leading part of radiation present in the Hall for the SoLID spectrometer is originating from the target area and the closer surface of the magnet. In this plot, we show the 1MeV neutron equivalent flux per cm^2 on the volume surfaces estimated for 3000h of continuous running with a beam current of $15\mu\text{A}$ (This is the expected beam-time with the SIDIS configuration). In order to better show the behavior of the radiation leaking, different planes of observation have been inserted (at a distance from the center of the Cryostat of the magnet of $\Delta z = -10m$, $\Delta z = -6m$, $\Delta z = 6m$, $\Delta z = 10m$, $\Delta z = 15m$, $\Delta z = 20m$, $\Delta z = 24m$). The level of radiation leaking increases as one moves farther from the target, reaching a maximum $< 10^{14} \frac{\text{NMeV}}{\text{cm}^2}$. These levels of radiation are on the “mild to severe” damage range for commercial semiconductors (as one can see comparing them with Estimate of the tolerance of different material plots [136](#)). This area is not expected to host any delicate equipment.

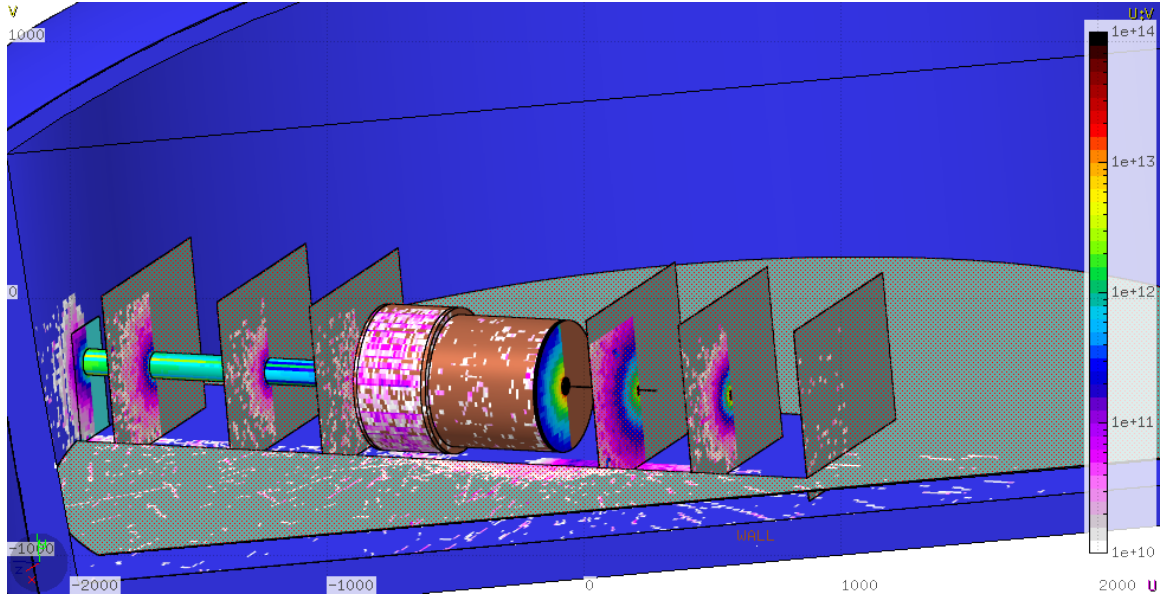


Figure 151: Estimate of radiation damage in the Hall with the SoLID spectrometer and the J/Ψ configuration with a 15cm Liquid Hydrogen target. The leading part of radiation present in the Hall for the SoLID spectrometer is originating from the target area and the closer surface of the magnet. In this plot, we show the 1MeV neutron equivalent flux per cm^2 on the volume surfaces estimated for 60 days of continuous running with a beam current of $3\mu A$ (This is the expected beam-time with the J/Ψ configuration). In order to better show the behavior of the radiation leaking, different planes of observation have been inserted (see Fig. 149a for reference of the position of each plane). The Color scale is different than in the previous cases in order to enhance the details in the desired region.

15 Slow Controls

Slow Controls typically covers the “infrastructure support” systems and logging for the detector package as a whole. This includes real-time controls and status monitoring of power, vacuum, temperatures, etc., in addition to integrated safety interlocks and alarm functions. Typical measurement and response times for such systems are on the order of 100s of milliseconds to seconds. More rapid response times are also available if needed. Common examples of slow controls involve the high- and low-voltage power supplies for all detector apparatuses, gas composition and flow regulation, control of gain-monitoring systems, etc.

This section *excludes* any discussion of slow controls for the target and solenoid magnet. Slow controls for those systems will be designed and implemented by their respective working groups. The systems covered here involve only the SoLID detector subsystems.

Due to the obvious interdependence between the hardware and the software used to control it, details of several slow control components will need to wait until the hardware design is better developed (*eg.* gas systems). We will give an overview of some baseline requirements and expectations that the Collaboration will abide by to ensure slow controls development and implementation will proceed smoothly.

It is understood that any fast interlocks (*i.e.* millisecond level or faster) that cross system boundaries need to be identified at the design stage. Examples may include tripping high-voltage if the gas flow is interrupted for the GEM system, disabling the flammable gas flows in the event of a fire alarm, etc.

15.1 General Requirements

The Collaboration agrees that all components must be able to interface with the EPICS (Experimental Physics and Industrial Control System) environment already present at Jefferson Lab. This imposes a common mid-level API for inter-system communication and allows the systems to take advantage of the well supported EPICS infrastructure at JLab. This includes local expert support from other experimental Halls (particularly Halls B & D), and the Accelerator Division for any necessary PLC, software and/or hardware IOC development, as well as taking advantage of JLab’s EPICS data archiver “MYA”.

15.2 Frontend GUIs

The graphical interface employed for all systems is expected to be based on the Control Systems Studio (CSS) environment. This toolkit has been slowly replacing the legacy EDM/MEDM GUIs developed during JLab’s 6 GeV period. Hall D and Hall B already make extensive use of the CSS toolkit, and Hall C will be migrating its legacy M/EDM GUIs as time permits.

The BEAST alarm handler, part of the CSS system, will be used to monitor EPICS variables and alert shift crew and/or external experts of problems.

Systems that require lower-latency response times than softIOCs and EPICS polling systems can provide will investigate the CompactRIO (cRIO) standard successfully used in Halls B & D.

The Hall B slow controls development experience, in particular, has been well documented by those involved and will provide an excellent local repository of interface code and management processes that SoLID can leverage.

15.3 High/Low Voltage Controls

High Voltage hardware will be standardized as much as possible. CAEN and Wiener systems are both in use at JLab. They each come with integrated EPICS support and pre-existing software support on-site. Detector, sub-detector, and individual channel control and monitoring will be provided. Legacy LeCroy HV systems will *not* be supported.

15.4 DAQ Crate Control

It is desired to have realtime monitoring of VME and other data acquisition crate power systems and temperatures. All DAQ crates are expected to provide an integrated ethernet interface and EPICS support. Examples of such hardware include the Wiener 60xx series in common use across JLab.

15.5 Gas Systems Requirements

In addition to the necessary EPICS interface, the Collaboration agrees that the various gas subsystems (Cherenkovs, GEMs, MRPC) will standardize any hardware that requires software support. This includes items such as mass flow controllers (MFCs) and hardware process controllers, etc. This will allow for a common spares inventory and simplify control software development and maintenance.

15.6 Detector Systems

The following list runs through the various sub-detectors and summarizes the necessary slow controls.

- **EC:** HV + LV control and monitoring for the PMT base design. Additional controls for an LED flasher system (to be designed) may also be required.
- **FA/LASPD:** HV + LV control and monitoring for the PMT base design. Additional controls for an LED flasher system (to be designed) may also be required.
- **GEM Tracking:** HV + LV control and monitoring. The non-recirculating gas system will use Ar/CO₂ at STP and will employ a basic gas mixer system with flow monitoring and control. We will track the gas flows and provide an interlock to trip the HV if the gas flow is interrupted.
- **LGC:** HV + LV control and monitoring for the PMT base design. The CO₂ and N₂ gases employed will operate at STP and will be served by a simple non-recirculating “flow-through” system. The gas flows will be monitored and logged. Additional controls for an LED flasher system (to be designed) may also be required.
- **HGC:** HV + LV control and monitoring for the PMT base design. C₄F₈ gas will be employed and used in large quantities. Such a system will require a somewhat sophisticated fill and recapture/purification/recirculation infrastructure involving PLC/IOC controls that remain to be designed. The gas flow rates (during fill/purge), pressure, and temperatures will be monitored and logged. Additional controls for an LED flasher system (to be designed) may also be required.

In addition to the above items, gain-monitoring systems have been discussed that would also require some nominal controls. It is not expected that such systems would be a significant burden.

16 Electron Beam Polarimetry

The interpretation for polarization-dependent measurements relies on precise correction for finite beam polarization, with an accurate absolute normalization to 0.4% accuracy at both 11 GeV and 6.6 GeV required for the parity-violation program. This will be achieved using two independent measurement techniques with independent sources of calibration errors, which can be directly cross-checked to high precision. This is an ambitious goal, but compatible with goals for other planned experiments at Jefferson Lab [312]. Compton polarimetry is well-suited for the energy and intensity of the upgraded Jefferson Lab beam. The best candidate for a second, high-precision, independent measurement is Møller polarimetry.

Compton polarimetry is a very promising technique for high precision polarimetry at beam energies above a few GeV. Beam interactions with a photon target are non-disruptive, so Compton polarimetry can be employed at high currents as a continuous polarization monitor. The photon target polarization can be measured and monitored with a very high precision, and the scattering between a real photon and free electron has no theoretical uncertainty, such as the atomic or nuclear effects which can complicate other measurements. Radiative corrections to the scattering process are at the level of 0.3% and are very precisely known. Compton polarimetry at JLab has previously achieved 0.6% precision on electron beam polarization and provided the basis for estimating that this technique is capable of achieving precision better than 0.4%.

The Møller polarimeter measures the scattering of beam electrons from polarized atomic electrons in a ferromagnetic foil. The use of a solid target is disruptive to the beam and limits the technique to low average beam current, but the approach provides a rapid, high statistics measurement with systematic uncertainties that are entirely independent from Compton polarimetry. The Hall A Møller polarimeter is operationally robust and commonly used by experiments with polarized scattering.

A capital improvement plan at JLab (HIPPOL) has been initiated to support several important upgrades to the Compton polarimeter, while the MOLLER project includes some upgraded components for the Møller polarimeter. It is expected that the polarimeter hardware at the conclusion of the MOLLER project will be sufficient to support the needs to the SOLID measurements. The existing polarimeters and these plans for future improvements are described below.

16.1 The Hall A Compton Polarimeter

As pictured in Fig. 152, the Hall A Compton polarimeter [314] is located in a chicane, about 15 meters long, which deflects the beam to intersect with a laser cavity 21 cm below the primary (straight-through) beamline. After passing the electron-photon interaction point, the electron beam is bent about 3.5 degrees by the third chicane magnet to be restored to the primary beamline. Electrons scattered from the photon target are separated from the primary beam by this bend and detected using silicon microstrips just before the fourth chicane magnet. Scattered photons pass through the bore of the third chicane magnet to be detected in a calorimeter.

The photon target is a 0.85 cm long Fabry-Perot cavity crossing the electron beam at an angle of 1.4° . The laser system produces green (532 nm) light. Power levels of 10 kW have been stored in this resonant optical cavity for intersection with the electron beam, while more typical operation uses about 2 kW of stored power. The laser light can be toggled between opposite polarizations of highly circularly polarized light. The feedback loop which locks the laser to the cavity resonance can be disabled to dump the stored light and enable measurements of background from all non-Compton-scattering processes. To reduce overhead from the time required to re-lock the cavity, the transition between laser states is typically performed with a period of 1-2 minutes. The polarization

of the transmitted light from the locked cavity and the reflected light from the unlocked cavity are each monitored and can be used to characterize the laser polarization at the interaction point.

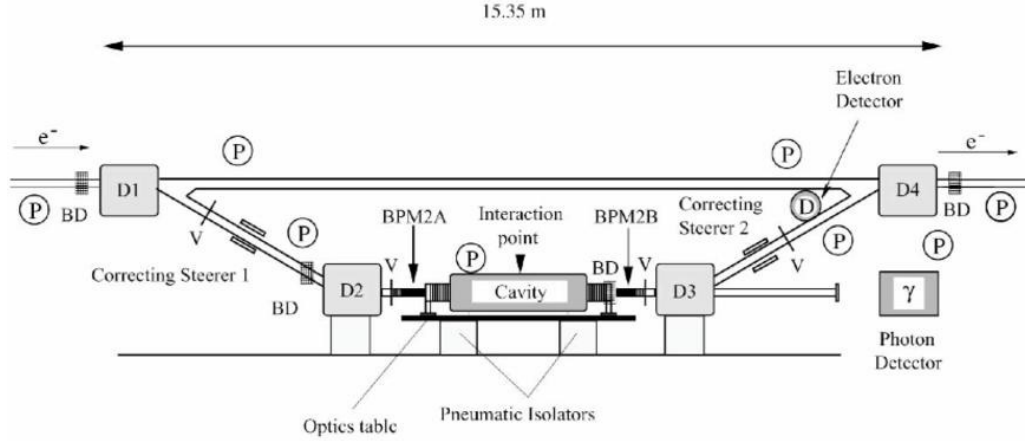


Figure 152: *Schematic of the Hall A Compton polarimeter. Figure from [314].*

At 11 GeV, with 2 kW stored laser power, the Compton-scattered rates would be approximately $1.5 \text{ kHz}/\mu\text{A}$ and the asymmetry will range from 17.8% to -4% over the energy spectrum. At 6.6 GeV, the rate is similar while the asymmetry ranges from 20.9% to -4.7%. If backgrounds remain comparable to recent operation, statistical precision of 0.4% would be possible in about 5 minutes, depending on the specific detection and analysis approach which is considered.

The vacuum in the interaction region is at the level of $\text{few} \times 10^{-8}$ torr, implying a photon background rate due to Bremsstrahlung scattering from residual gas of around $5 \text{ Hz}/\mu\text{A}$. The dominant source of background in the photon detector is thought to be tails of the beam halo distribution interacting with the apertures in the interaction region. In contrast, for the electron detector the background is thought to be dominated by energy tail or position halo of the primary beam since electrons from aperture scattering would presumably not cleanly transit the third dipole. When well-tuned, the background rates in the photon and electron detectors have been seen to be roughly similar: around $<100 \text{ Hz}/\mu\text{A}$ in recent use. The polarimeter was operated with 11 GeV beam during the 2016 run period, with photon backgrounds consistent with this expectation.

16.1.1 Laser System

As described above, the laser system stores up to 10 kW power in a resonant cavity for intersection with the electron beam. The system consists of a 1064 nm ND:YAG seed laser coupled to a Ytterbium-doped fiber amplifier to produce about 5 W power. This is converted to 1-2 W of 532 nm light using a Periodically-Poled Lithium Niobate (PPLN) doubling crystal. The light is prepared in a suitable polarization state with a combination of quarter-wave and half-wave birefringent optics, then transported through mode-matching optics and directed through a vacuum window and onto the cavity mirror. Resonance is maintained with a Pound-Drever-Hall (PDH) lock using retro-reflected light analyzed at the polarization preparation station, with feedback and modulation sidebands through the 1064 nm seed laser. This system was first used for the PREX-I experiment in 2010 and has been operated since that time, typically configured for a factor of 2000 in cavity gain providing power levels of about 2 kW.

One challenge is the precise determination of the inter-cavity polarization, which cannot be directly measured with the cavity in resonance. This challenge is complicated by the birefringence of the vacuum windows, which is in part stress-induced and changes significantly under vacuum load. The polarization of light arriving at the cavity entrance can be inferred from light reflected back from the cavity and analyzed with the same apparatus used to create the initial polarization state, measuring a single power level [316]. This technique was employed in Hall C during the Qweak experiment to maximize the circular polarization of light injected in the cavity and to monitor the polarization during the run. It was verified to work by two methods. In the first, with the cavity under vacuum in running conditions, a scan over a broad range of initial polarization states was performed, and the recorded analyzed reflected power was shown to be well described by the simple hypothesis of optical reversibility. A more direct verification was made with the cavity opened, directly measuring the polarization of the injected light in the cavity and correlating this with the analysis of the reflected light. The correlation is shown over the full range of the scan, and zoomed in for measurements at maximum circular polarization, in Fig. 153. In operation, the Hall C Compton polarimeter ran with the reflected light very near minimum, with an implied uncertainty on the circular polarization within the cavity of 0.1%.

The technique has been implemented and further studied in the Hall A polarimeter, which makes use of a significantly higher cavity gain compared to the system in Hall C. It was found that intrinsic birefringence in this cavity was a significant effect, which significantly complicates this approach. The cavity birefringence must be characterized and incorporated into this scheme, as was done for the 2019 PREX-2 and CREX experimental runs. The stability of this determination can be cross-checked using the polarization analysis station in the transmitted beamline. While this process requires significantly more calibration and preparation to control for cavity birefringence, it is expected that it will be capable of determining and monitoring the circular polarization in the cavity to the level of 0.2%.

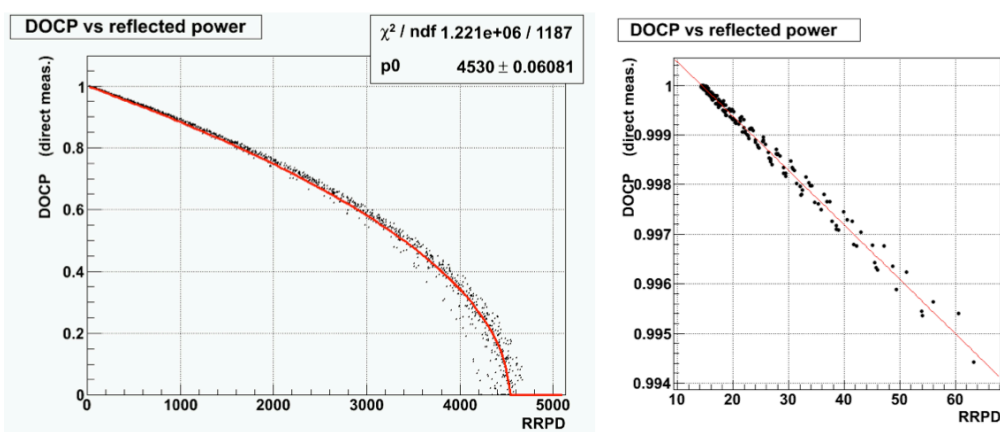


Figure 153: Measured degree of circular polarization in the Hall C Compton laser cavity vs. the polarization-analyzed reflected light, measured over a broad scan of initial polarization states. The figure on the right is zoomed in the region of maximum circular polarization.

16.1.2 Electron Detector

Presently, electrons are detected in a set of 4 planes of silicon microstrip detectors located just before the 4th dipole. Each microstrip plane instruments 192 strips with a pitch of 240 μm , with strips

running in the horizontal direction so as to provide resolution in the vertical (dispersive) direction. Custom readout electronics pre-amplify and discriminate signals from the microstrips, implement a simple tracking algorithm to reduce non-directional backgrounds, and count hits in each strip over specified integration gates corresponding to the helicity pattern of the electron beam. Presently, this system is operating at low efficiency with poor signal size for a minimum ionizing track compared to environmental noise on individual strips. In addition, the active area of these planes is smaller than ideal for high precision measurements, when used with 532 nm light at 11 GeV.

An upgrade for this detector system is required. Plans for the HIPPOL capital improvement project include an upgrade to diamond microstrip detectors. Such microstrips were successfully used for the Hall C Compton polarimeter in the Qweak measurement [315]. Diamond microstrips are more radiation hard and less susceptible to low-energy photon backgrounds. They are more difficult to procure than silicon strips, but a recent SBIR has led to a new commercial availability. In this upgrade, the front end amplifier/discriminator boards would be remade to be optimized for the signal size and shape expected from the diamond, while the readout system would otherwise remain the same.

An alternative development for silicon pixel detectors based on HVMAP technology is also underway. These detectors would incorporate amplifier, discriminator, and multiplexed readout circuitry on the same radiation-hard silicon substrate as the pixel detectors. An FPGA readout of the multiplexed signal would be designed to implement tracking, and geometry cuts for the 2-D readout. A prototype system is currently being developed at Manitoba, in research funded by NSERC.

16.1.3 Photon Detector

The calorimeter for detecting scattered photons lies about 7 meters downstream of the interaction point. The strong forward boost of scattered photons leads to a tightly collimated photon beam (< 1 mrad for $> 1\%$ of the Compton edge), so the primary consideration for calorimeter size is energy resolution through shower loss. The photon detector is composed of an array of four PbWO_4 crystals, with a total transverse size of $6 \times 6 \text{ cm}^2$ and length 20 cm, instrumented with a single photomultiplier tube. The PbWO_4 materials is ideal for its high density and fast response, and the light yield provides sufficient resolution for the high energy photons (up to 1.2 GeV at 6.6 GeV beam energy) that will dominate the measurement. The PMT signal is split between two parallel data acquisitions: one with a fast-counting, buffered ADC self-triggered on pulses from the photon detector, and the other utilizing a 250MHz flash ADC (fADC) to integrate the total signal over periods corresponding to the helicity pattern of the electron beam. The fADC system can also record a very low rate of individual pulses for calibration. Each of these dual readouts can be analyzed independently. The fast counting ADC readout and the sample pulses in the fADC system can both be triggered using the electron detector, providing an electron-photon coincidence spectrum for calibration.

At 11 GeV, synchrotron radiation from the dipole magnets threatens to be a significant background in the photon detector, potentially overwhelming the Compton scattered signal by a factor of 10. This radiation is reduced using a lead shield in front of the photon detector, but it is desirable to keep this shield thin to minimize the effect of the measured Compton spectrum. For this reason, the synchrotron light is suppressed using a modification of the chicane magnets, and a remote-adjustable vertical collimator is installed to cut much of the remaining synchrotron radiation.

In order to reduce the synchrotron radiation in the region of acceptance for Compton scattered electrons, the fringe fields at the edges of the chicane dipoles were modified with magnetic “shims” to soften the bend into and out of the interaction region. Figure 154 shows the energy spectrum

of synchrotron light attenuated by lead shielding between 1–5 mm thick, depending on the beam energy. On the left, the spectrum for 11 GeV with unmodified magnets is compared to calculations for the recent runs of HAPPEX-III (3 GeV) and PV-DIS (6 GeV). On the right, the energy spectrum (“Fringe 2”) is shown when iron extensions, 15 cm in length, are added to the dipole magnets in order to provide an extended region of reduced field. This reduced magnetic field produces synchrotron light with lower energy range and with reduced intensity, for the portion of the electron beam trajectory that projects to the photon detector. With this modification, the bending strength of the magnet remains the same but the synchrotron light radiated into the detector is reduced by a factor of 10^4 . The magnetic field extensions were modeled using TOSCA. They have been installed and used in 2016 with 11 GeV operation of the polarimeter.

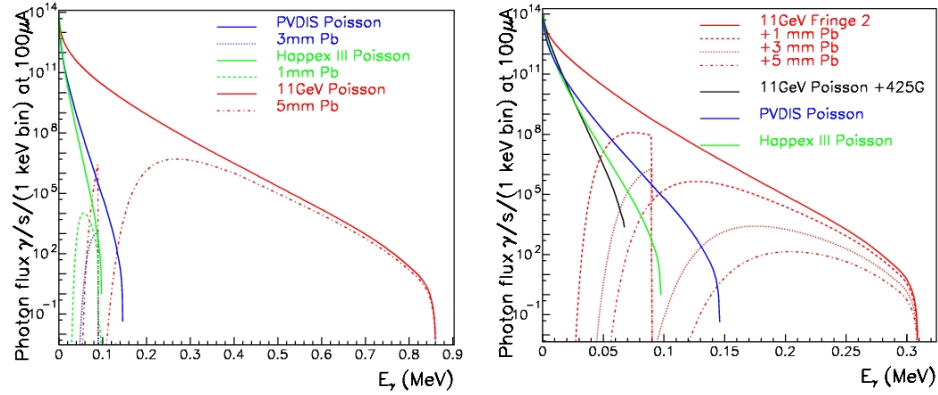


Figure 154: *Energy spectrum of synchrotron radiation penetrating lead shielding of thickness listed. Plot on left shows unmodified chicane magnets, plot on right shows energy spectrum when using magnetic shims which reduce the field for the bend radiating into the Compton photon detector acceptance. Note the different horizontal scales between the plots.*

A vertical collimator was developed to further cut the synchrotron radiation level. These provide a horizontal slit just in front of the photon detector, with the vertical size of the slit precisely controlled with a remote actuator. The collimator can be positioned to block the vertical stripe of synchrotron radiation, below the Compton photons due to the second chicane dipole and above the Compton photons due to the third chicane dipole. Very near the Compton photon acceptance, the synchrotron radiation is significantly reduced by the magnetic shims. Together, the shims and vertical “jaw” collimator have been seen to provide excellent suppression of synchrotron radiation.

16.1.4 Systematic Uncertainties in the Compton Polarimeter

The Hall A Compton polarimeter described above should assure operability and sufficient precision at 11 GeV. Although all of the challenges that will be encountered on the path to 0.4% precision cannot be predicted, it is useful to review the techniques and understandings that lead to the conclusion that this will be within reach. Table 32 summarizes the goals for various contributions to systematic uncertainty, based on the collaboration’s experience with Compton polarimeter from high-precision experiments such as PREX and Qweak. The first four rows list sources of uncertainty which are highly or completely correlated between the electron and photon analyses. The other tabulated uncertainties arise in detector readout or calibration and are mostly or entirely decorrelated between the analyses. Each of these separate categories of potential systematic uncertainty: correlated,

Relative error (%)	electron	photon
Position asymmetries*	-	-
E_{Beam} and λ_{Laser} *	0.03	0.03
Radiative Corrections*	0.05	0.05
Laser polarization*	0.20	0.20
Background / Deadtime / Pileup	0.20	0.20
Analyzing power Calibration / Detector Linearity	0.25	0.35
Total:	0.38	0.45

Table 32: *Goals for systematic errors for the Hall A Compton polarimeter at 11 GeV. Topics marked * are common systematic errors between the photon and electron analyses, while the others are largely independent between the detector systems.*

electron-only, and photon-only, will be discussed in the following sections.

Sources of Correlated Error Any error associated with the Compton scattering process will be a common source of systematic error between the electron- and photon-detector analyses. One example lies in the energy normalization of the scattering process. The analyzing power is a function of both electron energy and photon energy, so these must be precisely determined. The photon wavelength will be determined to better than 0.1 nm and the electron energy to 0.05%, which leads to an uncertainty at the level of 0.03%. A similarly small uncertainty will come from radiative corrections, which are calculable [321] with high precision and will contribute at the level of $< 10^{-3}$.

Helicity-correlated changes in luminosity of the laser/electron interaction point can introduce a false asymmetry. Various causes of luminosity variation must be considered, such as electron beam intensity, beam motion or spot-size variation. The control of helicity-correlated beam asymmetries is now a standard technology at Jefferson Lab, and typically achievable results (few part per million intensity, 10's of nanometers beam motion, $< 10^{-3}$ spot size changes) will suitably constrain the electron-photon crossing luminosity variations. Another possible source of false asymmetry would be electronics pickup of the helicity signal, which could potentially impact an integrating photon analysis. However, the demands of the primary experiment for isolation of the helicity signal exceed those for polarimetry by several orders of magnitude. In addition, the laser polarization reversal provides an additional cancellation for asymmetries correlated to the electron beam helicity. For these reasons, beam asymmetries are expected to be a negligible source of uncertainty in this measurement.

A more significant potential source of error comes from the uncertainty in the photon polarization. As described above, the determination of photon polarization will require calibration of the intrinsic birefringence of the cavity and will utilize the analysis of light reflected from the cavity input mirror and transmitted through the cavity. Together, these will provide robust and precise control and measurement of the polarization state in the cavity with a precision of 0.2%.

Systematic Errors for the Electron Detector The electron detector is composed of 4 planes of microstrips normal to the electron beam trajectory and positioned on the low-energy side of the beam trajectory in the dispersive chicane. Electrons which have given up energy to a scattering process are separated from the primary beam by the third chicane dipole, and the energy of a detected electron

is implied by the distance of the track from the primary beam with a dispersion of about 0.45% of the beam energy per millimeter. Models of the chicane magnets are used to calculate the electron energy as a function of position in the detector. The absolute normalization of the energy of the electron detected in each strip is sensitive to details of the magnetic chicane and beam position, and is the key challenge in normalizing the observed asymmetry spectrum.

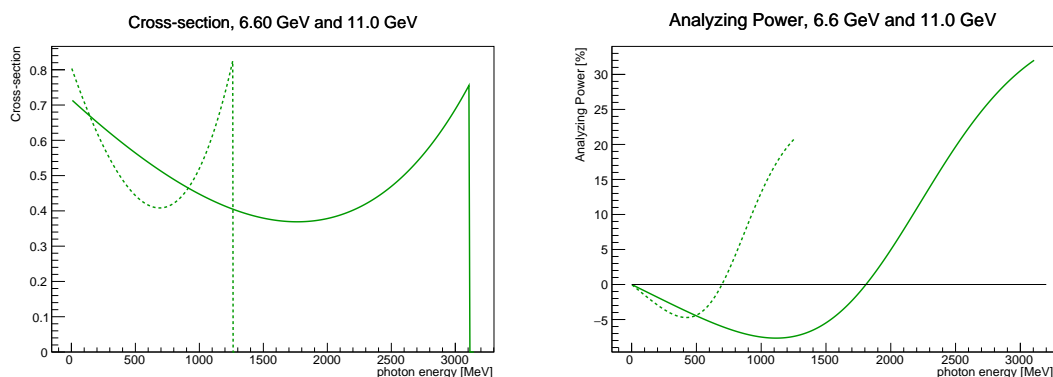


Figure 155: *The cross-section and asymmetry plotted versus Compton scattered photon energy for the Hall A polarimeter at 11 GeV (solid line) and at 6.6 GeV (dotted line) with 532 nm light.*

The cross-section and asymmetry as a function of Compton scattered photon energy is plotted in Figure 155 for an 11 GeV and 6.6 GeV electron beam. The Compton edge (the kinematic endpoint of the Compton energy spectrum) is observed in the electron detector and used to calibrate the distance of the detector from the primary beam. In addition, the asymmetry as a function of photon energy k exhibits a zero crossing. Determining the location of this asymmetry zero crossing (0xing) provides a second absolute energy calibration point, so together the Compton edge and 0xing can be used to calibrate two parameters: the detector location relative to the beam and the strength of the magnetic field in dipole 3. In this way, survey results and magnetic field maps serve as a cross-check to a beam-based self-calibration of the Compton energy spectrum. The precision of this calibration is limited by delta-ray production in the microstrips, which distorts the measured spectrum, and efficiency variations between the microstrips.

The recent analysis of the Hall C Compton polarimeter for the Qweak experiment provides the best example of the potential of this technique [315]. The chicane had been optimized to low energies, and with a large bend angle and 532 nm light, the 0xing was 8.5 mm from the primary beam for the 1 GeV beam energy. At this distance, backgrounds were reasonably low, and the diamond microstrip detector could be positioned close enough to the primary beam to accept well beyond the zero-crossing. While the microstrip detector exhibited significant efficiency variations from between strips, the asymmetry distribution was not distorted by this effect. The rate and asymmetry distribution are shown in Fig. 156. The shape of the asymmetry spectrum over microstrip position, which is slightly non-linear in electron momentum, was calculated in Monte Carlo simulation of the Compton spectrometer using magnetic models of the chicane magnets. This shape template was fit to the asymmetry distribution, returning a scale factor corresponding to the spectrometer dispersion, the location of the Compton edge, and the polarization of the electron beam. The fit results were stable and robust, with no observable, systematic deviations in the residuals of the fit to the asymmetry spectrum shape. Simulation was used to demonstrate that the results were very insensitive to a broad range of possible systematic errors, including uncertainties in magnet Bdl or field map, detector noise, detector alignment, or the effect of triggering algorithms. Delta-ray

production from the electron interacting in the detector was also seen to be important, so that results from the later detector planes had to be significantly corrected due to distortions in the asymmetry spectrum from the multiple tracks; the correction in the first plane of the detector was negligible. The most significant systematic error contributions, about 0.4%, were a result of dead-time in the fast-triggering DAQ algorithms, which could be complicated by noisy or inefficient strips. Over the run, the electron detector normalization in this analysis was estimated to be known to 0.56%. It was also clear that improvements in the DAQ algorithms would be able to further improve on this precision.

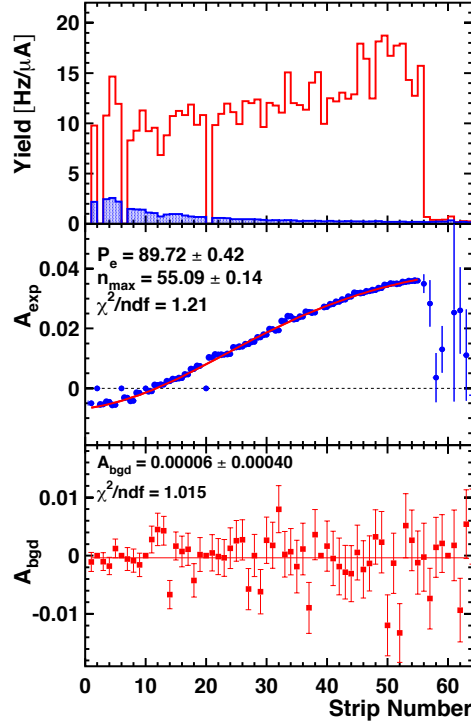


Figure 156: *The measured rate and asymmetry spectrum in the Hall C Compton polarimeter measured in the first plane of the electron detector, as a function of microstrip number from the detector edge which is about 6 mm from the primary beam. top: measured rate with laser on (red) and off (blue); middle: background-subtracted asymmetry spectrum, fit to expected shape with free parameters for spectrometer calibration and polarization; bottom: measured background asymmetry, uniform and consistent with zero.*

In the Hall A system at 11 GeV (6.6 GeV), the 0xing will be around 33 mm (20 mm) from the primary beam, which should allow for robust operation. Improvements in the DAQ system suggested by the Hall C experience should lead to a reduction of the rate-dependent DAQ inefficiencies that were the largest source of systematic uncertainty. The high statistical power of the measurement will also be important; for example, high precision studies can be performed to benchmark models of the readout system against changes in the laser power or the parameters of the triggering (preamp levels, logical gate lengths, coincidence levels, etc). Based on the Qweak experience at the 1 GeV beam energy, it is expected that the electron detector analysis at high energy will be normalizable to a level significantly better than 0.4%.

The large statistical power also enables alternative analyses with significantly different systematic uncertainties. Using only the last, single silicon strip at the Compton edge will be capable of 0.4% statistical precision on time-scales of around one hour. The rate of change of the asymmetry in this region is only 0.5% / mm. Locating this strip, relative to Compton edge, to a little better than half its own width should provide a robust accuracy on the analyzing power better than 0.4%. This technique would be sensitive to determination of the location of the Compton edge, but otherwise very insensitive to other calibration parameters.

Similarly, the asymmetry minimum, which lies about 19 mm from the 11 GeV primary beam (or about 11 mm from the 6.6 GeV beam), could be used. The statistical power is much lower in this region, with a single strip requiring 30 hours to achieve 0.4% statistical precision on the polarization (assuming signal-noise ratio of 10:1). However, here the asymmetry is not changing with position, so there is minimal calibration error in selecting a strip in this minimum. Beam position and angle may vary the location of the asymmetry minimum on the detector over hundreds of microns during this time span, but such changes can be tracked using beam position monitors or the Compton edge. The analyzing power varies by only about 0.4% of itself over a range of ± 1.6 mm, suggesting minimal corrections will be necessary.

Regardless of the analysis, contributions from deadtime and pileup will need to be understood. The fast-counting DAQ can take very high rates with low deadtime, and deterministic deadtime intervals are enforced in readout and acquisition electronics stages. The segmentation will keep rates in individual microstrips to < 2 kHz. The high statistical power of the measurement is of significant use here; high precision studies can be performed to benchmark models of the readout system against changes in the laser power or the parameters of the triggering (preamp levels, logical gate lengths, coincidence levels, etc).

Backgrounds are also a potential but small source of systematic uncertainty. Backgrounds are studied with the laser cavity unlocked, allowing both the background level and asymmetry to be well determined. However, high backgrounds could impact the systematic error due to deadtime or pile-up corrections. There is also the possibility of backgrounds from Compton-scattered electrons, which can produce delta rays when scattering in the detector or in its shielding. These tracks can themselves be sufficiently forward-going to pass the trigger, thus changing the analyzing power as a function of energy. Simulation will be used to study these contributions, and empirical studies of track distribution and electron-tagged photon energy spectra can be used to identify such effects in the data.

Systematic Errors for the Photon Detector The precise determination of the analyzing power as a function of energy is more difficult for the photon calorimeter than for the electron detector due to the width and shape of the detector response function. In order to fit the asymmetry as a function of detected photon energy, the analyzing power must be calculated as a convolution of the response function with the theoretical analyzing power curve. In general, determining the effect of a low-energy threshold on the analyzing power depends sensitively on the shape of the response function; at low energies this is a major source of uncertainty. At high energies, the improved resolution and consistency of the response function shape over the range of interest should significantly reduce this problem. The response function shape and energy calibration can be simulated, and studied using the photon tagging through coincidence triggers with the electron detector. Characterization of the phototube response as a function of both pulse-size (to correctly check the analyzing power determination) and rate (to correctly measure the asymmetry) will also be important.

The pulse-counting analysis in the photon detector is also sensitive to pile-up and deadtime effects, which distort the asymmetry distribution. Background and rate distributions will serve as

inputs to simulation for corrections to the analyzing power. In the current Hall A analysis, pile-up corrections are estimated at the level of 1%, and the effect can be controlled at a level better than 10% of itself.

Uncertainties related to the threshold, response function shape, absolute energy calibration, deadtime and pile-up can also be eliminated by integrating the photon calorimeter signal, without threshold [322]. These previous problems are then replaced with a requirement on the linearity of the average response to the photon energy. Because the analyzing power integral is energy-weighted, the statistical figure-of-merit is not badly degraded by the negative asymmetry region at low photon energies.

The PREX experiment, with a beam energy near 1 GeV, relied on the integrating photon method for polarimetry at the level of 1% precision. Simulations of the photon response function were sufficient to control the analyzing power uncertainties for those measurements. The dominant uncertainty in the asymmetry measurement arises from variation in the photomultiplier response with changes in average rate which introduces a systematic error through background subtraction.

At high energies, with the ability to study response function with the electron-detector-tagged photon beam over a large fraction of the energy range, the photon detector analyzing power normalization uncertainty in the range of 0.3% should be achievable.

Summary of Compton Polarimetry The prospects for 0.4% Compton polarimetry are excellent. This ambitious goal will require vigorous and dedicated efforts to reduce sources of systematic uncertainty. At lower beam energies, precision has reached 1% (PREX at 1 GeV), 0.8% (HAPPEX-3 at 3 GeV) and, most recently, 0.7% (Qweak at 1 GeV). It is worth noting that, in each case, the systematic uncertainty of polarimetry was significantly better than required for the experiment. These measurements all used lower beam energies, with a reduced energy range of the Compton-scattered spectrum and smaller scattering asymmetries. At the higher energies employed for SoLID, the kinematics are favorable for an improvement in precision.

A dominant systematic uncertainty in the previous Hall A measurements was the determination of the laser polarization in the optical cavity. Techniques, first developed during the Qweak experiment and since further refined in Hall A, will provide control on laser polarization to 0.2% or better.

In the case of the electron detector, the “self-calibration” technique (using the shape of the analyzing power between the Compton edge and zero crossing) was successfully employed with the Hall C Compton polarimeter at 1 GeV for the Qweak measurement. The fit to the shape of the asymmetry spectrum proved to be remarkably resilient to calibration errors, with an estimated uncertainty in the analyzing power normalization of 0.56%. With the increase in the scattered energy spectrum at the higher 11 GeV beam energy, it is expected that the electron detector analysis will be precise at a level much better than 0.4%.

For the photon detector, the integration readout method has been successfully used in the HAPPEX-3 and PREX experiments, with the primary limitation being the characterization of the phototube response over the range of signal levels. At 11 GeV, coincidence measurements between the photon and electron detectors will also provide a significant cross-check to the response function and energy calibrations, enabling a counting measurement which is far more precise than what has been possible in previous runs at low beam energies.

It is expected that some significant fraction of data production time will be used for studies of the Compton polarimeter system which are not disruptive to the experiment, for example, scans of detector positions, laser power and polarization, and data acquisition parameters. The scattering asymmetry at 11 GeV is relatively large which, for some analysis approaches, will provide statis-

tical precision at the level of $\sim 0.5\%$ in about five minutes of data collection. This rapid access to high statistical power, which is so powerful for cross-checking potential sources of systematic uncertainty, has never before been available for Compton polarimetry at JLab. Given this high statistical power, beam-based studies will be an effective method for constraining many of the possible experimental systematic uncertainties.

As described above, recent experience with analysis techniques, laser polarization measurements, and the favorable kinematics of the higher electron beam energy have opened the door to robust 0.4% precision Compton polarimetry for the SoLID program.

16.2 Møller Polarimetry

Møller polarimeters exploit the helicity dependence of polarized Møller scattering $e^- + e^- \rightarrow e^- + e^-$ to extract the beam polarization by using a polarized electron target of known polarization. Møller scattering has a very high analyzing power, with a maximum of 7/9 for 90° scattering in the center of mass, a very large cross section, and the two electrons with high energies in the final state make it easy to detect their coincidence and reduce background to negligible values. Such polarimeters have been in use for more than three decades and many potential systematic effects are now controlled at a level below 1%.

Inserting foils into the beam is a “destructive” measurement requiring periodic measurements at a beam current of a few to tens of μA , thus precluding continuous polarization monitoring at high beam current. Consequently, Møller polarimetry with foil targets will be used as a cross check on measurements with the Compton polarimeter, gathering high statistics in a short amount of time and with different attendant systematic errors. The principal challenge is to achieve high precision ($\sim 0.4\%$ on the beam polarization) through careful control of the systematic effects.

Møller Scattering Electron-electron scattering, with arbitrary spin orientation for the beam and target, has been calculated in lowest order QED by many authors [323–326], and the basic formulas for (non parity-violating) polarized Møller scattering are given in many places. For example, following [327], the cross section at high energies in the center of mass frame can be written as

$$\frac{d\sigma}{d\Omega_{\text{cm}}} = \frac{\alpha^2}{s} \frac{(3 + \cos^2 \theta)^2}{\sin^4 \theta} [1 - P_{\text{long}}^{\text{B}} P_{\text{long}}^{\text{T}} A_{\text{long}}(\theta) - P_{\text{tran}}^{\text{B}} P_{\text{tran}}^{\text{T}} A_{\text{tran}}(\theta) \cos(2\phi - \phi_{\text{B}} - \phi_{\text{T}})] \quad (13)$$

Here, $s = (2E)^2$ for electron energy E , θ is the center-of-mass scattering angle, $P_{\text{long,tran}}^{\text{B,T}}$ are the longitudinal and transverse polarizations of the beam and target electrons, ϕ is the azimuthal scattering angle, and $\phi_{\text{B,T}}$ are the azimuthal angles of the beam and target polarizations. The analyzing powers are

$$A_{\text{long}}(\theta) = \frac{(7 + \cos^2 \theta) \sin^2 \theta}{(3 + \cos^2 \theta)^2} \quad \text{and} \quad A_{\text{tran}}(\theta) = \frac{\sin^4 \theta}{(3 + \cos^2 \theta)^2} \quad (14)$$

which are maximized at $\theta = 90^\circ$ with $A_{\text{long}}(90^\circ) = 7/9$ and $A_{\text{tran}}(90^\circ) = 1/9$. The electron laboratory scattering angle for $\theta = 90^\circ$ is $(2m/E)^{1/2}$, rather small for GeV electron beams.

A Møller polarimeter makes use of Eq. 13 to measure the beam polarization vector $\vec{P}^{\text{B}} = (P_{\text{long}}^{\text{B}}, P_{\text{tran}}^{\text{B}})$ by incorporating a target with a known electron polarization vector $\vec{P}^{\text{T}} = (P_{\text{long}}^{\text{T}}, P_{\text{tran}}^{\text{T}})$ into a spectrometer to detect one or both of the scattered electrons. By reversing the beam polarization vector $\vec{P}^{\text{B}} \rightarrow -\vec{P}^{\text{B}}$, one can deduce its magnitude, and perhaps its direction, through the analyzing powers (14). The ideal Møller polarimeter, for determining longitudinal beam polarization $P_{\text{long}}^{\text{B}}$, is set at $\theta = 90^\circ$ with maximal (minimal) target longitudinal (transverse) polarization $P_{\text{long(tran)}}^{\text{T}}$.

Magnetization of Ferromagnetic Targets Møller polarimeters typically make use of ferromagnetic foil targets polarized using an applied magnetic field. The electron polarization for iron in saturation is about 8%, that is, roughly two electrons in the d -shell of each iron atom are polarized. The exact value cannot be calculated from first principles but must be inferred from calibration measurements of magnetization from specific samples, with corrections for the expected contribution of orbital angular momentum. The accuracy of this determination is the fundamental limitation to precision polarimetry with this type of target.

Typically, Møller polarimeters have made use of ferromagnetic alloy foils, with a high magnetic susceptibility μ , that saturate at relatively small applied magnetic fields. In such a polarimeter, the magnetization occurs in the plane of the foil, and the foil is tilted relative to the electron beam to provide a significant component of the electron spin polarization along the beam axis. While these systems were sufficient for polarimetry at the level of a few per cent, they are not amenable to high precision measurements. In such a foil, the local magnetization may vary significantly over the position on the foil, varying with high sensitivity to thickness variations and thermal or mechanical annealing history. The best techniques have produced relative target polarization accuracy approaching 2%.

A significant improvement has been achieved by using pure iron foils in a strong longitudinal field approaching 4T to achieve full saturation of the magnetization. In this case, the foil is magnetized perpendicular to the plane of the foil, and the foil mounted normal to the incident electron beam. At very high fields, the magnetization of the foil will match the “saturation” magnetization for iron, which is a property of the material and has been measured to high precision in previous material studies. In those studies, measurements of the saturation magnetization were performed at various temperatures, fields, and sample shapes. The evolution of magnetization with temperature and applied field, are used to determine the magnetization in the saturation fields and finite temperatures of the operating conditions. An additional correction of $\approx 4\%$, based on measurements of the magneto-mechanical factor, is needed to subtract the contribution from orbital angular momentum. Accounting for these corrections, an accuracy of 0.25% in the determination of the electron spin polarization in a “saturated” iron foil is reported [330] for the Møller polarimeter in Hall C at JLab. Our review of the literature places this uncertainty to be slightly higher, at the level of 0.3%.

16.3 The Hall A Møller Polarimeter

Magnetized Iron Foil Target Measurements in *pure* iron or nickel suggest a very precise knowledge of their magnetization parameters [342, 343]. The approach used by the Basel/Hall C group [328–330] is to not only use pure iron foil targets, but to polarize them with a very high (several tesla) field, provided by superconducting coils. The device has performed well, reporting a measurement of beam polarization to a precision of 0.5% [328]. In addition to the long operational experience with the Hall C polarimeter, the Hall A Møller polarimeter was upgraded to use a similar approach before the 2010 PREX measurement and has been used in this way in 2019 for the PREX-2 and CREX measurements. Much of the updated design of the Hall A Møller polarimeter target system is based on the Hall C experience.

The Hall A Møller polarimeter uses a high purity iron foil in a superconducting coil to create up to a 4T field aligned with the electron beam axis. The Figure 157 includes a photograph of the high-field target magnet system in Hall A. A vertical target ladder with 4 foils is controlled from above this cryostat. For PREX-2 in 2019, a foil thickness of 10 μm was used, but various thickness or non-ferromagnetic targets can be used to cross-check the measured asymmetries.

The target holder must precisely align the plane of the foil to the magnetic field in order to assure that the magnetization is in saturation. Calculations of the longitudinal magnetization of a

foil placed perpendicularly (or nearly so) to an applied field are quite difficult. Figure 158, taken from [329, 330], shows the calculated magnetization (relative to its maximum value) of a pure iron foil as a function of applied magnetic field, for different angles between the field and the normal to the foil. This calculation is in fact of a model of non-interacting prolate ellipsoidal domains [345], and the extent to which it applies to a pure iron foil is not clear, but in order to avoid excessive uncertainty the system must provide a robust alignment of the foil normal to the field ($\sim 1^\circ$) and a high field (~ 4 T) to assure saturation.



Figure 157: The Hall A Møller polarimeter target chamber installed on the beamline. The hardware above the cylindrical cryostat controls the vertical target ladder.

Møller Spectrometer The Møller scattering spectrometer needs to have a well defined acceptance in the neighborhood of maximum analyzing power at $\theta_{CM} = 90^\circ$, so the average analyzing power can be determined to sufficient precision. One also needs to understand uncertainties due to the Levchuk effect [346, 347], which results from the most deeply bound (and unpolarized) atomic electrons having a very different momentum distribution. The momentum p_e of K-shell electrons in iron is ~ 100 keV/c, small relative to the beam momentum but a potential significant change in initial angle, with an effect goes like p_e/m that breaks the expected angle-momentum correlation between the Moller scattered pair.

The Hall A Møller spectrometer system [331, 332], uses four quadrupoles to capture and focus the Møller scattered electron pair around the horizontal plane, and then a dipole for momentum

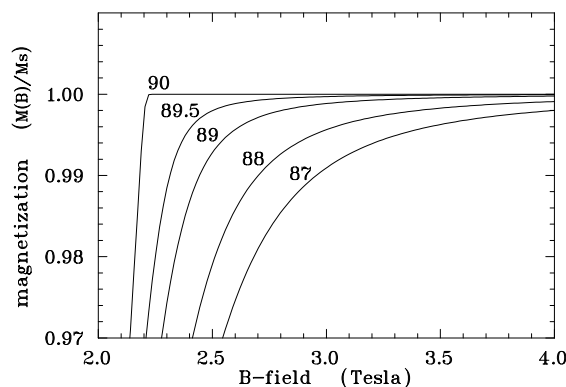


Figure 158: Simulations of foil magnetization for angles between the foil plane and the B-field direction close to 90 degrees. Errors due to imperfect alignment or a slight warp of the foil could produce such a result. Taken from [329, 330], which uses a calculation [345] of magnetization curves for uniformly magnetized prolate ellipsoidal domains.

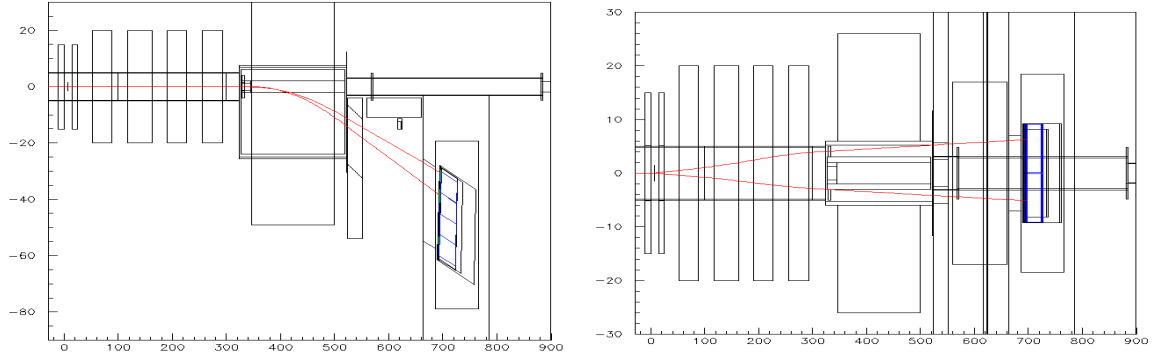


Figure 159: Diagram of the Møller polarimeter QQQQD spectrometer showing the approximate trajectory of accepted rays, in side view (left) and top view (right)

analysis to separate them from Mott scattering backgrounds, as illustrated in Figure 159. The primary beam (and scattered particles in the vertical direction) are shielded from the dipole magnetic field with a thick steel insert around the beampipe through the bore of the dipole magnet.

The accepted electrons are deflected by the dipole magnetic field to a total absorption lead-scintillator spaghetti calorimeter below the primary beamline. This calorimeter is vertically segmented with read-out by four PMTs each on the left- and right-hand side of the beam line. A fast scaler counting DAQ is used to tabulate left/right coincidence counts as well as individual detector counts. The readout is also directed to a data acquisition based on flash ADCs which will provide greater flexibility in comparing hits and coincidences between detector segments.

The details of the acceptance through the spectrometer and into the calorimeter are critical for normalizing the analyzing power of the measurement. Modeling of the magnetic system in GEANT4 has been carefully performed in preparation for the PREX-2 measurement in 2019, and various options for the optics configuration for 11 GeV have been investigated. The baseline optics design avoids clipping the acceptance for Møller scattered electron pairs in the quadrupoles or dipole, and places a momentum cut using the finite vertical extent of the detector segments. This uses the dispersion of the dipole bend to tightly select momenta corresponding to the maximum analyzing power around the center of mass angle of 90° . The result is highly insensitive to initial angle but very selective of initial momentum, which is exactly the prescription needed to avoid a significant Levchuk effect on the analyzing power.

Two upgrades are planned to better define the acceptance of the Møller scattered pairs. The first is additional collimation either before or after the 4Q spectrometer, to better define the initial acceptance. The second is a set of tracking GEM chambers, which are needed to benchmark the simulation model of the accepted kinematics. These additions are both included in the MOLLER experiment project budget.

Systematic Uncertainties with Møller polarimetry Table 33 shows the current and projected list of systematic errors for Møller polarimeters at Jefferson Lab. The uncertainties for the Hall C Møller polarimeter are taken from [328]. The corresponding columns for Hall A are anticipated, based on previous experience with the Hall C system and anticipated performance of the apparatus.

Variable	Hall C	Hall A
Target spin polarization	0.25%	0.30%
Target angle	‡	‡
Analyzing power	0.24%	0.20%
Levchuk effect	0.30%	0.20%
Target temperature	0.05%	0.05%
Dead time	‡	0.10%
Background	‡	0.10%
Others	0.10%	0.10%
Total	0.47%	0.45%

‡: not estimated

Table 33: *Systematic error summary for Møller polarimeters at JLab, including anticipated uncertainties for future prospects. The Hall C polarimeter [328] uses a high field pure iron target [329, 330] with a simple two-quadrupole spectrometer. Uncertainties quoted for that system are taken from a publication detailing calibration of the analyzing power. The Hall A Møller polarimeter [331, 332] uses a similar iron target, and a spectrometer with a dipole magnet following four quadrupoles. Uncertainties for this system are the anticipated performance.*

17 Integration and Expected Performance

17.1 Overview

System integration incorporates several tasks : 1) Quality control of the engineering of the apparatus so that all the pieces fit and the system satisfies *all* of the experimental program with minimal turnover between experiments; 2) Integration of the detectors so that they work together and form efficient triggers, and we can predict the combined PID performance; 3) Control of calibrations and systematic uncertainties; and 4) Commissioning plans.

In a preliminary engineering study done at Argonne National Lab by Paul Reimer, scenarios for assembling and disassembling of the apparatus have been developed which allow for switching rapidly between PVDIS and SIDIS, as well as for allowing other experiments to share Hall A during the SoLID running era. We believe we can switch between running setups in approximately three months.

For the second topic, we have carried out studies of the combined particle ID using the gas Cherenkov and the calorimeters, see Figure 160 where the resulting π/e ratios are shown. A similar PID performance was achieved by the Hermes spectrometer [287]. Our study was performed by using the pion rejection factor and electron efficiency as a function of particle scattering angle and momentum for both detectors for both the PVDIS and SIDIS configurations based on Geant simulations of the current detector designs. The results here, shown for PVDIS, are preliminary since the detector designs and the analysis strategies are still evolving. Nevertheless, the preliminary results are encouraging and show that we will meet the minimum pion rejection factor of 10^{-3} , with a possibility of improving that rejection factor using a more sophisticated multi-variable integrated analysis. High background rates in the LGC are not expected to strongly affect the pion rejection efficiency, but pre-R&D studies are underway to better measure their impact.

In the following sections, we will present the study of the acceptance, efficiency, systematics, and calibration for various experiments.

17.2 SIDIS Program

The acceptance and efficiencies of the SIDIS configuration with a 40 cm long polarized ^3He target was studied using the whole simulation. The particles detected by the detectors were compared to those of the original particles from a full-length target. We have good electron detection efficiency from all sub-detectors. They vary slightly across the phase space and the average efficiency values are shown in Table 34. The acceptance is ~ 0.7 due to the two target window collimators. Figure 161 shows the combined effect of acceptance and efficiency (except tracking). We will continue to fine-tune the design and the reconstruction algorithm to improve the efficiency.

Table 34: Average electron detection efficiencies of all SoLID sub-detectors and the total SoLID efficiency.

Detector	EC	Cherenkov	Scintillator pad and MRPC	GEM tracking	Total
average efficiency	95%	95%	98%	90%	80%

We have conducted a careful study of the systematic uncertainties of the SIDIS experiments and the results are presented below.

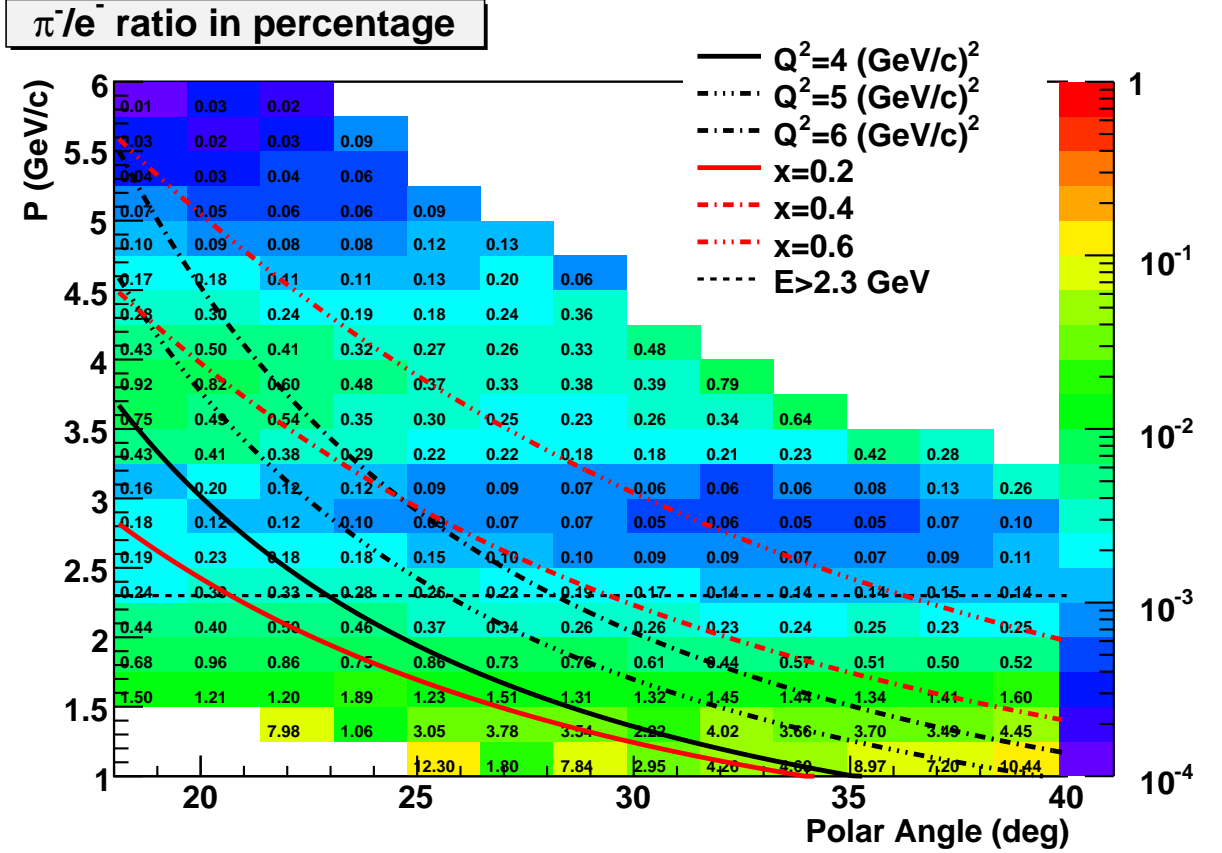


Figure 160: The π^-/e^- ratio from combined Cherenkov and Calorimeter detector performance as a function of the scattered momentum P and polar angle θ . The numerical values are the ratios corresponding to that cell in (P, θ) . The curves indicate various regions of Q^2 x or scattered energy E .

The SIDIS cross section is in general expressed as [288]

$$\frac{d\sigma}{dx dy dz dP_{h\perp}^2 d\phi_h d\phi_S} = \frac{\alpha^2}{xyQ^2} \frac{y^2}{2(1-\varepsilon)} \left(1 + \frac{\gamma^2}{2x}\right) [F_{UU}(x, z, Q^2, P_{h\perp}) + \text{asymmetric terms}]. \quad (15)$$

In the simulation, we model the SIDIS cross section by assuming factorization to express the structure function as a convolution of TMD distribution and fragmentation functions

$$F_{UU}(x, z, Q^2, P_{h\perp}) = x \sum_a e_a^2 \int d^2k_\perp d^2p_\perp \delta^{(2)}(P_{h\perp} - p_\perp - zk_\perp) f_1^a(x, k_\perp) D_1^a(z, p_\perp). \quad (16)$$

The unpolarized TMD distribution function $f_1(x, k_\perp)$ and fragmentation function $D_1(z, p_\perp)$ are parameterized as

$$f_1(x, k_\perp) = f_1(x, Q^2) \frac{e^{-k_\perp^2/\langle k_\perp^2 \rangle}}{\pi \langle k_\perp^2 \rangle}, \quad (17)$$

$$D_1(z, p_\perp) = D_1(z, Q^2) \frac{e^{-p_\perp^2/\langle p_\perp^2 \rangle}}{\pi \langle p_\perp^2 \rangle}, \quad (18)$$

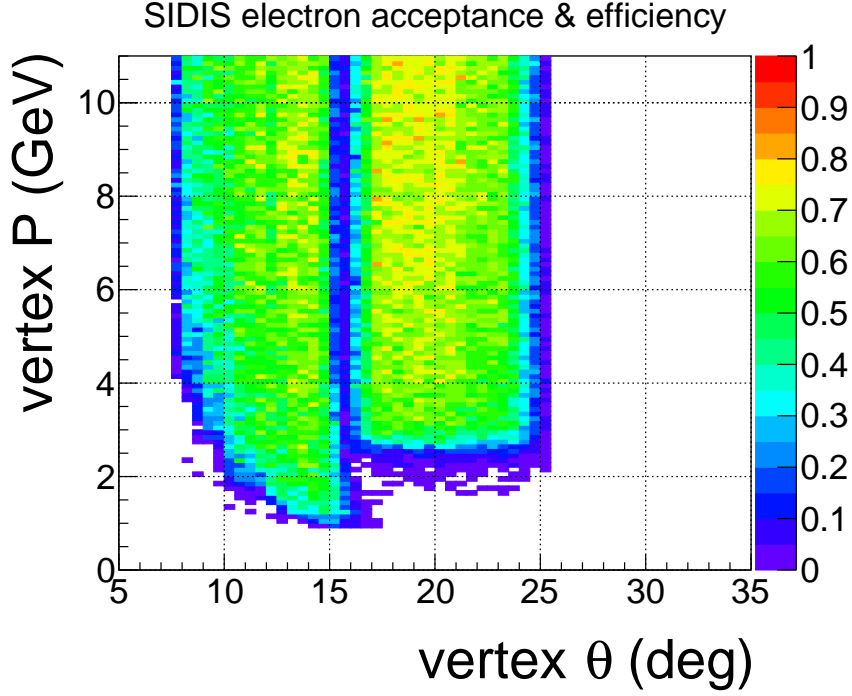


Figure 161: Electron acceptance and efficiency (except tracking) of SoLID SIDIS with the 40 cm ^3He target and two target window collimators. The result for J/ψ has a similar shape, but higher values because it has a 15 cm long target and no collimator.

where $f_1(x, Q^2)$ and $D_1(z, Q^2)$ are collinear distribution and fragmentation functions. In our simulation, we use CT14 leading order collinear PDF parameterization [289] and DSS leading order collinear FF parameterization [290]. The two parameters describing the transverse momentum dependence are chosen as $\langle k_\perp^2 \rangle = 0.25$ and $\langle p_\perp^2 \rangle = 0.20$ [84]. For the three leading twist single spin asymmetry (SSA) terms, the Sivers, the Collins, and the pretzelosity, we use the phenomenological models [81, 291, 292] as inputs to the simulation. To take into account the detector efficiency effect, we use 85% of the statistics for the estimation of the uncertainties.

Taking the advantage of the 2π azimuthal coverage, we are able to reduce the systematic uncertainties associated with luminosity and detection efficiencies by defining the target single spin asymmetry as

$$A_{UT}(\phi_h, \phi_S) = \frac{2}{P_1 + P_2} \frac{\sqrt{N_1(\phi_h, \phi_S)N_2(\phi_h, \phi_S + \pi)} - \sqrt{N_1(\phi_h, \phi_S + \pi)N_2(\phi_h, \phi_S)}}{\sqrt{N_1(\phi_h, \phi_S)N_2(\phi_h, \phi_S + \pi)} + \sqrt{N_1(\phi_h, \phi_S + \pi)N_2(\phi_h, \phi_S)}}, \quad (19)$$

where the subscripts 1, 2 represents a target spin flip pair. $N_1(\phi_h, \phi_S)$ and $N_1(\phi_h, \phi_S + \pi)$ are taken at the same time with target polarization P_1 , while $N_2(\phi_h, \phi_S)$ and $N_2(\phi_h, \phi_S + \pi)$ are taken at the same time with target polarization P_2 . Thus, the luminosity at different times will cancel. Since $N_1(\phi_h, \phi_S)$ and $N_2(\phi_h, \phi_S + \pi)$, $N_1(\phi_h, \phi_S + \pi)$ and $N_2(\phi_h, \phi_S)$ are taken in the same detector region, the acceptance and detector efficiency will also cancel to first order. The time-dependent detector efficiencies will be monitored with single electron and pion rates. With a ^3He target spin flip rate of 1/(10 minutes) (20 minutes for each pair), we expect to control the time-dependent detector efficiency uncertainty to better than 1%. In 48 days with 11 GeV beam,

we will have 3456 pairs, and in 21 days with 8.8 GeV beam, we will have 1512 pairs. Then, the systematic uncertainty of the raw asymmetry is estimated as $1.0\%/\sqrt{3456} = 1.7 \times 10^{-4}$ for 11 GeV data, and $1.0\%/\sqrt{1512} = 2.6 \times 10^{-4}$ for 8.8 GeV data. With a proton (ammonia) target spin flip rate of 1/hour (2 hours for each pair), we expect to control the time-dependent detector efficiency uncertainty to under 2%. In 55 days with 11 GeV beam, we will have 660 pairs giving an estimated systematic uncertainty of $2.0\%/\sqrt{660} = 7.8 \times 10^{-4}$. In 27.5 days with 8.8 GeV beam, will have 330 pairs, and the systematic uncertainty is estimated as $2.0\%/\sqrt{330} = 1.1 \times 10^{-3}$. The derived absolute systematic uncertainties of the SSA data associated with the raw asymmetry are obtained by dividing these numbers by the target polarization and the dilution factor in each bin.

The knowledge of the target polarization is at the 3% level. This translates to a 3% relative systematic uncertainty of the SSA data. The knowledge of the target polarization direction is about 0.2 degree. The corresponding uncertainty of the target polar angle translates into 6×10^{-6} relative uncertainty of the SSA. The uncertainty of the target azimuthal angle is included in the uncertainty of the azimuthal angle ϕ_S together with the detector resolution effect.

The systematic uncertainties associated with detector resolutions are estimated based on the track fitting studies. The resolutions of the kinematic variables in the Trento convention for each bin are obtained by Monte Carlo sampling according to the resolutions of the lab frame variables shown in Figure 127. The resolutions of the kinematical variables in the Trento convention are summarized in Table 35. The systematic uncertainty associated with the resolution mostly comes from the uncertainties of the azimuthal angles ϕ_h and ϕ_S which affect the separation of the SSA terms. It is estimated by smearing the pseudo-data according to the resolution, separating the SSA term with the smeared pseudo-data, and then comparing them to the model input of the simulation. The absolute systematic uncertainty of the SSA due to the resolution is less than 1×10^{-4} , which is negligible compared to the other uncertainties.

$E_{\text{beam}} (\text{GeV})$	x	z	$Q^2 (\text{GeV}^2)$	$P_{h\perp} (\text{GeV})$	$\phi_h (\text{rad})$	$\phi_S (\text{rad})$
11	0.002	0.003	0.02	0.006	0.015	0.006
8.8	0.002	0.004	0.02	0.006	0.018	0.006

Table 35: Resolution of kinematical variables (in the Trento convention) with the ^3He target setup.

Nuclear effects contribute to the systematic uncertainty when we extract the SSA of the neutron from ^3He data. We derive the SSA of the neutron from that of ^3He as

$$A_n = \frac{A_{^3\text{He}} - 2P_p f_p A_p}{P_n f_n}, \quad (20)$$

where the SSA of proton A_p will also be measured with SoLID in the same kinematic region. We assign 10% relative uncertainty of the knowledge of the proton SSA. The $f_{p/n}$ are the dilution factors associated with the hydrogen and the ^3He target, respectively. The light-front spectral function of ^3He including the final state interaction effect was recently developed [293]. With a theoretical calculation of the nuclear effect of the SSAs in the SoLID kinematic region [294], we estimate that the relative uncertainty in the extraction of the neutron SSAs due to the nuclear effect is about 4~5%.

The random coincidence background is estimated using single electron and single pion rates. By assuming a 1 ns time resolution, we choose a plus-minus three-sigma time window of 6 ns. For the ^3He target, we also apply a three-sigma vertex cut according to the track fitting results. As the SIDIS signal rate drops with increasing $P_{h\perp}$, we summarize the signal background ratio with

respect to $P_{h\perp}$ in Table 36. The relative systematic uncertainties due to the random coincidence background are estimated by varying the background rate by 20% for each bin.

$P_{h\perp}$ (GeV/c)	[0.0, 0.2]	[0.2, 0.4]	[0.4, 0.6]	[0.6, 0.8]	[0.8, 1.0]	[1.0, 1.2]
11 GeV beam (π^+)	110	160	150	105	75	40
11 GeV beam (π^-)	120	160	140	90	70	50
8.8 GeV beam (π^+)	75	95	80	50	45	
8.8 GeV beam (π^-)	65	95	75	50	45	

Table 36: The ratio of SIDIS signal and random coincidence background within 6 ns. These values are estimated with the ^3He target. Similar results are obtained for the proton target.

The radiative correction effect of SIDIS is simulated with HAPRAD, which was developed based on the QED calculation at the one-loop level [295, 296]. The systematic uncertainties from the radiative corrections are estimated by varying the model parameters $\langle k_{\perp}^2 \rangle$ and $\langle p_{\perp}^2 \rangle$ of the SIDIS model in our simulation by a factor of 2 (multiplied and divided). This gives relative uncertainties of about 2.5% for the 11 GeV data and about 2% for the 8.8 GeV data. A summary of the systematic uncertainties is in table 37.

Table 37: The systematic uncertainties on the asymmetry measurements of SIDIS.

Systematic (abs.)		Systematic (rel.)	
Raw asymmetry	0.0014	Target polarization	3%
Detector resolution	< 0.0001	Nuclear effect	(4 – 5)%
		Random coincidence	0.2%
		Radiative correction	(2 – 3)%
		Diffraction meson	3%
Total	0.0014	Total	(6 – 7)%

17.3 PVDIS Program

17.3.1 Acceptances, efficiencies, and systematic uncertainties for PVDIS

We now have a full Monte Carlo simulation that includes all elements of the PVDIS apparatus, layer by layer energy deposition in the electromagnetic calorimeter (EC) and optical physics in the light gas Cherenkov (LGC). At present we have preliminary GEM responses and tracking under realistic backgrounds, both of which are under continued development. We now also have recent data from newly constructed GEMs which are being employed at Jefferson Lab to refine our simulations. For the present results, true values of track hit positions in the GEMs are used. Neither the GEMs nor the calorimeter are segmented in the simulation. However, since the GEM sector boundaries will be far from the baffle-defined signal regions and the tracks entering the EC will not be parallel to the module boundaries, the effects of GEM and EC segmentation on our acceptance are expected to be negligible.

Input events to the Monte Carlo are electrons from a DIS generator using cross sections from CTEQ6 parton distribution fits [297]. Our analysis integrates primary electrons which reach the active area of the EC after passing through the active areas of all five GEMs and the front window of the LGC. The acceptance is shown in Figure 162 as a function of p and θ (left panel) and as a

function of Q^2 and x_{bj} (right panel). Lines on these plots show the boundaries of the kinematic region of interest: $Q^2 > 6 \text{ GeV}^2$, $W > 2 \text{ GeV}$, and $x_{bj} > 0.55$. Our acceptance in this region is typically 40%.

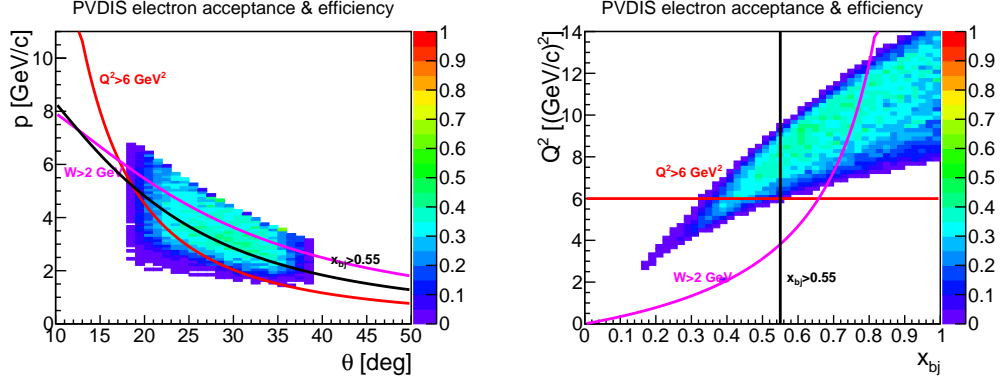


Figure 162: Left: PVDIS acceptance and efficiency as a function of p and θ . Right: PVDIS acceptance and efficiency as a function of Q^2 and x_{bj} . Curves show bounds of the kinematic range with $Q^2 > 6 \text{ GeV}^2$, $W > 2 \text{ GeV}$, and $x_{bj} > 0.55$.

Contributions to the efficiency are as follows:

Calorimeter: Efficiency of $\sim 95\%$ as reported in subsection 10.7.

LGC: The minimum trigger requirement of ≥ 2 photoelectrons in each of ≥ 2 PMTs in the sector matching the EC yields 96% efficiency.

Tracking: The GEM detection efficiency is 97% per plane. From our studies using a tree search algorithm with realistic and correlated superimposed backgrounds and our current model of digitization, a track finding efficiency of $\sim 90\%$ appears to be achievable. Development of the track finding software is continuing.

Combining the above contributions yields an estimate of 82% for our overall efficiency.

The systematic errors on our measurement of the parity violating asymmetry are summarized in Table 38.

The systematic error on the polarization of the beam $\Delta P/P$ is required to be better than 0.4% [298]. The best achievable precision of such measurements is 0.6% at present, but 0.4% are considered to be within reach [315]. The dominant systematic error in [298] is the laser polarization, which was estimated to be 0.3% but is given in [315] to be below 0.2%. The higher analyzing power and large-angle characteristics of the 11 GeV beam relative to the Qweak 1 GeV beam result in a better precision for SoLID. We also expect to understand better the systematic errors of the polarimetry by building on the experience of the MOLLER experiment, where polarimetry plays a particularly important role.

The radiative corrections are similar to those computed for the HERA experiments [300]. Many of the important radiative corrections come from tails of events at larger x , which are small for the SoLID high- x kinematics. We have assembled a team including A. Aleksejevs, S. Barkanova and W. Melnitchouk, who will assist in performing the necessary calculations. We estimate an error of 0.2% from radiative corrections.

Finally, systematics on the asymmetry due to reconstruction errors, including DAQ issues and particle identification, will be kept to the 0.2% level. The pion contamination is expected to be below 1% for most bins and the required corrections should be valid to at least 10% of that. Work

on the DAQ is in progress to demonstrate that the pile-up and dead-time corrections can be kept to below 0.15%.

The total systematic error is 0.6%, unchanged from the proposal value, allowing sufficient sensitivity to meet our physics goals.

Polarimetry	0.4
Q^2	0.2
Radiative corrections	0.2
Reconstruction errors	0.2
Total	0.6

Table 38: Summary of PVDIS systematic errors, in percent.

17.3.2 Kinematics, Resolution and Calibration for PVDIS

In this section, we describe the general method of measuring the momentum p and the scattering angle θ of each track. In addition, we discuss the resolution of x , and Q^2 , the relevant variables for the analysis. Finally, we discuss the calibration of the average value of Q^2 . The most critical requirements are the x resolution, on the order of 0.01 to avoid kinematic smearing and that the average Q^2 , which is proportional to the asymmetry, is calibrated to 0.1%.

We start with a first order approximation of the momentum resolution of the SoLID spectrometer for PVDIS. Fig. 163 shows a side view of the spectrometer with a typical high-momentum track. We approximate field as uniform within the rectangle and zero outside. All tracking is done outside the field, so only the position and direction of the track are measured.

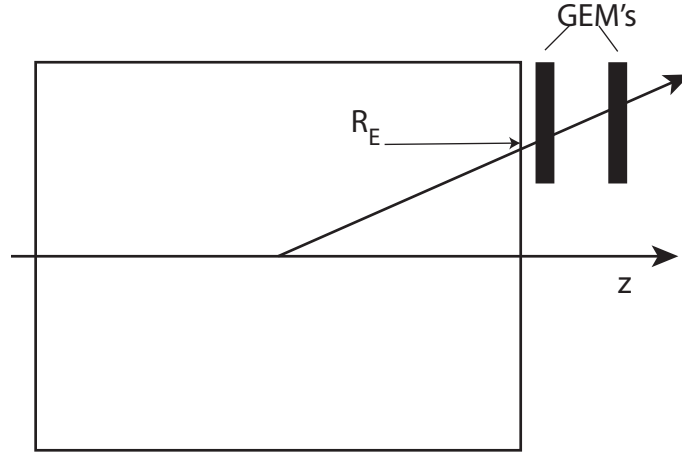


Figure 163: Plan view of SoLID with a high-momentum track. The field is approximated as uniform inside the rectangle and zero outside. To first order, it looks straight. The trajectory leaves the magnetic field a distance R_E from the beamline.

To first order, the track looks straight in Fig 163. Moreover, the location of the interaction along the beam line is unknown, so no information is available about the little curvature present. Fig. 164 shows the track in a vertical plane (with the magnetic field pointing out of the page.) Here the radius

of curvature $\rho \propto p$ of the track can be observed. The effect is that the projected track misses the beam line by the distance d of the dotted line in the figure. In this plane, the position of the origin of the track, which is the beam line, is precisely known. The displacement is given by

$$\delta = \frac{1}{2} \frac{R_E^2}{\rho}$$

The resolution $\delta p/p \propto \delta \rho/\rho$ is determined by the fraction error in the distance $\delta d/d$. For SoLID, $\delta d \sim 1$ mm and $d \sim 10$ cm.

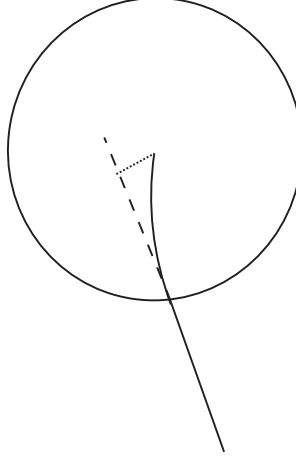


Figure 164: View of the trajectory in a plane normal to the magnetic field. The radius of the circle is R_E . The dashed line is the extrapolated straight line. It misses the beamline by the length of the dotted line which is defined to be d .

The method that we use to reconstruct the tracks, determining the scattering angle and momentum, is easiest to understand in the approximation of a uniform field. Based on this method, we can explain our alignment tolerances and systematic errors. We then show how to make the corrections for the realistic case. These corrections do not alter most of the tolerances.

In order to be more quantitative, we look at the track in the x - y plane as shown in Figure 165. All we require is hits in two GEM detectors. The one closest to the target is labeled GEM_i and the other is GEM_j . Since the beam is small ($300 \mu\text{m}$ by $250 \mu\text{m}$), it provides a third point which is sufficient to determine the radius of curvature ρ of the helix. The transverse momentum of the electron is then κ/ρ , where κ is a constant proportional to the magnetic field. The transverse distance between the beam and the first GEM is R and between the two GEM's is D . The angle between the line segments R and D is $(\psi + \delta)/2$. From the diagram, we have

$$\frac{1}{\rho} = \frac{2(\sin(\psi/2) + \sin(\delta/2))}{(R + D)} \approx \frac{\psi + \delta}{R + D}, \quad (21)$$

where the approximation is for small angles. Since

$$\frac{\sin(\psi/2)}{\sin(\delta/2)} = \frac{R}{D}$$

and $(\psi + \delta)/2$ is measured, Eq. 21 can be evaluated exactly.

For the helix, the angle θ between the trajectory and the z -direction is constant, and thus is the scattering angle. If Δz is the difference in the z -coordinates of the GEM's, then

$$\tan \theta = \frac{\rho}{\Delta z} \sin^{-1} \frac{D}{\rho} \approx \frac{D}{\Delta z}. \quad (22)$$

From the approximation, we see that the error in ρ contributes little to the error in θ .

Finally, we note that

$$Q^2 = 4E \frac{\kappa}{\rho} \tan(\theta/2).$$

Thus the fractional error in Q^2 is the sum in quadrature of the fractional errors in ρ and θ .

Thus with two GEM points and a narrow beam, we can reconstruct the important variables for DIS. In addition, the distance r from the first GEM to the beam line in the x - y plane and the azimuthal angle of the first GEM hit are measured. The first can be used to determine the z -coordinate of the interaction, which can be used as a check that the track is valid and also determine if it came from the front or rear target windows.

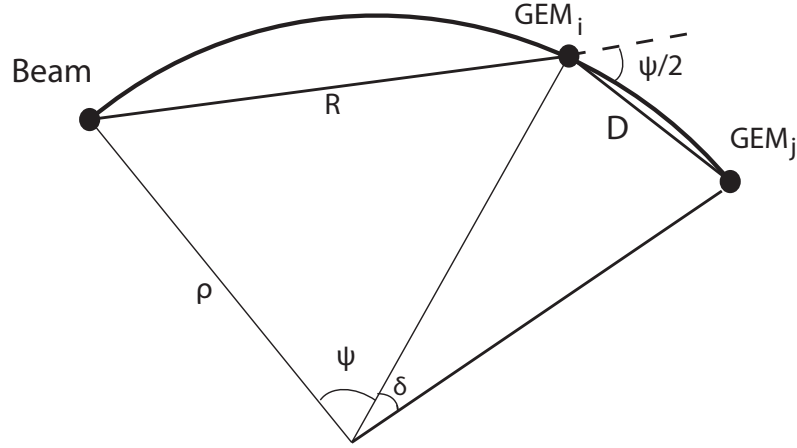


Figure 165: Projection of the track in the $x - y$ plane. The projected radius of curvature is ρ .

For realistic magnetic fields, we generated with our Monte Carlo many trajectories and determined the discrepancies with Eqs. 21 and 22. These discrepancies could be parameterized in terms of the measured variables $\psi + \delta$, D , R , and r and used as corrections. With the corrections, ρ and θ can be determined from the GEM hits with a precision better than 0.1%.

Rather than $\psi + \delta$, we used the angle α between the line segment R and the line joining the beam with the hit in GEM_j . Then

$$\alpha \approx \frac{\psi + \delta}{2} \frac{D}{R + D},$$

and

$$\frac{1}{\rho} = \frac{2\alpha}{D}.$$

Thus our precise and realistic equation for ρ is

$$\frac{1}{\alpha\rho} = \frac{2}{D} + F_\rho(R, D, r, \Delta z). \quad (23)$$

An important feature is that the angle α only appears in the left side. This feature is useful for our momentum calibration method shown below. For θ ,

$$\tan \theta = \frac{D}{\Delta z} + F_\theta(R, D, r, \Delta z, \alpha). \quad (24)$$

There are two effects that contribute to F_θ . The first is the approximation in Eq. 22. The second is the fact that radial components of the magnetic field change the angle that the trajectory makes with the z -axis. Thus F_θ depends slightly on α .

Since F_ρ and F_θ are small, the errors in their arguments do not contribute significantly to the errors in ρ or θ . The requirements for calibration can be obtained from the leading approximations.

The momentum resolution, which is dominated by multiple scattering, mostly in the air, is about 1%, independent of momentum. The angular resolution, dominated by GEM resolution, is about 0.5%. The resolution in Q^2 is 1.5% and in x is 1%. The z -resolution is 7 mm. These numbers are obtained with our simulation with realistic GEM signals.

The first step in momentum calibration is alignment of the GEM trackers. To make estimates of the systematic errors in track momentum reconstruction we use artificial displacements of GEM hits in our simulation. In the simple case of a uniform field and a thin target the minimum distance between the beam axis and the line through two GEM hits is linearly related to $1/p$. That distance is of order 10 cm, implying a need to calibrate the GEM transverse positions to $\sim 100 \mu\text{m}$ in order to achieve a systematic error on the relative momentum $\Delta p/p$ of order 10^{-3} .

For a more realistic estimate we use a Monte Carlo simulation incorporating a realistic field and a long target to study the effects on our momentum and angle reconstruction of all elementary displacements: lateral and transverse position shifts, and rotations in and perpendicular to the detector plane, of one or both GEMs. Results are shown in Table 39. Due to the symmetry of the apparatus, Q^2 is insensitive to all these misalignments to first order except for single GEM angular displacement in-plane. We find that we need to understand transverse GEM positions relative to straight tracks to within about $200 \mu\text{m}$, and absolute positions parallel to the beam axis at the level of about 3 mm.

Within a GEM, strip positions relative to one another will be known to within $25 \mu\text{m}$. With standard surveys, relative strip positions within a full GEM plane can be established to better than $500 \mu\text{m}$. To achieve our resolution goal and to monitor possible motion of the tracking chambers, straight-through electrons with the magnetic field off and low energy photons with the field off and on will be used to calibrate the relative transverse positions of the GEMs with the required precision. A thin carbon target about 10 cm upstream of the LD₂ target has lines of sight to most of the area of the GEMs, as shown in Figure 166. For x-ray studies, an absorber ring with holes, or conversely a set of absorbing beads mounted on a ring of light material, will provide the fiducials.

Once the positions of the GEMs are known, the magnetic field is calibrated as follows. First a map is obtained with a precision of about 1%. With this map the radial fields are known well enough so that F_θ can be precisely determined. To improve the calibration of the momentum to the 0.1% level, we use electron hydrogen elastic scattering data at beam energies of 4.4 and 6.6 GeV as well as at different magnetic field settings. Since the beam energy is known to better than 0.1% and the angle can be measured to that precision, the location of the elastic peak provides a calibration of the magnetic field. One issue is that for one beam energy, there is only one track energy at each angle, whereas for DIS, the angle and energy are much less correlated. However, the correction F_ρ

1/p and θ residuals for GEMs 1, 4					
transform	GEM(s)	$\delta p(\text{mean})$	$\delta p(\text{width})$	$\delta \theta(\text{mean})$	$\delta \theta(\text{width})$
transverse displacement	1, 4	$-0.01\%/mm$	$0.77\%/mm$	$0.00\%/mm$	$0.00\%/mm$
	4	$0.00\%/mm$	$0.76\%/mm$	$0.00\%/mm$	$0.08\%/mm$
longitudinal displacement	1, 4	$0.05\%/mm$	$0.00\%/mm$	$0.00\%/mm$	$0.00\%/mm$
	4	$0.08\%/mm$	$0.01\%/mm$	$0.06\%/mm$	$0.00\%/mm$
in-plane rotation	1, 4	$0.00\%/mrad$	$0.00\%/mrad$	$0.00\%/mm$	$0.00\%/mm$
	4	$1.61\%/mrad$	$0.15\%/mrad$	$0.01\%/mm$	$0.01\%/mm$
out-of-plane rotation	1, 4	$0.00\%/mrad$	$0.08\%/mrad$	$0.00\%/mm$	$0.03\%/mm$
	4	$0.00\%/mrad$	$0.09\%/mrad$	$0.00\%/mm$	$0.06\%/mm$

Table 39: Momentum and angle reconstruction sensitivities to various displacements of GEMs 1 and 4: transverse, longitudinal, and rotational (in and perpendicular to the detector plane) displacements of both GEMs or of GEM 4 only. “ $\delta p(\text{mean})$ ” and “ $\delta \theta(\text{mean})$ ” are the changes in the mean of the $1/p$ and θ residuals and “ $\delta p(\text{width})$ ” and “ $\delta \theta(\text{width})$ ” are the changes in those residuals’ width per unit displacement. Due to detector symmetry, the displacement to which we are most sensitive is single GEM in-plane rotation.

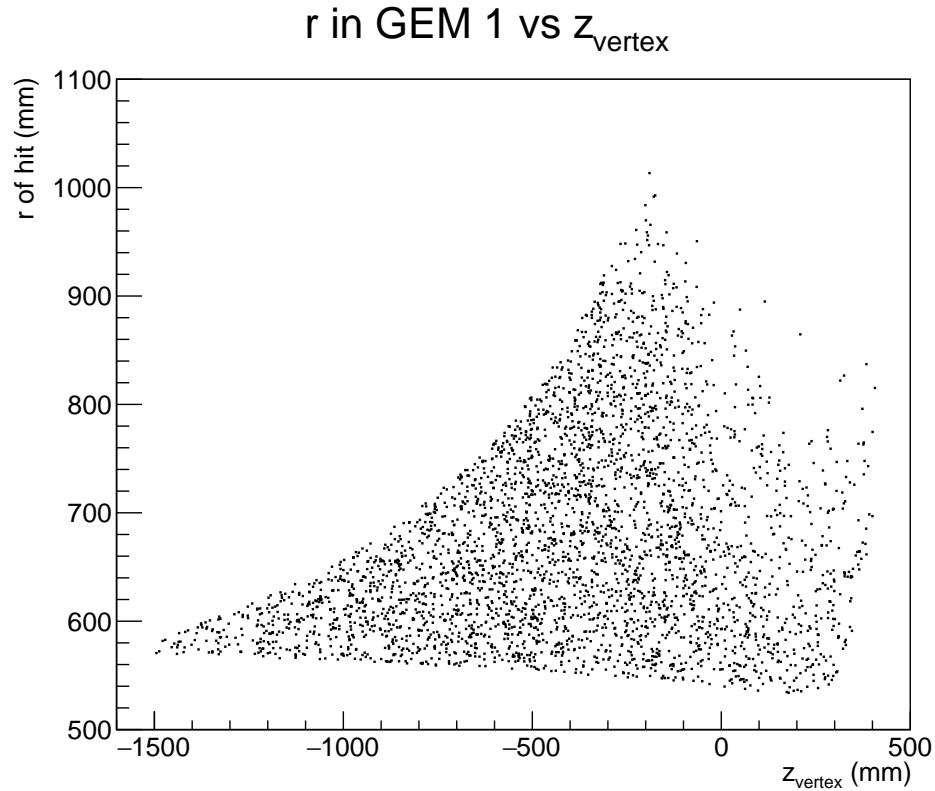


Figure 166: Radial coordinates of photon hits in GEM 1 versus vertex z position. Most of the detector area is covered for vertex at $z = -200$ mm, corresponding to a position about 10 cm upstream of the LD₂ target. Similar results are seen in the other GEMs.

in Eq. 23 is independent of α , so a single momentum at each angle is sufficient. In other words, the importance difference between two similar fields is the value of $\int B_z ds_\perp$ which is a scale factor for all momenta. Hence a single momentum from the elastic scattering is sufficient to make a precise correction.

Clean separation of the elastic peak will be required. Figure 167 shows results from simulations where the green histograms are elastics and the blue histograms are the inelastic background from a Christy-Bosted parameterization [301]. Target and detector materials were included and momenta were smeared by 1% to simulate detector resolution. At both energies the elastic peaks are cleanly resolved. Rates are ample for calibration; see Figure 168. At 6.6 GeV, the integrated rate is about 150 Hz per μA of beam current. At 50 μA , sufficient data can be collected in only a few minutes.

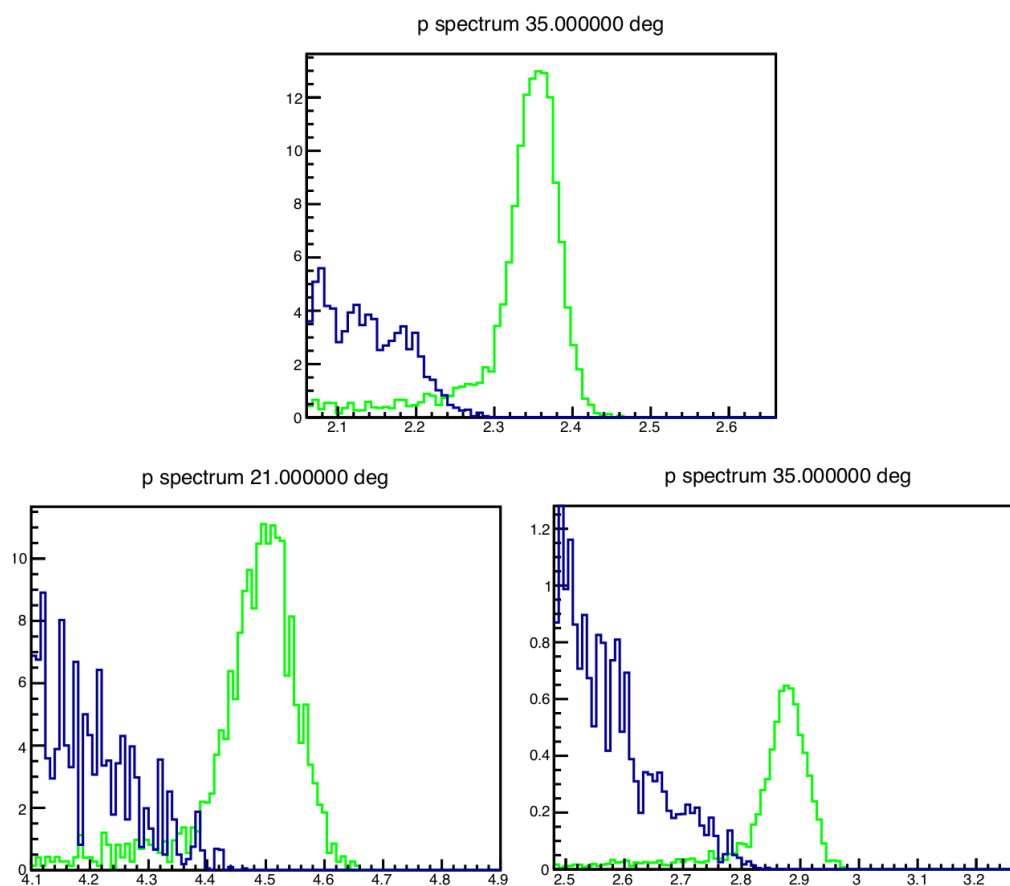


Figure 167: Elastic (green) and inelastic (blue) spectra for 4.4 GeV (top) and 6.6 GeV (bottom) electrons on a hydrogen target, at scattering angles of 21° (bottom left) and 35° (top and bottom right).

17.4 J/ψ Program

Recent simulation studies of J/ψ production have been performed including approximate radiative effects. External bremsstrahlung was applied to both the incident and scattered electrons. The incident electron radiation loss is calculated with the peaking approximation through the target material

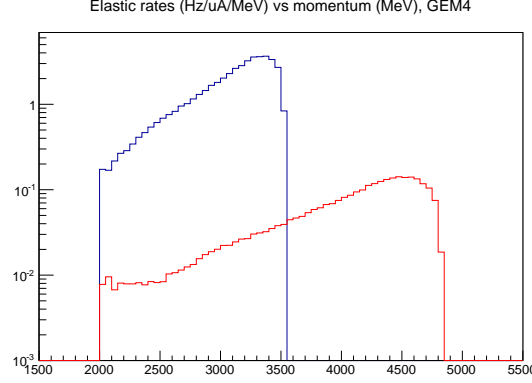


Figure 168: Elastic rates at GEM 4 for 4.4 GeV/c (blue line) and 6.6 GeV/c (red line) electrons on LH2, as a function of momentum in MeV/c. Rates are in Hz per μA per MeV/c. Target and detector materials are included.

up to the reaction vertex. The external radiative loss for the scattered electron is calculated within the framework of Geant4/GEMC and folded into the total resolution smearing of the track. Internal bremsstrahlung is calculated according to the Q^2 dependent equivalent radiator method, and applied to both the incident and scattered electrons. These radiative calculations are well known and widely used and have historically described radiative losses with reasonable precision. A more robust and explicit calculation would allow for a more precise unfolding of the radiative losses, however such an endeavor is non-trivial and would require a significant investment of manpower. For the approximate calculations, one can see in Figure 169 the effects of bin-migration along W , and the estimated correction needed to recover the unradiated cross-section. The plotted calculations were simulated with a 4-fold coincidence; the 3-fold coincidence has identical radiative losses (incident electron, scattered electron). Additionally, the internal radiative corrections in the equivalent radiator method are near zero when in the quasi-real photon kinematics of the 2-fold coincidence measurement. We plan to continue developing our radiative corrections procedure with exact calculations, accurate unfolding, and tests of model dependence.

A physics generator which includes acceptance effects was developed for the experimental proposal and has since been extended to include resolution effects and the radiation effect approximations outlined above.

Because the J/ψ experimental configuration is very similar to the SIDIS setup: a target position offset by 35 cm being the only difference. the acceptance and efficiencies are in-line with the SIDIS ^3He program shown in Figure 161 and Table 34. The only difference is that the J/ψ setup has higher acceptance because its 15 cm long LH2 target requires no collimators as SIDIS ^3He

As stated in the original proposal, we expect the systematic uncertainty to be dominated by the acceptance ($<10\%$), with an additional contribution of a few percent from sub-detectors, luminosity, target windows and background contamination. We take the total systematic uncertainty to be 11%. Without radiative corrections of the data, systematics due to bin migration can be estimated from Figure 169. However, much of these systematics can be corrected by accurately simulating and properly unfolding the radiative effects (see section above).

An updated analysis of the J/ψ experiment's di-lepton trigger from the decay lepton pairs and triple lepton trigger with additional scattered electron were preformed, similar to what the PVDIS and SIDIS ^3He programs have done. This simulated trigger study included the signal and combi-

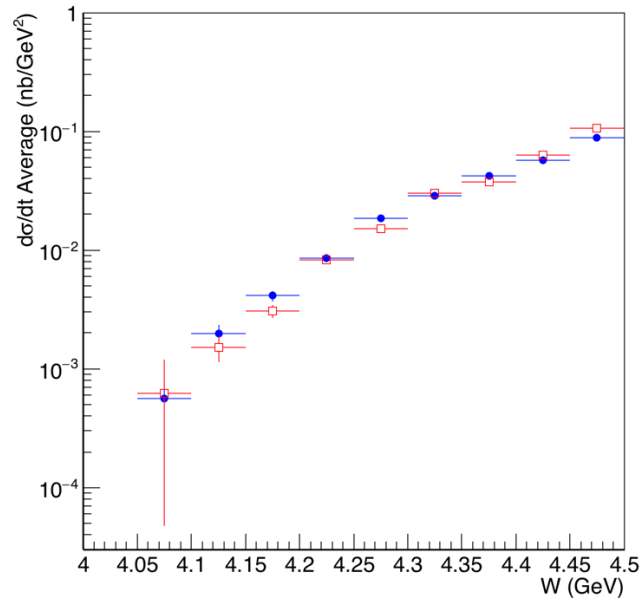


Figure 169: Simulation of cross-section including acceptance effects but no additional radiative losses (blue circles) for comparison with the expected cross-section measurement including acceptance smearing and all radiative effects listed in the text (red squares).

natorial background from leptons, pions, and additional hadrons over both forward and large angle acceptance including the most up-to-date EC, LGC, and SPD response. The resulting di-lepton trigger and triple lepton trigger are calculated to have a coincidence rate about 60 kHz and 30 kHz respectively. The triple lepton trigger will be our main trigger and it's also possible to take some pre-scaled di-lepton triggers to preserve photoproduction data. We are working on improving the trigger rate estimation and fine tuning the trigger design to see what's the best way to maximize the physics program under reasonable trigger limit.

18 Supports and Infrastructure

18.1 Magnet Support

The plan used for estimating the cost is to build a stationary frame, based off of the design used for CLEO II, and distribute the approximate 1000 ton load of the modified CLEO-II magnet section using eight 200 ton enerpac jacks. Steel plates and large steel blocks and/or large I-beams will be used to distribute the load out over a safe area. The 200 ton jacks will be used for vertical alignment and have locking rings which allow for a full mechanical connection and not rely on hydraulic pressure for stationary support.

18.2 Endcap Support Structure and Motion Mechanism

The endcap will have a support structure that cradles each half the cylindrical ring. The structure will be integrated into a track system that is mounted to steel plates resting upon the concrete floor. The initial design concept for the track system requires a set of longitudinal (downstream direction) tracks for moving the endcap away from the magnet. A second set of tracks that would separate the endcap halves in the lateral direction would ride on top of the longitudinal tracks. The endcap support structure would then be attached to the top lateral track system. Motion can be achieved by using hydraulic or electric cylinders to push and pull the entire system into position.

18.3 Support Structure for Equipment Located Inside Cryostat Bore

The magnet will be located adjacent to the existing Hall A center pivot/target mount area and will have limited access to the front of the magnet. The insertion of the large angle detector packages that will reside internal to the cryostat will be accomplished from the downstream side of the magnet using a supporting framework to roll the packages in and out. This will require the detector hut to be moved downstream to allow access to the cryostat.

An internal frame system is needed to mount the lead baffles in the PVDIS experiment. See Figure 170. The frame cannot come into contact with the inside bore of the cryostat. This requires the frame to span the entire length of the cryostat and mount to the return yoke iron. A stainless steel cylinder will be mounted between the two coil collars to bridge across the length of the cryostat. It's outside diameter will be 2" less than the diameter of the cryostat bore allowing a 1" gap of clearance with the bore. The downstream end will be mounted directly to the coil collar through a spacer ring. The upstream end will mount through an annular plate that attaches to the front piece. The front piece resides inside the bore of the upstream coil collar. Since the front piece has to be movable to balance the magnetic forces on the coils the annular plate will be attached to the front piece with studs. This will allow the framework to remain stationary if the front piece has to be adjusted. Individual rails similar to those used in the endcap will bolt directly to the stainless cylinder to allow the internal detector packages to roll into place. The same rail system can be used for the SIDIS experiment for mounting the large angle calorimeter and GEMs.

18.4 Power Requirements

The projected electrical power load is 1.6 MVA, maximum current for magnet at 3266A. The present power consumption for Hall A is less than 1 MVA. An upgrade to the Hall substation to have 2 MVA is required. (A funded infrastructure project to upgrade substation is expected to finish in 2020).

The CLEO-II magnet is designed to have a low cryogenic heat load with passive cooling. The HRS arms will not be operational during SoLID, so it is expected that the refrigeration heat load

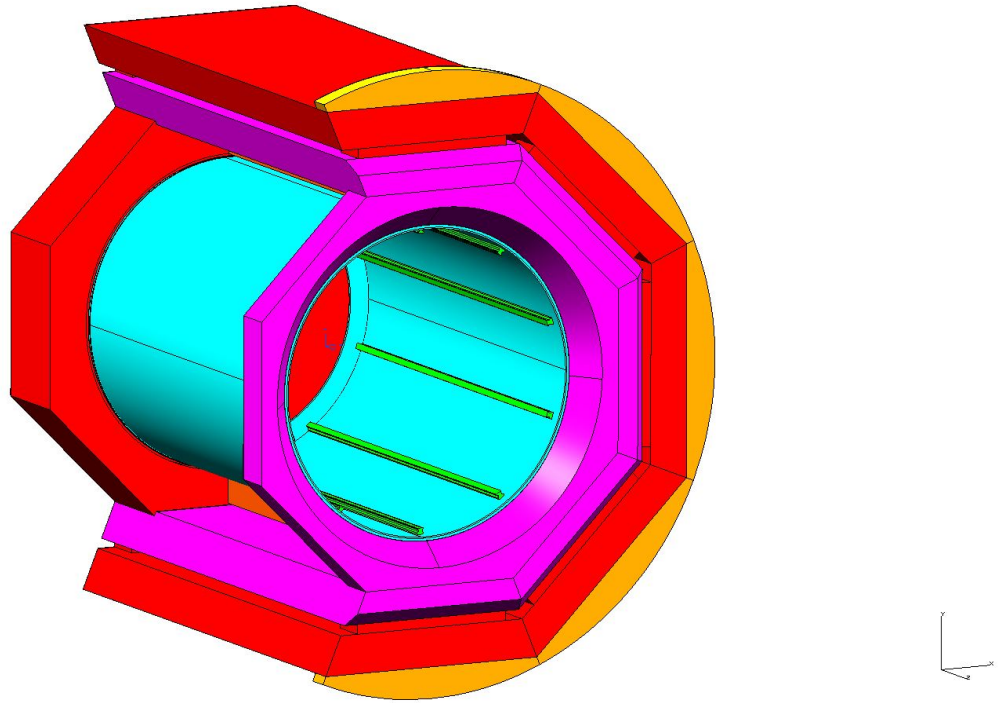


Figure 170: The internal rail system will be used to mount all parts inside the barrel, including PVDIS baffle, SIDIS large angle calorimeter and GEM's

will be less than needed for HRS. The refrigeration need for the cryotarget is discussed in the target section (Section 5).

19 Installation

19.1 Experimental Layout

An initial check of the experimental equipment layout in Hall A has been completed and no major obstructions were found. The experiment layout puts the beam left HRS arm at 90 degrees to the beamline and the beam right HRS arm at a forward angle of 145 degrees. The forward angle of the BR arm allows a direct path from the wall opening at the bottom of the truck ramp to the assembly area. The target will be 145 cm downstream of the nominal pivot location with the center of the CLEO-II magnet 350 cm downstream of the target center.

19.2 Magnet Moving and Placement

In evaluating the use of the CLEO magnet for SoLID, consideration is given to how the CLEO magnet can be transported into Hall A and how Hall A structurally meets the requirements of CLEO.

The SoLID magnet and detectors encompass an area of 5.8 meters in diameter and 7.3 meters long. With the magnet on beamline center, clearance to the Hall floor ranges from 10 to 38 cm. The weight of the CLEO-II magnet, detector hut and detectors is estimated to be 1000 tons. The floor in this installation region is designed for 250 tons for a 12 square foot pad. The footprint of the SoLID spectrometer supports will be approximately 95 square feet. SoLID will create an approximate floor loading of 126 tons per 12 square feet.

The existing Hall A equipment consists of the two High Resolution Spectrometers mounted at the center pivot and all related infrastructure. To accommodate installation of SoLID, the SIDIS target will need to be mounted 145 cm downstream from the existing support location in order for the magnet to clear the HRS bearing assembly. Placing the CLEO magnet on beamline height gives 15 inches clearance to the floor for adequate support and alignment.

Hall A is 174 feet in diameter. The bird's eye view Figure 171 and the back side Figure 172 show SoLID in Hall A with the two HRS arms in position. The SoLID detector hut is retracted backwards and a crane and lowboy tractor-trailer are shown to indicate there is sufficient room to offload and assemble SoLID components within Hall A.

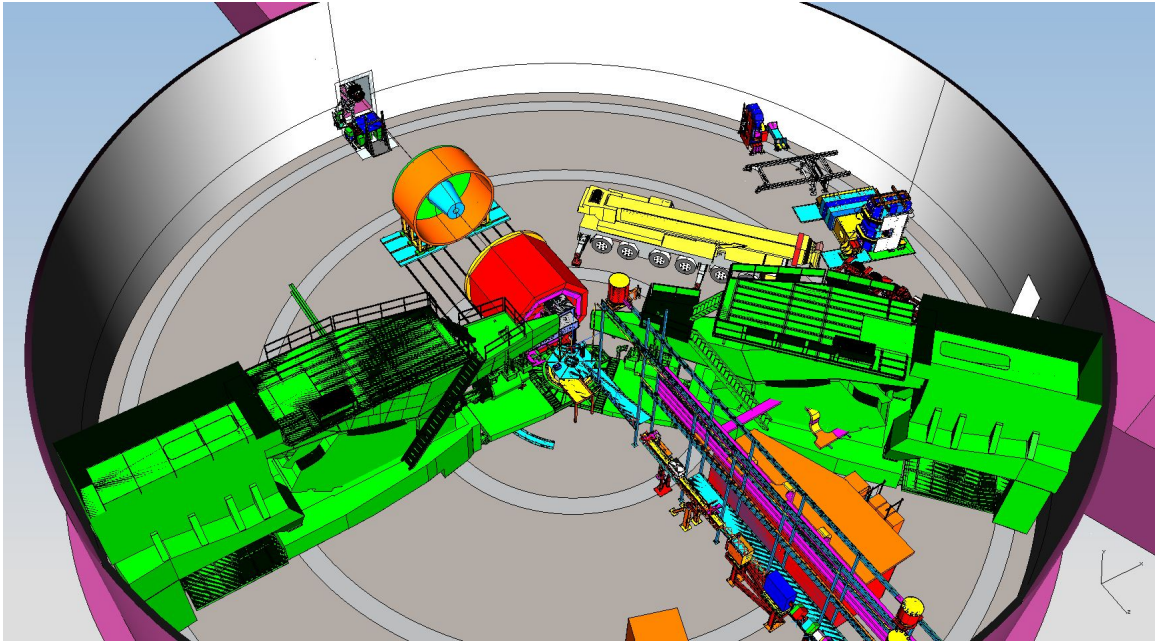


Figure 171: The bird's eye view of SoLID in Hall A

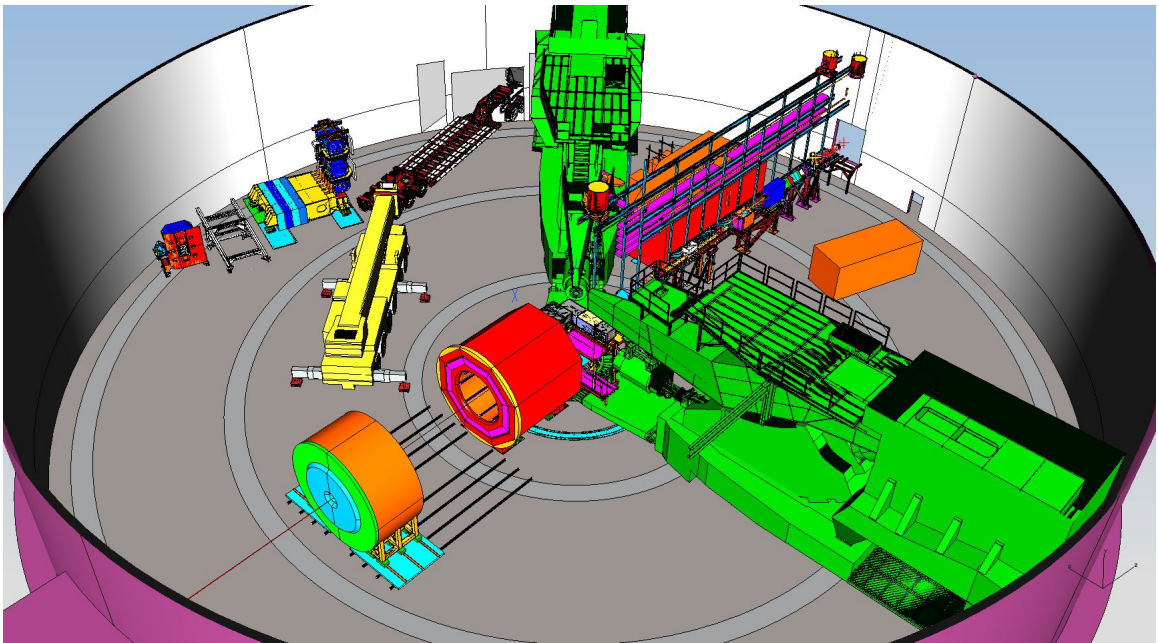


Figure 172: The back side view of SoLID in Hall A

The CLEO-II magnet was disassembled and loaded on trucks for shipping by the Cornell personnel with oversight by Jefferson Lab. The coils, coil collars and cryostat of the CLEO-II magnet arrived at JLab in 2016. The cryostat (44k lbs) and coil collars are stored in the climate controlled Test Lab. The two layers of return iron was delivered during the summer of 2019 and is being stored in the Central Material Storage Area (CMSA).

In developing the installation plan for SoLID, the largest part to transport into the hall is the cryostat. The cryostat is 12.3 feet long, 11.8 feet in diameter and weighs 22 tons. The height of the truck ramp into Hall A is limited to 14 feet in height. This will require the cryostat to be moved into the Hall on a roller structure rather than a flatbed type truck. This type of procedure has been completed several times at Jefferson Lab. See Figure 173, Figure 174, and Figure 175.

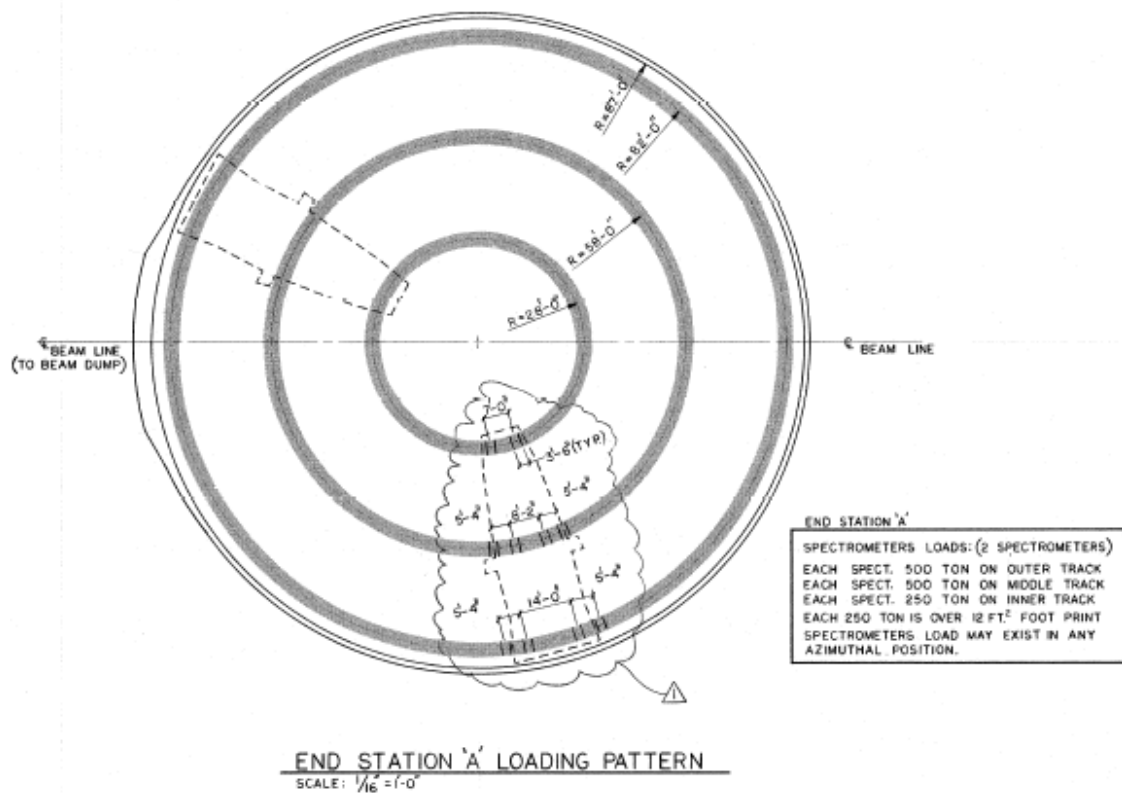


Figure 173: Hall A loading pattern.

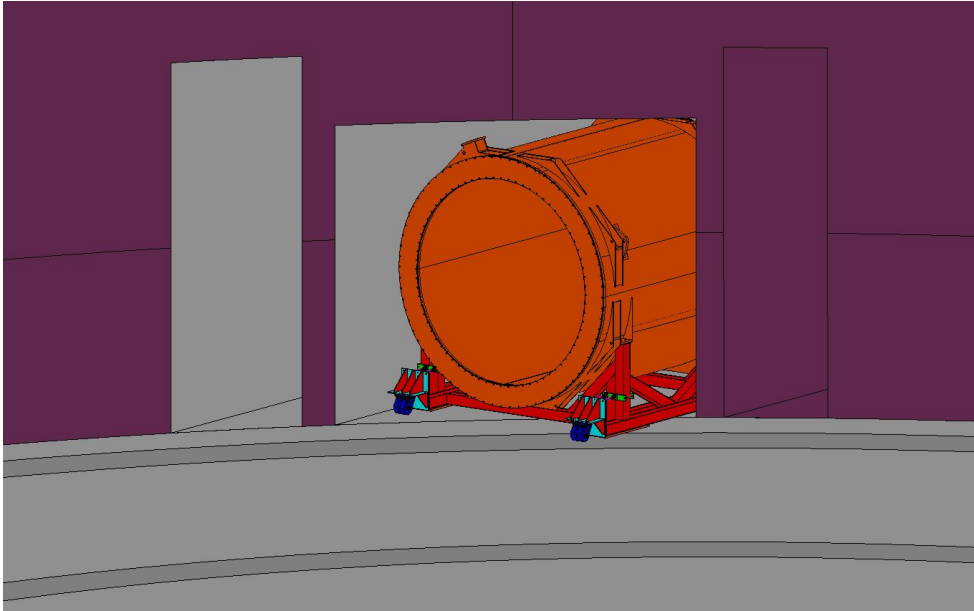


Figure 174: Moving CLEO cryostat through Hall A truck ramp wall opening.

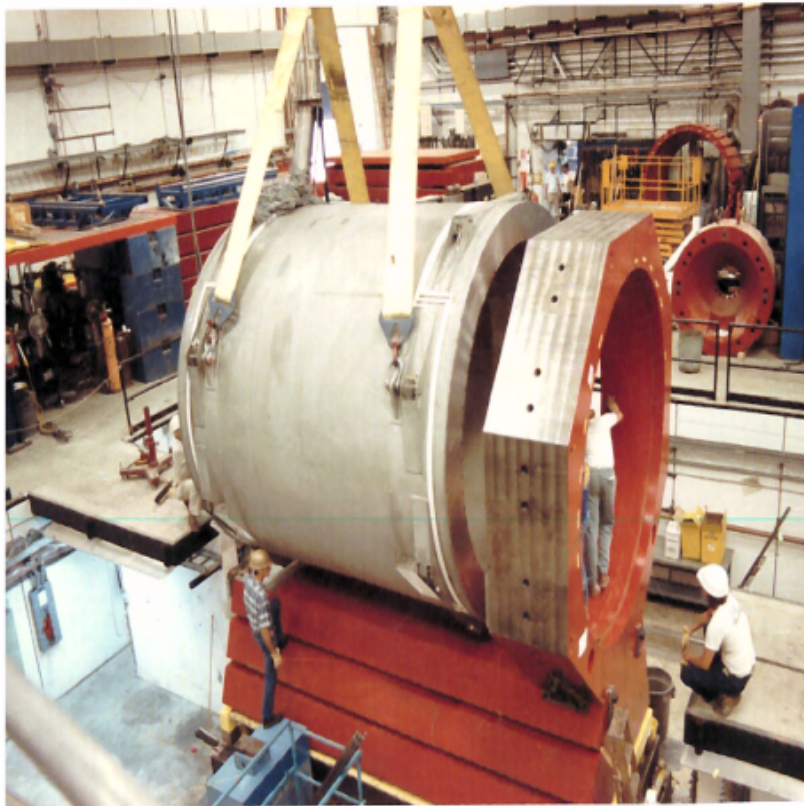


Figure 175: CLEO cryostat lifted during the installation at Cornell.

19.3 Helium Dewar Support and Upper Access Platform

An upper personnel access platform that is capable of supporting the helium dewar will be mounted to the top of the magnet. A similar platform was used for the CLEO II experiments. See Figure 176.

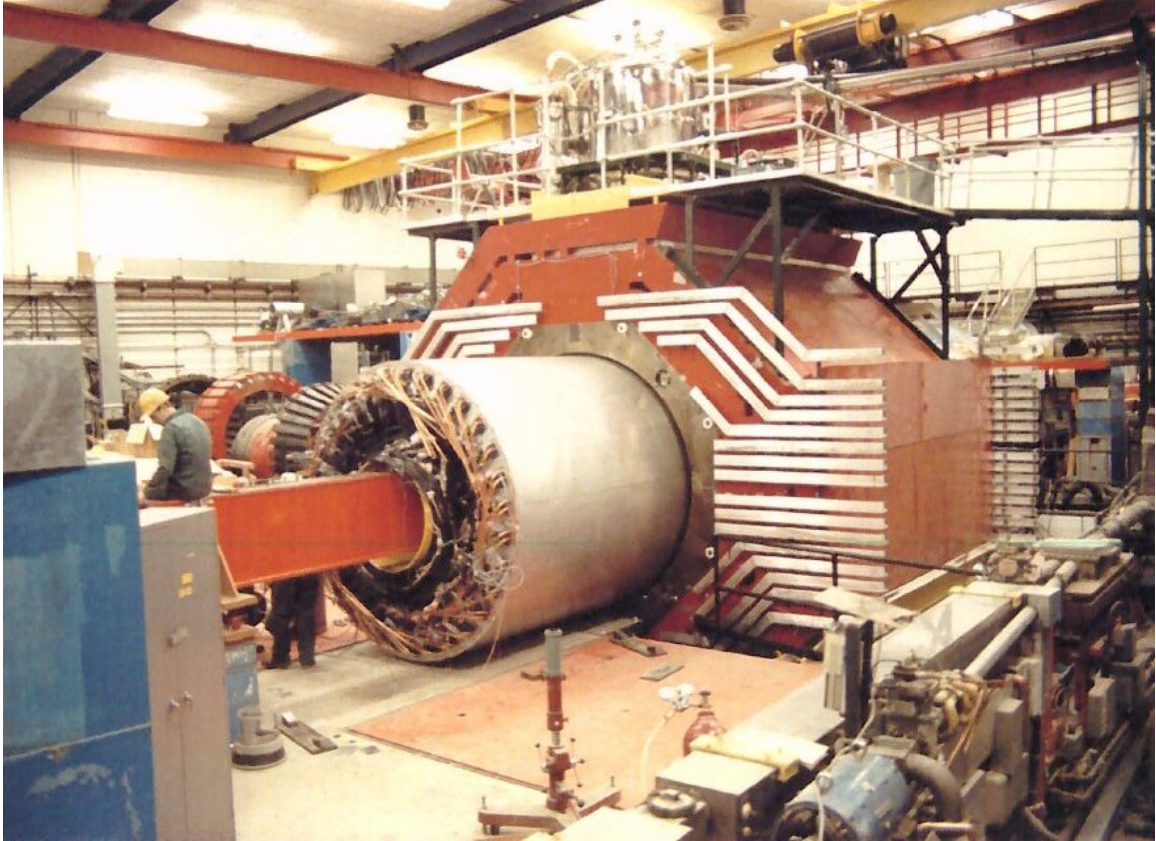


Figure 176: Helium dewar support upper access platform and detector loading inside of cryostat.

19.4 Endcap Forward Angle Detector Package Installation Structure

The basic design concept for the detectors mounted inside the endcap will have them supported by individual rails mounted to the inner circumference of the cylindrical ring and on rails attached to the outer horizontal circumferential surface of the nose if needed. A large universal installation fixture is envisioned to load each of the detector packages onto the endcap rails. The framework design is intended to accommodate the various endcap detectors with interchangeable fixturing specific to each group. Personnel access to the endcap will be through man lifts and/or a specialized scaffolding as needed.

19.5 Large Angle Detector and Baffle Installation Mechanism

An installation mechanism is needed to load the large angle detector packages and baffle system into the internal support structure mentioned in the last section. This mechanism will likely be mounted to the longitudinal track system used for the endcap movement and can utilize the tracks for rolling the detectors and baffles into the cryostat and transferring the load to the internal frame. Depending

on the final design of the detectors and baffle system the support could be a simple beam that runs through the middle of the detectors and baffles. See Figure 176 for similar approach at Cornell University.

19.6 Light Gas Cherenkov Installation Structure

The light gas Cherenkov will mount to the external downstream end of the magnet and will not traverse with endcap. When the endcap is in the operational position the light gas Cherenkov will be enclosed within the cylindrical ring along with the rest of the forward angle detectors. The light gas Cherenkov detector will be made up of six pie shaped sections that will need to be bolted to the downstream side of the magnet. A space frame similar to a scaffolding system would hold and position each section while being attached to magnet. The space frame would attach to the rail system and could be movable along the rails if needed. The space frame will be suitable for personnel access to allow workers to perform the installation and maintenance of the detectors.

19.7 Installation Plan

SoLID project installation inside of Hall A can commence upon the removal of the preceding experiment and the return of the hall to the baseline configuration. The removal of the previous experiment and hall baseline reset is not funded under the SoLID Project. The two HRS spectrometers will already be in the positions described above.

The installation process consists of several main tasks. These tasks will overlap where possible based on available manpower and workspace to provide the shortest duration. The main tasks include magnet assembly and alignment, endcap assembly and alignment, cryo, instrumentation & control (I&C) and electrical connections to the magnet, Phase 2 full current magnet cold testing, detector staging, assembly into modules and checkout testing if needed, detector installation and final checkout.

The installation will start with magnet assembly. The Hall A 20 ton overhead crane does not have the capacity to perform the majority of the lifts required for magnet assembly. A mobile crane contractor will be required for the magnet and endcap assembly and has been budgeted into the SoLID project installation. The majority of the floor space on the beam right side of the hall will be allocated for mobile operations, truck traffic for steel deliveries and return steel staging. Due to the dangers of tractor trailer traffic and overhead lift operations, work in the hall will be limited to only essential personnel required for magnet and endcap assembly.

Endcap assembly will occur next and will also require a mobile crane inside of Hall A for the larger lifts. Pre-assembly of components will occur where possible prior to transit into the hall. After the completion of the endcap installation the mobile cranes will not be required and multiple installation tasks can occur in parallel. As utilities (electrical, cryo and I&C) are connected to the magnet, detector systems can start to be staged inside the hall.

Detector groups will be able to assemble their sub-assemblies into modules ready to install into the SoLID spectrometer and perform checkouts while the magnet utilities are connected and magnet testing begins. Detector Installation Fixtures will be assembled during this time period too. After the final magnet testing the detectors will be installed.

Magnet testing will consist of I&C checkout and calibration, cryo system pressure/leak test and purification, low current and full current test and field mapping.

The estimated duration for the SoLID installation is 1.5 years and requires 14.2 FTEs of labor.

Bibliography

- [1] Z. B. Kang, A. Prokudin, P. Sun and F. Yuan, Phys. Rev. D **93**, 014009 (2016).
- [2] Z. Ye *et al.*, Phys. Lett. B. **767**, 91-98 (2017).
- [3] D. Wang *et al.* (PVDIS Collaboration), Nature **506**, 67 (2014).
- [4] E. Eichten, K. D. Lane and M. E. Peskin, Phys. Rev. Lett. **50**, 811 (1983).
- [5] J. Erler, C. J. Horowitz, S. Mantry and P. A. Souder, Ann. Rev. Nucl. Part. Sci. **64**, 269 (2014).
- [6] S. Durr *et al.*, Science **322**, 1224 (2008).
- [7] Q. Wang, X. H. Liu and Q. Zhao, Phys. Rev. D **92**, 034022 (2015).
- [8] S. An *et al.*, Nucl. Instrum. Meth. A **594**, 39 (2008).
- [9] M. Chiu *et al.*, Progress Report of (Sub) 10 Picosecond Timing Detectors for Generic Detector R&D for an Electron Ion Collider, https://wiki.bnl.gov/conferences/images/c/c8/ERD10_Report_2015-06.pdf.
- [10] M. Boglione *et al.*, Phys. Lett. B **766**, 245 (2017).
- [11] J. Ashman *et al.* (European Muon Collaboration), Phys. Lett. B **206**, 364 (1988).
- [12] B. W. Filippone and X. D. Ji, Adv. Nucl. Phys. **26**, 1 (2001).
- [13] S. E. Kuhn, J.-P. Chen and E. Leader, Prog. Part. Nucl. Phys. **63**, 1 (2009).
- [14] X. Artru and M. Mekhfi, Z. Phys. C **45**, 669 (1990).
- [15] P. J. Mulders and R. D. Tangerman, Nucl. Phys. B **461**, 197 (1996) [Erratum: B **484**, 538 (1997)]
- [16] D. Boer and P. J. Mulders, Phys. Rev. D **57**, 5780 (1998).
- [17] X. d. Ji, J. P. Ma and F. Yuan, Phys. Lett. B **597**, 299 (2004).
- [18] K. Hidaka, E. Monsay and D. W. Sivers, Phys. Rev. D **19**, 1503 (1979).
- [19] J. P. Ralston and D. E. Soper, Nucl. Phys. B **152**, 109 (1979).
- [20] R. L. Jaffe and X. D. Ji, Phys. Rev. Lett. **67**, 552 (1991).
- [21] V. Barone, Phys. Lett. B **409**, 499 (1997).
- [22] C. Bourrely, J. Soffer and O. V. Teryaev, Phys. Lett. B **420**, 375 (1998).
- [23] J. Soffer, Phys. Rev. Lett. **74**, 1292 (1995).
- [24] W. Vogelsang, Phys. Rev. D **57**, 1886 (1998).
- [25] G. R. Goldstein, R. L. Jaffe and X. D. Ji, Phys. Rev. D **52**, 5006 (1995).
- [26] J. Ralston, private communications.

- [27] M. Gockeler *et al.* (QCDSF and UKQCD Collaborations), Phys. Lett. B **627**, 113 (2005).
- [28] H. x. He and X. D. Ji, Phys. Rev. D **52**, 2960 (1995).
- [29] B. Q. Ma, I. Schmidt and J. Soffer, Phys. Lett. B **441**, 461 (1998).
- [30] L. P. Gamberg and G. R. Goldstein, Phys. Rev. Lett. **87**, 242001 (2001).
- [31] I. C. Cloet, W. Bentz and A. W. Thomas, Phys. Lett. B **659**, 214 (2008).
- [32] M. Wakamatsu, Phys. Lett. B **653**, 398 (2007).
- [33] B. Pasquini, M. Pincetti and S. Boffi, Phys. Rev. D **72**, 094029 (2005).
- [34] J. C. Collins, Nucl. Phys. B **396**, 161 (1993).
- [35] K. Abe *et al.* (Belle Collaboration), Phys. Rev. Lett. **96**, 232002 (2006).
- [36] A. Airapetian *et al.* (HERMES Collaboration), Phys. Lett. B **693**, 11 (2010).
- [37] A. Airapetian *et al.* (HERMES Collaboration), Phys. Rev. Lett. **103**, 152002 (2009).
- [38] A. Airapetian *et al.* (HERMES Collaboration), Phys. Rev. Lett. **94**, 012002 (2005).
- [39] M. G. Alekseev *et al.* (COMPASS Collaboration), Phys. Lett. B **692**, 240 (2010).
- [40] V. Y. Alexakhin *et al.* (COMPASS Collaboration), Phys. Rev. Lett. **94**, 202002 (2005).
- [41] D. W. Sivers, Phys. Rev. D **41**, 83 (1990).
- [42] X. Qian *et al.*, Phys. Rev. Lett. **107**, 072003 (2011).
- [43] G. L. Kane, J. Pumplin and W. Repko, Phys. Rev. Lett. **41**, 1689 (1978).
- [44] M. Anselmino, M. Boglione and F. Murgia, Phys. Lett. B **362**, 164 (1995).
- [45] J. C. Collins, Phys. Lett. B **536**, 43 (2002).
- [46] A. V. Belitsky, X. Ji and F. Yuan, Nucl. Phys. B **656**, 165 (2003).
- [47] D. Boer, P. J. Mulders and F. Pijlman, Nucl. Phys. B **667**, 201 (2003).
- [48] S. J. Brodsky, D. S. Hwang and I. Schmidt, Phys. Lett. B **530**, 99 (2002).
- [49] X. d. Ji and F. Yuan, Phys. Lett. B **543**, 66 (2002).
- [50] L. P. Gamberg, G. R. Goldstein and K. A. Oganessyan, Phys. Rev. D **67**, 071504 (2003).
- [51] M. Burkardt, Phys. Rev. D **69**, 057501 (2004).
- [52] M. Burkardt, Phys. Rev. D **72**, 094020 (2005).
- [53] S. J. Brodsky and S. Gardner, Phys. Lett. B **643**, 22 (2006).
- [54] J. Huang *et al.*, Phys. Rev. Lett. **108**, 052001 (2012).
- [55] T. c. Meng, J. c. Pan, Q. b. Xie and W. Zhu, Phys. Rev. D **40**, 769 (1989).

- [56] M. Anselmino, M. Boglione and F. Murgia, Phys. Rev. D **60**, 054027 (1999).
- [57] A. Bacchetta, A. Schaefer and J. J. Yang, Phys. Lett. B **578**, 109 (2004).
- [58] Z. Lu and B. Q. Ma, Nucl. Phys. A **741**, 200 (2004).
- [59] L. P. Gamberg, G. R. Goldstein and M. Schlegel, arXiv:0708.2580 [hep-ph].
- [60] A. Bacchetta, F. Conti and M. Radici, Phys. Rev. D **78**, 074010 (2008).
- [61] B. Pasquini and F. Yuan, Phys. Rev. D **81**, 114013 (2010).
- [62] F. Yuan, Phys. Lett. B **575**, 45 (2003).
- [63] D. Amrath, A. Bacchetta and A. Metz, Phys. Rev. D **71**, 114018 (2005).
- [64] A. Bacchetta, L. P. Gamberg, G. R. Goldstein and A. Mukherjee, Phys. Lett. B **659**, 234 (2008).
- [65] H. H. Matevosyan, A. W. Thomas and W. Bentz, Phys. Rev. D **86**, 034025 (2012).
- [66] A. Kotzinian, H. H. Matevosyan and A. W. Thomas, Phys. Rev. Lett. **113**, 062003 (2014).
- [67] A. Metz, Phys. Lett. B **549**, 139 (2002).
- [68] J. C. Collins and A. Metz, Phys. Rev. Lett. **93**, 252001 (2004).
- [69] L. P. Gamberg, A. Mukherjee and P. J. Mulders, Phys. Rev. D **77**, 114026 (2008).
- [70] G. R. Goldstein and L. Gamberg, hep-ph/0209085.
- [71] Z. Lu and B. Q. Ma, Phys. Rev. D **70**, 094044 (2004).
- [72] H. Avakian, A. V. Efremov, P. Schweitzer and F. Yuan, Phys. Rev. D **78**, 114024 (2008).
- [73] J. She, J. Zhu and B. Q. Ma, Phys. Rev. D **79**, 054008 (2009).
- [74] B. Pasquini, S. Cazzaniga and S. Boffi, Phys. Rev. D **78**, 034025 (2008).
- [75] S. Boffi, A. V. Efremov, B. Pasquini and P. Schweitzer, Phys. Rev. D **79**, 094012 (2009).
- [76] V. Barone, Z. Lu and B. Q. Ma, Phys. Lett. B **632**, 277 (2006).
- [77] V. Barone, A. Prokudin and B. Q. Ma, Phys. Rev. D **78**, 045022 (2008).
- [78] M. Anselmino *et al.*, Phys. Rev. D **75**, 054032 (2007).
- [79] E. S. Ageev *et al.* (COMPASS Collaboration), Nucl. Phys. B **765**, 31 (2007).
- [80] M. Alekseev *et al.* (COMPASS Collaboration), Phys. Lett. B **673**, 127 (2009).
- [81] M. Anselmino *et al.*, Eur. Phys. J. A **39**, 89 (2009).
- [82] M. Anselmino *et al.*, Phys. Rev. D **72**, 094007 (2005).
- [83] M. Anselmino *et al.*, hep-ph/0511017.
- [84] M. Anselmino *et al.*, Phys. Rev. D **71**, 074006 (2005).

- [85] J. C. Collins *et al.*, Phys. Rev. D **73**, 014021 (2006).
- [86] V. Barone, A. Drago and P. G. Ratcliffe, Phys. Rept. **359**, 1 (2002).
- [87] Jefferson Lab Experiment E12-10-006, Spokespersons: J.-P. Chen, H. Gao (contact), X. Jiang, J. C. Peng, and A. Qian.
- [88] Jefferson Lab Experiment E12-11-007, Spokespersons: J.-P. Chen, J. Huang (contact), Y. Qiang, and W. B. Yan.
- [89] Jefferson Lab Experiment E12-11-108, Spokespersons: K. Allada, J.-P. Chen, H. Gao (contact), and Z.-E. Meziani.
- [90] D. Crabb *et al.*, Phys. Rev. Letts. **64**, 2627 (2008).
- [91] C. Keith *et al.*, Nucl. Instrum. Meth. A **501**, 327 (2003).
- [92] G. S. Atoian *et al.*, Nucl. Instrum. Meth. A **531**, 467 (2004).
- [93] G. S. Atoian *et al.*, Nucl. Instrum. Meth. A **584**, 291 (2008).
- [94] M. Anselmino and A. Prokudin, private communications.
- [95] J. Huang and Y. Qiang, Maximum likelihood estimation of asymmetry and angular modulation for transversity (2010), <http://www.jlab.org/~jinhuang/Transversity/MLE.pdf>.
- [96] T. Hobbs and W. Melnitchouk, Phys. Rev. D **77**, 114023 (2008).
- [97] A. D. Martin, R. G. Roberts, W. J. Stirling and R. S. Thorne, Eur. Phys. J. C **35**, 325 (2004).
- [98] S. Mantry, M. J. Ramsey-Musolf and G. F. Sacco, Phys. Rev. C **82**, 065205 (2010).
- [99] M. R. Buckley and M. J. Ramsey-Musolf, Phys. Lett. B **712**, 261 (2012).
- [100] M. Aaboud *et al.* (ATLAS Collaboration), JHEP **1710**, 182 (2017).
- [101] D. Androić *et al.* (Qweak Collaboration), Nature **557**, no. 7704, 207 (2018).
- [102] A. M. Sirunyan *et al.* (CMS Collaboration), JHEP **1904**, 114 (2019).
- [103] A. Falkowski, M. González-Alonso and K. Mimouni, JHEP **1708**, 123 (2017).
- [104] D. Becker *et al.*, arXiv:1802.04759 [nucl-ex].
- [105] F. E. Close and A. W. Thomas, Phys. Lett. B **212**, 227 (1988).
- [106] E. Sather, Phys. Lett. B **274**, 433 (1992).
- [107] E. N. Rodionov, A. W. Thomas and J. T. Londergan, Mod. Phys. Lett. A **9**, 1799 (1994).
- [108] G. P. Zeller *et al.* (NuTeV Collaboration), Phys. Rev. Lett. **88**, 091802 (2002). [Erratum: **90** 239902 (2003)].
- [109] J. T. Londergan and A. W. Thomas, Phys. Lett. B **558** 132 (2003).
- [110] J. T. Londergan and A. W. Thomas, J. Phys. G **31** 1151 (2005).

- [111] M. Gluck, P. Jimenez-Delgado and E. Reya, Phys. Rev. Lett. **95** 022002 (2005).
- [112] M. Traini, Phys. Lett. B **707**, 523 (2012).
- [113] I. C. Cloet, W. Bentz and A. W. Thomas, Phys. Rev. Lett. **102**, 252301 (2009).
- [114] W. Melnitchouk and A. W. Thomas, Phys. Lett. B **377** 11 (1996).
- [115] W. Melnitchouk, I. R. Afnan, F. Bissey and A. W. Thomas, Phys. Rev. Lett. **84** 5455 (2000).
- [116] S. I. Alekhin, Phys. Rev. D **63**, 094022 (2001).
- [117] R. J. Holt and C. D. Roberts, Rev. Mod. Phys. **82**, 2991 (2010).
- [118] A. Accardi, L. T. Brady, W. Melnitchouk, J. F. Owens and N. Sato, Phys. Rev. D **93**, no. 11, 114017 (2016).
- [119] Jefferson Lab Experiment E12-10-103 (MARATHON), spokespersons: G. G. Petratos, J. Arrington, M. Katramatou and R. D. Ransome.
- [120] A. J. Tropiano, J. J. Ethier, W. Melnitchouk and N. Sato, Phys. Rev. C **99**, no. 3, 035201 (2019).
- [121] S. Tkachenko *et al.* (CLAS Collaboration), Phys. Rev. C **89**, 045206 (2014), [Addendum: C **90**, 059901 (2014)].
- [122] Jefferson Lab Experiment E12-06-113, spokespersons: S. Bueltmann, M. Christy, H. Fenker, K. Griffioen, C. Keppel, S. Kuhn, W. Melnitchouk, V. Tvaskis.
- [123] M. B. Voloshin, Phys. Lett. B **476**, 297 (2000).
- [124] A. Ali *et al.* (GlueX Collaboration), Phys. Rev. Lett. **123**, no. 7, 072001 (2019)
- [125] S. J. Brodsky and G. A. Miller, Phys. Lett. B **412**, 125 (1997).
- [126] S. J. Brodsky, I. A. Schmidt, and G. F. de Téramond, Phys. Rev. Lett., **64**, 1011 (1990).
- [127] M. E. Luke, A. V. Manohar, and M. J. Savage. Phys. Lett. B **288**, 355 (1992).
- [128] A. B. Kaidalov and P. E. Volkovitsky, Phys. Rev. Lett., **69**, 3155 (1992).
- [129] G. F. de Téramond, R. Espinoza, and M. Ortega-Rodriguez. Phys. Rev. D **58**, 034012 (1998).
- [130] V. I. Shevchenko, Phys. Lett. B **392**, 457 (1997).
- [131] A. Hayashigaki, Prog. Theor. Phys., **101**, 923 (1999).
- [132] K. Yokokawa, S. Sasaki, T. Hatsuda, and A. Hayashigaki, Phys. Rev. D **74**, 034504 (2006).
- [133] T. Kawanai and S. Sasaki, Phys. Rev. D **82**, 091501 (2010).
- [134] K. Tsushima, D. H. Lu, G. Krein, and A. W. Thomas, Phys. Rev. C **83**, 065208 (2011).
- [135] K. Tsushima, D. H. Lu, G. Krein, and A. W. Thomas, AIP Conf. Proc. **1354**, 39 (2011).
- [136] M. Binkley *et al.*, Phys. Rev. Lett. **48**, 73 (1982).

- [137] B. H. Denby *et al.*, Phys. Rev. Lett. **52**, 795 (1984).
- [138] M. D. Sokoloff *et al.*, Phys. Rev. Lett. **57**, 3003 (1986).
- [139] R. Barate *et al.*, Z. Phys. C **33**, 505 (1987).
- [140] P. L. Frabetti *et al.*, Phys. Lett. B **316**, 197 (1993).
- [141] S. Aid *et al.*, Nucl. Phys. B **472**, 3 (1996).
- [142] J. Breitweg *et al.*, Z. Phys. C **76**, 599 (1997).
- [143] U. Camerini *et al.*, Phys. Rev. Lett. **35**, 483 (1975).
- [144] B. Gittelman *et al.*, Phys. Rev. Lett. **35**, 1616 (1975).
- [145] B. Knapp *et al.*, Phys. Rev. Lett. **34**, 1040 (1975).
- [146] R. L. Anderson, SLAC-PUB-1471.
- [147] D. Kharzeev, Proc. Int. Sch. Phys. Fermi **130**, 105 (1996).
- [148] D. Kharzeev, H. Satz, A. Syamtomov, and G. Zinovjev, Eur. Phys. J. C **9**, 459 (1999).
- [149] S. J. Brodsky, E. Chudakov, P. Hoyer, and J.M. Laget, Phys. Lett. B **498**, 23 (2001).
- [150] A. Sibirtsev, S. Krewald, and A. W. Thomas, J. Phys. G **30**, 1427 (2004).
- [151] M. A. Shifman, A. I. Vainshtein, and V. I. Zakharov, Phys. Lett. B **65**, 255 (1976).
- [152] V. A. Novikov, M. A. Shifman, A. I. Vainshtein, and V. I. Zakharov, Nucl. Phys. **B136**, 125 (1978).
- [153] . A. Shifman, A. I. Vainshtein, and V. I. Zakharov, Nucl. Phys. **B136**, 157 (1978).
- [154] A. Sibirtsev and M. B. Voloshin, Phys. Rev. D **71**, 076005 (2005).
- [155] R. B. Baldini, S. Pacetti and A. Zallo, arXiv:0812.3283 [hep-ph].
- [156] M. Ablikim *et al.* (BESIII Collaboration), Phys. Rev. Lett. **108**, 112003 (2012).
- [157] O. Gryniuk and M. Vanderhaeghen, Phys. Rev. D **94**, 074001 (2016).
- [158] J. J. Wu, R. Molina, E. Oset, and B.-S. Zou, Phys. Rev. Lett. **105**, 232001 (2010).
- [159] P. Bosted *et al.*, Phys. Rev. C **79**, 015209 (2009).
- [160] Jefferson Lab Experiment E12-07-106, spokespersons: P. Bosted, E. Chudakov (contact), and J. A. Dunne.
- [161] Jefferson Lab Experiment E12-12-006, spokespersons: K. Hafidi, X. Qian, N. Sparveris, Z.-E. Meziani (contact), and Z. W. Zhao.
- [162] Jefferson Lab Experiment E12-10-007, contact person: P. A. Souder.
- [163] X. Qian *et al.*, Phys. Rev. C **81**, 055209 (2010).

- [164] S. J. Brodsky *et al.*, Phys. Lett. B **498**, 23 (2001).
- [165] K. Schilling and G. Wolf, Nucl. Phys. **B61**, 381 (1973).
- [166] R. Fiore *et al.*, Phys. Rev. D **80**, 116001 (2009).
- [167] Aaij, Roel *et al.* (LHCb Collaboration), Phys. Rev. Lett., **115**, 072001 (2015).
- [168] C. Adloff *et al.*, Eur. Phys. J. C **13**, 371 (2000).
- [169] L. W. Whitlow, Ph. D. thesis, Stanford University, SLAC-Report-357 (1990).
- [170] Developed by J. W. Lightbody and J. S. O’Connell in 1988.
- [171] D. E. Wiser, Ph. D. thesis, Univ. of Wisconsin (1977).
- [172] X. Qian, Ph. D. thesis, Duke University.
- [173] T. Abe, Comp. Phys. Comm. **136**, 126 (2001).
- [174] PYTHIA, <http://projects.hepforge.org/pythia6/>, 2006.
- [175] Y. Kubota *et al.*, Nucl. Instrum. Meth. A **320** (1992).
- [176] Poisson Superfish, http://laacg1.lanl.gov/laacg/services/download_sfp.html.
- [177] G. Atoian *et al.*, Nucl. Instrum. Meth. A **584**, 291 (2008).
- [178] W. Anderson *et al.*, arXiv:1103.4277 [physics.ins-det].
- [179] B. Azmoun *et al.*, IEEE Trans. Nucl. Sci. **56-3**, 1544 (2009).
- [180] C. Lu and K. T. McDonald, Nucl. Instrum. Meth. A **343**, 135 (1994).
- [181] Y. Wang *et al.*, Chin. Phys. C **33**, 374 (2009).
- [182] A. Ali *et al.* (GlueX Collaboration), Phys. Rev. Lett. **123**, no. 7, 072001 (2019).
- [183] S. R. Beane *et al.*, Phys. Rev. D **91**, no. 11, 114503 (2015).
- [184] X. D. Ji, Phys. Rev. D **52**, 271 (1995).
- [185] X. D. Ji, Phys. Rev. Lett. **74**, 1071 (1995).
- [186] E12-12-006, “Near-Threshold Electroproduction of J/ψ with a 11 GeV Beam”, Spokespersons: K. Hafidi, Z.-E. Meziani (contact), X. Qian, N. Sparveris, and Z.-W. Zhao.
- [187] M. Karliner and J. L. Rosner, Phys. Lett. B **752**, 329 (2016).
- [188] V. Kubarovskiy and M. B. Voloshin, Phys. Rev. D **92**, no. 3, 031502 (2015).
- [189] A. N. Hiller Blin *et al.*, Phys. Rev. D **94** (2016) no.3, 034002.
- [190] Z. E. Meziani *et al.*, arXiv:1609.00676 [hep-ex].
- [191] S. J. Brodsky, P. Hoyer, C. Peterson, and N. Sakai, Phys. Lett. **93B**, 451 (1980).

- [192] S. J. Brodsky, C. Peterson and N. Sakai, Phys. Rev. D **23**, 2745 (1981).
- [193] W. C. Chang and J. C. Peng, Phys. Lett. B **704**, 197 (2011).
- [194] B. W. Adams *et al.*, arXiv:1603.01843.
- [195] M. Alfred *et al.*, [PID Consortium for an integrated program for Particle Identification \(PID\) at a future ElectronIon Collider](#), EIC Detector R&D Progress Report (2015).
- [196] E12-10-007 “Precision Measurement of Parity-violation in Deep Inelastic Scattering Over a Broad Kinematic Range” Contact person: P. Souder.
- [197] M. Anselmino and A. Prokudin, private communications. Predictions are based on the extractions of Ref. [198].
- [198] M. Anselmino *et al.*, arXiv:0807.0173.
- [199] W. Vogelsang and F. Yuan, private communications.
- [200] B. Pasquini, private communication.
- [201] X. Qian, Mod. Phys. Lett. A **27**, 1230021 (2012).
- [202] Y. Zhang *et al.*, Chin. Phys. C **36**, 610 (2012).
- [203] L. W. Whitlow, SLAC-Report-357 (1990).
- [204] J. W. Lightbody and J. S. O’Connell, Comp. Phys. **2**, 57 (1988).
- [205] D. E. Wiser, Ph. D. thesis, Univ. of Wisconsin (1977).
- [206] E. Chudakov *et al.*, [Study of modifying CLEO II magnet for SoLID](#).
- [207] Y. Kubota *et al.*, Nucl. Instrum. Meth. A **320**, 66 (1992).
- [208] D. M. Coffman *et al.*, IEEE Trans. Nucl. Sci. **37**, 1172 (1990).
- [209] X. Qian *et al.*, Phys. Rev. Lett. 107, (2012) 072003. J. Huang *et al.*, Phys. Rev. Lett. 108 (2012) 052001.
- [210] T.D. Averett, *et al.*, Nucl. Instrum. Meth. A **427**, 440 (1999).
- [211] J. Maxwell *et al.*, submitted to Nucl. Instrum. Meth. A.
- [212] C.D. Keith, *et al.*, Nucl. Instrum. Meth. A **684**, 27 (2012).
- [213] C.D. Keith, *et al.*, Nucl. Instrum. Meth. A **501**, 327 (2003).
- [214] Design Report rfq 14231, Oxford Instruments Nanotechnology Tools Ltd.
- [215] F. Sauli, Nucl. Instrum. Meth. A **386**, 531 (1997).
- [216] B. Ketzer *et al.*, Nucl. Phys. B (Proc. Suppl.) **125**, 368 (2003).
- [217] W. Xiong, *et al.*, Nature **575**, 147 (2019).
- [218] K. Gnanvo *et al.*, Nucl. Instrum. Meth. A **782**, 77 (2015).

- [219] K. Gnanvo *et al.*, Nucl. Instrum. Meth. A **808**, 83 (2016).
- [220] D. Di, PhD Thesis, University of Virginia, 2019.
- [221] M. Villa, *et al.*, Nucl. Instrum. Meth. A **628**, 182 (2011).
- [222] M. Alfonsi *et al.*, Nucl. Instrum. Meth. A **617**, 151 (2010).
- [223] D. Abbaneo *et al.*, Nucl. Instrum. Meth. A **718**, 383 (2010).
- [224] M.J. French *et al.*, Nucl. Instrum. Meth. A **466**, 359 (2001).
- [225] F. Sauli, RD51-NOTE-2012-007, Revised Sep. 21, 2012.
- [226] D. Abbaneo *et al.*, RD51-NOTE-2012-012, Nov. 16, 2012.
- [227] W. Whyte, Cleanroom Technology: Fundamentals of Design, Testing and Operation (2001).
- [228] P. Walker, *et al.*, J. Phot. Sci. **18**, 150 (1970).
- [229] J. M. Shaw *et al.*, IBM J. Res. Dev. **41**, 81 (1997).
- [230] R. Wang, Y. Huang and Z. Xiao, Nucl. Instrum. Meth. A **701**, 54 (2013).
- [231] S. P. Malace, B. D. Sawatzky and H. Gao, JINST **1309**, P09004 (2013).
- [232] Composite Mirror Applications, Inc. 1638 S. Research Loop, Suite 100 Tucson, Arizona 85710, <http://www.compositemirrors.com>
- [233] S. Amato *et al.* (LHCb Collaboration), [LHCb RICH Technical Design Report](#).
- [234] Hamamatsu flat panel type multianode photomultiplier tube assembly H8500 series specifications are found at http://jp.hamamatsu.com/products/sensor-etd/pd002/pd394/H8500C/index_en.html.
- [235] Amuneal Manufacturing Corporation. 4737 Darrah Street Philadelphia, PA 19124, USA. www.amuneal.com.
- [236] Magnetic Shield Corporation. Perfection Mica Company. 740 N. Thomas Drive, Bensenville, IL 60106 U.S.A www.magnetic-shield.com.
- [237] GEMC: A GEant4 Monte Carlo, <https://gemc.jlab.org/gemc/html/index.html>.
- [238] GEANT4: A toolkit for the simulation of the passage of particles through matter: <http://geant4.web.cern.ch/>.
- [239] M. Artuso *et al.*, Nucl. Instrum. Meth. A **558**, 373 (2006).
- [240] A. Bulla, Ph.D. thesis, (1997); E. Fokitis *et al.*, Nucl. Instrum. Meth. A **371**, 255 (1996).
- [241] G.J. Barber *et al.*, Nucl. Instrum. Meth. A **593**, 624 (2008).
- [242] G. S. Atoian *et al.*, Nucl. Instrum. Meth. A **584**, 291 (2008).
- [243] H. Avakian *et al.*, Nucl. Instrum. Meth. A **417**, 69 (1998).

- [244] E. Picatoste Olloqui *et al.* (LHCb Collaboration), J. Phys. Conf. Ser. **160**, 012046 (2009).
- [245] Y. V. Kharlov *et al.*, Nucl. Instrum. Meth. A **606**, 432 (2009).
- [246] D. A. Morozov *et al.*, J. Phys. Conf. Ser. **160**, 012021 (2009).
- [247] ATLAS Tile Calorimeter Technical Design Report (1996).
- [248] L. Aliaga *et al.* (MINERvA Collaboration), Nucl. Instrum. Meth. A **743**, 130 (2014).
- [249] M. J. Varanda, M. David, A. Gomes and A. Maio, Nucl. Instrum. Meth. A **453**, 255 (2000).
- [250] LHCb Tracker Upgrade Technical Design Report.
- [251] V. Sulkosky *et al.*, Nucl. Instrum. Meth. A **827**, 137 (2016).
- [252] Y. Wang *et al.*, Nucl. Instrum. Meth. A **538**, 425 (2005).
- [253] Y. Wang *et al.*, Nucl. Instrum. Meth. A **537**, 698 (2005).
- [254] A. Akindinov *et al.*, Nucl. Instrum. Meth. A **602**, 709 (2009).
- [255] A. Akindinov *et al.*, Nucl. Instrum. Meth. A **533**, 74 (2004).
- [256] Y. Wang *et al.*, Chin. Phys. C **33**, 374 (2009).
- [257] J. B. Wang *et al.*, JINST **7** P10004 (2012).
- [258] Jefferson Lab Experiment E08-027, spokespersons: A. Camsonne, J. P. Chen, D. Crabb and K Slifer.
- [259] V. Gyurjyan *et al.*, J. Phys. Conf. Ser. **331**, 032013 (2011).
- [260] D. Lawrence, J. Phys. Conf. Ser. **119**, 042018 (2008).
- [261] M. Al-Turany *et al.*, J. Phys. Conf. Ser. **396**, 022001 (2012).
- [262] C. Green *et al.*, J. Phys. Conf. Ser. **396**, 022020 (2012).
- [263] See *e.g.*, E. Sexton-Kennedy, A Review of Event Processing Frameworks used in HEP, <http://indico.cern.ch/event/304944/contributions/1672690/>.
- [264] R. Brun and F. Rademakers, Nucl. Instrum. Meth. A **389**, 81 (1997).
- [265] ROOT/C++ Analyzer for JLab Hall A, <https://hallaweb.jlab.org/podd>, code repository <https://github.com/JeffersonLab/analyzer>.
- [266] <https://github.com/sPHENIX-Collaboration/coresoftware>.
- [267] <https://cdcvns.fnal.gov/redmine/issues/15372>.
- [268] M. Al-Turany *et al.*, J. Phys. Conf. Ser. **664**, 072001 (2015).
- [269] Fluka, <http://www.fluka.org>
- [270] Geant4, <http://geant4.cern.ch/>

- [271] GEMC, <https://gemc.jlab.org/>
- [272] Poisson superfish, http://laacg1.lanl.gov/laacg/services/download_sf.phtml.
- [273] Tosca, <http://www.chilton-computing.org.uk/inf/eng/electromagnetics/p001.htm>.
- [274] C. Altunbas *et al.*, Nucl. Instrum. Meth. A **490**, 177 (2002).
- [275] J. Huston *et al.*, JHEP 07 (2002) 012.
- [276] David E. Wiser, PhD thesis, Wisconsin University Madison, 1977.
- [277] S. Riordan, X. Zheng, Z. W. Zhao and N. Ton, Comparison between Wiser π^- rates calculation and data from transversity and PVDIS experiments, 2014.
- [278] R. Beminiwattha, https://hallaweb.jlab.org/DocDB/0002/000212/001/HallD_Gen_Summary.pdf.
- [279] Mark Ito, private communication (2014).
- [280] Eugene Chudakov, private communication (2014).
- [281] V. M. Budnev, I. F. Ginzburg, G. V. Meledin and V. G. Serbo, Phys. Rept. **15**, 181 (1975).
- [282] J. Beringer *et al.* (Particle Data Group), Phys. Rev. D **86**, 010001 (2012).
- [283] Y.-S. Tsai, Rev. Mod. Phys. **46**, 815 (1974).
- [284] R. E. Kalman, Trans. ASME J. Basic Eng. **82**, 35 (1960).
- [285] R. Mankel, Rept. Prog. Phys. **67**, 553 (2004).
- [286] M. Capogni, E. Cisbani, G.M. Urciuli, [Note on GEM digitization modeling](#).
- [287] H. Avakian *et al.*, Nucl. Instrum. Meth. A **417**, 69 (1998).
- [288] A. Bacchetta *et al.*, JHEP **0702**, 093 (2007).
- [289] S. Dulat *et al.*, Phys. Rev. D **93**, 033006 (2016).
- [290] D. de Florian, R. Sassot and M. Stratmann, Phys. Rev. D **75**, 114010 (2007).
- [291] M. Anselmino *et al.*, Phys. Rev. D **87**, 094019 (2013).
- [292] C. Lefky and A. Prokudin, Phys. Rev. D **91**, 034010 (2015).
- [293] L. P. Kaptari, A. Del Dotto, E. Pace, G. Salmè and S. Scopetta, Phys. Rev. C **89**, 035206 (2014).
- [294] A. Del Dotto, private communication.
- [295] I. Akushevich, N. Shumeiko and A. Soroko, Eur. Phys. J. C **10**, 681 (1999).
- [296] I. Akushevich, A. Ilyichev and M. Osipenko, Phys. Lett. B **672**, 35 (2009).

- [297] J. Pumplin *et al.*, JHEP **0207**, 012 (2002).
- [298] “SoLID Preliminary Conceptual Design Report”, The SoLID Collaboration, unpublished (2014).
- [299] A. Narayan *et al.*, Phys. Rev. X **6**, no. 1, 011013 (2016).
- [300] H. Spiesberger, Phys. Rev. D **52**, 4936 (1995).
- [301] M. E. Christy and P. E. Bosted, Phys. Rev. C **81**, 055213 (2010).
- [302] S. Martoiu, H. Muller and J. Toledo, 2011 IEEE Nuclear Science Symposium Conference, Record 2036 (2011).
- [303] M.J. French *et al.*, Nucl. Instrum. Meth. A **466**, 359 (2001).
- [304] G. Iakovidis (ATLAS Muon Collaboration), PoS MPGD **2017**, 035 (2019).
- [305] A. Neiser *et al.*, J. Instrum. **8**, C12043 (2013).
- [306] E12-12-006, “Near-threshold Electroproduction of J/ψ with a 11 GeV Beam”, Spokespersons: K. Hafidi, Z.-E. Meziani (contact), X. Qian, N. Sparveris, and Z.-W. Zhao.
- [307] *The FLUKA code: Description and benchmarking* G. Battistoni, S. Muraro, P.R. Sala, F. Cerutti, A. Ferrari, S. Roesler, A. Fassio, J. Ranft, Proceedings of the Hadronic Shower Simulation Workshop 2006, Fermilab 6–8 September 2006, M. Albrow, R. Raja eds., AIP Conference Proceeding 896, 31-49, (2007).
- [308] *FLUKA: a multi-particle transport code* A. Ferrari, P.R. Sala, A. Fassio, and J. Ranft, CERN-2005-10 (2005), INFN/TC_05/11, SLAC-R-773.
- [309] K. Y. Hare *et al.*, Phys. Rev. D **68**, 072001 (2003).
- [310] A. Vasilescu and G. Lindstroem, http://hepweb03.phys.sinica.edu.tw/opto/Irradiation/Documents/NIEL_scaling/gunnar.htm.
- [311] https://solid.jlab.org/DocDB/0000/000025/001/zana_solid_radiation_and_activation_mar_2017.pdf.
- [312] J. Benesch *et al.* (MOLLER Collaboration), arXiv:1411.4088 [nucl-ex].
- [313] K. Abe *et al.* (SLD Collaboration), Phys. Rev. Lett. **84**, 5945 (2000).
- [314] N. Falletto *et al.*, Nucl. Instrum. Meth. A **459**, 212 (2001).
- [315] A. Narayan *et al.*, Phys. Rev. X **6**, no. 1, 011013 (2016).
- [316] N. Vansteenkise, P. Vignolo, and A. Aspect, J. Opt. Soc. Am. A **10**, no. 10, 2240 (1993).
- [317] R.J. Loewen, SLAC-R-0632 (2003).
- [318] S. Miyoshi *et al.*, Nucl. Instrum. Meth. A **623**, 576 (2010).
- [319] A. Variola *et al.*, Nucl. Instrum. Meth. A **608**, S83 (2009).
- [320] V. Brisson *et al.*, Nucl. Instrum. Meth. A **608**, S75 (2009).

- [321] A. Denner and S. Dittmaier, Nucl. Phys. B **540**, 58 (1999).
- [322] M. Friend *et al.*, arXiv:1108.3116 [physics.ins-det].
- [323] G. W. Ford and C. J. Mullin, Phys. Rev. **108**, 477 (1957) [Erratum: **110**, 1485(E) (1958)].
- [324] A. M. Bincer, Phys. Rev. **107**, 1434 (1957).
- [325] P. Stehle, Phys. Rev. **110**, 1458 (1958).
- [326] A. Raćzka and R. Raćzka, Phys. Rev. **110**, 1469 (1958).
- [327] G. Alexander and I. Cohen, Nucl. Instrum. Meth. A **486**, 552 (2002).
- [328] M. Hauger *et al.*, Nucl. Instrum. Meth. A **462**, 382 (2001).
- [329] M. Loppacher, Inaugural Dissertation, Universität Basel, (1996).
- [330] L. V. de Bever *et al.*, Nucl. Instrum. Meth. A **400**, 379 (1997).
- [331] A. V. Glamazdin *et al.*, Fizika B **8**, 91 (1999).
- [332] E. A. Chudakov *et al.*, Prob. Atom. Sci. Tech. **40**, 43 (2002).
- [333] E. Chudakov and V. Luppov, IEEE Trans. Nucl. Sci. **51**, 1533 (2004).
- [334] E. Chudakov and V. Luppov, Eur. Phys. J. A **24**, S2, 123 (2005).
- [335] P. S. Cooper *et al.*, Phys. Rev. Lett. **34**, 1589 (1975).
- [336] B. Wagner *et al.*, Nucl. Instrum. Meth. A **294**, 541 (1990).
- [337] J. Arrington *et al.*, Nucl. Instrum. Meth. A **311**, 39 (1992).
- [338] K. B. Beard *et al.*, Nucl. Instrum. Meth. A **361**, 46 (1995).
- [339] H. R. Band, G. Mitchell, R. Prepost and T. Wright, Nucl. Instrum. Meth. A **400**, 24 (1997).
- [340] P. Steiner, A. Feltham, I. Sick, M. Zeier and B. Zihlmann, Nucl. Instrum. Meth. A **419**, 105 (1998).
- [341] G. G. Scott and H. W. Sturmer, Phys. Rev. **184**, 490 (1969).
- [342] J. Crangle and G. M. Goodman, Proceedings of the Royal Society of London, Series A **321**, 477 (1971).
- [343] C. D. Graham, Jr., J. Appl. Phys. **53**, 2032 (1982).
- [344] G. G. Scott, Rev. Mod. Phys. **34**, 102 (1962).
- [345] E. C. Stoner and E. P. Wohlfarth, Phil. Trans. Royal Soc. London, Series A **240**, 599 (1948).
- [346] L. G. Levchuk, Nucl. Instrum. Meth. A **345**, 496 (1994).
- [347] M. Swartz *et al.*, Nucl. Instrum. Meth. A **363**, 526 (1995).
- [348] D. Gaskell, D. G. Meekins, and C. Yan, Eur. Phys. J. A **32**, 561 (2007).

- [349] E. Chudakov and V. Luppov, Tech. Rep., JLab, 2005, http://www.jlab.org/~gen/hyd/loi_3.pdf.
- [350] I. F. Silvera, Phys. Rev. B **29**, 3899 (1984).
- [351] I. F. Silvera and J. T. M. Walraven, Phys. Rev. Lett. **44**, 164 (1980).
- [352] I. F. Silvera and J. T. M. Walraven, Prog. Low Temp. Phys. **X**, 139 (1986).
- [353] T. Roser *et al.*, Nucl. Instrum. Meth. A **301**, 42 (1991).
- [354] M. Mertig, V. G. Luppov, T. Roser, and B. Vuaridel, Rev. Sci. Instrum. **62**, 251 (1991).
- [355] M. D. Miller and L. H. Nosanow, Phys. Rev. B **15**, 4376 (1977).
- [356] M. Poelker, J. Grames, J. Hansknecht, R. Kazimi, J. Musson, Phys. Rev. ST Accel. Beams **10**, 053502 (2007).
- [357] https://hallaweb.jlab.org/12GeV/SoLID/download/doc/Estimated_SoLID_Offline_Effort-v4.ods.
- [358] <https://halldsvn.jlab.org/repos/trunk/docs/offline/ProjectProgress/OfflineComputingActivities2013.xlsx>.
- [359] EventDisplay3D project in the *art* workbook, available from <https://cdcvs.fnal.gov/redmine/projects/art-workbook>.

Appendix A Summary of Subsystems

In responding to the recommendations from JLab physics division, we add this section, aiming to provide a brief description of the key assumptions for each subsystem, namely where the subsystem will be built, which groups will build it, where the fund comes from, how long it will take and what is needed from JLab to support it. Anything unique to the system which drives the project will also be listed.

A.1 Magnet

The solenoid magnet provides the magnetic field required for measuring the momentum of the track in the experiment. The detectors for SoLID will be mounted on the magnet yoke. The collaboration has identified the CLEO-II magnet as the one to be used for SoLID after modifications. The JLab Hall A engineering team, with assistance from JLab Engineering Division and also from the SoLID collaboration, is responsible for the transportation and modification of the magnet.

The coils and cryostat of the magnet arrived at JLab in 2016 and the exterior steel arrived at JLab in August 2019. The transportation (disassembling and shipping) of the magnet from Cornell to JLab and initial static and low current cold test to verify the magnet is in good health for physics experiments is covered by the JLab Physics Division (operation fund). The cost for the modifications specific to SoLID is to be part of the SoLID MIE to DOE.

The refurbishing of the CLEO II magnet started in the Fall of 2019 and is scheduled to take approximately 26 months. Modification specific to SoLID will be part of the project and will take 2.5 years to complete. JLab will perform most of the work. Space has been allocated at JLab for refurbishing, modification and storage.

A.2 GEM

- **Where the system will be built and who will build it:** It is assumed that the SoLID GEM tracker will be built by the GEM detector groups at the University of Virginia (Liyanage) and Temple University (Sorrow). Five member institutions of the Chinese SoLID GEM collaboration will collaborating: CIAE, LZU, THU,USTC and IMP.

- **Who will fund it ?**

The funding for the SoLID GEM tracker will be requested from the US DoE as part of the SoLID baseline project. The Chinese institutions plan to also apply to the Chinese funding agencies. If the Chinese funding application is successful, it will be used for enhancement to the baseline design.

- **How long will it take ?**

The pre-R&D phase of the project would take about 1.5 years. It will take 4 more years for engineering and design, prototyping, construction, testing and installation.

- **What is needed from JLab to support it ?**

Jlab engineering support will be needed for the design of the GEM module mounting structure, and DAQ support will be needed to integrate the GEM readout into the hall A DAQ framework.

A.3 Light Gas Cherenkov

The light gas Cherenkov prototyping and construction will be performed by the Temple University Nuclear Physics Group led by Dr. Sparveris and the Medium Energy Physics group at Argonne National Lab led by Dr. Zein-Eddine Meziani. All of the construction will be done at these two institutions, with the possible exception of any specific materials needed to adapt and integrate the subsystem into the larger SoLID detector. Funds for the project will be requested by the groups from DOE and/or NSF. The light gas Cherenkov detector will also be designed by the two groups with the expectation that communication with the SoLID project engineers at Jefferson Lab, as well as access to schematics and documentation, will be made available concerning interfacing the sub-detector design with the larger SoLID design. We expect the project to take 4 years total from design to delivery.

A.4 Heavy Gas Cherenkov

The Heavy Gas Cherenkov (HGC) detector will provide the required particle identification of pions in a background of kaons. It will be built by Prof. Haiyan Gao's Medium Energy Physics group at Duke University with engineering and technical help from the Triangle Universities Nuclear Laboratory (TUNL), and by Prof. Garth Huber's group from the University of Regina in Canada. Funds for the project will be requested from DOE and/or from NSF. It will take about 4 years and 3 months to design and build the detector. We need the JLab Design Authority to review the design and the test plan to ensure that the pressure system satisfies the JLab ESH&Q rules. The JLab Hall A engineering group will design and build the gas system and help with tests and the installation. We also expect that the JLab electronics group will help design and support the readout electronics.

A.5 Electromagnetic Calorimeter and Scintillator-Pad Detector

The Electromagnetic Calorimeter (EC), in combination with other detectors, provides the main trigger and the particle identification for the SoLID experiments. The SPDs in the SIDIS configuration will provide photon rejection and TOF (for large angle).

- **Who will fund it ?**

The funding for EC and SPD will be requested from the US DOE as part of the SoLID baseline project.

- **Who will build it?**

We currently plan to procure from SDU and THU groups, members of the SoLID collaboration, the fully assembled shashlyk and preshower modules including initial cosmic testing. The Russian IHEP can also build both preshower and shashlyk modules, which can serve as an alternate/backup vendor.

SPDs will be procured from Eljen and assembled by the UVa group.

- **How long will it take ?**

It will take two years to finalize the design of the calorimeter and its module supporting frame, and to design PMT bases for readout. Construction will take slightly more than two years if assuming 10 assembly stands (each module must be compressed for 48-72 hours on the stand, thus 1800 modules will require 90 weeks). Modules will be shipped to JLab and tested immediately using cosmics. Modules will be loaded to the supporting frame once testing is complete.

Construction of SPD modules will take 6-12 months depending on the availability of cosmic test stands.

- **What is needed from JLab to support it ?**

We expect the JLab electronics group will design and test the PMT bases with preamp gain specified by SoLID. Shashlyk modules need to be cosmic-tested upon receiving from the construction site, and it is most convenient to conduct such tests at JLab. We will need test lab space to stack shashlyk modules and we expect JLab to provide cosmic testing stands along with partial staff support to assist with the tests.

A.6 MRPC

The Multi Gap Resistive Plate Chamber (MRPC) will be used by the SIDIS experiment for hadron particle identification by means of time of flight in the enhanced baseline configuration. A MRPC can achieve a timing resolution better than 50 ps under clean condition. Under more realistic conditions with large background rates, timing resolution of 80 ps has been demonstrated. An R&D effort is ongoing with a funding from NSFC aiming to improve the time resolution to better than 30 ps, which is needed for Kaon particle identification.

- **Who will build it:**

Tsinghua University and USTC;

- **Where the system will be built:**

At Tsinghua University, Beijing; readout system at USTC, HEfei, China;

- **Who will fund it:**

NSFC (China) for the detector and for the readout system.

- **How long will it take:**

4 years

- **What is needed from JLab to support it:**

Beam tests will be needed at JLab including electronics and DAQ system in order to test the detector and optimize it under realistic beam conditions. In the enhanced configuration, since it is planned to include the MRPC in the trigger to reduce the background, a special board from JLab will be required to send the logic signals to the trigger.

- **Anything unique to that system that's a project driver:** This is the first high rate TOF system in hadron physics experiments and is needed for the Kaon particle identification and also will enhance the pion particle identification.

A.7 DAQ

The SoLID experiment is a large acceptance detector designed to run at high luminosity. The trigger rates expected for PVDIS are of the order of 600 KHz and for SIDIS up to 100 KHz. This pipelined electronics is crucial to generate a selective trigger in the very large background present in the detector.

- **Where the system will be built and who will build:**

Jefferson Lab and Rutgers University with the group of Prof. Ronald Gilman's group will be

in charge of the high resolution timing measurement aspects of the development and production for the electronics and help with the testing of the Flash ADCs. (Similar to what was done for Hall D.)

- **Who will fund it?**

The electronics will be funded by the DOE request.

- **How long it will take?**

The project will take 1.5 years of preRD, 4 years of design, production and testing, and installation.

- **What is needed from JLAB to support it?**

Since SoLID will be using the Jefferson Laboratory Pipelined Electronics, the JLAB Fast electronics group will be largely involved in the development, tests and deployment of the electronics. An estimate of the electronics and DAQ group is summarized in the table in addition to the JLab physics staff person.

Appendix B Software Development Effort Estimate

In the following, we present an estimate of the overall effort expected to be spent on developing all SoLID software for reference. Section B.3 discusses the components included in the project.

B.1 Total Effort Estimate

A preliminary assessment of the effort required to carry out all SoLID offline computing-related tasks, assuming adoption of the *art* framework [262] as an example, yields approximately 570 FTE-weeks. With contingency and overhead, explained below, this number increases to a total of 950 FTE-weeks, or about 22 FTE-years, assuming 44 work weeks per year per developer. A spreadsheet with this calculation can be found online [357].

This estimate covers simulations, reconstruction, calibrations and alignment, data challenges, production and analysis, where “analysis” represents a baseline set of replay configurations (PVDIS, SIDIS-³He, SIDIS-*p*, *J/ψ*), data quality checks, plots, production output variables, corrections, cuts and histograms. Not included in the estimate are DAQ software (firmware, front-end and trigger programming, run control etc.), online analysis and monitoring, and the intellectual effort to understand and interpret the results of the simulations and experimental data analysis. The latter is excluded because it is largely an open-ended creative process.

For each covered area, we have counted the work required to develop the actual software, test the code and validate results, coordinate efforts (meetings, wikis and similar), write and generate user and developer-level documentation, and to configure and monitor offline computing operations (simulation and production passes, data challenges). The time estimates at this point are subjective best guesses, based on our experience with similar efforts. They assume expert developers who are fully familiar with all task requirements, programming languages, framework paradigms, library APIs, tools etc. This yields a sum of 570 FTE-weeks. A contingency of 25% is added to this total to account for missed tasks, time overruns, etc. Furthermore, since developers are never the ideal experts assumed above, we estimated an average “developer efficiency” of 75%, *i.e.* on average each developer is assumed to spend an extra 1/3 of the estimated task time on preparations such as collecting requirements and learning. A more precise estimate of this efficiency factor would have to be made on a task-by-task basis under consideration of the personnel assigned to the task, information which is incomplete at this time. With contingency and overhead, the total effort estimate is 950 FTE-weeks.

B.2 Comparison with GlueX

In comparison to a similar project, GlueX have estimated their offline computing effort at 1866 FTE-weeks [358]. (This number excludes 110 FTE-weeks that GlueX allocate for “online” tasks (beamline commissioning and monitoring), which is outside of our scope.) It is unclear if the GlueX numbers include developer overhead, *i.e.* the time spent on task preparations and learning discussed above, but given the generous allowances made generally, we assume that they do.

The offline computing effort requirements estimated by GlueX and SoLID are summarized in Table 40. To make the GlueX estimates comparable to ours, we combined certain line items of the GlueX offline computing effort document [358] as follows:

- The quoted “Simulation” effort includes “Geant3 simulation”, “Geant4 simulation” plus 1/4 of “Integration/QC” and “Coordination” (total of 16.5 FTE-weeks) from the Miscellaneous section.

- “Reconstruction” counts all of “Reconstruction” plus “DAQ Translation”, “Event Viewer”, “Documentation”, “Integration of Slow Controls”, 1/2 of “Recon/analysis code Q/A” and again 16.5 FTE-weeks for integration and coordination.
- “Calibration” is taken as the total of “Calibrations” plus 1/4 of “Integration/QC” (11 FTE-weeks).
- “Production” comprises “DST Generation”, “MC Studies for Detector Optimization” and again 11 FTE-weeks of “Integration/QC”.
- “Analysis” takes all of “Analysis” less 1/2 of “Recon/analysis code Q/A” already counted under “Reconstruction” plus 1/2 of “Coordination”.
- The “Data Challenges” estimate is taken as is.

These allocations make the top-level categories approximately comparable.

Task Group	Labor estimate (FTE-weeks)		Main reasons for difference (see text)
	GlueX [358]	SoLID [357]	
Simulation	192	240	Simulation to be integrated into framework.
Reconstruction	787	335	Adoption of existing framework. Re-use of algorithms. Smaller number of subsystems.
Calibration	275	103	Smaller number of subsystems.
Production	275	155	Standard data format. Re-use of workflow tools.
Analysis	275	94	No PWA analysis and no grid implementation of analysis.
Data Challenges	62	23	No PWA data challenge.
Totals	1866	950	

Table 40: Offline computing effort estimates for SoLID and GlueX

SoLID estimates a larger simulation effort than GlueX, possibly because GlueX make approximate estimates of time already spent on finished work, while SoLID is using a detailed breakdown of anticipated future tasks. Also, SoLID plans to integrate simulations into the overall software framework, while GlueX’s simulations are standalone.

The estimated SoLID effort for reconstruction is significantly lower than GlueX’s. The difference is to a great extent due to the fact that SoLID proposes to adopt an existing framework rather than write a new one and that SoLID anticipates to reuse well-tested existing algorithms for standard tasks such as track fitting, *e.g.* from the `genfit` library, and calorimeter cluster reconstruction. Documentation effort is reduced in SoLID’s case also due to the already very good user-level documentation of the proposed *art* framework. Furthermore, the difference can be attributed to the smaller number of detector subsystems in SoLID than in GlueX, 5 vs. 7, the lower complexity of these systems (one vs. two tracker systems, Cherenkovs vs. multiple calorimeter systems), and the more challenging multi-particle final state reconstruction and PID in GlueX. Lastly, a SoLID

event viewer can be readily assembled from an existing MC geometry with minimal effort (days vs. months) using ROOT's `TEve` framework within *art*, as demonstrated by *art* example code [359].

Calibration effort for SoLID is also estimated lower than in GlueX, again in part due to fewer main detector systems, smaller channel counts and easier calibration of SoLID's GEMs vs. GlueX's drift chambers.

The lower estimated time for Production (DST generation) is attributable to the fact that we do not anticipate spending time on developing and maintaining a custom file format (it is defined by *art*) and expect to be able to reuse the job control and workflow tools currently under development for GlueX and CLAS12.

Finally, SoLID estimates much lower analysis effort than GlueX because no kinematic fitting and PWA analysis is foreseen for SoLID nor is SoLID planning a grid implementation at this point as the JLab compute farm resources are expected to be sufficient for us. For similar reasons, our estimate for data challenges is lower.

B.3 Effort Required for Project Goals

Within the scope of the project, we aim to achieve the following goals for software and simulations:

1. Put in place an end-to-end simulation, digitization and reconstruction chain in order to provide an integrated software environment for essentially all SoLID data processing⁴.
2. Carry out simulations necessary to inform the design of detector subsystems and other hardware components (shielding, DAQ and trigger, etc.), optimize the figures-of-merit of experiments, and quantify and understand experimental backgrounds.
3. Provide reconstruction and analysis tools to facilitate experiment commissioning and initial data quality assessment.

Selecting from the detailed task list provided in [357] only those software-related tasks with direct bearing on these project goals, we arrive at a base effort of 96 FTE-weeks to carry out design-relevant simulations. Ideally, this labor would be expended early in the project's lifetime, say during the first 1–1.5 years, since it is intended to guide later R&D. Task durations are set accordingly. Similarly, we arrive at a base effort of 139 FTE-weeks for implementing the commissioning phase data analysis infrastructure and basic reconstruction algorithms, such as track reconstruction, detector/PID analysis, event display, etc. Development or porting (from existing prototypes) of these components could be done in parallel to the simulations, but in practice might start somewhat later so that simulated data for testing reconstruction routines are available and experience with the software environment has been gained. Duration of the reconstruction software development is expected to be 1.5 years. 235 out of the total 570 FTE-weeks of software base effort, estimated in section B.1 above, are thus within project scope.

We intend to meet the software-related project goals within approximately two years from the start of the project. 235 FTE-weeks of effort are expected to be covered by project funds. The remaining software labor of 335 FTE-weeks is expected to be funded externally from university and lab research and/or operations budgets.

⁴Physics event generators and final interactive analysis will be run outside of the framework. Event generation can be a very compute-intensive task well suited for HPC machines, where deploying the full framework may be too resource-consuming and impractical. Interactive analysis is best suited for ROOT and similar tools, which are standalone packages.